The superconducting properties, composition and microstructure of nanocrystalline $A15\ \textnormal{Nb}_{3}(\textnormal{Al}_{1-x}\textnormal{Ge}_{x})$ superconductors for high magnetic field applications

PUSCEDDU, ELISABETTA

The superconducting properties, composition and microstructure of nanocrystalline A15 $Nb_3(Al_{1-x}Ge_x)$ superconductors for high magnetic field applications

Elisabetta Pusceddu

Department of Physics, University of Durham, United Kingdom

2010

Abstract

We report on the fabrication and properties of state-of-the-art nanocrystalline $Nb_3Al_{1-x}Ge_x$ superconductors with $0 \leq x \leq 1$. High-energy ball milling was used to produce disordered nanocrystalline powders from binary compounds and from pure elemental powders. A detailed analysis of powders milled for up to 30 h was performed using X-ray diffraction, differential scanning calorimetry and AC magnetic moment measurements. Powders milled for 6 h (bcc) and 20 h (amorphous) were consolidated using a hot isostatic press (HIP) operating at 2000 atm in a temperature range from 600 ^{o}C to 1200 ^{o}C. The role of isochronal post-HIP heat treatments was investigated for those materials HIP'ed at 600 ^{o}C and 1200 ^{o}C. For comparison purposes, heat treatments were also performed on milled powders.

Nanocrystalline bulk materials were characterized using a.c. magnetometry, resistivity and SQUID measurements in magnetic fields up to 9 T to measure the critical temperature and the upper critical field. X-ray diffraction and scanning electron microscopy coupled with energy dispersive X-ray analysis were used to investigate the constituent phases, the distribution of compositions and to estimate the volume phase percent of each phase.

Bulk materials fabricated from milled compounds showed a partial crystallisation recovery after HIP'ing at 600 ^{o}C but subsequent annealing does not further improve the superconducting properties. For material fabricated from elemental powders, after equivalent processing using milling and HIP'ing, the material is more disordered. In contrast to compound precursors, post-HIP annealing produces significant changes in the superconducting properties. In particular, a strong enhancement of T_C and B_{C2} was achieved after a post-HIP anneal of nanophase Nb_3Ge and $Nb_3Al_{1-x}Ge_x$ materials. In this work, bulk material fabricated from milled elemental powders and HIP'ed at 600 ^{o}C produced Nb_3Ge (A15) in bulk form with record T_C values of ~ 12 K and B_{C2}(T) ~ 13 T. We find that the role of the optimal post-HIP anneal of highly disordered material is to enhance the A15 crystal nucleation while minimising the crystallisation of oxides and secondary phases that occurs at higher temperatures and competes with superconductivity.

Publications

E. Pusceddu and D.P. Hampshire "*Nanocrystalline bulk Nb_3Ge with a critical temperature of 12 Kelvin*", Applied Physics Letters (Submitted, July 2010).

E. Pusceddu and D.P. Hampshire "*Superconducting properties and microstructure of nanocrystalline bulk $Nb_3(Al,Ge)$*", Journal of Applied Physics (Submitted, July 2010).

E. Pusceddu, S. Charlton, D.P. Hampshire "*Nanocrystalline Nb-Al-Ge mixtures fabricated by using wet mechanical milling*", Journal of Physics: Conference Series, 97 (2008) 012241.

S. Sanna, S. Agrestini, M. Filippi, G. Concas, F. Cogiu, E. Pusceddu, N.L. Saini, A. Bianconi "*The phenomenological relation between superconductivity and the planar Cu-O bond length in cuprate: the case of $Ca_xLa_{1-x}Ba_{1.75-x}La_{0.25+x}Cu_3O_y$*" to be submitted to the Journal of Superconductivity or European Physics Journal B.

Conferences and courses

IoP Superconductivity Group seminar, Development and applications of HTS conductors, 15 January 2010, Institute of Physics, London.

The European Conference of the Applied Superconductivity, September 13-17, 2009, Dresden, Germany.

Oral presentation: "*Fabrication of nanocrystalline Nb_3Ge and $Nb_3Al_{0.7}Ge_{0.3}$ superconductors from elemental powders for high field applications*" E. Pusceddu and D.P. Hampshire

IoP Annual general meeting, January 2009, London.

Poster presentation: "*Fabrication of nanocrystalline $Nb_3(Al_{1-x}Ge_x)$ superconductors for high fields applications*" E. Pusceddu and D.P. Hampshire

Applied Superconductivity Conference, August 17-22, 2008, Chicago, Illinois USA.

Poster presentation: "*Fabrication of nanocrystalline $Nb_3(Al_{1-x}Ge_x)$ superconductors for high fields applications*" E. Pusceddu and D.P. Hampshire; session title: Nb_3Al and others; poster number: 2MPN08.

Attended course: "Superconducting Materials Development - Current Status and Future Direction"

8th European Conference of the Applied Superconductivity, September 16-20, 2007, Brussels, Belgium.

Poster presentation: "*Nanocrystalline Nb-Al-Ge mixtures fabricated by using wet mechanical milling*" E. Pusceddu, S. Charlton, D.P. Hampshire; session title: Bulk materials; poster number: 0477.

7th SCENET School of Superconducting Materials and Applications, July 17-29, 2006, Camerino, Macerata, Italy.

Poster presentation: "*The relationship between the Cu-O distance and the transition temperature T_C in an isoelectronic family of cuprates*" E. Pusceddu, S. Sanna, S. Agrestini, M. Filippi, N. Saini, G. Concas and A. Bianconi.

Declaration and Copyright

I hereby declare that the work contained in this thesis is my own original work and nothing that is the result of collaboration unless otherwise stated. No part of this thesis has been submitter for a degree or other qualification at this or any other university.

E. Pusceddu

July 2010

Acknowledgements

I would like to thank many people who helped me over the past few years.

Firstly, to my supervisor Professor Hampshire, for his continuous guidance and endless encouragement during this Ph.D. course. I thank Professor Evans and everyone from his group for kind access to their XRD machines as well as helpful advice. I am grateful to Professor Flükiger for helpful discussion on the metallurgical aspect of superconductors. I would like to acknowledge Dr Terry for access to the SQUID magnetometer and for showing me how to make the measurements. For performing ICP measurements, I thank Dr Ottley. I would like to thank Dr Mossang for his hospitality at the Grenoble magnetic high field facility. I am grateful to Dr Mendis and Leon Bowen for their kind collaboration with the electron microscopy data. Special thanks go to Leon for performing the SEM measurements.

I wish to thank all of the support staff in the Department of Physics in Durham, often far beyond the call of duty. In particular, Phil Armstrong, Steve Lishman, Andrew Crosby and Malcom Robertshaw with the rest of the mechanical workshop for dealing with the unusual materials and piece of equipment I kept bringing in. For technical support, I express my gratitude to Wayne Dobby, John Summerill and Ian Manfren. I would also like to thank Dr Stockdale, Andrew Hunter and Ian Johnson for IT assistance. I wish to thank Norman Thompson, Duncan McCallum, David Pattinson for help with the safety issue and Dr Woodward, Tabitha Willis, Claire Davies, Clare Thompson, Sarah Noble, Vicki Greener, Sue Little, Ashley Crosby for administrative and secretarial work.

In the superconductivity group, I acknowledge all present and previous members for the benefit of their expertise and for being fabulous people. Especially Dr Armstrong, Dr Higgins, Dr Lu, Dr Xiang, Stephen Pragnell and Mark Raine for constructive discussion, prompt help during computer-related issue and assistance in the lab. Particular thanks go to Steven Charlton for his work on wet milled Nb_3Al.

Outside of work, I would like to thank my friends for making my stay in Durham more enjoyable. Finally, I thank my parents, Arianna, Ken and all my relatives for their support without whom I would not have completed this course.

My gratitude also goes toward the Regional Agency for Work of Sardinia for funding this research under grant no. MAB 2.2 2005-169 Prot.N10162 and to the Engineering and Physical Science Research Council.

Table of contents

Chapter 1

Introduction

Superconductivity is a unique and powerful phenomenon of nature that occurs in certain materials below a critical temperature. Superconducting materials can carry electricity without heating and can transmit current without losses. This state enables a range of innovative technological applications.

The major commercial applications of superconductivity currently involve the use of Low Temperature Superconductors (LTS) to produce stable and homogeneous magnetic fields. Since the current densities are high, superconducting magnet systems are quite compact and occupy only a small amount of laboratory space. Superconducting magnets are the main components of Magnetic Resonance Imaging (MRI) scanners [1], widely used in medical diagnostic to image the inside of objects and to study changes in living tissue. They are also essential for Nuclear Magnetic Resonance (NMR) spectrometers and plasma fusion reactors [2]. In high-energy physics research, superconducting magnets are used extensively to accelerate, focus, manipulate and analyse beams of charged particles. State-of-the-art superconducting magnets have made possible inside the Large Hadron Collider (LHC) the creation of collisions at energies of 14 TeV [3].

At the present time, the LTS materials of main interest are: NbTi, Nb_3Sn and $Nb_3(Al_{1-x}Ge_x)$. NbTi is the most important commercial superconductor because of its ductility, low cost and low filament size. Its applications cover a wide range of device and machines: high field NMR [4], LHC main ring, ATLAS detector and CSM detector [5]. Nb_3Sn is a leading high field superconductor for producing fields above 10 Tesla. Nb_3Sn strands are under development for the next generation of high field accelerator magnets (LHC Upgrade, ITER). They can provide high critical current ($3000A/mm^2$) at high field (12 T) [6]. Their properties depend strongly on the microstructure and composition. $Nb_3(Al_{1-x}Ge_x)$ superconductors are also being considered as a promising alternatives to Nb_3Sn since they have higher B_{C2} and better strain tolerance than Nb_3Sn. Although a practical fabrication process for developing $Nb_3(Al_{1-x}Ge_x)$ long length wires has not yet been established because of the poor workability of Al-Ge alloy, the developments in powder-in-tube technology [7] means that long-length $Nb_3(Al_{1-x}Ge_x)$ wires may yet become important .

The aims of the work reported in this thesis are the fabrication of state-of-the-art nanocrystalline A15 $Nb_3(Al_{1-x}Ge_x)$ bulk materials with $0 \leq x \leq 1$ and the improvement of their superconducting properties. The role of microstructure and composition when the grain size of these materials is refined down to the nanometre level was also investigated. High-energy ball milling was the metallurgical powder processing used to produce disordered nanocrystalline powders. The consolidation in bulk form was then performed using the hot isostatic press (HIP), HIP'ing and subsequent annealing and annealing alone. The different fabrication techniques provided nanocrystalline multiphase materials with unique microstructural and superconducting properties. Structurally disordered HIP'ed nano-sized materials have the potential to be a metastable precursor phase to produce optimised superconducting materials. This comprehensive research on $Nb_3(Al_{1-x}Ge_x)$ alloys investigates aspects of the physics and the metallurgy of superconductors, which play an important role in the research and the development of high-field superconductors and magnets.

This thesis is structured as follows: Chapter 2 presents the fundamental properties of superconductors, the major physical parameters, and the different groups of superconducting materials. The current understanding of nano-sized superconductors is also reported. Chapter 3 is a comprehensive review of $Nb_3Al_{1-x}Ge_x$ for $0 \leq x \leq 1$, which covers the basic A15 structure, the phase diagrams and the effect of structural and compositional factors on superconducting properties. The key fabrication methods are presented in conjunction with the results. Chapter 4 is an overview of the structure and the physical properties of nanocrystalline materials. The high-energy ball milling (HEBM), which is the powder metallurgical processing used in this work, is presented together with the relevant processing variables and characteristic properties of ball milled materials. Chapter 5 describes the experimental equipment and procedures used to investigate our nanocrystalline samples. The last three chapters contain the main experimental results and analysis. Chapter 6 reports the properties of wet milled Nb-Al-Ge elemental powders. Chapter 7 and 8 reports on the fabrication and the characterisation of dry mechanically alloyed Nb_3Ge and $Nb_3(Al_{1-x}Ge_x)$ with $0 \leq x \leq 0.3$, respectively. An innovative combination of well-known processing techniques was shown to produce optimised superconducting materials with a well-characterised microstructure. Some suggestion for future work is given by Chapter 9.

Chapter 2

Superconductivity-fundamental and nanocrystalline properties

2.1 Introduction

Chapter 2 is an introduction to the basics of superconductors. Section 2.2 describes their distinctive properties and the two classes of superconductors. Typical critical superconducting parameters including critical current are provided by section 2.3. The nature of the mixed state in clean and dirty superconductors is explained through relevant equations in section 2.4. In section 2.5, different groups of superconducting materials are reported including the pnictides. Finally in sections 2.6 and 2.7, we review recent results, the current understanding of nanocrystalline superconductors in high magnetic fields and the fabrication and properties of nanocrystalline Nb_3Al – which are important themes in this thesis.

2.2 Fundamentals of superconductors

Superconductors exhibit distinctive properties below a critical temperature (T_C).

Perfect conductivity. The complete disappearance of electrical resistivity was the first property of superconductors [8] that was discovered. Measurements for over two and a half years of the decay of electrical currents in a superconducting ring have yielded decay times of 10^5 years. This indicates that the resistivity of a superconductor is smaller than 10^{-23} Ωm. This value is 18 orders of magnitude smaller than the resistivity of copper at room temperature. The perfect conductivity disappears if the superconductor carries a current higher than the critical current [9] or the magnetic field is higher than the critical field.

Perfect diamagnetism. The property of zero magnetic field inside the bulk of the superconductor, known as the Meissner effect, was discovered by Meissner and Ochensfeld in 1933 [10]. The screening currents oppose the applied magnetic field so that the field $\mathbf{B} = \mu_0 (\mathbf{H} + \mathbf{M})$ is zero inside the superconductor. This unique effect cannot be explained just by the zero electrical resistance but must be considered a

separate unique property. The perfect diamagnetism disappears when the magnetic field exceeds a critical value.

Type I and II superconductors. Type I and type II superconductors can be distinguished by considering the magnetic field dependence of a superconductor at temperatures below T_C. In a large magnetic field the superconductor eventually goes through its transition from the superconducting to the normal state. The variation of the magnetization as a function of the magnetic field for the two types of superconductor is shown in Figure 2.1. Type-I superconductors exclude the magnetic flux (i.e. in the Meissner state) up to the thermodynamic critical field, H_c. At this value, the magnetization drops discontinuously to zero. Therefore a first order transition drives a type-I superconductor into the normal state. Type-II superconductors are in the Meissner state up to the lower critical field, H_{c1}. At H_{c1} the magnetic flux partially penetrates the superconducting specimen in the form of quantised lines ($\Phi_0 = 2.07 \times 10^5$ Wb). They are referred to as flux lines or fluxons. They are surrounded by vortices of supercurrents. The superconductivity is only destroyed and the normal state resistance restored when the applied field is greater than the upper critical field, H_{c2}. At this value the magnetization approach to zero is continuous. Hence, it is a second order transition that drives type-II superconductors into the normal state.

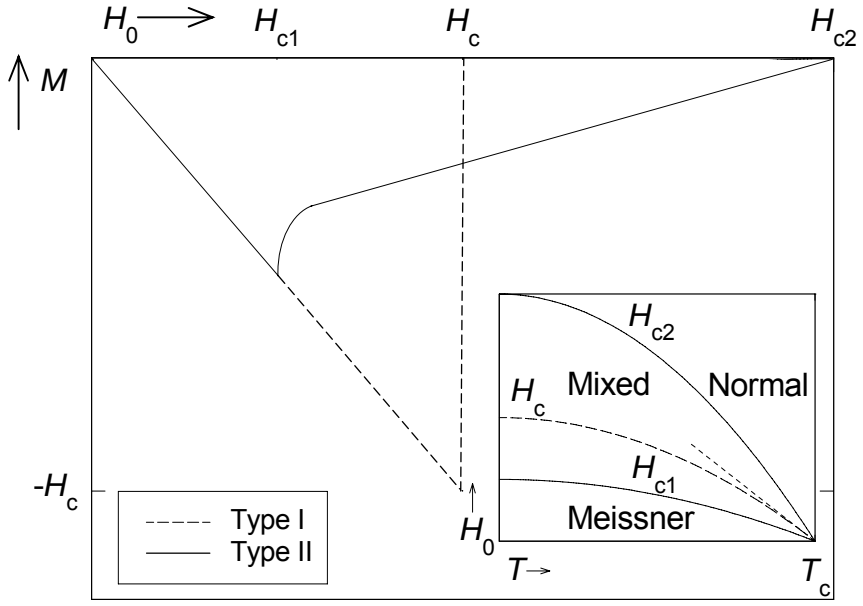

Figure 2.1 Variation of the magnetization as a function of the magnetic field for a type-I (broken line) and type-II superconductors (full line). Variation of critical field, B_{c1} and B_{c2}, as a function of temperature is also sketched [11].

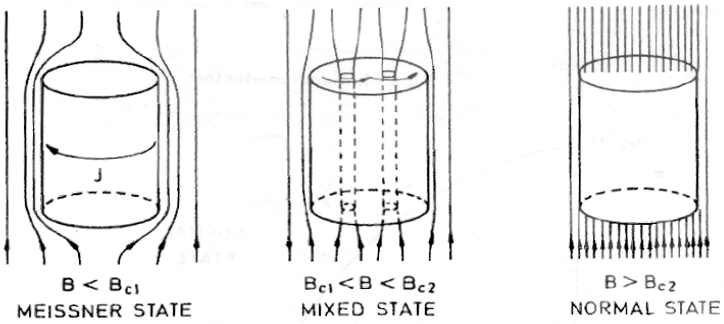

Figure 2.2 Flux penetration in the mixed state [9].

Figure 2.2 sketches the flux screening, the incomplete Meissner effect and the normal state type II superconductors.

2.3 Superconducting critical parameters

A schematic three-dimensional phase diagram of the A15 type superconductor is given in Figure 2.3 [12].

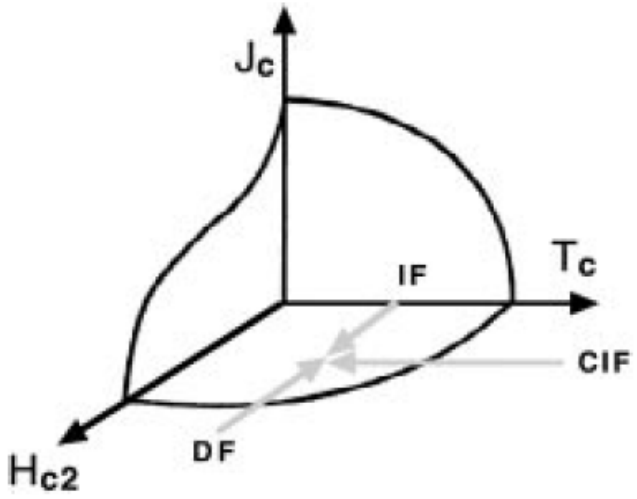

Figure 2.3 A schematic three-dimensional phase diagram of the A15 type superconductor. Various path to the final state in the field temperature plan are also shown: CIF, cooling in field; IF increasing field; DF, decreasing field [12].

There are three critical superconducting parameters that can characterize a superconducting material. They are: the superconducting transition temperature (also known as the critical temperature), T_C, the upper critical field, H_{c2} (or B_{C2}), and the critical current density, J_C (which is defined as the critical current, I_C, divided by the cross sectional area, S, of the superconductor). These three parameters characterise the utility of a superconducting conductor for high field applications. They are interconnected and strongly dependent on the microstructure of the superconductor.

Historically H_{C2} and T_C have been treated as intrinsic characteristic material parameters because they are less sensitive to the material microstructure. Table 2.1 shows their values for relevant A15 compounds.

Compound	T_C **(K)**	B_{C2} **(T)**
Nb_3Sn	18	24
Nb_3Al	18.8	29.5
Nb_3Ge	23	38
$Nb_3(Al,Ge)$	15	44

Table 2.1 Superconducting properties of some A15 materials; B_{C2} is given at 4.2 K [12].

The third parameter, J_C, depends strongly on the microstructure of the final conductor and on the procedure to approach the final state. Precipitates embedded in the superconducting layer can produce a dramatic decrease of J_C while H_{C2} and T_C keep almost the same value. The preservation of the continuity of the A15 layer and the maximization of the pinning force are relevant for industrial applications [12-14].

Flux lines experience a pinning force due to various kinds of imperfections (i.e. grain boundaries, stacking faults, points defect) [15]. Vortex lines experience also the Lorentz force when a current passes through the conductor. This force is perpendicular to both field and current direction and causes the fluxons to move. When this happens a voltage is generated across the sample. The balance between the Lorentz force and the pinning force establishes the critical state [16]. The global pinning force frequently exhibits scaling behavior with the reduced magnetic field b, ($b = B/B_{C2}$), Ginzburg-Landau parameter, κ, and upper critical field B_{C2}:

$$F_p = BJ_C = KB_{C2}^n b^p (1-b)^q / \kappa^m \tag{2.1}$$

where K is a geometrical function of the microstructure and p, q, n and m are characteristic parameters describing the pinning mechanisms.

2.4 Physical length-scales and the flux-line-lattice

The behaviour of superconductors in a magnetic field and the superconducting parameters are defined by two major physical parameters. The first one is the London penetration depth, λ_L, and the second important parameter is the intrinsic or BCS coherence length, ξ_0. λ_L describes the exponential decay of the magnetic field penetrating the interior of the superconductor and is given by:

$$\lambda_L = \frac{m}{\mu_0 n_s e^2} \tag{2.2}$$

where m is the effective electron mass, e is the electronic charge, μ_0 is the permeability of the vacuum, n_s is the density of superelectrons at zero temperature. ξ_0 represents the length scale over which the order parameter Ψ ($|\Psi|^2 = n_s$) can be considered constant and is given by:

$$\xi_0 = \frac{h v_F}{k_B T_C} \tag{2.3}$$

where v_F is the Fermi velocity ($E_F = m v_F^2$), h is the Planck constant, $2\Delta = 3.5 k_B T_C$ is the energy necessary to break an electron Cooper pair, k_B is the Boltzmann constant. Both λ_L and ξ_0 are temperature independent parameters.

Physical parameters in a dirty superconductor. In a dirty superconductor the mean free path of electrons, l_e, is much shorter than ξ_0. The penetration depth, λ, and the coherence length, ξ, become dependent on the electron mean free path and are given by:

$$\lambda(T) = 0.64 \lambda_L \sqrt{\xi_0 l_e} \left(\frac{T_C}{T_C - T} \right)^{1/2} \tag{2.4}$$

$$\xi(T) = 0.85 \sqrt{\frac{\xi_0}{l_e}} \left(\frac{T_C}{T_C - T} \right)^{1/2} \tag{2.5}$$

The ratio $\kappa = \lambda(T)/\xi(T)$ is the dimensionless Ginzburg-Landau parameter. The Ginzburg-Landau theory shows that superconductors are Type II if κ is larger than 0.707.

In the mixed state flux lines arrange themselves into a triangular flux-line lattice, called the Abrikosov lattice. In this configuration, the overall forces between vortices become zero. Figure 2.4 shows the dependence of the distance between flux lines in a triangular lattice and magnetic field. Figure 2.5 shows the screening currents, the variation in order parameter Ψ and the magnetic field in the mixed state at low and high magnetic field.

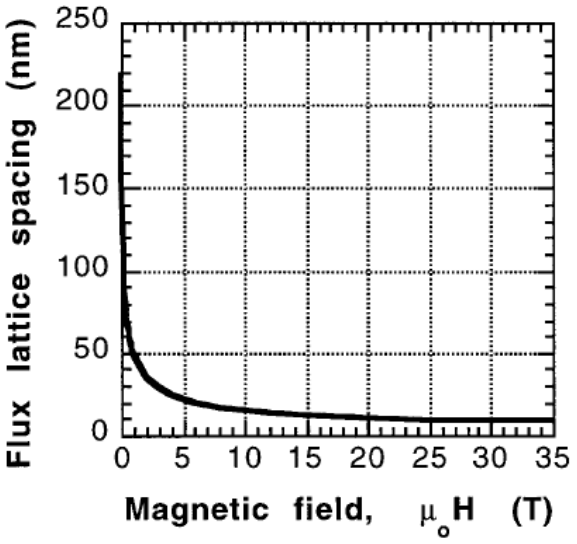

Figure 2.4 Dependence of the distance, a_0, between flux lines in a triangular lattice and magnetic field ($a_0 = 2\,\Phi_0/3^{0.5}B$) [12].

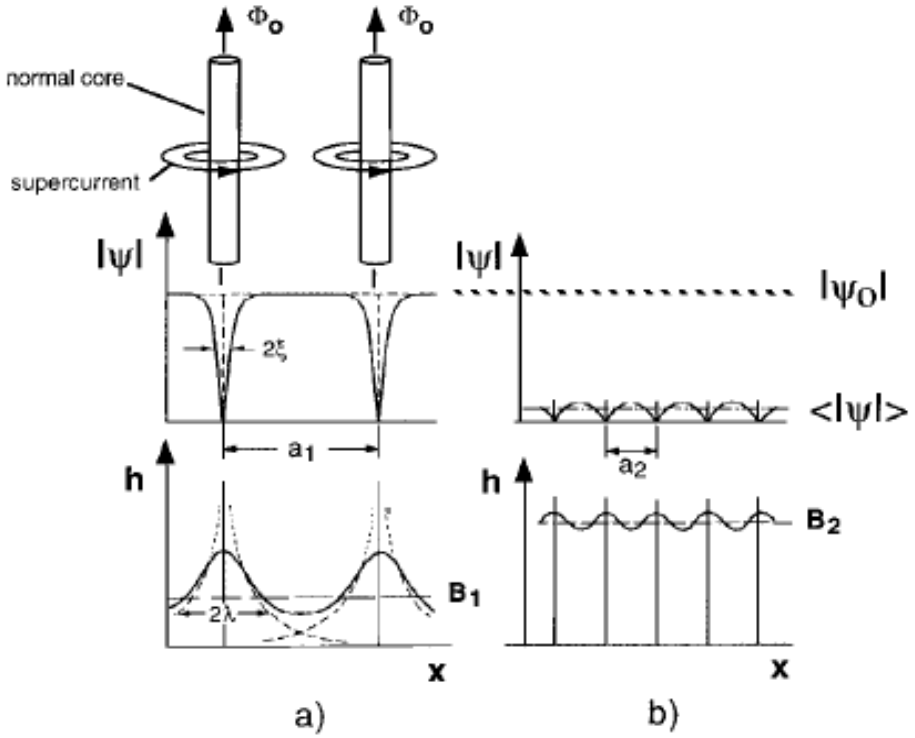

Figure 2.5 Spatial distribution of the order parameter Ψ and the microscopic magnetic field h in the mixed state at (a) low magnetic field (B_1 average value) and (b) high magnetic fields (B_2 average value). a_1 and a_2 are the space between flux lines in the above conditions, respectively [12].

Screening currents circulate around isotropic flux lines of radius ξ. Superconducting currents are confined within a larger region of radius λ. At low flux densities, the distance between flux lines (a_1) is much larger than ξ. At high flux densities, their separation (a_2) is comparable with ξ (Figure 2.5(a) and (b)). As the magnetic field increases and reaches B_{C2}, the superconductor becomes normal and $\langle|\Psi|\rangle = 0$ [12].

2.5 Conventional and Unconventional Superconducting materials

Superconducting elements. The observation of superconductivity in many elements not previously known to be superconducting was enabled through recent progress in physical instrumentation. In 2005 Buzea *et al.* produced an updated periodic table of superconducting elements [17]. Metallic elements are generally type I superconductors.

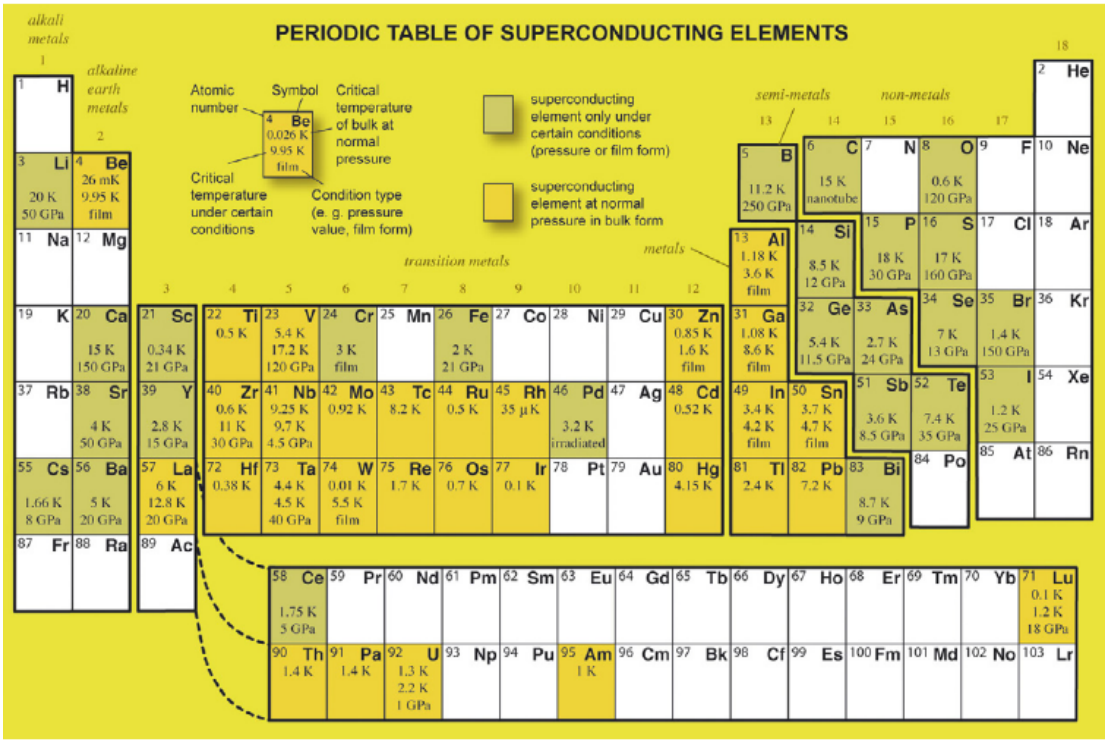

Figure 2.6 Periodic table of superconducting elements [17].

Superconducting compounds. The superconducting systems relevant for practical high field applications are Type II superconductors. Table 2.1 reports several superconducting systems with their critical parameters.

Compound	T_C **(K)**	B_{C2} **(T)**
Nb-Ti	10	14
Nb_3Sn	18	24 - 30
Nb_3Al	18.8	33
MgB_2	39	35 - 60
$PbMo_6S_8$	15	60
$YBa_2Cu_3O_7$	92	>100
$Bi_2Ca_2Sr_2Cu_3O_{10}$	110	>120
$Tl_2Ca_2Ba_2Cu_3O_{10}$	125	>130
Pnictides	53	> 150 T (4.2 K)

Table 2.2 Main superconducting system with their superconducting parameters [9,18].

Conventional superconductors. Superconducting properties of conventional superconductors can be explained using the BCS theory. The major commercial applications of superconductivity currently involve the use of low temperature superconductors (LTS) to produce stable and homogeneous magnetic fields. At the present time, the LTS materials of most interest are: NbTi, Nb_3Sn and $Nb_3(Al_{1-x}Ge_x)$. NbTi is the dominant commercial superconductor because of its ductility, low cost and low filament size. Its applications cover a wide range of device and machines: MRI, high field NMR, LHC main ring, ATLAS detector and CSM detector [19,20]. Nb_3Sn is a leading high field superconductor. Nb_3Sn strands are under development for the next generation of high field accelerator magnets (LHC Upgrade, ITER). They can provide high critical currents ($2500A/mm^2$) in high fields (14 T). $Nb_3(Al_{1-x}Ge_x)$ superconductors are considered to be promising alternatives for Nb_3Sn since they have higher B_{C2} and better strain tolerance than Nb_3Sn.

Another important material is MgB_2. It was found to be a superconductor in 2001. The main advantages of MgB_2 are that grain orientation is not required, low materials cost, good mechanical properties, low density and higher T_C than LTS [1].

In 1981, Chevrel and co-workers discovered the molybdenum chalcogeneides of the type $M_xMo_6X_8$ where M stands for a large number of metals and rare earths (RE) and X for the chalcogens: S, Se or Te. $PbMo_6S_8$ has the highest *T*c and also an unusually high critical field of 60 T for a conventional superconductor [9].

Unconventional superconductors. Unconventional superconductors are those classes of materials whose superconductivity cannot be explained using the BCS theory. Most notable are the high temperature superconductors (HTS) that were discovered in 1986 by Bednorz and Muller. They found evidence for superconductivity at ~ 30 K in LaBaCuO ceramics. In 1987, it was discovered that the $YBa_2Cu_3O_7$ ceramic has a T_C = 92 K. Early in 1988 Bi- and Tl-cuprate oxide were discovered with T_C = 110 K and 125 K, respectively [9]. The charge density of CuO_2 planes is thought to play an important role in the superconductivity of these compounds [9]. More recently, in January 2008 a Japanese group showed the existence of superconductivity in the iron-based layered $La[O_{1-x}F_x]FeAs$ with a (x = 0.05 – 0.12) with T_C = 26 K [21] now known as the pnictides. Since this discovery, scientists have made a number of analogue compounds mainly by substituting other rare earth ions for La. With either doping or pressure, it has been possible to achieve a T_C above 50 K [22]. Pnictides are antiferromagnetic at low doping. An increase of doping destroys the antiferromagnetism and leads to superconductivity. Pnictides show many similarities with the HTS family (i.e. structure, phase diagram). They might eventually be helpful to understand the mechanism of cuprate high T_C superconductivity. It is still open the question if pnictides are conventional or unconventional superconductors [23].

2.6 Nanocrystalline Superconducting materials

This section reports recent investigation on the critical temperature and the critical field of superconducting nanostructures.

The critical temperature of superconducting of nanostructures. Attempts to understand the superconducting properties of nanosized materials have been carried out for In, Nb, Al, Sn, Pb and $PbMo_6S_8$ [24,25]. Changes in superconducting properties may be expected when the effective size of a superconductor is reduced below its characteristic length scales, such as the London penetration depth $\lambda_L(T)$, the coherence length $\xi(T)$ and the mean free path l_e [26]. Relevant results on nanocrystalline Al are reported below. The critical superconducting properties of nanocrystalline Al were found to be superior compared to their bulk counterparts. Recent data on aluminium nanostructures are shown by Figure 2.7 and Figure 2.8.

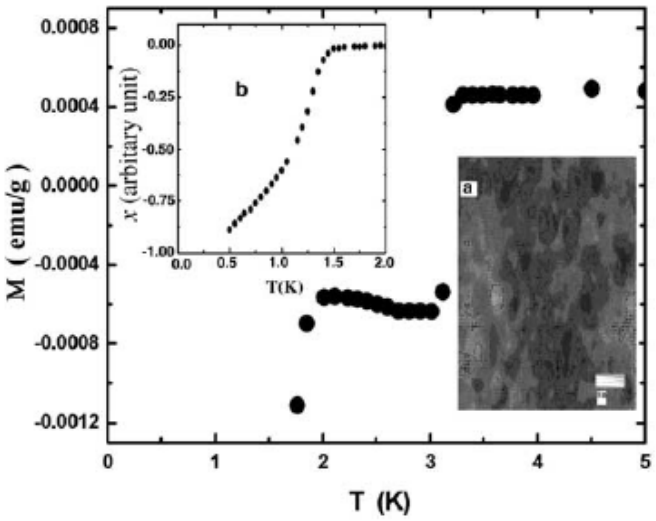

Figure 2.7 Magnetisation versus temperature of aluminum nanoparticles (25 nm) in the range 1.7 to 5 K. Measurements were carried out using a commercial Quantum Design. Inset (b): magnetic susceptibility in the range 0.3 – 2 K obtained by a home made DC squid magnetometer. Inset (a): HRTEM photograph of Al nanoparticles [27].

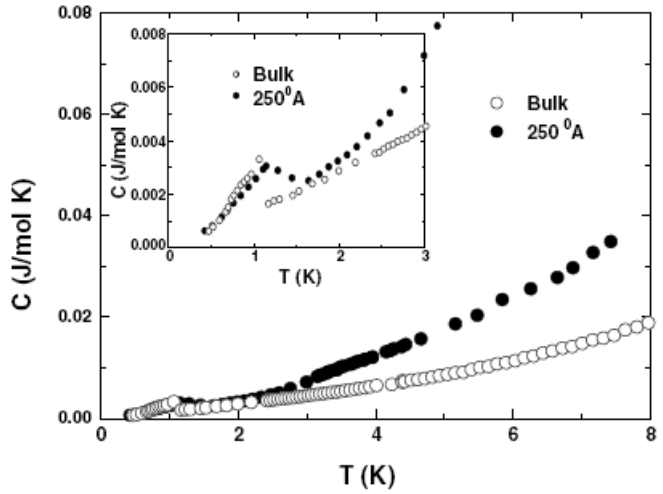

Figure 2.8 Heat capacity of aluminum bulk and nanoparticles from 0.4 to 8 K. The inset show the details of the superconducting transition region [27].

Figure 2.7 shows the multiple superconducting transitions at 1.5, 1.8 and 3.2 K of nanocrystalline Al. These superconducting transitions were considerably higher than the bulk value of 1.16 K. Figure 2.8 compares the heat capacity of aluminium bulk and nanoparticles. The aluminium bulk shows a sharp transition in heat capacity, whereas Al nanoparticles a broadened transition from 1.2 to 1.6 K. This broad transition may have originated from the thermodynamic fluctuation near the superconducting temperatures and also from a non homogeneous particle size distribution in the specimen [27,28]. The

superconducting transition measured by specific heat is consistent with 1.5 K (DC squid data). All superconducting multiphase transitions were associated with the size and the surface effects of the particles [27]. Successive research [26] provided evidence that the superconductivity at nanometre level is primarily affected by changes in the electronic density of the states rather than changes in the electron-phonon coupling due to surface effect.

The critical field of superconducting nanostructures. A novel experimental process to enhance the upper critical field has been invented in the Physics Department of Durham University by Niu and Hampshire [20]. Large increases in the upper critical field $B_{C2}(0)$ were achieved in disordered nanocrystalline $PbMo_6S_8$ [29] and Nb [30] with corresponding $B_{C2}(0)$ values of ~ 100 T and ~ 3 T. The conventional counterparts have $B_{C2}(0)$ ~ 50 T and ~ 0.5 T, respectively. The new optimization method comprises two steps. The first is the conversion of the microcrystalline precursor powders to nanocrystalline amorphous state by ball milling. The second is the crystallization and compaction by hot isostatic pressing. Figure 7.9 reports the upper critical fields as a function of temperature for conventional and the nanocrystalline niobium [30].

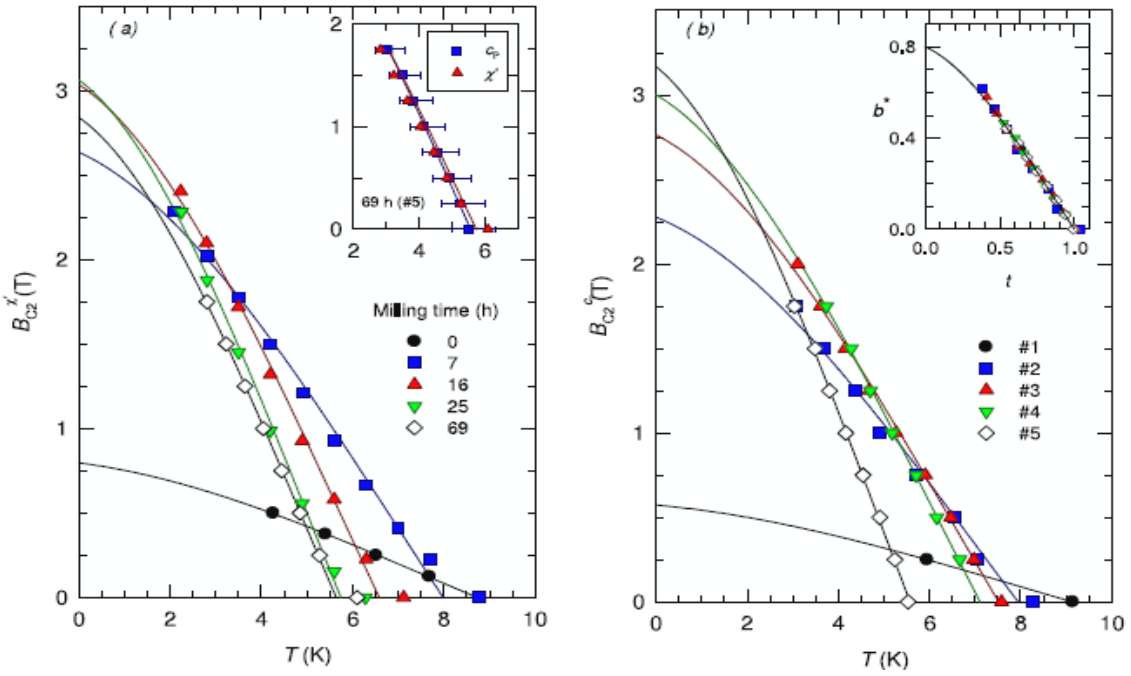

Figure 2.9 Upper critical field as a function of temperature for conventional (#1) and nanocrystalline niobium samples milled for 69 h (#5) and HIP'ed at 750 °C (#2), 600 °C (#3) and 450 °C (#4) (a) susceptibility data (b) specific heat data [30].

Following the theoretical work by Taylor et al. [30], $B_{C2}(0)$ for a superconductor at zero temperature is related to various microscopic properties through the following GLAG expression [30]:

$$B_{C2}(0) = 0.973\mu_0^{1/2}\eta\kappa^*(0,\lambda_{tr})R(\lambda_{tr})^{-1} \times \left[7.30\times10^{37}(\gamma T_C / S) + 2.78\times10^{16}\gamma T_C\rho_n\right] \quad (2.6)$$

where μ_0 is the vacuum magnetic permeability, $\eta \approx 1$ is a strong coupling correction, $\kappa^*(0,\lambda_{tr})$ is the ratio of the Ginzburg-Landau parameter at zero temperature to that at the critical temperature, $R(\lambda_{tr}) \approx 1$ is part of the Gorkov function, $\lambda_{tr} = 3.81\times10^{-32}\ S^2\rho_n/(\gamma T_C)$ is the impurity parameter, γ is the Sommerfeld constant, ρ_n is the normal state resistivity and S is the Fermi surface.

Experimental evidence suggests that electronic mean-free-path reduction strongly affects the parameters in equation (6) and leads to improved B_{C2} values without significantly reducing the superconducting transition temperature and γ [29,30]. The critical temperature of a disordered superconductor is given by:

$$k_B T_C = \frac{\hbar\overline{\omega}_1}{1.20} exp\left(-\frac{1.04(1+\lambda)}{\lambda - \mu^*[1+0.62\lambda]}\right) \quad (2.7)$$

where $\overline{\omega}_1$ is the electron-phonon moment of the electron-phonon spectrum function $\alpha^2F(\omega)$, λ is the electron-phonon coupling parameter and μ^* is the Coulomb pseudopotential. In Taylor's work, the relation $\lambda \propto N(E_F)$ is also used where the term $N(E_F)$ represents the density of states at the Fermi energy (E_F). The relation between $N(E_F)$ and γ is $\gamma = \frac{2}{3}\pi^2k_B^2N(E_F)(1+\lambda)$. The decrease in γ with increasing resistivity can be expressed using a simplified version of the lifetime broadening model. This leads to the following peak in the density of states at E_F:

$$N(E_F) = N_0(E_F)\left(\frac{(4/\pi)(\hbar/\tau E_0)tan^{-1}(\hbar/\tau E_0) - 1}{(\hbar/\tau E_0)^2 - 1}\right) \quad (2.8)$$

$N(E_F)$ is a Lorentzian of half-width E_0. The broadening function is a Lorentzian with half-width $\hbar/\tau$ where $\tau = 1.65\times10^{19}\gamma/(S^2\rho_n)$ is the mean scattering time. Increased resistivity or short scattering events reduce $N(E_F)$ and hence γ, λ and T_C [30].

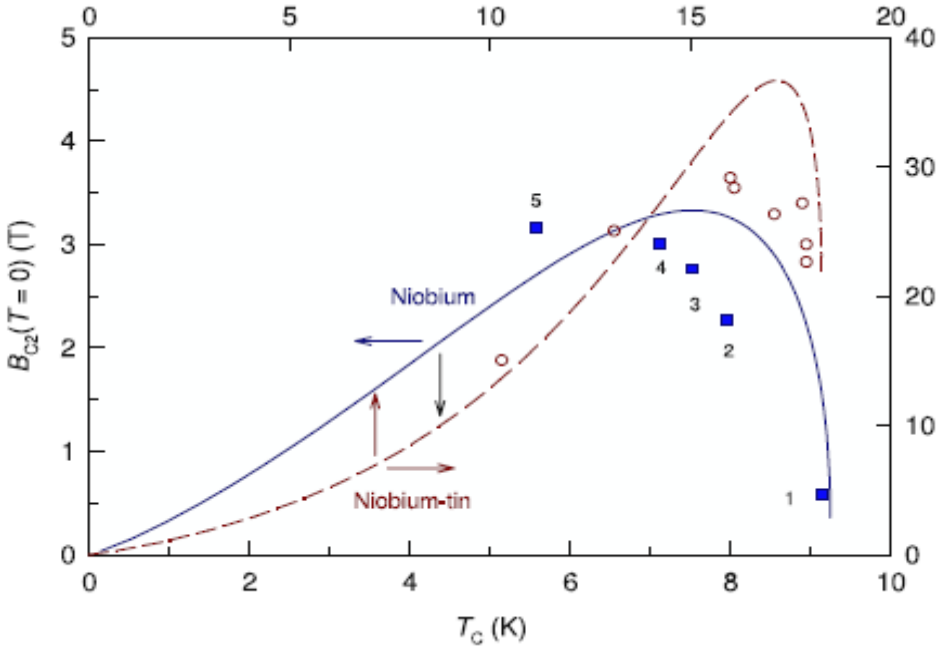

Figure 2.10 Upper critical field of nanocrystalline niobium and niobium thin. The lines show the theoretical values obtained by increasing resistivity. The symbols show the experimental data. The data for the Nb samples for conventional (#1) and nanocrystalline niobium samples milled for 69 h (#5) and HIP'ed at 750 C (#2), 600 C (#3) and 450 C (#4) are reported. The data for Nb_3Sn are also shown [30].

Figure 2.10 shows B_{C2} as a function of T_C for nanocrystalline niobium and niobium-tin. Theoretical fitting and experimental data are both reported for increasing resistivity. As the resistivity increases, eventually $B_{C2}(0)$ reaches its peak value when the increase of ρ_n is more than compensated for reductions in T_C and γ. Microscopic theory suggests that electron-phonon, Coulomb and self energy interactions also affect the upper critical field but are not considered in detail in the literature yet [31]. Nevertheless Figure 2.10 confirms that these additional effects do not have a large influence on $B_{C2}(0)$ [30].

Fabrication and properties of nanocrystalline Nb_3Al. Mondal et al. reported on the fabrication and superconducting properties of nanocrystalline Nb_3Al [25,32]. The constituent elements were arc-melted in stoichiometric proportions. A rapidly quenched melt resulted most of the time in small Nb_3Al nanoparticles of up to ~ 9 nm embedded in a bcc Nb-Al solid solution. The resulting sample consists of a mixture of two or more phases. The polycrystalline and multiphase nature of these nanocrystalline sample was investigated using X-ray diffraction and TEM measurements. The superconducting properties were also investigated. The X-ray diffraction (Figure 2.11) shows two major phases: the A15 structure and the Nb-Al bcc phase.

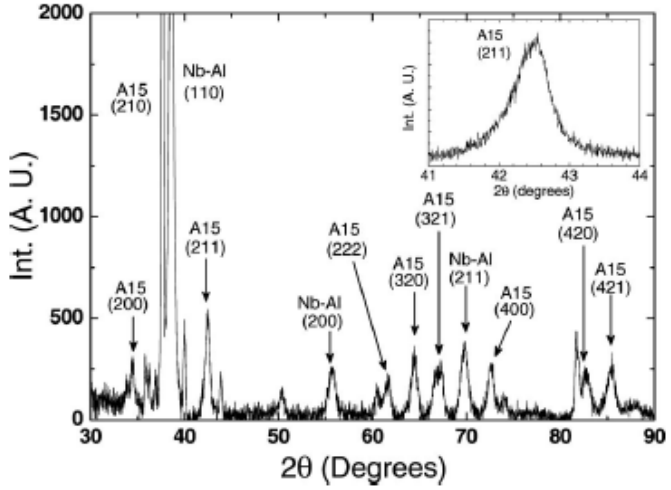

Figure 2.11 The X-ray diffraction pattern show the presence of two major phases: Nb_3Al and bcc Nb-Al solid solution [25].

The TEM measurements (Figure 2.12) show a dark field micrograph (a), an indexed diffraction pattern (b) and the grain size distribution. Figure 2.12(a) is a dark field micrograph for grains oriented along the [211] direction. The dark regions include differently oriented grains for the A15 phase and randomly oriented Nb-Al bcc grains. The crystallites are embedded in an amorphous matrix (most probably of Nb-Al). Figure 2.12(b) shows the electron diffraction rings indexed for the A15 phase. Figure 2.12(c) shows a grain size distribution that peaks at ~ 3.5 nm.

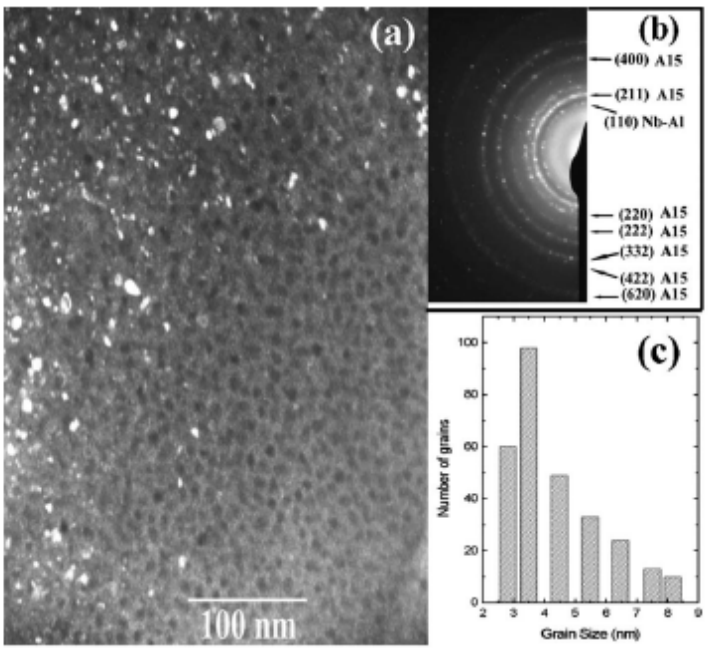

Figure 2.12 Results of TEM measurements. (a) Dark field image. (b) Diffraction pattern indexed for the A15 structure. (c) Grain size distribution [32].

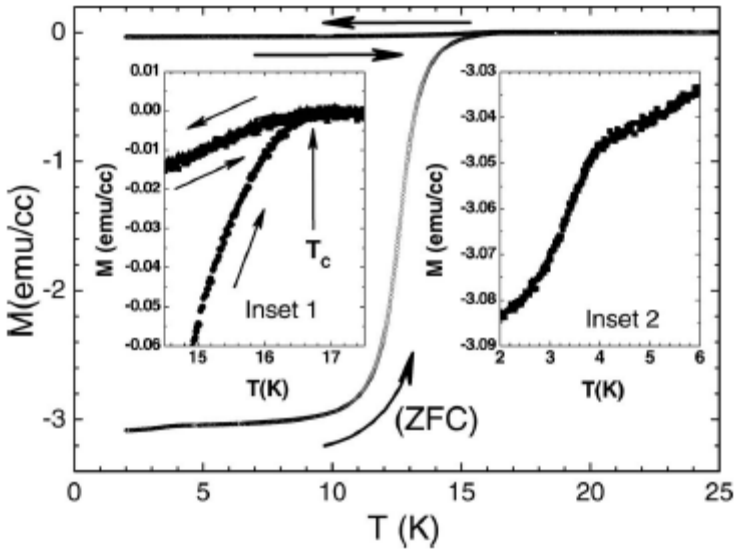

Figure 2.13 Magnetization as a function of temperature. The protocol consists of three measurements: the zero-field-cooled (ZFC), the field-cooled-cooling (FCC) and the field-cooled-warming (FCW). Inset 1 shows the T_C identification using ZFC and FCC; FCC and FCW superimpose. Inset 2 shows a second superconducting phase at ~ 4 K [25].

Figure 2.13 shows the magnetization for three different field histories: the zero-field-cooled (ZFC), the field-cooled-cooling (FCC) and the field-cooled-warming (FCW). The large irreversibility in-between ZFC and FCC is typical of type II superconductors whereas the complete reversibility of FCC and FCW is an unusual behaviour. The numerous grains eventually drive this novel flux pinning mechanism rather then the conventional pinning centres [33]. The presence of two superconducting phase at ~ 17 K and ~ 4 K is shown by inset 1 and 2 [25].

2.7 Concluding comments

A complete understanding of the nature of superconductivity at nanometre length scale has not yet been achieved [26]. Modification of the superconductivity may take place when the size of the basic building blocks of the microstructure is reduced or comparable to fundamental length scales: mean free path of electrons, l, the penetration depth, λ, and the coherence length, ξ [25,34,35]. Microstructure and complex grains-interaction at the nanometre scale could also affect the traditional distinction between intrinsic (e.g. B_{C2} and T_C) and extrinsic (e.g. J_C) superconducting properties [30]. Hence, it will be of great interest probing how superconducting properties evolve in the nanometre range.

A conventional optimization procedure involves the introduction of pinning sites whereas the new paradigm for making high field superconductors uses as a precursor material highly disordered or amorphous powder prior to crystallization [25,30]. The upper critical field B_{C2} of these disordered superconducting materials is enhanced dramatically because of the decrease in coherence length compared to the conventional materials [29]. It is clear that nanocrystalline superconductors, which are a central theme in this thesis, have the potential to offer a new paradigm for making a new class of high-field superconductors and potentially a new generation of high-field magnets [30].

Chapter 3

Review of $Nb_3(Al_{1-x}Ge_x)$ for $0 \leq x \leq 1$

3.1 Introduction

Chapter 3 is a review of the literature on $Nb_3(Al_{1-x}Ge_x)$ for x = 0, 0.3, 1. Section 3.2 focuses firstly on the basic A15 structure and superconducting properties. The influence of atomic ordering and off-stoichiometry on superconducting parameters is also reported. Section 3.3 shows detailed Nb-Al-Ge phase diagrams. Section 3.4 provides a comprehensive review and outlines the main processing methods and correlated properties for $Nb_3(Al_{1-x}Ge_x)$ bulk, wire, film materials and ball milled powders.

3.2 Structure and superconducting properties of $Nb_3(Al_{1-x}Ge_x)$

Superconductivity was discovered in compounds with the A-15 structure by Hardy and Hulm in 1953 [36]. The *A15* structure generally occurs at the stoichiometric composition A_3B. In this structure type the atom *A* is a transition metal of the 4^{th}, 5^{th}, 6^{th} column of the periodic table and the atom *B* is either a transition or non-transition metal [37]. Of noticeable interest are those compounds of general formula Nb_3B where *B* is Sn (R_{Sn} = 1.72 Å), Al (R_{Al} = 1.82 Å), Ga (R_{Ga} = 1.81 Å) and Ge (R_{Ge} = 1.52 Å). It has been shown that as the size of the atomic radius, *R*, decreases, T_C generally increases. However, with increasing T_C, it is increasingly more difficult to fabricate a well-ordered A15 phase of the correct stoichiometry. Thus the size of the B atom appears to play a dual role in these compounds [38].

Structure. $Nb_3(Al_{1-x}Ge_x)$ is a superconducting A15 compound formed by transition (Nb) and non transition elements (Al, Ge). It has a cubic cell of 21 atoms and belongs to the space group Pm3n (223). Its unit cell is shown in Figure 3.1. The substance is ideally a solid solution between the solid cell of Nb_3Al and Nb_3Ge [38-40]. The $Nb_3(Al_{1-x}Ge_x)$ structure has Al or Ge atoms at the bcc sites according to the ratio 1-x : x. The Nb atoms are located in pairs along the cubic faces forming three mutually orthogonal chains [41]. The distance between nearest neighbours within a Nb-chain is about 20% less than the distance between inter-chain Nb nearest neighbors [12].

Electronic structure calculations show that the *d* electrons of Nb chains are important in the superconductivity of the niobium based intermetallics [36,42].

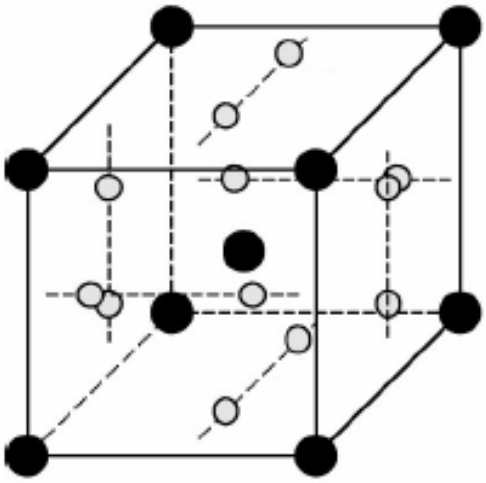

Figure 3.1 A schematic representation of an ordered A15-structure $Nb_3(Al_{1-x}Ge_x)$ compound. Black and grey circles represent Al/Ge and Nb atoms, respectively [41].

In general, changes in T_C can be ascribed to both atomic disorder and composition. These two relevant effects are discussed below [43].

Atomic ordering. The superconducting properties of A_3B are very sensitive to the degree of atomic ordering. The maximum degree of atomic ordering is obtained when the A sites are occupied by A atoms and B sites occupied by B atoms. The introduction of B atoms into the A chain (anti-site disorder) breaks the continuity of the chain and leads to a strong reduction of the critical temperature T_C, the upper critical field B_{C2} and the critical current density J_C [44,45]. The mechanism for this degradation is attributed to the sensitivity of electronic density of states, n(E), at the Fermi level, E_F, to atomic order. A dramatic effect on the electronic structure of the metal can also be produced by vacancies, interstitials, new atoms [46] and gaseous impurities [43]. Low-T_C ($T_C < 12$ K) A15 compounds support this concept [46,47]. A narrow width of the superconducting transition is expected for a given degree of order in the Nb chains [46] and homogeneous composition [48]. The atomic ordering and homogeneity depend considerably on preparation conditions and the heat treatment [47,49]. Figure 3.2 shows a dramatic increase of the transition temperature for a Nb-based A15 compound at about 800 ^oC. The variations of critical temperature and lattice constant at different annealing temperatures and compositions for microcrystalline $Nb_3Al_{0.7}Pt_{0.3}$ are summarised by Figure 3.3.

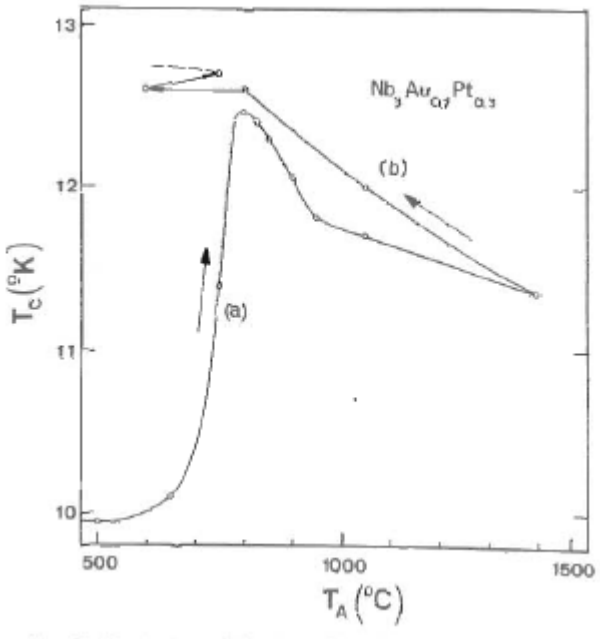

Figure 3.2 Variation of the transition temperature with increasing and decreasing the annealing temperature [47].

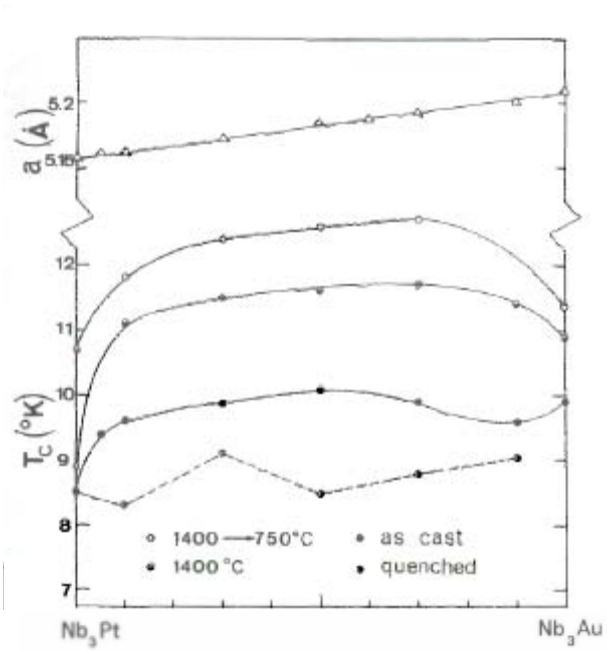

Figure 3.3 Transition temperature T_C and lattice constant a for the system $Nb_3Au_xPt_{1-x}$. at different annealing temperatures [47].

Composition. In practice, all A15 phases exist over a range of compositions. Sometimes this range comes close, but does not include the ideal A_3B [36]. Deviation from the stoichiometric composition degrades significantly the critical temperature of A15 Nb-based compounds as shown in Figure 3.4. Zackay et al. [43] estimated the total number of valence electrons per unit cell volume and linked the changes of the transition temperature to the structural properties for different families of superconducting compounds. The effects of structure, composition and microstructure on superconducting properties are summarised by Table 3.1 [43].

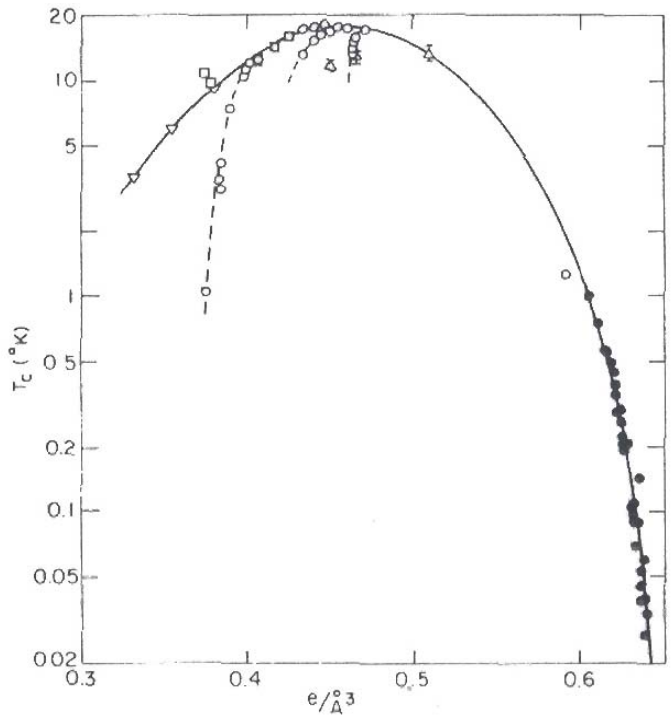

Figure 3.4 Estimated variation of the critical temperature with the number of valence electrons per unit volume. Empty circles represent NbN compounds, full circles iridium solid solution, squares $ZrN_{1.0}$ solutions, up-poiting triangles MoC_{1-x} , down-poiting triangles NbC-ZrC solution {Zackay, 1970 #3363}.

Effect on	Crystal structure	Composition	Microstructure
T_C	Large	Large	Negligible
B_{C2}	?	Large	Slight
J_C	Negligible	Slight	Large

Table 3.1 Effect of structural parameters on superconductive properties [43].

Superconductivity can be used as a probe into the structure and composition of important classes of compounds. Historically, the relation between superconducting

properties and metallurgical factors was done in combination with the determination of phase diagrams.

3.3 Phase diagrams of $Nb_3(Al_{1-x}Ge_x)$

The Nb-Ge and Nb-Al phase diagrams discussed below were produced by Jorda et al. [50,51]. Alloys were prepared by arc melting in a copper crucible under argon atmosphere. Subsequently samples were given a homogenization anneal for 24 h at 50 ^{o}C. The master ingots were then broken into small pieces. Subsequently they were argon quenched from various temperatures. High temperature data ($T \geq 1800$ ^{o}C for Nb-Ge and $T > 1940$ ^{o}C for Nb-Al) were collected on splat-cooled samples. The resulting foils of 50-100 μm thickness were argon quenched after a brief annealing. The analysis of the samples was carried out by X-ray, microprobe analysis, thermal analysis and observation of the superconducting transition [52]. The authors mention that the phase diagram results can be influenced by the volatility of one component (low melting point metals: Ga, Al, Sn…), impurities in the heating chamber and contamination via crucible material and gaseous impurities. The proper choice of heat treatment and the sample dimensions can also play a role [50,52]. The Nb-Al-Ge phase diagrams show the intermetallic phases and solid solutions as a function of annealing temperature and stoichiometry. Most of these studies were done between the 1970's [53] and 1980's [4,50,51], however the type of reactions and the compositions are dissimilar. Nb-Al-Ge phase diagrams have been studied by Muller [54] and Pan [53]. Comment on Pan's work is not made on the original (Russian) papers but from recent literature [12].

Nb-Ge phase diagram. The Nb-Ge phase diagram shows a niobium solid solution and three intermediate phases: Nb_3Ge, Nb_5Ge_2 and $NbGe_2$ [55]. An exhaustive investigation of the Nb-Ge phase diagram is reported in Figure 3.8 and details of the A2 and A15 phases in Figure 3.6 and Figure 3.7. The single phase niobium solid solution (A2-type phase) extends up to 11.5 at.% Ge at 1900 ^{o}C. The A15 phase is formed by a peritectic reaction L + A2 ↔ A15 at 1900 ^{o}C at 18 at.% Ge. Unfortunately the A15 phase only extends up to 23 at.% Ge at the eutectic temperature of 1865 ± 10 ^{o}C (L + A15 ↔ A15 + Nb_5Ge_3) which rules out forming the stoichiometric A15 compound in equilibrium. The lattice constant of the A15 phase has been found to vary linearly with the composition. For splat-cooled samples the superconducting transition has been found to extend from 17 K to 6 K [50]. A partial transition at 6 K has always been

observed. For higher Ge concentration, the next intermediate phases are Nb_5Ge_3 and $NbGe_2$. The tetragonal Nb_5Ge_3 (I4/MCM) is formed by congruent melting at 2180 ^oC. This phase has been found to extend from 38 at.% Ge at 1865 ^oC to 44 at.% Ge at 1580 ^oC. The hexagonal $NbGe_2$ (P6222) is formed by congruent melting at 1680 ^oC at 66 at.% Ge.

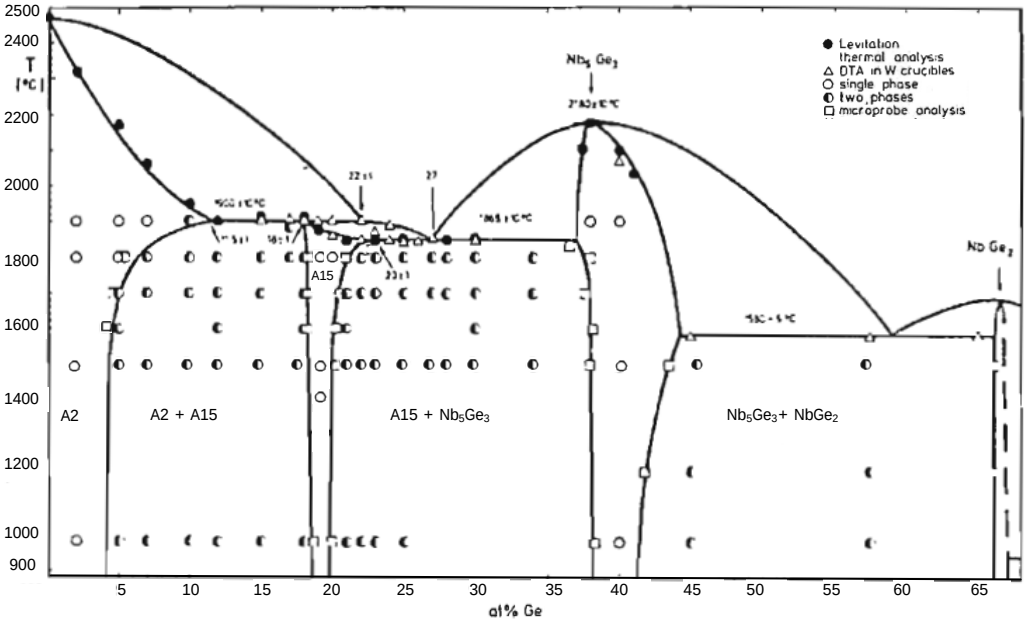

Figure 3.5 The Nb-Ge system up to 70 % Ge [50].

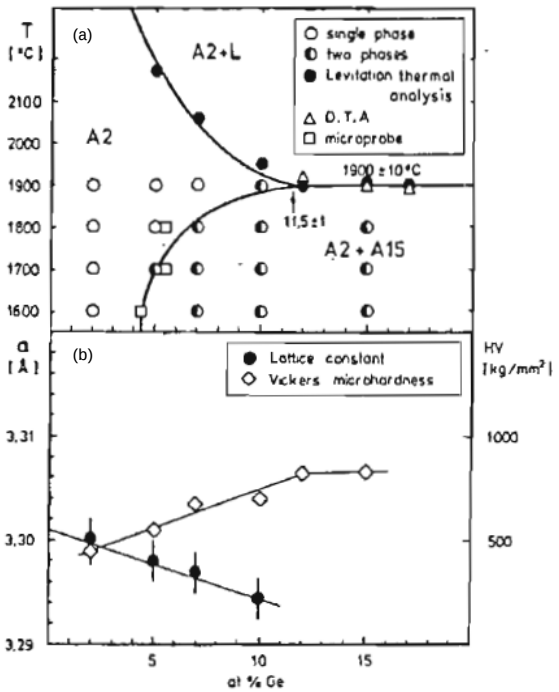

Figure 3.6 The Nb-rich solid solution: (a) solubility of Ge in Nb at high temperature; (b) lattice constant vs. Ge concentration [50].

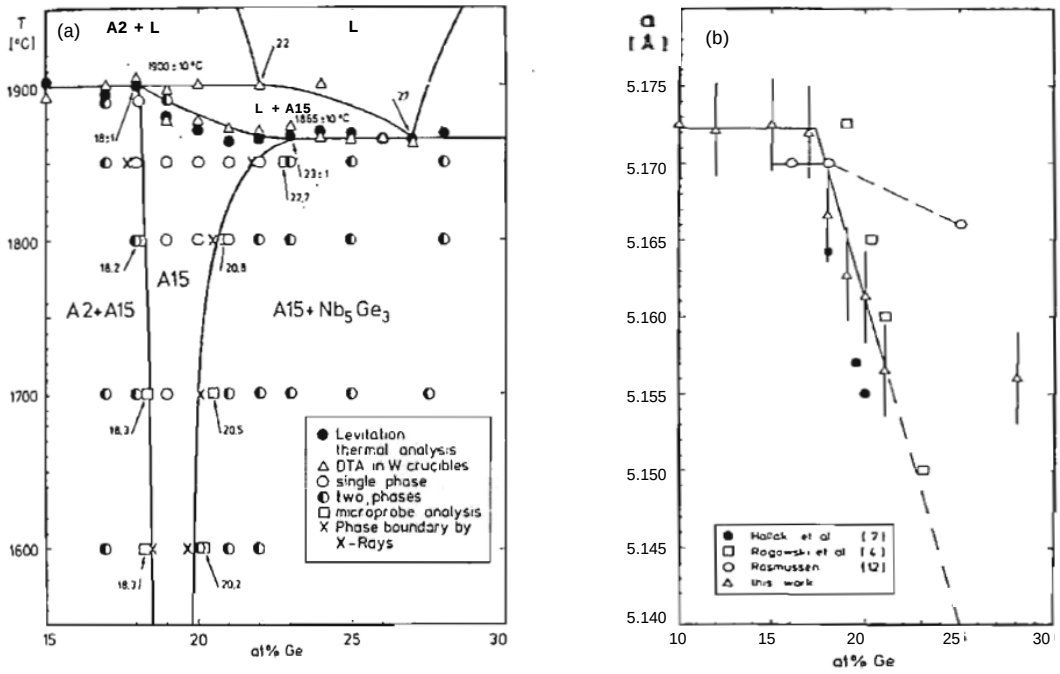

Figure 3.7 The A15 phase range: (a) details of the A15 phase of the Nb-Ge phase, (b) lattice parameter of the A15 phase of Nb-Ge; comparison is made with other determinations on samples prepared in different ways [50].

Nb-Al phase diagram. The Nb-Al phase diagram shows a niobium solid solution and three intermediate phases: Nb_3Al, Nb_2Al (σ phase) and $NbAl_3$ [55]. An exhaustive investigation of the Nb-Al phase diagram is reported in Figure 3.8 [51].

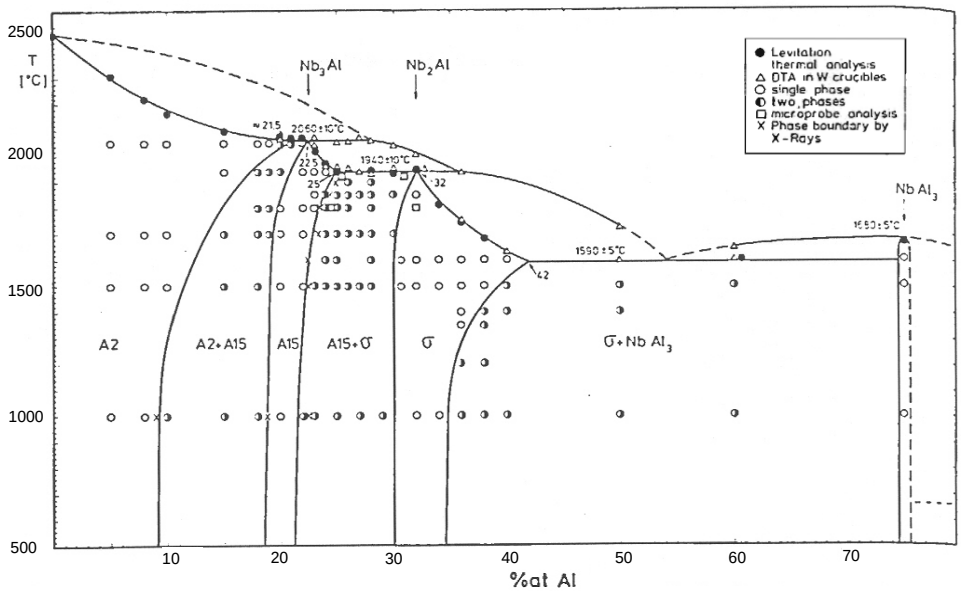

Figure 3.8 The Nb-Al phase diagram by Jorda et al. in 1970 [51].

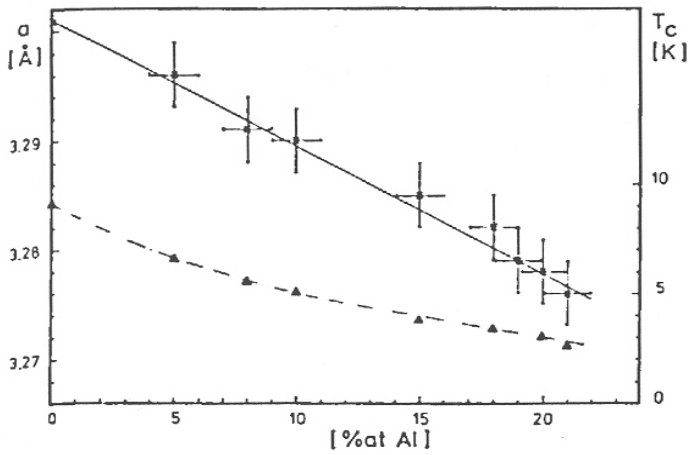

Figure 3.9 Nb-Al solid solution's lattice parameter (cross) and critical temperature (triangles) [51].

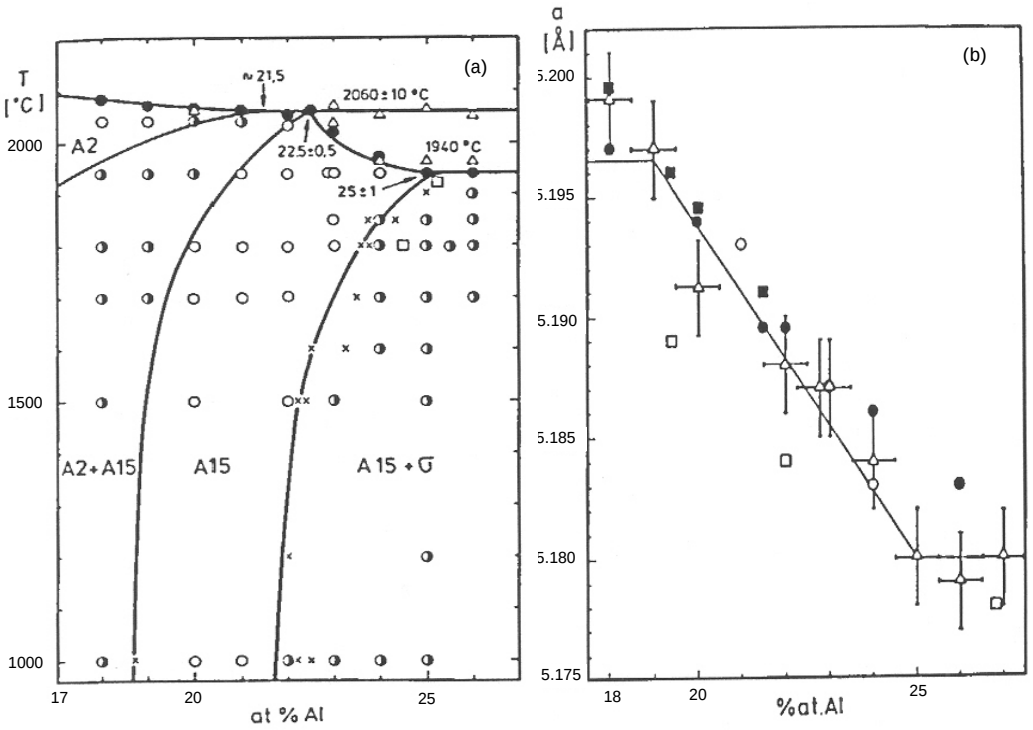

Figure 3.10 The A15 phase range: (a) details of the A15 phase of the Nb-Al phase; (b) lattice parameter of the Nb-Al A15 phase [51].

From 19 to 21.5 at.% Al, the niobium solid solution and the A15 phase are stable at different temperatures [Figure 3.10(a)]. Figure 3.10(b) shows the relationship between the lattice parameter of the A15 phase and the composition which was found to be linear in the range from 19 % to 25 at.% Al. The peritectic reaction of the A15 phase formation is A2 + L ↔ $Nb_{0.775}Al_{0.225}$ at 2060 ^oC [51]. For higher aluminium content the tetragonal σ phase (P42/MNM) is formed by A15 + L ↔ $Nb_{68}Al_{32}$ at 1940 ^oC. The

tetragonal $NbAl_3$ (I4/MMM) is formed by congruent melting at 1680 °C at 75 at.% Al. Jorda et al.'s work on Nb_3Al [51,56] has been recently reviewed by Glowacki [12]. Figure 3.11 gives the lattice parameter at room temperature and T_C of Nb_3Al. Compositional and ordering effect of Nb-Al samples are compared in Figure 3.12.

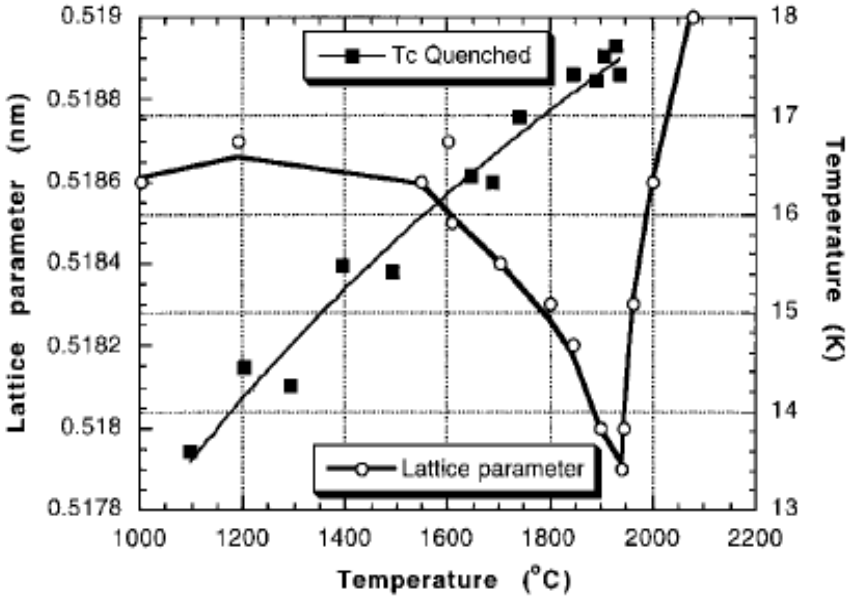

Figure 3.11 Lattice parameter and T_C for Nb_3Al. Data up to 1940 °C are from argon-jet quenched samples. Data above 1940 °C up to 2060 are from splat-cooled samples [12].

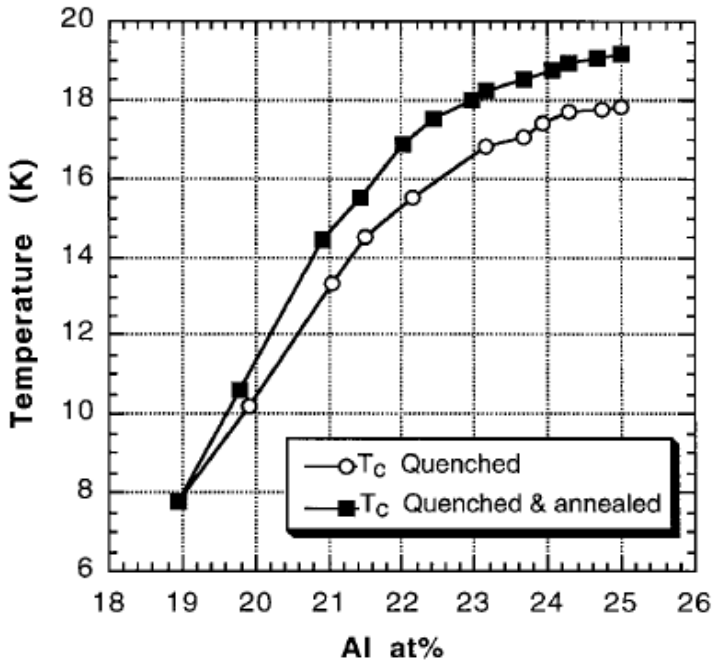

Figure 3.12 Compositional and ordering effects of the Nb-Al [12].

Nb-Al-Ge phase diagram. There is some very limited work on the ternary Nb-Al-Ge phase diagram. In Figure 3.13(a) and (b), the ternary diagram of Nb-Al-Ge at 1000 ^oC and 1700 ^oC near the Nb corner is reproduced [12,53].

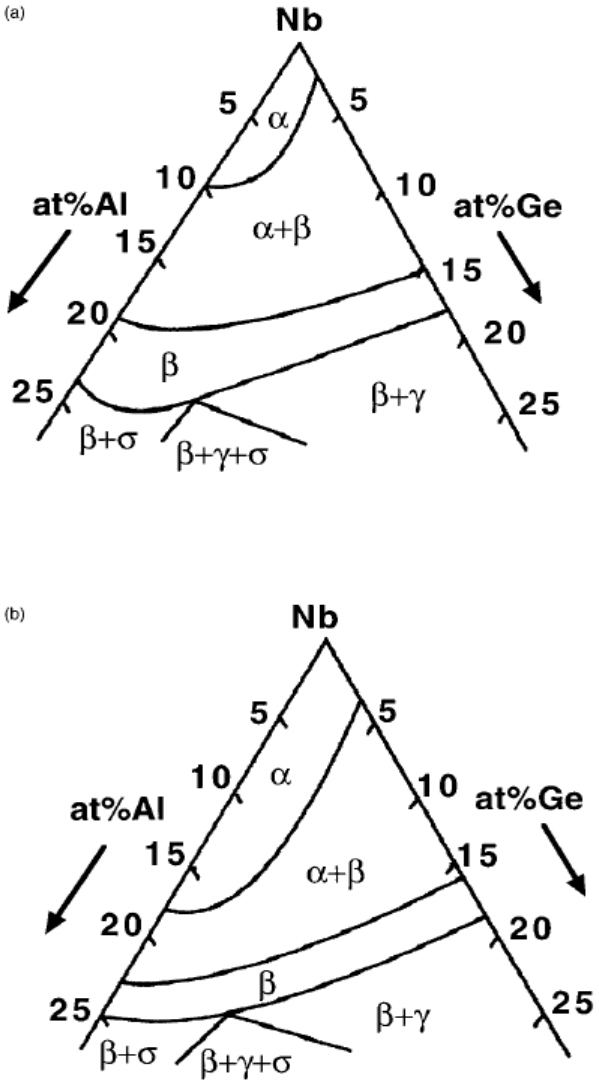

Figure 3.13 The Nb-corner of the phase diagram Nb-Al-Ge (a) 1000 ^oC, (b) 1700 ^oC; α, $Nb(Al_{1-x}Ge_x)$; β, $Nb_3(Al_{1-x}Ge_x)$; σ, $Nb_2(Al_{1-x}Ge_x)$; γ, $Nb_5(Al_{1-x}Ge_x)_3$. After Pan et al. [12, 53].

3.4 Fabrication and properties of $Nb_3(Al_{1-x}Ge_x)$

The A15-structure $Nb_3(Al_{1-x}Ge_x)$ with x = 0, 0.3 and 1 can be prepared by a variety of methods. A review of fabrication methods is presented below together with relevant structural and superconductive properties. Significant routes of manufacture are illustrated for each of three different materials in turn. Fabrication of bulk materials, wires, films, ball milled and hot isostatically pressed materials are considered in turn.

The A15 $Nb_3(Al_{1-x}Ge_x)$ group is recognised by the superconductivity community as an excellent source for future superconducting multifilamentary conductors capable of operation at magnetic fields higher than 25 T under extreme mechanical and irradiation conditions [12]. In particular the A15 $Nb_3(Al_{0.7}Ge_{0.3})$ ternary compound has the optimal combination of high critical temperature T_C and extremely high upper critical field B_{C2} of 41 T at 4.2 K [36,62,63].

3.4.1 Bulk material

Nb-Ge bulk materials. The A15 structure Nb-Ge was first synthesized and identified by Carpenter and Searcy in 1956 [57]. Geller was the first to recognize that the compound Nb_3Ge was non-stoichiometric in bulk form. Previous fabrications by conventional arc-melting, annealing techniques or rapid quenching from the molten state produced Nb_3Ge bulk materials with T_C values of 6-7 K, whose the lattice constant was found to extend up to the non-stoichiometric value 5.166 Å [37,50,58]. In bulk material the Nb:Ge ratio was found to be 4 [58,59].

Nb-Al bulk materials. The A15 intermetallic compound Nb_3Al was discovered by Wood et al in 1958. Its superconducting state temperature was 17.5 K. It was prepared by heating an aluminium-niobium pressed pellets in a helium arc furnace. The lattice constant ranged from 5.185 Å to 5.194 Å. This material was found to contain some trace of impurities [60]. In 1968 Willens et al. produced Nb_3Al with a critical temperature of 18.8 K. Samples were prepared by mixed powders subsequently compressed into bars. They were then reacted in the A15 compound via an r.f. coil in a purified argon atmosphere. The Nb_3Al bars were 95% single phase. Annealing was performed at high temperature (1700 ^oC) for homogenisation and/or low temperature (700 ^oC) for ordering [49]. In 1971 Foner at al. prepared Nb_3Al samples at ~ 1700 ^oC. The upper critical field $B_{C2}(0)$ was found to improve from 31 T for as-reacted alloy to 32.4 T after heat treatment 700 $^oC \times 7.5$ h. Correspondingly T_C changed form 17.75 K to 18.72 K [61] - consistent with the importance of atomic ordering in these compounds.

Nb-Al-Ge bulk materials. In 1970 Foner et al. were the first to fabricate the A15 ternary compound $Nb_3Al_{0.7}Ge_{0.3,}$. A T_C value of 20.7 K and an upper critical field, $B_{C2}(4.2\ K)$, of 41 T were achieved [36,62,63]. Nb-Al-Ge ternary alloys were arc-melted in an argon atmosphere, sealed in quartz with He gas and annealed over the range

650 °C to 1000 °C for a period of 1 to 20 days. The lattice constant was found (5.174 ± 0.001) Å for a large range of composition [63]. The authors described the materials as a solid solution of Nb_3Al and Nb_3Ge [39] but also mentioned the large amount of other phases [49]. The fabrication of $Nb_3(Al,Ge)$ presents several problem due to the complexity of the Nb-Al-Ge phase diagram being the stoichiometric composition of A15 Nb_3Al or $Nb_3(Al,Ge)$ stable at elevated temperature beyond ~ 1800 °C [64]. Another issue is the substantial amount of other phases present such as the Al-rich phase $Nb_2(Al,Ge)$, the Ge-rich phase $Nb_5(Al,Ge)_3$, the Nb solid solution and eventually the presence of oxides [49,65,66]. Furthermore, the A15 $Nb_3(Al,Ge)$ phase might appear concurrently with A15 phases Nb_3Al and Nb_3Ge as indicated in corresponding phase diagram [67].

3.4.2 Wires

Nb-Ge wires. No work concerning Nb_3Ge wires has been mentioned in the scientific literature so far. Most work has been done to produce film depositions.

Nb-Al wires. In 1989 Foner at al. produced Nb_3Al wires by rapid quenching from high temperatures [68]. This investigation was done on short length wires to probe the feasibility of the bcc solid solution to A15 transformation process in wire manufacture [68]. A copper billet was filled with a mixture of Nb and Al powders. Subsequently the billet was evacuated, sealed and compressed by swaging. The copper jacket was removed and the billet was fitted in a Nb sleeve. This prevented Al evaporation and contained any liquid formed during annealing. The Nb sleeve was inserted in a copper can. A very homogeneous deformation was achieved by slow hydrostatic extrusion at room temperature. The copper jacket was then removed by etching and replaced by another ductile alloy. After the final area reduction this jacket was removed by etching. Finally, a wire of 0.33 – 0.75 mm diameter was heat treated. Ohmic heating (heating by passing a current through the wire) was done for a few seconds. The surface temperature was adjusted to be in the range 1550 - 1830 °C. During this heat treatment the wire was inserted into a low melting alloy bath. The X-ray diffraction pattern shows that the as-quenched material was a bcc solid solution with a lattice constant of 3.271 Å. To recover the A15 phase a second heat treatment was done in the range 850 - 1100 °C. A lattice constant of 5.185 Å was found. J_C was 1 A·mm^{-2} at 22 T and T_C was 17.8 K.

Nb-Al long length wires. In 1994 Iijima et al. developed a device to produce long Nb_3Al multifilamentary wires [69]. This wire fabrication is commonly named Rapid Heating Quenching and Transformation (RHQT). A state-of-the-art RHQT device is shown in Figure 3.14 [70]. The Nb-Al wire, moving at 1 $m \cdot sec^{-1}$, carried a high ac current for 0.1 sec between the electrode pulley and the gallium bath to achieve rapid heating. The wire was then rapid quenched in the gallium bath [1,69,71]. The microstructure of the Nb-Al bcc solid solution composite is shown in Figure 3.15 [72]. The as-quenched bcc solid solution composite was then transformed into A15 phase by annealing. Figure 3.16 shows its X-ray diffraction patterns before and after annealing 800 ^oC x 10 h. The Nb_3Al lattice parameter vs. T_C is given by Figure 3.17.

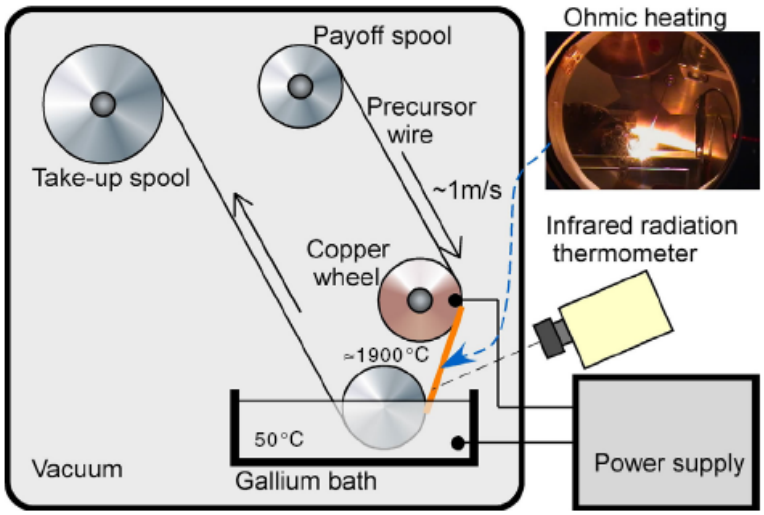

Figure 3.14 Diagram of rapidly/heating quenching and transformation (RHQT) process device [70].

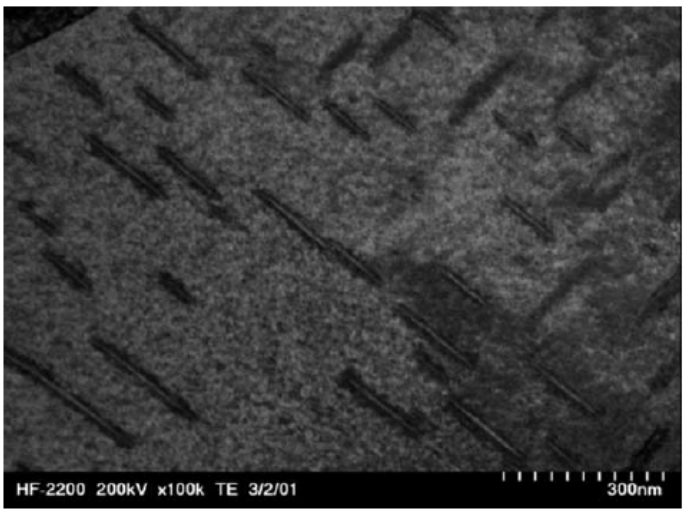

Figure 3.15 TEM image of Nb-Al bcc solid solution at about 400 ^oC by direct observation using a sample heating holder. The nano-disk are Nb-Al oxide [72].

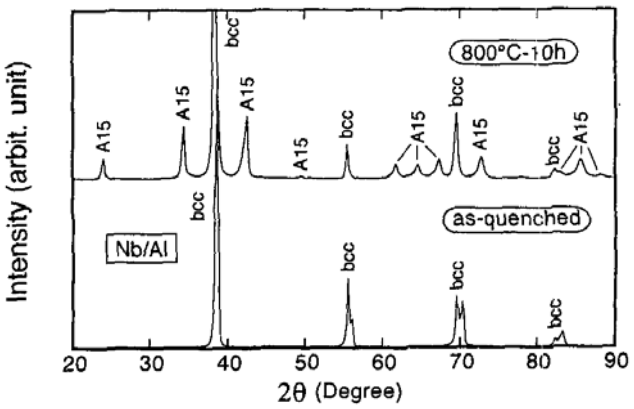

Figure 3.16 The X-ray diffraction pattern of as-quenched and post annealed material Nb/Al wire [71].

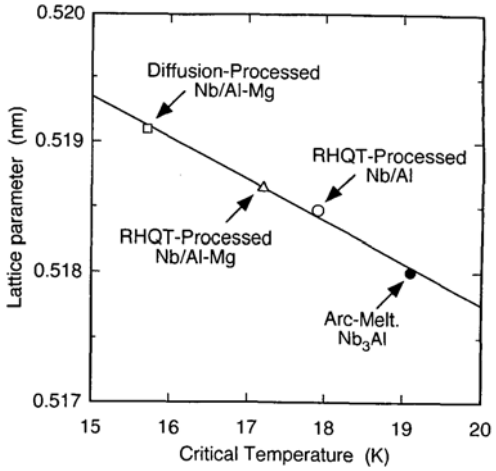

Figure 3.17 Lattice parameter vs. T_C of Nb/Al wires processed using different techniques [71].

Nb_3Al jelly roll composite wire RHQT-processed have typical values of T_C, B_{C2} (4.2 K) and J_C(20 T , 4.2 K) are 17.8 K, 26.3 T and ~ 2×10^2 A·mm^{-2}, respectively [73,74].

In 2001 Kikuchi et al. achieved further improvement through the double rapidly heating quenching (DRHQ) technique [73,74]. In this process, the transformation from the bcc phase to the A15 phase was done on a jelly roll Nb-Al by a second resistive pulsed heating. Additional annealing at 800 $^oC \times 12$ h was necessary to recover the long range order of the A15 crystal structure. Figure 3.18 shows an increase of ~ 4 K for T_C after the 2nd RHQ operation and subsequent annealing.

Figure 3.19 shows J_C versus B curves of DRHQ and RHQT processed Nb_3Al multifilametary wires. Nb-Ti and $(Nb,Ti)_3Sn$ data are also shown for comparison. The improved superconducting performance of the DHRQ processed multifilamentary wires were attributed to the formation of near stoichiometric Nb_3Al [73,74]. Figure 3.20 provides the TEM micrographs of the Nb_3Al wires processed with the DRHQ and

RHQT techniques. The A15 superconducting grains show densities of stacking faults that are lower in the DRHQ than the RHQT material. The decrease of stacking faults, which are probably pinning centres, seems to cause the degradation of J_C in fields below than 18 T. Nb_3Al jelly roll composite wire DHQT-processed have typical values of T_C, B_{C2}(4.2 K) and J_C(25 T, 4.2 K) are 18.4 K, 30 T and 200 A·mm^{-2}, respectively [73,74].

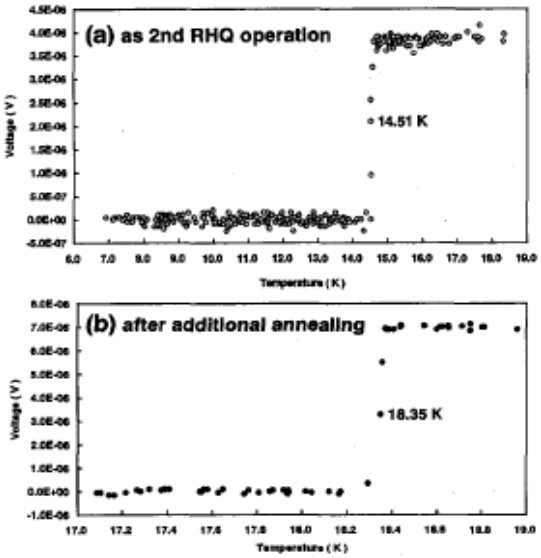

Figure 3.18 Superconducting transitions of Nb_3Al multifilamentary wires at different stages of the DRHQ [73].

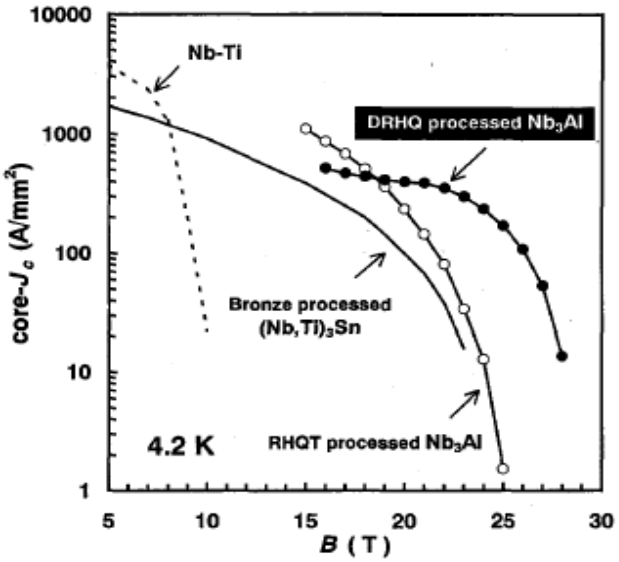

Figure 3.19 J_C performance of DRHQ processed Nb_3Al multifilamentary wires and commercialised Nb-Ti and $(Nb,Ti)_3Sn$ wires [73].

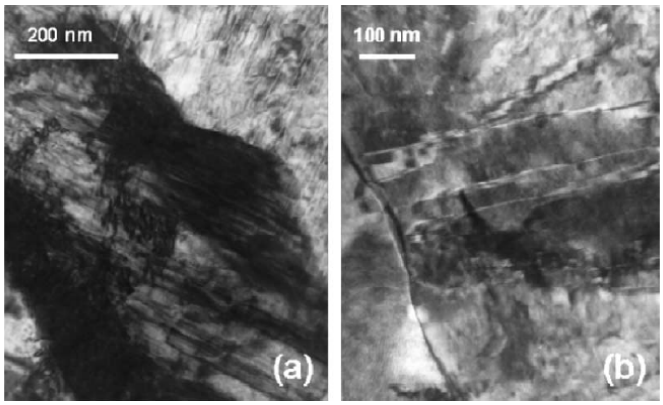

Figure 3.20 TEM micrographs of RHQT (a) and DRHQ (b) processed multifilamentary Nb_3Al wires [74].

Candidate ITER large scale Nb_3Al coil. Nb_3Al is considered as a practical alternative to Nb_3Sn for its superior T_C, B_{C2} and very good strain (ε) tolerance [75]. The engineering critical current density (J_E: critical current divided by the cross sectional area of the wire) is sufficiently high to make Nb_3Al strand a candidate for the International Thermonuclear Experimental Reactor (ITER). The Japan Atomic Energy Research Institute (JAERI) developed the world first large Nb_3Al toroidal field coil. Figure 3.21 shows the strand manufactured for this project [70].

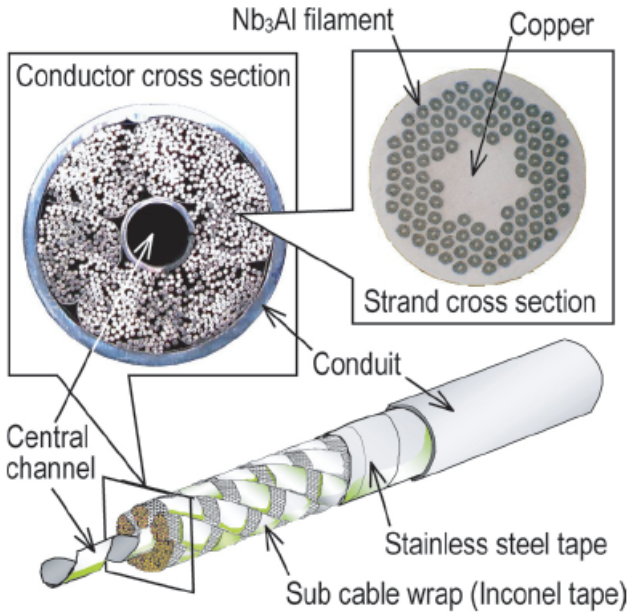

Figure 3.21 Cable used for large scale Nb_3Al coil [70].

A newly designed Nb-Al strand was processed by RHQT. Indeed conventional copper-jacketed Nb-Al strands cannot be used in RHQT since the ohmic heating temperature (~ 1900 ^oC) is higher than the melting point of copper (1084 ^oC). This issue

was overcome using external copper wires to stabilise the whole system, as shown in Figure 3.22. In this new design, the bcc RHQT-processed Nb-Al strand is embedded in cluster of Cu wires. This system was compressed to obtain a sufficiently good electrical and thermal contact between Nb-Al and Cu wires prior to heat treatment (~ 770 ^{o}C). Figure 3.23 shows the circuit model and the simulation results used to evaluate the mutual reversibility from normal to superconducting state between Nb_3Al strand and copper wires.

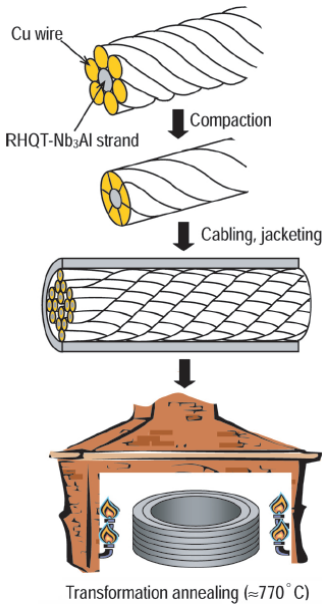

Figure 3.22 Stabilization of the RHQT Nb_3Al strand using external copper wires [70].

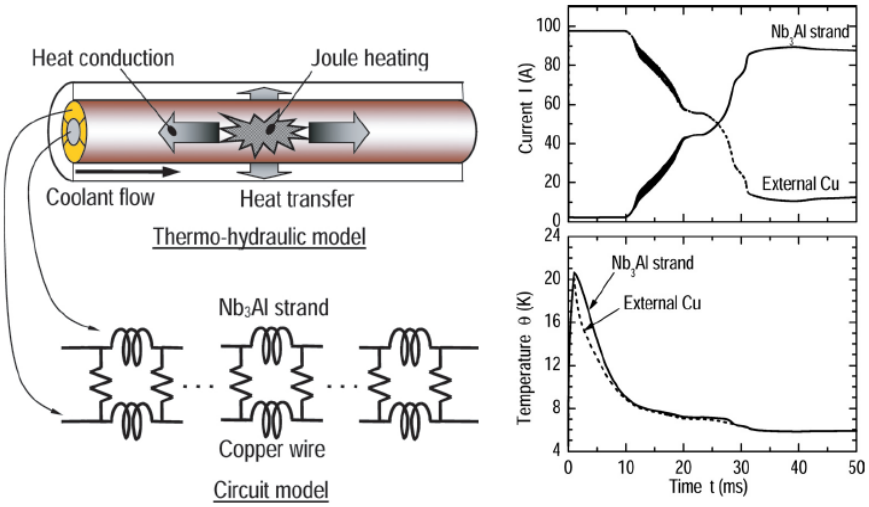

Figure 3.23 Circuit model of Nb_3Al strand embedded in a set of Cu wires (right side); Simulation results of the current and the temperature (left side). The conductance and heat transfer coefficient between the Nb_3Al and the external copper are 10 MS m^{-1} and 10 $kW \cdot m^{-2} \cdot K^{-1}$, respectively [70].

When a part of the conductor becomes normal, the current can be transferred from the Nb_3Al strand to the external copper wires because the copper wires resistance is much lower than that of the Nb_3Al strand in the normal state. The recovery to the superconducting state depends on the cooling efficiency and on the effectiveness of the current transfer between Cu wires and Nb_3Al strand. A simulation of the current transfer and temperature changes was performed using values for the conductance (10 $MS \cdot m^{-1}$) and heat transfer (10 $kW \cdot m^{-2} \cdot K^{-1}$) which are available in the present technology. The simulation results indicate that the current transfer from the Nb_3Al strand to the copper occurs quickly and the temperature decreases quickly. As the strand temperature goes down, the current in the strand increases but it does not reach the original value owing to the temperature rise in the coolant. The Joule heating affects the wire locally because it is too small to make the entire conductor normal. The supply of a new fresh coolant eliminates the undesired heating. This newly designed Nb_3Al cable was tested in 2002. A field of 13 T and a current of 46 KA were successfully obtained [70].

Nb-Al-Ge wires. The ternary compound $Nb_3Al_{0.7}Ge_{0.3}$ has not yet been developed in the form of standard processed commercial wires because of the poor workability of Al-Ge alloy [12, 76]. In 1999 Iijima et al. fabricated A15 Nb_3(Al-Ge) multifilamentary wires by RHQT [71,77]. Nb/Al-Ge precursor wires were made using rod-in-tube processing with a Al-20 at.% Ge starting alloy. Figure 3.24 compares the X-ray diffraction patterns of the as quenched and annealed wires. The as quenched Nb/Al-Ge wire X-ray pattern shows peaks of Nb-Al-Ge solid solution, A15 phase, and σ phase. The values of T_C and B_{C2}(4.2 K) were 14.9 K and 20 T. T_C values were increased from 14.9 K to 19.4 K by subsequent annealing consistent with better atomic ordering of the Nb chains. Figure 3.25 reports critical temperatures of RHQT processed Nb/Al-Ge wire versus the aging time in the range 700 ^oC - 900 ^oC. Figure 3.26 reports typical J_C(4.2 K) versus B curves for RHQT-processed Nb/Al-Ge subsequently annealed at 800 ^oC for 12 h. As shown in Figure 3.25, T_C of the RHQT-processed Nb/Al-Ge wire increased from 14.9 K to 19.4 K with the increasing with the aging time. This probably resulted result from the improvement in long-range order in the A15 crystal structure. As shown in Figure 3.26, the J_C(4.2 K) of the RHQT-processed Nb/Al-Ge wire was relative low in the fields lower than 18 T, but not so low in the high fields above 20 T. J_C(4.2 K) reached 100 $A \cdot mm^{-2}$ at 25 T at 4.2 K, which is promising for practical use. Figure 3.27 shows core-J_C (4.2 K) versus B curves for Nb_3(Al,Ge) wires with 0.3 μm (#E) and 1.5 μm (#D) Al-Ge

alloy core size (Al - 20 at.% Ge). The TEM microstructure of wire #D and #E is given by Figure 3.28 and Figure 3.29, respectively.

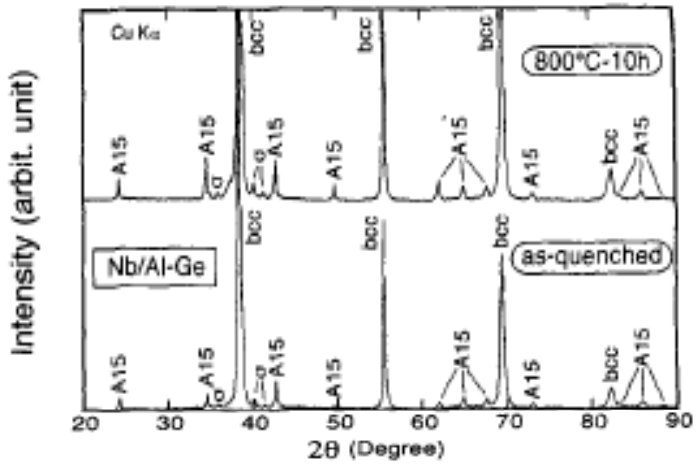

Figure 3.24 X-ray diffraction pattern for the as quenched and annealed wires at 800 °C for 10 h [71].

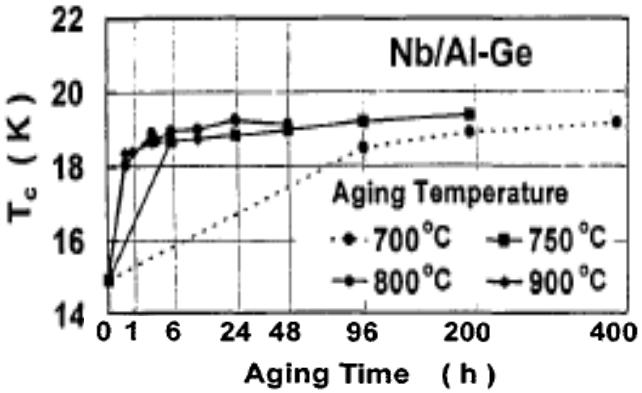

Figure 3.25 Isochronal annealing at different temperatures of the as quenched material [71].

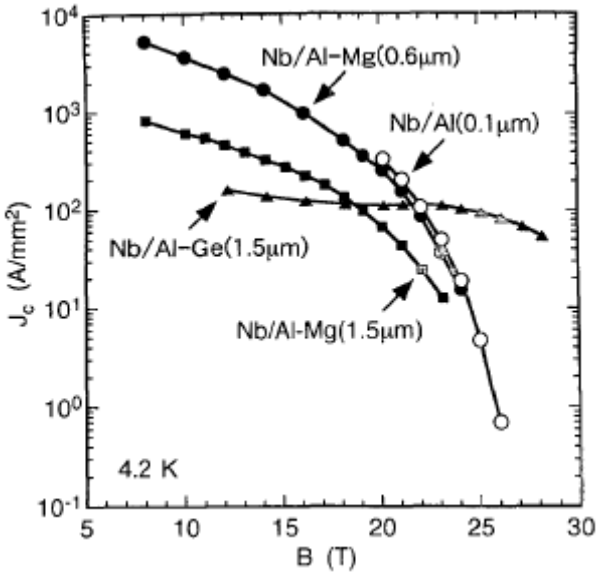

Figure 3.26 Typical J_C vs. B curves for RHQT-processed Nb/Al-Ge [71].

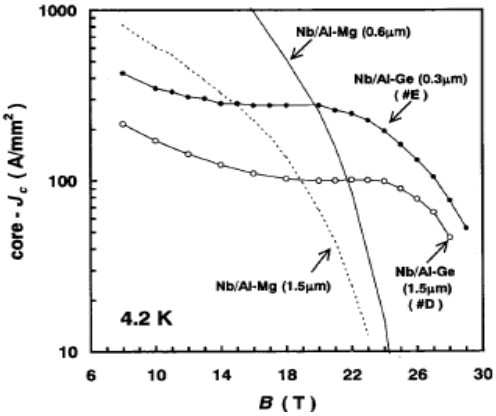

Figure 3.27 Core-J_C (4.2 K) versus B curves for $Nb_3(Al,Ge)$ wires with different Al-Ge core size The Ge concentration in the starting materials is 20 at.%. After the RHQ process wires were given an additional annealing at 800 ^oC for 12 h [77].

The TEM structure of sample #D (Figure 3.28) shows that the A15-$Nb_3(Al,Ge)$ phase is embedded in a matrix of Nb solid solution and $Nb_3(Al,Ge)_5$. Its grain size is about 100 nm in diameter. Convergent-beam electron diffraction (CBED) patterns of three A15 grain are really different from each other. The Nb_3Al phase (grain a) is surrounded by large-angle grain boundaries and shows many stacking faults [77]. The TEM structure of sample #E (Figure 3.29) shows that the volume fraction of the A15 phase increases with decreasing the Al-Ge core size. Correspondingly J_C(4.2 K) behaves in the same way (Figure 3.27). The grain size of A15-$Nb_3(Al,Ge)$ is about 100 nm in diameter and seems to be independent from the Al-Ge core size. The reduction of the Al-Ge alloy core size is very effective to improve J_C(4.2 K). Unfortunately B_{C2}(4.2 K) is very similar for wires #D and #E.

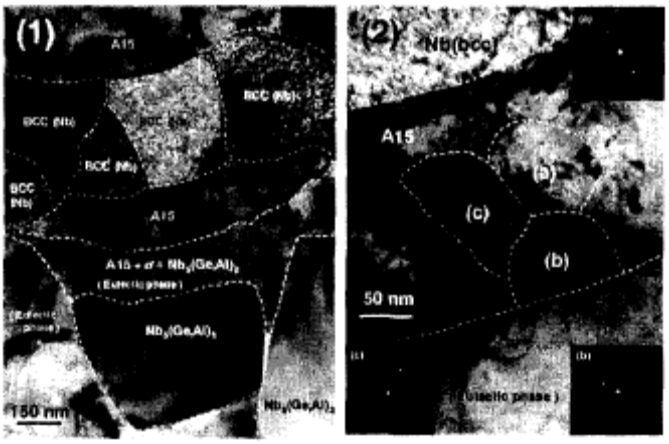

Figure 3.28 TEM structure of the RHQ-processed multifilamentary $Nb_3(Al,Ge)$ wire (D#). The Ge concentration and the core size of the Al-Ge alloy are 20 at.% and 1.5 μm. (2) Enlarged TEM image selected from (1) and CBED patterns of three A15 grains: (a), (b), (c) [77].

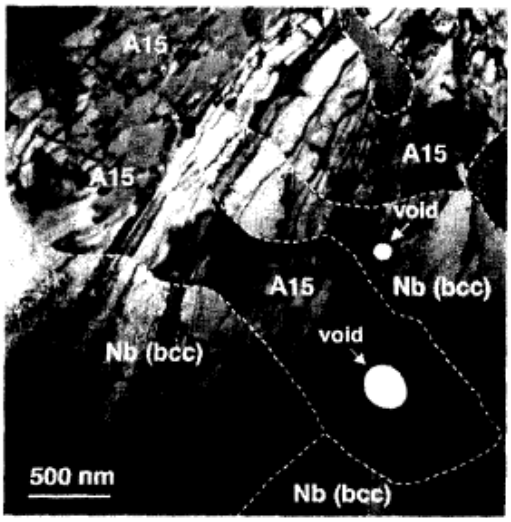

Figure 3.29 TEM structure of the RHQ-processed multifilamentary Nb3(Al,Ge) wire (E#). The Ge concentration and the core size of the Al-Ge alloy are 20 at.% and 0.3 μm, respectively [77].

3.4.3 Films

Nb-Ge films. In 1965 Matthias et al. [37] modified the quenching technique to produce splat-cooled Nb_3Ge. The lattice parameter was found to be (5.149 ± 0.005) Å. It corresponds within the limit of accuracy to a stoichiometric alloy [37,78]. The "approximate" Nb_3Ge shows a very broad superconducting transition beginning at ~ 17 K. Higher and lower germanium concentrations were found to increase or decrease T_C, respectively [37]. Figure 3.30(a) and (b) compare T_C's achieved in Nb-Ge bulk compound and "nearly stoichiometric" splat-cooled Nb_3Ge [58]. Figure 3.30(c) show a ~ 7 K transition of the splat-cooled sample after annealing 1100 ^oC x 4 days [37].

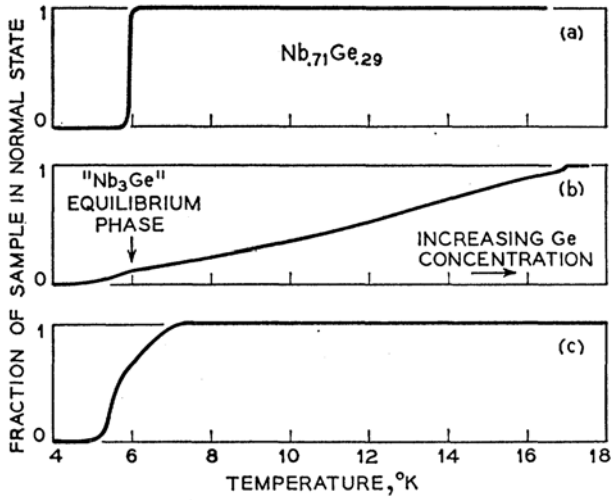

Figure 3.30 Superconducting transition of a melt of composition $Nb_{0.71}Ge_{0.29}$: (a) arc-melted; (b) splat-cooled and after annealing at 850 ^oC X 3 days and 1000 ^oC X 16 h ; (c) above mentioned splat-cooled sample after 1100 ^oC X 4 days [37].

In 1973 Gavaler prepared Nb-Ge films by a high pressure dc sputtering on heated substrates in a high purity environment [79]. Films of ~ 1 μm thickness were deposited on different substrate at temperature ranging from ~ 700 °C to 950 °C. Figure 3.31 shows the superconducting to normal state transition for the Nb-Ge films obtained by Gavaler [79]. The T_C onset of these films was 22.3 K. This transition was attributed to the formation of a more nearly perfect stoichiometric Nb_3Ge compound. The X-rays of this film showed two phases. The predominant phase was the A15 structure with a lattice constant of (5.15 ± 0.01) Å. The second phase was the Nb_5Ge_3 phase (5-10 % of the total sample).

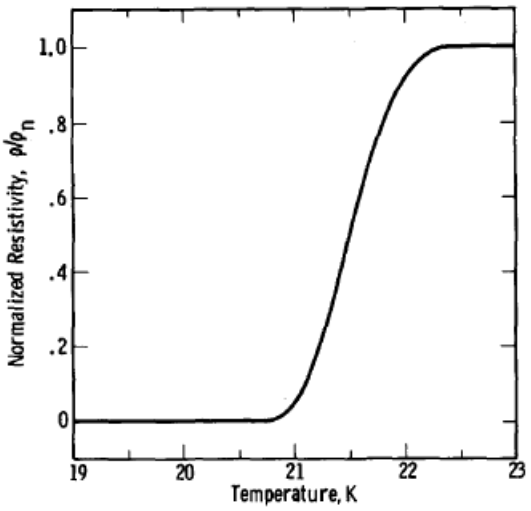

Figure 3.31 Superconducting to normal state transition for the Nb-Ge films obtained by Gavaler [79].

Further annealing of several films at 700-750 °C up to 24 h did not produce a significant change in T_C. In one case, the subsequent annealing of a film produced a large amount of Nb_5Ge_3 secondary phases (~ 30 - 40 %). The initial T_C onset of 21.4 K decreased up to ~ 16 K after 750 °C x 24 h. The annealing of this film activated Nb_5Ge_3 phase formation at the expense of the initial A15 phase [79].

Foner at al. in 1974 prepared Nb_3Ge films with the highest onset transition temperatures (~ 23 K) of any superconductor at that time [80]. They used the same technique used by Gavaler [79]. The upper critical field $B_{C2}(0)$ was found to be 37 T. In 1974, Testardi et al. repeated Gavaler's experiment on thin Nb_3Ge films with an improved T_C of (23.2 ± 0.2) K [81]. In 1975, Newkirk et al. prepared bulk films (0.02-0.06 mm thick) of Nb_3Ge by chemical vapour deposition (CVD) [40]. The CVD allows the formation of Nb_3Ge superconducting bulk at an elevated temperature according to (3.1):

$$3NbCl_5 + GeCl_4 + 9\frac{1}{2}H_2 \Leftrightarrow Nb_3Ge + 19HCl \qquad (3.1)$$

Figure 3.32 provides a relationship between T_C and the lattice spacing. The lattice spacing corresponding to the highest T_Cs are located in the region close to 5.146 Å. Powder XRD pattern indicate undesired traces of the compound Nb_5Ge_3. The specific heat versus temperature is given in Figure 3.33. The transition is quite broad probably as result of compositional inhomogeneity. A decrease of T_C was caused by annealing the material at 1000 $^oC \times 2$ h [40]. This can be ascribed to a decrease of the germanium content of Nb_3Ge to its equilibrium value [82].

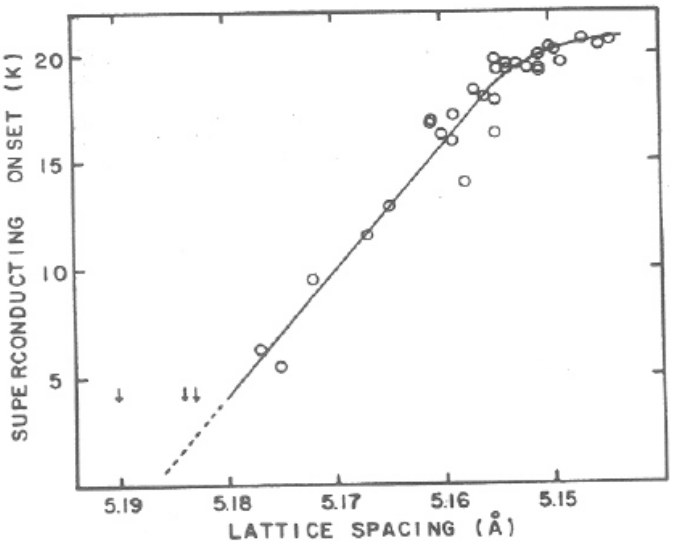

Figure 3.32 Variation of transition temperature with lattice spacing for Nb_3Ge [40].

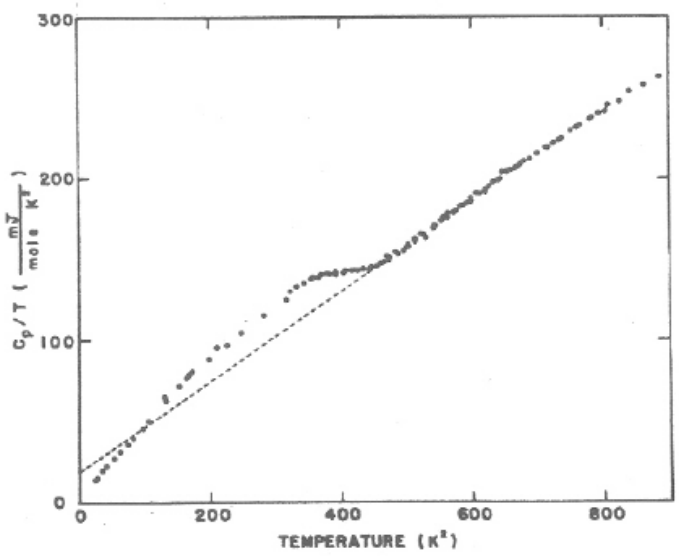

Figure 3.33 A Debye plot showing the variation of specific heat with temperature for Nb_3Ge [40].

In 1976 Rogowski at al. fabricated metastable Nb_3Ge thin films with a large compositional span from the Ge-rich to the Nb-rich end [83]. The substrate-target

configuration is given by Figure 3.34. As sputtered films were annealed ~ 24 h at 650, 725, 800, 840 and 940 ^{o}C. After each annealing all the films were characterised by standard powder x-ray diffractometry to determine structural and/or phase changes. Figure 3.35 shows the changes in the lattice parameters of the A15 phase, a_0, for each of Nb_3Ge films as a function of the annealing temperature.

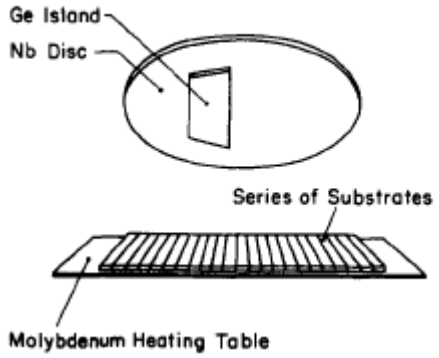

Figure 3.34 Substrate-target configuration used to prepare rf-sputtered Nb-Ge thin films [83].

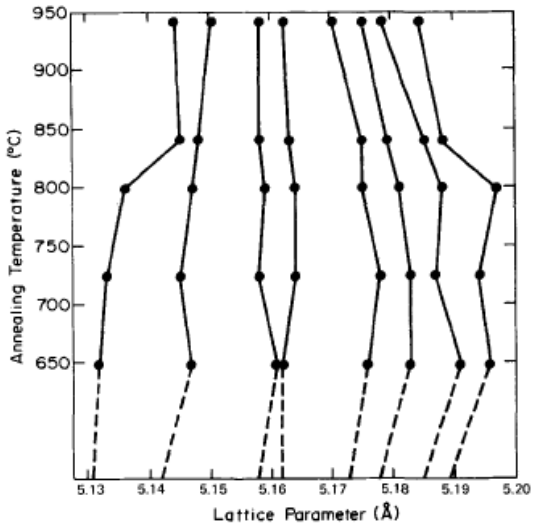

Figure 3.35 Variation of lattice parameter a_0 with annealing temperature. The base line represents as-sputtered a_0's [83].

Figure 3.35 indicates an anomalous increase in the lattice parameter up to 1.3 % in the metastable Ge-rich side with $a_0 < 5.167$ Å and in the metastable Nb-rich side with $a_0 > 5.176$ Å. The authors suggest that eventual compositional inhomogeneities (i.e. secondary phases) might have affected the stability of Nb_3Ge. In a related experiment similarly prepared Nb_3Ge films were annealed at 1200 ^{o}C for 24 h. The lattice parameter changes of all these sample led to a metastable Nb_3Ge phase for all compositions. Figure 3.36 shows the linear correspondence between T_C versus a_0.

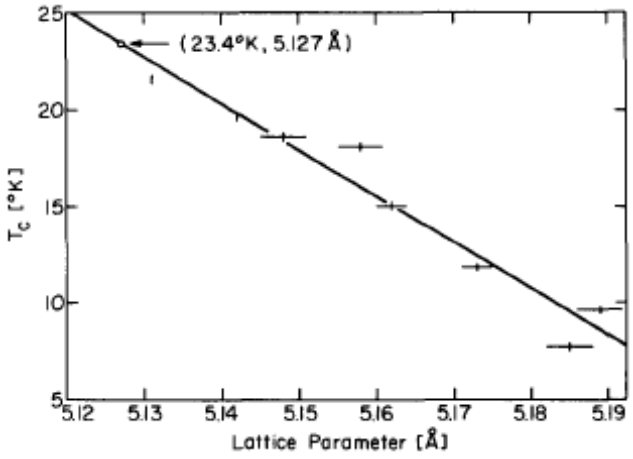

Figure 3.36 Variation of Tc with lattice parameter [83].

The figure above predicts for the ideal stoichiometric phase (5.127 Å) a T_C of 23.4 K. This value is very similar to that provided by Testardi et al. [81].

Much more recently, a study of Nb_3Ge thin films produced using chemical vapour deposition was completed by Saini et al. [41]. The resistivity of the Nb_3Ge film versus temperature is reported in Figure 3.37. It show a sharp transition (ΔT_C = 1 K) below 20.6 K. The indexed XRD pattern (inset of Figure 3.37) shows the A15 structure diffraction peaks and some traces of Nb_5Ge_3, estimated to be ~ 4 % [41]. The lattice parameter found by refinement of XRD pattern is (5.1398 ± 0.0007) Å. This value is consistent with earlier structural studies on high-quality stoichiometric Nb_3Ge films [41].

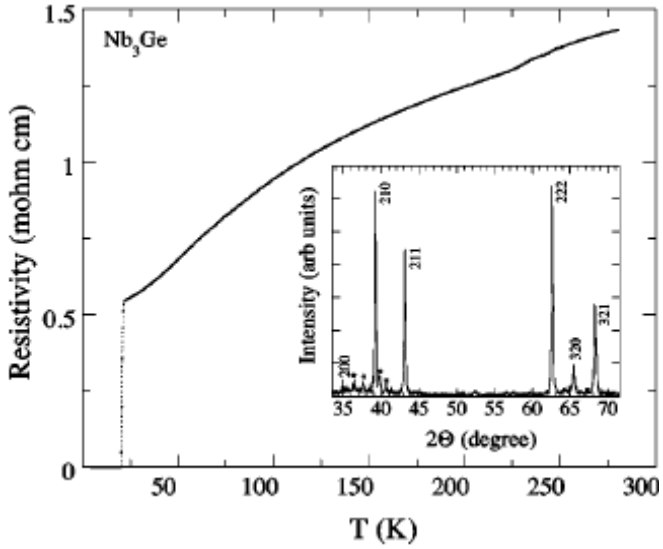

Figure 3.37 Resistivity of the Nb_3Ge film versus temperature and its XRD pattern [41].

Nb-Al films. In 1984 Bormann et al. prepared Nb-Al films by electron-beam coevaporation of the components [84]. This technique was used to avoid any influence

of impurity atoms, especially oxygen and nitrogen. Films of ~ 1 μm thickness were deposited on cooled sapphire substrate. They were pressed by Nb clips against a highly polished Nb block. The temperature was adjusted in the range between -195 °C and 1000 °C by a liquid N_2 cold finger and a heater. For substrate temperatures of 0 °C the homogeneity range of the bcc Nb-Al solid solution could be extended up to about 40 at.% Al and subsequently, the bcc alloys were transformed in A15 phase by heat treatment. The annealing was performed in the range 750 - 975 °C at a background pressure $\leq 10^{-8}$ mbar. Small amounts of σ-phase Nb_2Al and non-transformed bcc phase were shown by TEM and X-ray investigation. The lattice parameter of the A15 phase is reported in Figure 3.38. The T_C values of the A15 phases are given versus composition by Figure 3.39. Deviation from the stoichiometric composition leads to a decrease in T_C: typically 1 K/at.% Al.

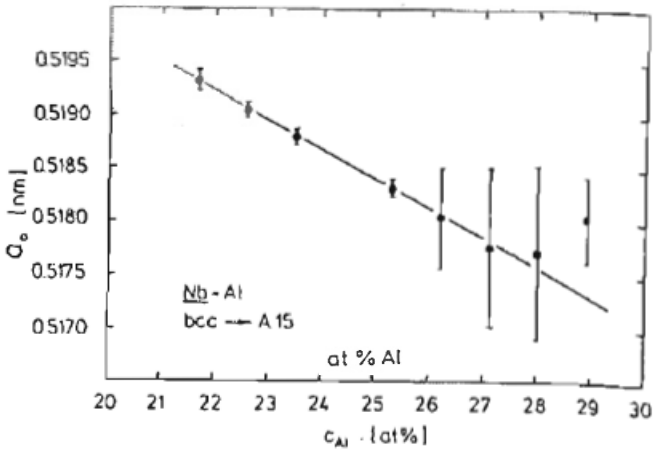

Figure 3.38 Lattice parameter of the A15 phase formed from a bcc matrix [84].

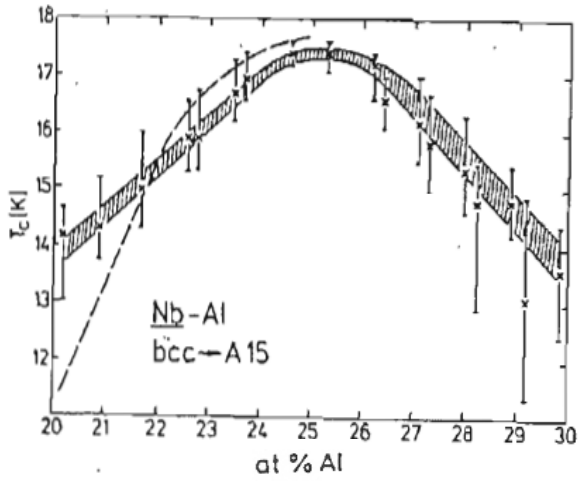

Figure 3.39 T_C of the A15 phase versus the composition of the sample [84].

Nb-Al-Ge films. In 1975 Dahgren produced Nb-Al-Ge and Nb-Al superconductors deposits using high rate sputtering technique [85]. The sputter deposition was done at

20 °C at the rate 1 μm/min from compacted elemental powder sputtering targets (99.5 % purity). The corresponding crystal structures were not clear for Nb-Al-Ge whereas Nb_3Al was clearly body-centred-cubic. Heat treatment at 750 °C × 1 day completely transformed the bcc deposits to A15 nanocrystalline grains (35 nm). Results for various heat treatment times at 750 °C are provided by Figure 3.40. Critical temperatures were about 15 K and the lattice parameters high for very short heat treatment. The highest critical temperature (18.3 K) was found in those samples containing undecomposed metastable A15 structure. Decomposition of the metastable A15 phase caused an increase in the Nb composition in the remaining A15 composition. This was indicated by an increase in the A-15 phase lattice parameter over 5 to 20 days of heat treatment and an increase in T_C. Decomposition was not detected in Nb_3Al until after 20 days at 750 °C. Thick sputter-deposited $Nb_3Al_{0.75}Ge_{0.25}$ had critical currents at 4.2 K up to 2.6×10^2 A·mm^{-2} at 20 T, which were attributed to the formation of extremely small grains during heat treatment.

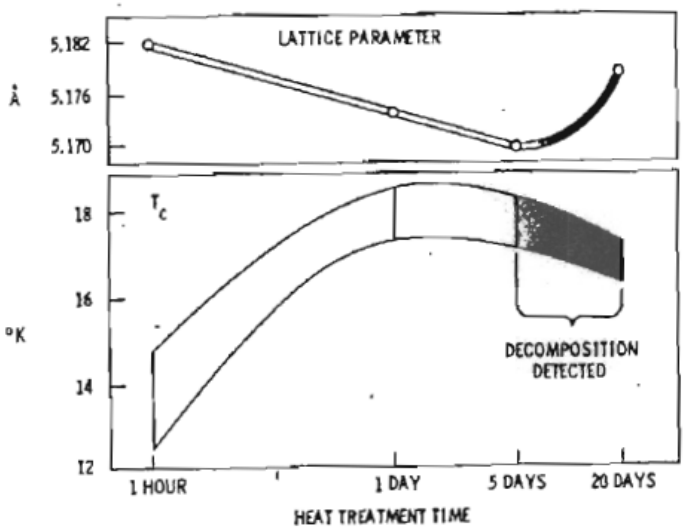

Figure 3.40 The A-15 lattice parameter and critical temperature, T_C, versus heat treatment time at 750 °C for sputter deposited $Nb_3(Al_{0.75}Ge_{0.25})$ made at 20 °C [85].

In 1982 Togano et al. prepared thin foils of the ternary $Nb_3(Al,Ge)$ alloy starting from a metastable bcc solid solution [86]. The fact that the T_C values were above 18 K and the critical current density values were 3.5×10^4 A·cm^{-2} at 4.2 K and 16 T opens the possibility for these materials to be considered for wire applications.

Starting ingots of Nb-Al-Ge alloy were prepared by conventional arc melting. Subsequently small amounts of material were rapidly quenched from the liquid state onto a thin Cu substrate. The quenched alloys were in shape of thin foils, typically

10-20 mm in width, and up to 20 μm in thickness. They were transformed into the A15 structure by annealing. Figure 3.41 shows the X-ray diffraction pattern of the as-quenched and annealed $Nb_3(Al_{0.8}Ge_{0.2})$. Figure 3.42 shows the effect of isochronal annealing and isothermal annealing at 850 °C. It was observed that A15 Nb-Al-Ge was metastable and decomposed into an off-stoichiometric A15 phase and a σ-phase after prolonged annealing [86]. The typical results of the J_C measurements are shown in Figure 3.43.

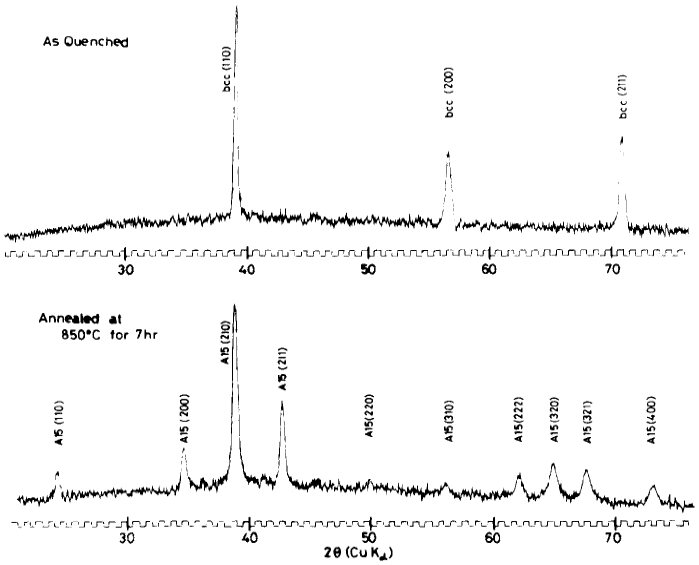

Figure 3.41 X-ray diffraction patterns of the as quenched and annealed bcc $Nb_3Al_{0.8}Ge_{0.2}$ solid solution (a = 5.173 Å) [86].

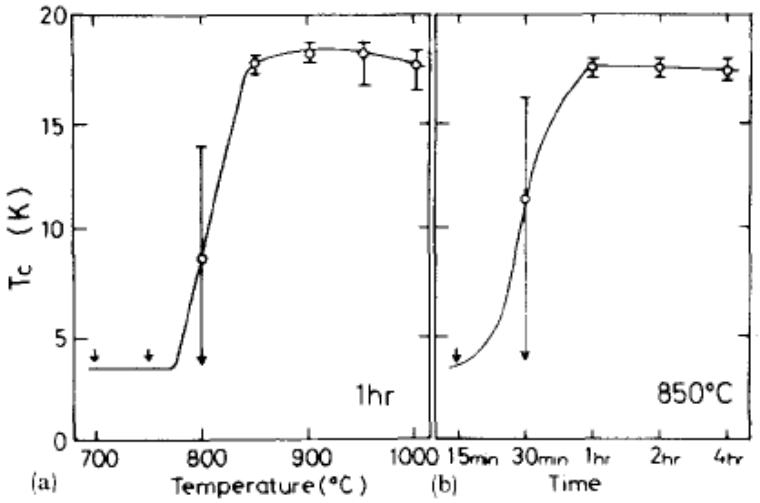

Figure 3.42 Effect of isochronal annealing for 1 h and isothermal annealing at 850 °C of the liquid quenched $Nb_3Al_{0.8}Ge_{0.2}$ [86].

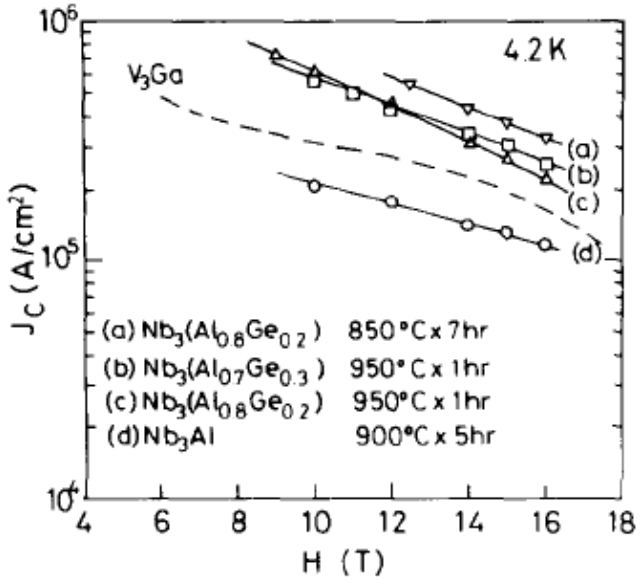

Figure 3.43 J_C vs. H curves of A15 Nb-Al-Ge for different compositions prepared by the liquid quenching and subsequent annealing [86].

The J_C of the stoichiometric A15 ternary compounds are ~ 2000 A·mm^{-2} at 16 T and 4.2 K. The high J_C values obtained in this work were attributed to the formation of extremely small A15 grains. The transmission electron micrograph of $Nb_3Al_{0.8}Ge_{0.2}$ formed after annealing at 850 ^oC for 1 h is provided in Figure 3.44. The converted A15 phase has an extremely small grain size of tens of nanometres consistent with XRD line broadening.

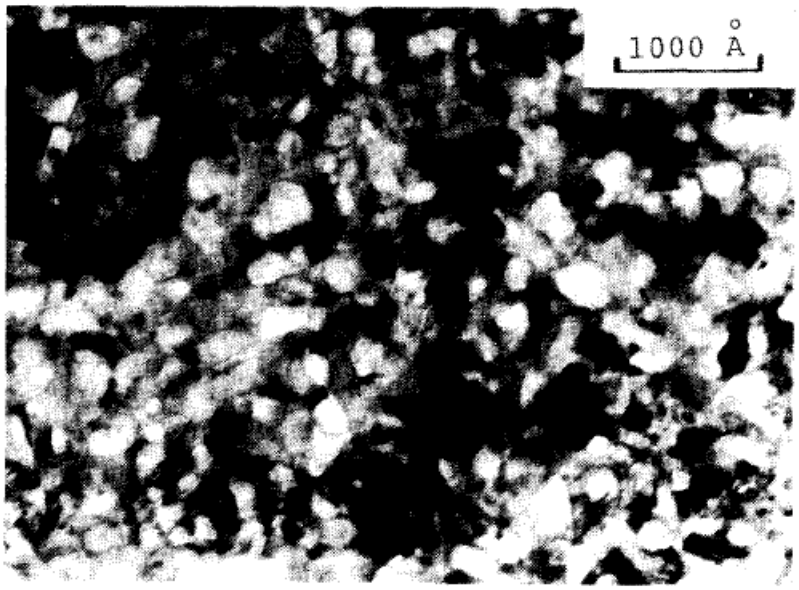

Figure 3.44 Transmission electron micrograph of $Nb_3Al_{0.8}Ge_{0.2}$ formed after annealing at 850 ^oC [86].

3.4.4 Ball milled material

Nb-Ge ball milled powders. In 1985 Politis prepared amorphous superconducting Nb_3Ge and $Nb_3Al_{1-x}Ge_x$ powders by mechanical alloying in a purified argon atmosphere [87]. Figure 3.45 shows X-ray patterns of Nb-Ge alloy versus milling time. After 8 h, the milled powders become gradually amorphous. The effective particle size of Nb-Ge and Nb-Al-Ge versus milling time is shown in Figure 3.46. Figure 3.47 shows the transition temperature (90 % of T_C onset) of the amorphous Nb-Al-Ge powders).

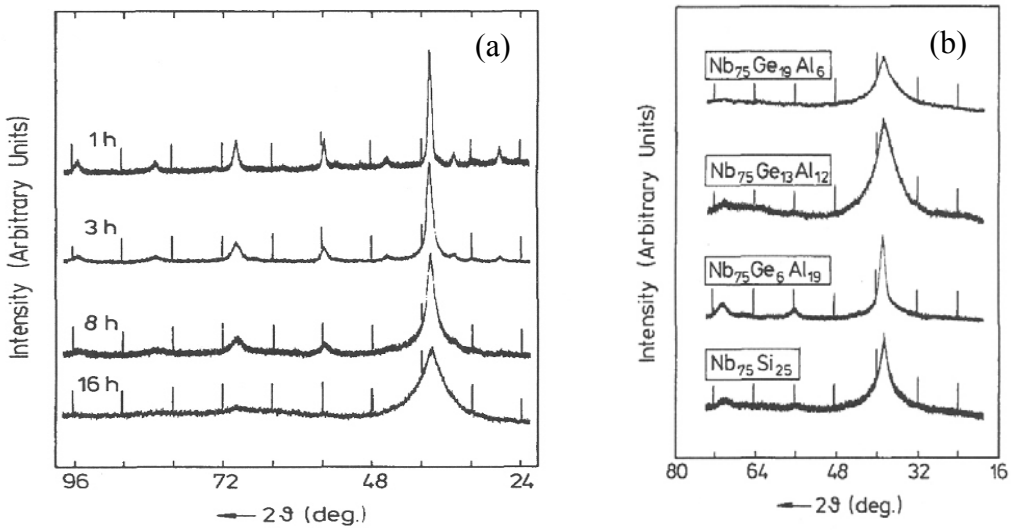

Figure 3.45 X-ray patterns of: (a) Nb-Ge alloys; (b) Nb-Al-Ge alloys after 8 h milling [87].

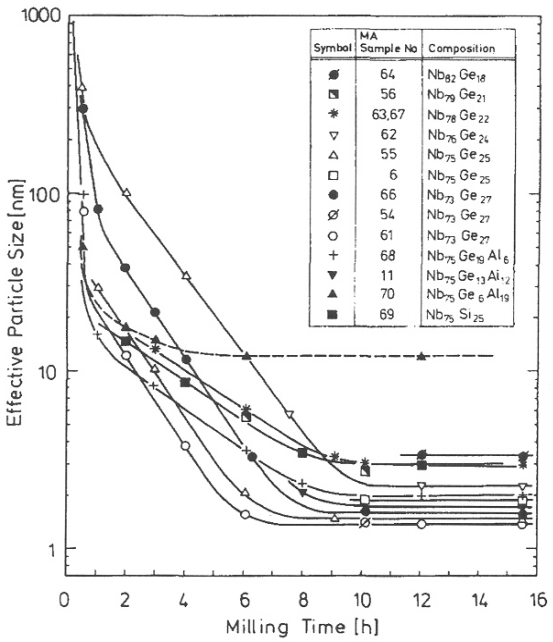

Figure 3.46 Effective particle size of milled Nb-Ge and Nb-Al-Ge as a function of the milling time [87].

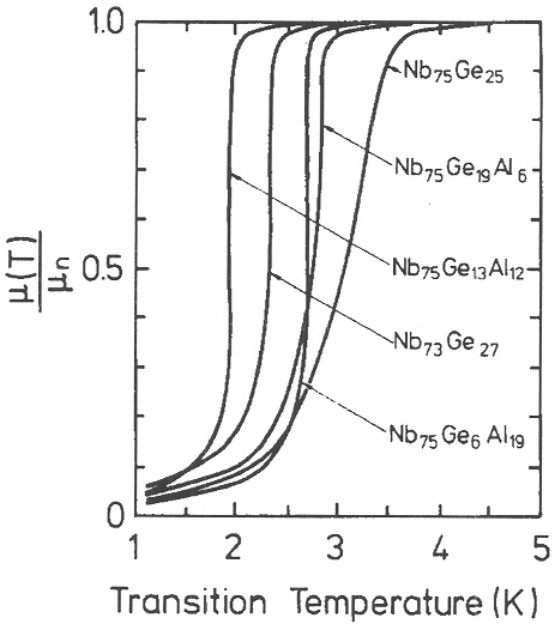

Figure 3.47 Transitions curves of amorphous Nb-Ge and Nb-Al-Ge powders. μ_n is the permeability value at 10 K [87].

In 1987 Kenik et al. studied the microstructural evolution of mechanically alloyed Nb-25 at.% Ge powders [88]. X-ray microanalysis revealed amorphous specimen regions and all the intermetallic phases shown in the Nb-Ge phase diagrams. The measured germanium contents were 8.6 at.% for the niobium solid solution, 20.0 at.% for the A15 phase, 25.6 at.% for the amorphous phase, 27.5 at.% for the Nb_5Ge_3 and 49.6 at.% for the $NbGe_2$ - very different from the initial (average) composition (25 at.%) probably due to the nonequilibrium nature of the mechanical alloying process [88].

Nb-Al ball milled powders. Ball milling Nb-Al requires the use of a process control agent to inhibit inter-particle welding. All the following procedures involved the use of about 1 wt.% stearic acid ($C_{18}H_{36}O_2$).

In 1976 Larson et al. used high energy ball milling of powders to prepare Nb_3Al [89]. Ten grams of Nb-Al powders mixture were ball milled in a small high-energy Spex mill. Niobium grinding balls were employed and milling was conducted for a period of several hours. Milled powders were subsequently annealed between 800 ^oC and 950 ^oC. Measurements of critical temperatures yielded a broad transition ranging from 15.8 to 10 K. X-ray diffraction of annealed powders reveals the presence of diffraction lines due to Nb-solid solution in addition to those for Nb_3Al indicating an off-stoichiometric composition. The lattice parameter of the Nb_3Al was 5.190 Å. The correlation between T_C and lattice parameter for various A15 compounds are shown in Figure 3.48**.**

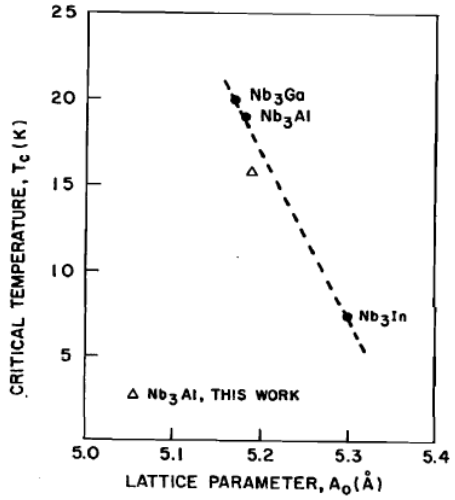

Figure 3.48 Correlation of critical temperature with lattice parameter for A15 compounds [89].

In 1988 Hellstern at al. prepared Nb-Al alloys by mechanical alloying of elemental crystalline powders with different alloy compositions [90]. Figure 3.49(a) and (b) show the X-ray diffraction pattern for Nb-Al (1:1) before (a) and after milling (b). Before milling, all expected Nb and Al peaks were present (Figure 3.49(a)). After 2 h milling most of Al is incorporated in the Nb-Al bcc solid solution (Figure 3.49(b)). After 60 h milling, a broad maximum was observed (Figure 3.49(c)). During milling the Nb lines had broadened considerably owing to the refinement of the crystallite size and to the introduction of the mechanical stresses. The authors underlined that the formation of an amorphous alloy occurred only for the equiatomic composition after 60 h milling, as shown in Figure 3.49(2).

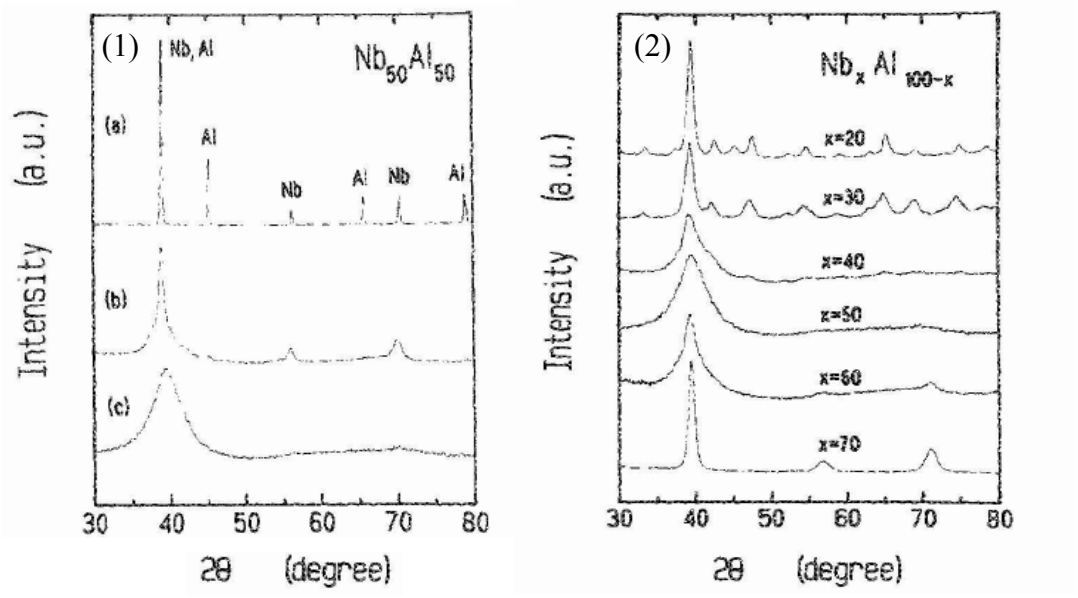

Figure 3.49 (1) XRD patterns of $Nb_{50}Al_{50}$ before milling (a), after milling for 2 h (b), and after 60 h milling (c); (2) XRD patterns of Nb_xAl_{100-x} at different compositions after 60 h milling [90].

After mechanical alloying the lattice constant of the A2 phase was 3.343 Å. This value is considerably larger than that of the elemental niobium (a_0 = 3.303 Å). This is probably due to the large lattice distortions from the high-energy ball milling process. Figure 3.50 shows X-ray diffraction pattern of Nb-Al (3:1) before (a) and after (b) annealing for 2 h at 825 ^{o}C. After the heat treatment, the bcc solid solution was transformed in A15 Nb_3Al.

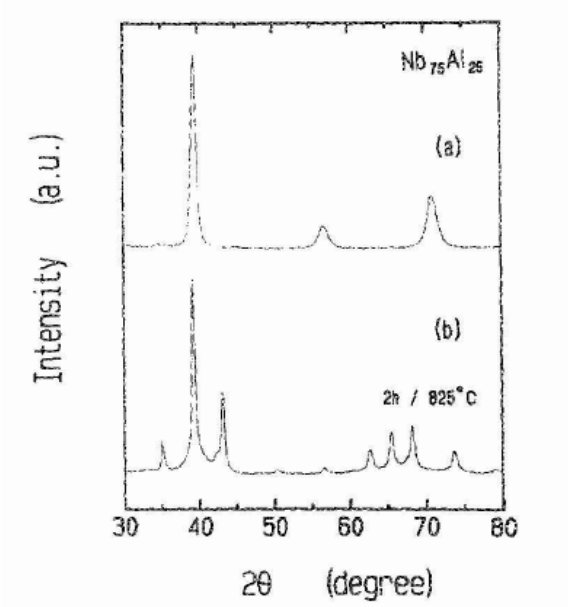

Figure 3.50 X-ray diffraction patterns of mechanically alloyed Nb-Al (3:1) before (a) and after annealing (b) [90].

In 1990 Ohering et al. studied the Nb-Al system by ball milling the intermetallic compound Nb_3Al [91,92]. The milling was performed with a planetary mill with hardened steel vials and balls (BPR: 5). In order to avoid atmospheric impurities, the milling was done in a glove-box with purified argon. Figure 3.51 shows the XRD patterns of the as-received and milled materials. The untreated material shows lines of the A15-Nb_3Al and σ-Nb_2Al phases. With increasing milling time, the lines expand and after 2.5 h milling the bcc Nb-Al solid solution can be detected. On further milling the intensity of the bcc peaks increase whereas that of the A15-peaks decreases. Figure 3.52 shows (a) the order parameter S/S_0, (b) crystallite size and the lattice strain determined from diffraction lines. Owing to a gradual degradation of the long-range order, high-energy ball milling of Nb_3Al resulted in a formation of a nanostuctured bcc Nb-Al solid solution. Heat treatment of this powder led to the re-formation of the A15-phase [93].

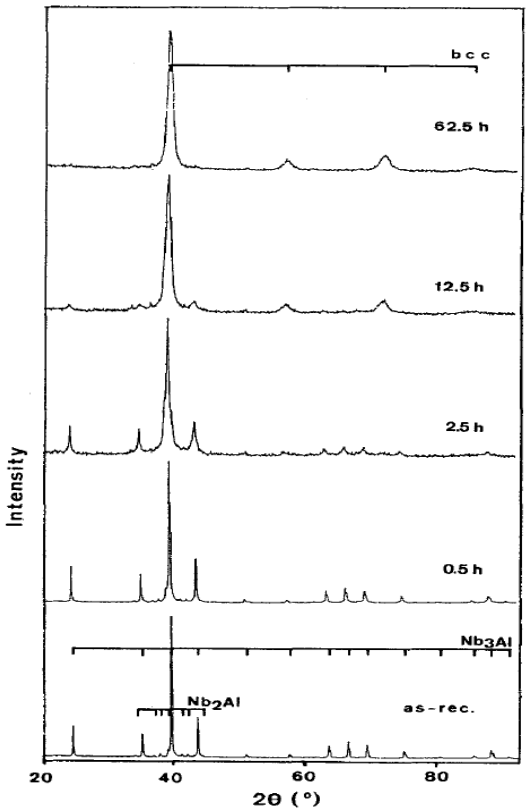

Figure 3.51 X-ray patterns observed on Nb_3Al powders milled for different times [92].

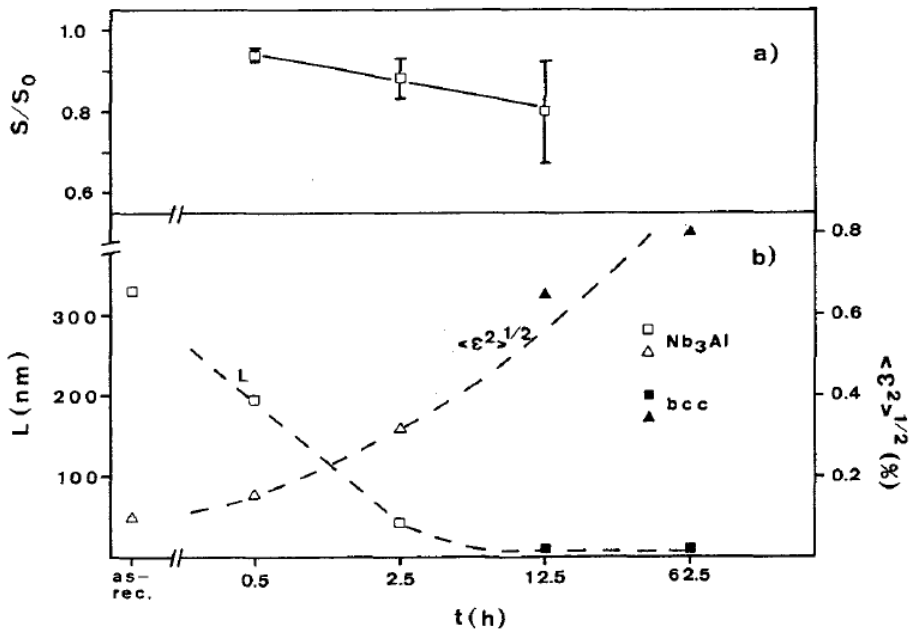

Figure 3.52 (a) Relative degree of order vs. milling time as determined from the intensity of diffraction lines; (b) Crystallite size (L) and averaged lattice strain ($<\varepsilon^2>^{1/2}$) determined from the line broadening vs. milling time [92].

In 1995 Rock and Okazaki calculated carefully the intermetallic phase volumes of the 77 % at. Nb-Al system during milling [94]. The XRD spectra were analysed by a non-linear curve fitting software. Amorphous-like peaks were deconvoluted into separated Gaussian peaks for different planes of the expected phases. A typical deconvolution is shown by Figure 3.53. Changes in volume fractions of Nb, Al, Nb_2Al and Nb_3Al are presented in Figure 3.54. Figure 3.55 shows the changes in volume fraction with different annealing temperatures for Nb_3Al and Nb_2Al. It appears that the solid-state reaction of the Nb_3Al formation during annealing is the following:

$$Nb_2Al + Nb \rightarrow Nb_3Al \tag{3.2}$$

Rock also completed some excellent analysis of combined DSC and XRD data to extract the activation energies associated with the formation of Nb_2Al and Nb_3Al. Nb_3Al formation occurred during annealing with a systematic grain growth. Figure 3.56 shows the crystallite size of Nb_3Al during isochronal annealing [94].

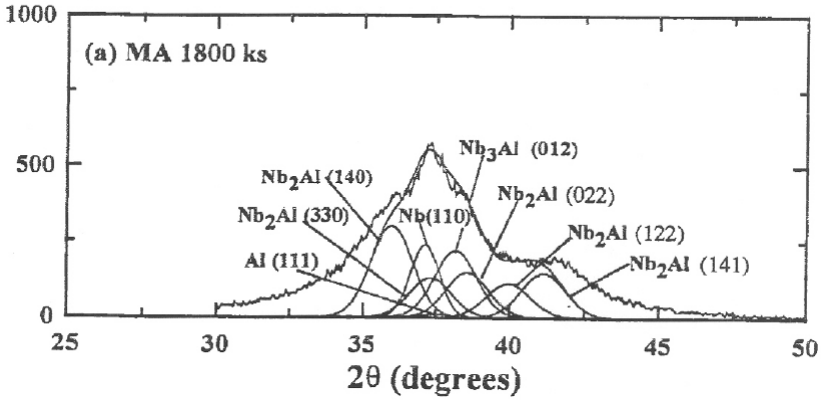

Figure 3.53 Typical deconvolution of XRD spectra for Nb-Al (Nb -23 %at.Al) milled for 500 h [94].

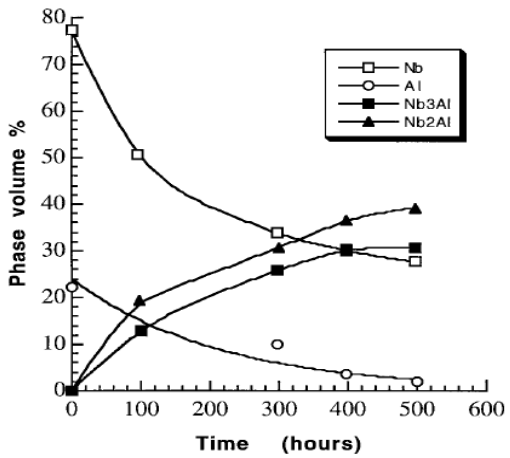

Figure 3.54 Change in volumes fractions of Nb, Al, Nb_2Al and Nb_3Al after different milling times [12,94].

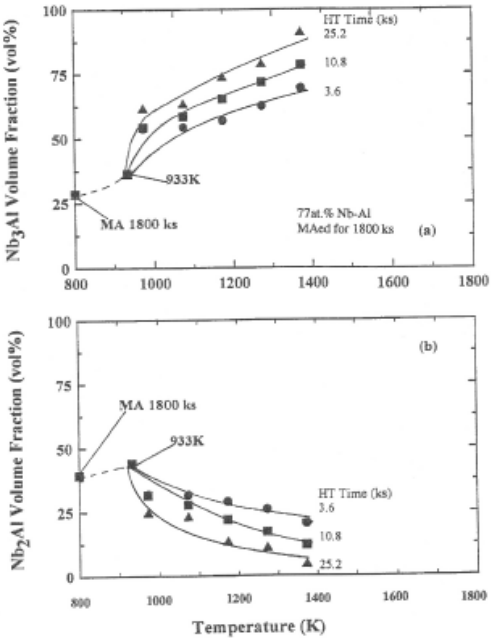

Figure 3.55 Changes in volumes fraction with different annealing temperatures for (a) Nb_3Al and (b) Nb_2Al [94].

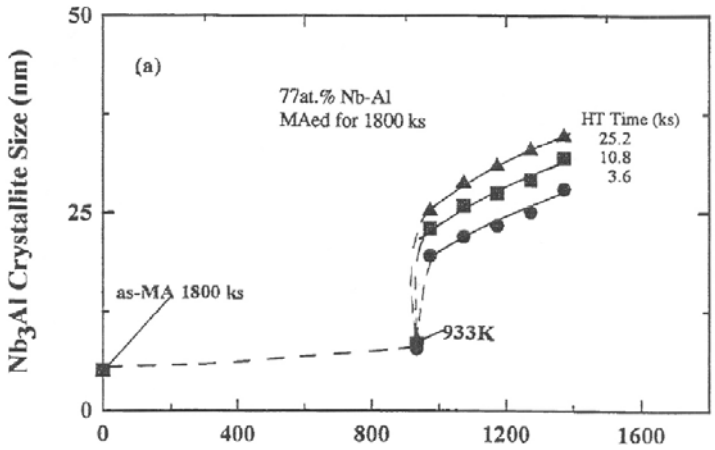

Figure 3.56 Isochronal annealing of Nb_3Al vs. temperature [94].

In 1996 Saida at al. investigated the growth of nano-grained structure produced by MA of Nb and Al [95]. A stoichiometric composition of elemental powders was mechanically alloyed. The as-MA'ed product had the volume distribution of 13 % Nb, 40 % Nb_2Al and 47 % Nb_3Al. The grain size were 4 nm for Nb and Nb_2Al and 3.8 nm for Nb_3Al, respectively. Figure 3.57 show that the various heat treatments converted the three phases into a two-phase mixture of ~ 80 - 90 % Nb_3Al and ~ 10 - 20% Nb_2Al. Powders were isochronally annealed from 600 ^oC up to 1150 ^oC. Figure 3.58 reports the isothermal grain growth for Nb_3Al and Nb_2Al phases. A larger increase of the crystallite size occurred above 900 ^oC.

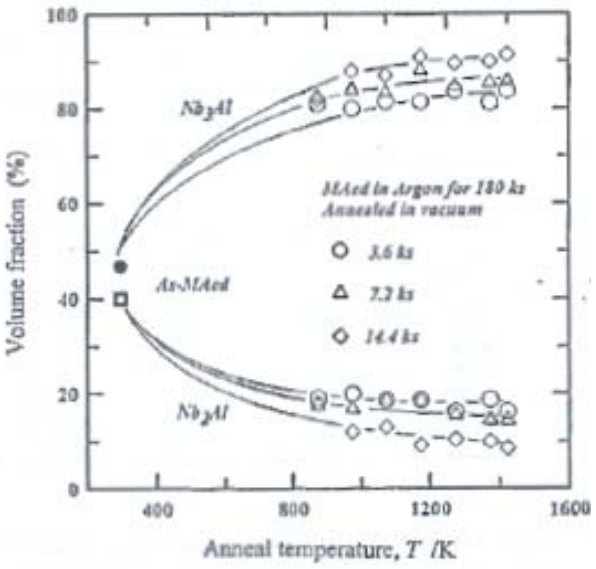

Figure 3.57 Changes in volume fractions of Nb_3Al and Nb_2Al [95].

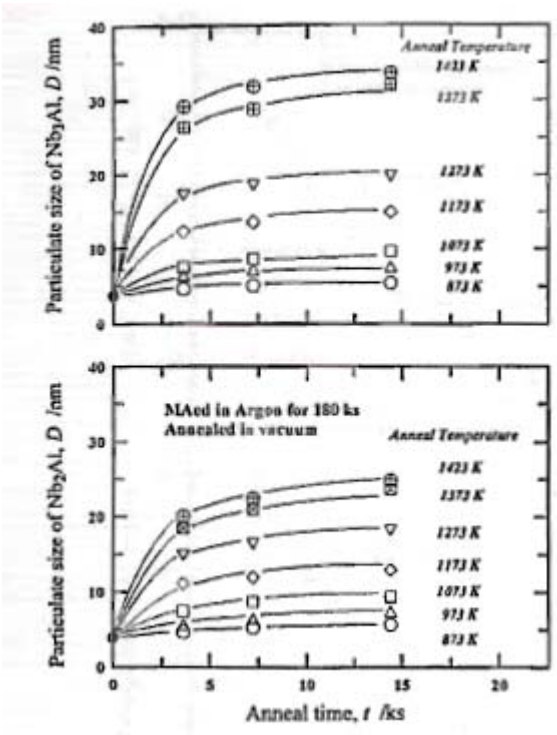

Figure 3.58 Isothermal grain growth in Nb_3Al and Nb_2Al phases [95].

In 1996 Peng et al. reported on high-energy ball milled Nb-Al powders [93]. Elemental niobium and aluminum powders were used as starting materials. The compositions investigated were 15, 25, 33.3, 50, 60, 65, 70, 85, and 90 at.% Al. Mechanical alloying of powders was carried out in a SPEX 8000 shaker mill. Hardened steel vial and balls were used. The ball to powder weight ratio was 10:1. Figure 3.59 reports the phase formation and corresponding milling times at different compositions. Figure 3.60 shows

the X-ray diffraction patterns of the powder mixture Nb-Al (3:1) milled for different times. After 5 h milling, only the Nb-Al bcc solid solution lines were present. The lattice parameter was found to be 3.306 Å. With increasing milling time, peaks become considerably broader and their intensities decreased. Formation of an amorphous phase was observed after 10 h milling [93,96]. A fcc phase was detected for higher milling times owing to NbN contamination. Figure 3.61 provides the A15 lines of the Nb-Al (3:1) solid solution after annealing at 825 ^{o}C for 2 h. The atomic ordering of the ground powder after annealing is a balance between the disordering from milling process and the thermally activated reordering. The mechanical alloying of Nb-Al leads to a grain refinement down the nanometre range, extension of solid solubility (up to ~ 60 at.% Al), formation of amorphous phases and direct synthesis of intermetallics [93].

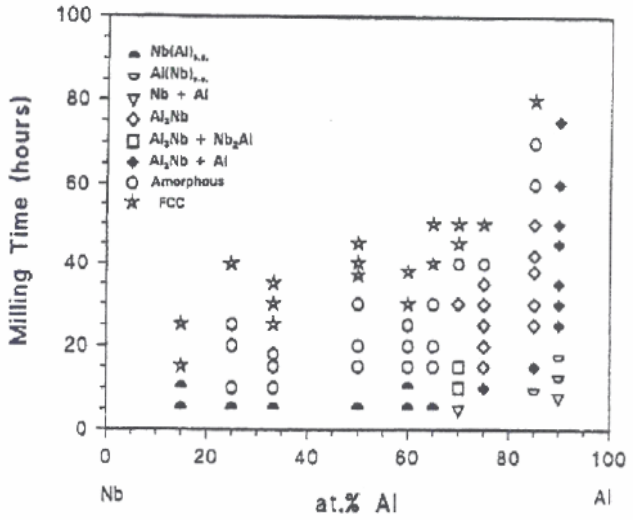

Figure 3.59 Phase formed at different compositions and milling times in mechanically alloyed Nb-Al powders. The bcc solid solution extends up to 65 at.% Al.

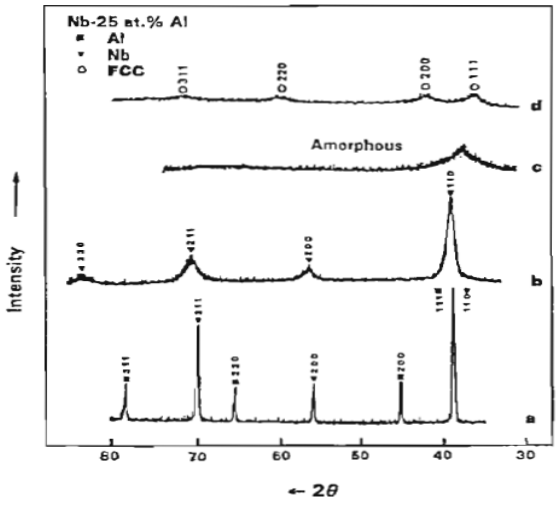

Figure 3.60 X-ray diffraction patterns of the Nb-Al (3:1) powder mixture mechanically alloyed for (a) 0 h, (b) 5 h showing the b.c.c. solid solution (c) 10 h showing the amorphous phase and (d) 40 h showing the fcc phase due to nitrogen composition [93].

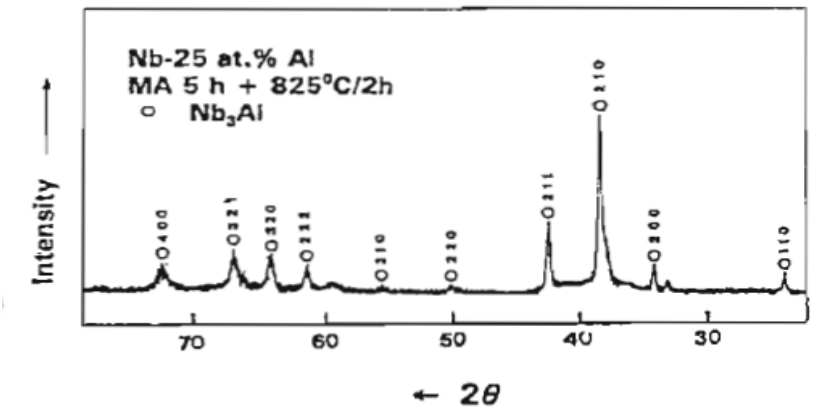

Figure 3.61 X-ray diffraction patterns of the Nb-Al (3:1) powder mixture mechanically alloyed for 5 h subsequently heat treated for 2 h at 825 ^{o}C [93].

Nb-Al-Ge ball milled powders. The only work the author is aware of was done by Politis in 1985 [87]. See Nb-Ge ball milled powders (subsection 3.4.4).

3.4.5 Hot pressed material

In the later nineties, work was done to densify ball milled powders into a solid bulk [97] using a hot pressing performed by Dymec at al. [98,99]. The materials investigated were produced by mechanical alloying of pure elemental powders. Two Nb-Al alloys containing 18 and 20 at.% Al were milled for 2 h at about -110 ^{o}C and 85 h at room temperature. The milling was carried out in a stainless steel vial using stainless steel balls. The ball to powder ratio was 11:1. Figure 3.62 shows the SEM of milled powders after milling prior to consolidation. Consolidation was carried out by hot-pressing (HP) in an argon atmosphere at 1150 ^{o}C for 2 h.

Figure 3.62 Scanning electron micrograph of Nb-Al as-milled powder. The read marker is 100 µm [98].

Figure 3.63 show the corresponding X-ray diffraction pattern. Three main phases were identified: Nb solid solution, the A15 Nb_3Al phase and a σ-type Nb_2Al tetragonal phase. Also small peaks coming from Al_2O_3 were recognized. Figure 3.64 shows the TEM typical microstructure of the HP'ed Nb-Al sample. The average grain size estimated from the electron micrograph is less that 1 μm. The intermetallic phases were distinguished from the Nb solid solution: niobium grains contain high dislocation density while Nb_3Al and Nb_2Al show numerous stacking faults. Al_2O_3 particles were found in rounded shapes both in other phases and in grain boundaries. Characteristic stacking faults of Nb_3Al are reported in Figure 3.65. Stacking faults of Nb_3Al phase at the grain boundary are given by Figure 3.66. Figure 3.67 shows several grains with different concentration of Al (at.%): A-23% (stoichiometric Nb_3Al), B-17% (off-stoichiometry Nb_3Al), C-Al_2O_3, D-4% (Nb-Al solid solution).

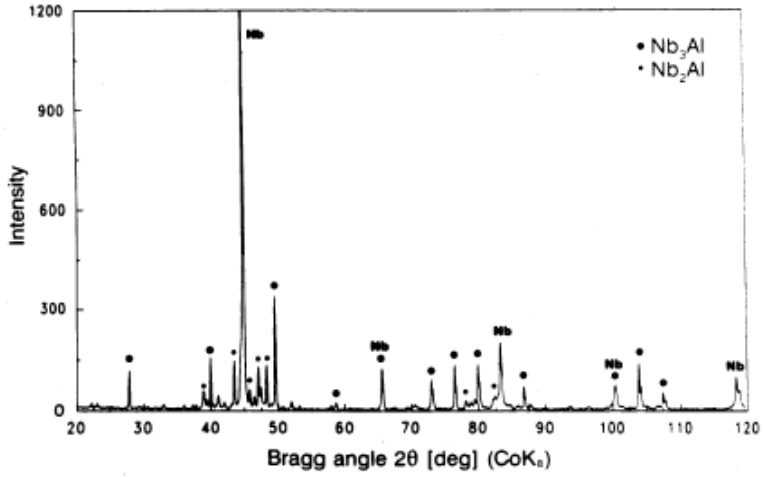

Figure 3.63 X-ray diffraction pattern after hot-pressing of the Nb-Al sample with nominal composition Nb - 18 at.% Al [98].

Figure 3.64 Typical microstructure of the as-hot-pressed Nb-Al sample with nominal composition Nb-18at.%Al [98].

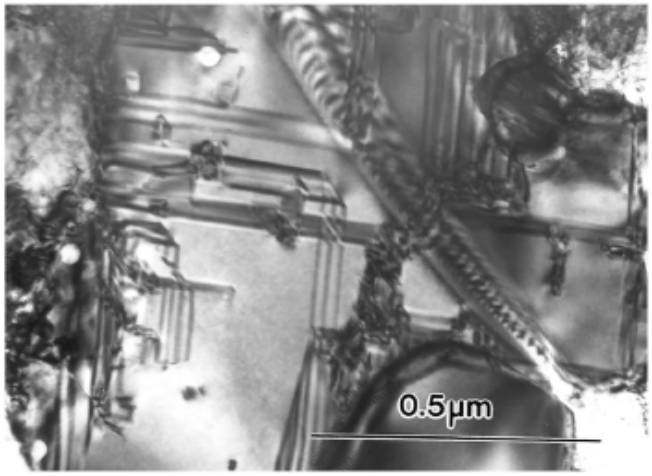

Figure 3.65 Characteristic stacking faults in the Nb_3Al phase [98].

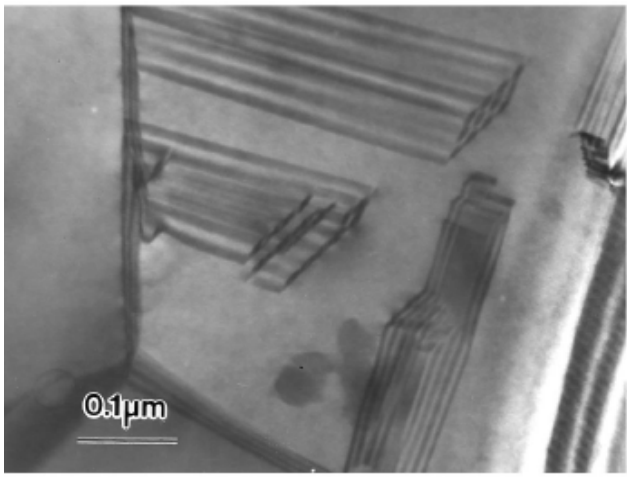

Figure 3.66 Stacking faults in the Nb_3Al phase at the grain boundary [98].

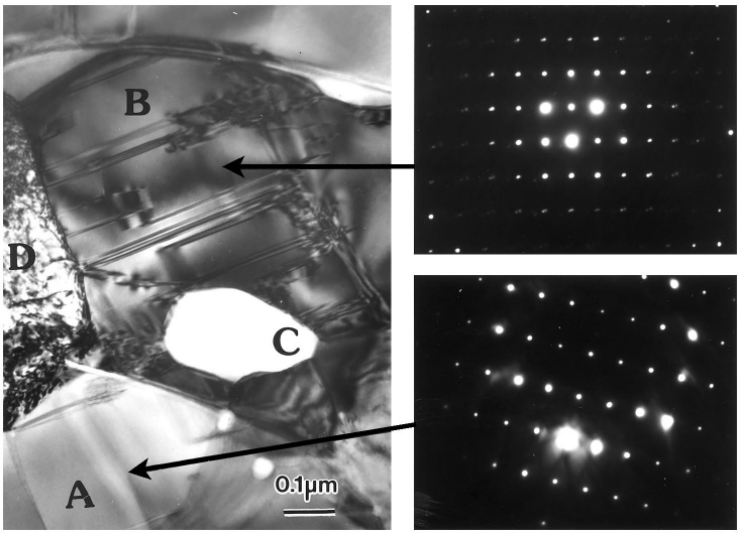

Figure 3.67 TEM Microstructure of Nb – 18 at.% Al alloy with corresponding selected area diffraction pattern. (A) Nb_3Al orientation [011]; (B) off-stoichiometric compound; (C) Al_2O_3; (D) Nb-Al solid solution [98].

3.5 Summary

Chapter 3 is a review of the most important results in the literature directed at forming Nb-Al-Ge A15 materials. A high degree of atomic order and compositional homogeneity are required to achieve state-of-the-art A15 materials. Secondary phases, impurities, phase segregation, and vaporization of the lower melting point elements degrade superconductivity dramatically. Critical temperature measurements in conjunction with X-ray diffraction and TEM have been used in the literature to investigate Nb-Al-Ge microstructure, atomic composition, and ordering. Much of the more recent work on Nb-Al-Ge involves the transformation from the metastable bcc phase to metastable A15. Preparation and annealing conditions affect considerably the superconducting properties. The best fabrication technology for producing the highest B_{C2}(4.2 K) values for Nb_3Al (30 T), $Nb_3Al_{0.7}Ge_{0.3}$ (41 T) and Nb_3Ge (37 T) are double rapidly heating quenching [77], arc-melting [62] and thin-film deposition [81], respectively.

Chapter 4

Fabricating nanostructured materials

4.1 Introduction

Chapter 4 includes a literature review of the methods used to produce and control nanocrystalline materials. Controlled manipulation of microstructure allows a wide variety of microstructures and hence properties [35]. The structures found in nanocrystalline materials together with their properties are presented in section 4.2. Section 4.3 has three parts, which review the fabrication routes used to produce nanocrystalline materials in bulk form. The first part considers non-milling techniques. Then the process of milling is described and in the third subsection the commercial milling systems available from which we have chosen to use high-energy ball milling are described. In section 4.4, a description of the approach to optimising ball milling is given. In the last section of this chapter, some properties of ball-milled metals in the literature will be reported. For a very comprehensive discussion of milling, the reader is referred to the extensive review of 'mechanical alloying and milling' by Suryanarayana in 2001 [100].

4.2 The structure and physical properties of nanocrystalline materials

Nanocrystalline materials (also referred to as nanostructures, nanophase materials, or nanometer-sized crystalline solids) are built up of single- or multi-phase nanometre-sized grains (typically less than 100 nm in at least one dimension) [35]. The nanocrystalline materials may contain crystalline, quasicrystalline and amorphous phases and can be metals, ceramics or composites. Nanocrystalline metals consist of two structural components: the nanometer-sized building blocks and the disordered interfacial component [35]. The first are commonly referred to as grains, crystallites or polycrystals. They may differ in their atomic structure, crystallographic orientation and/or their chemical composition. The interface component is built up by grain boundaries (the border between two adjacent grains) and triple junctions (the border between three or more adjoining crystals) [101]. Figure 4.1 provide a schematic representation of a two-dimensional nanocrystalline material. Figure 4.2 is a micrograph

of a nanophase material using high-resolution transmission electron microscopy (HRTEM).

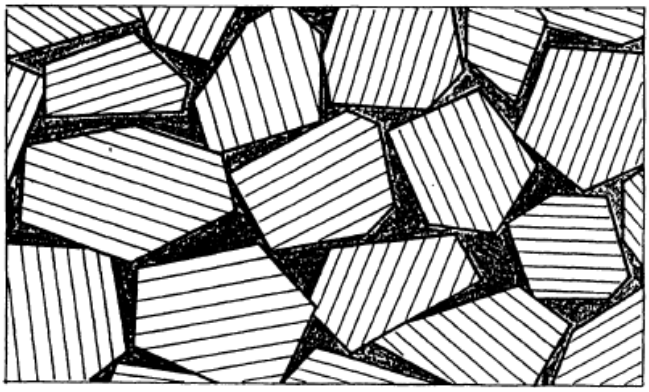

Figure 4.1 Two-dimensional model of a nanostructured material. The hatched areas represent the random texture of the nanocrystals. The dark regions are the disordered grain boundaries [102].

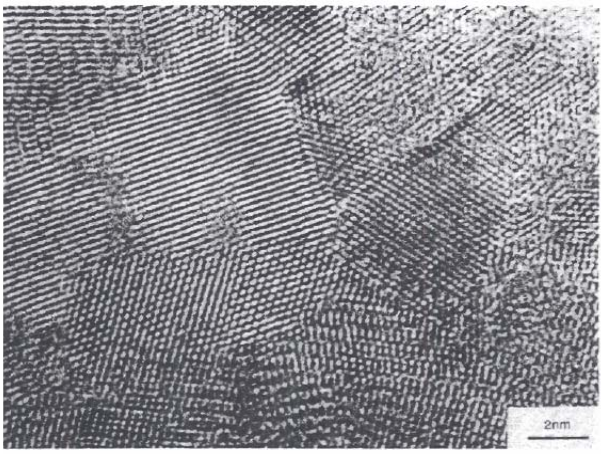

Figure 4.2 High resolution transmission electron micrograph of nanophase palladium [103].

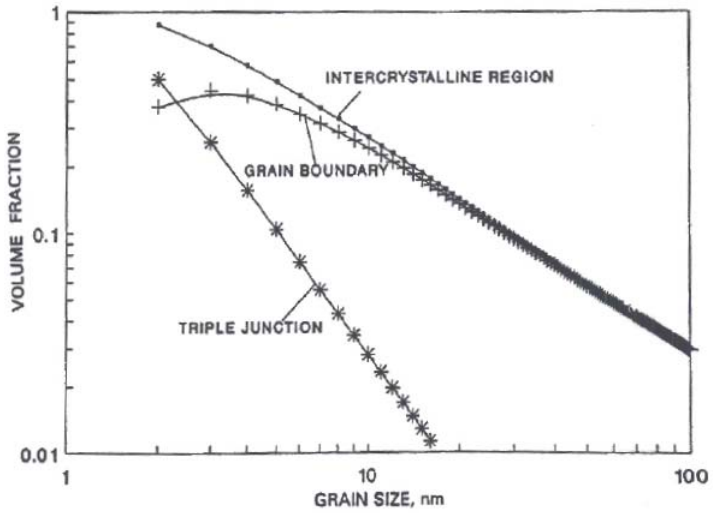

Figure 4.3 Intercrystalline, grain boundary and triple junction volume fractions versus grain size [101].

Assuming that grains have a spherical or cubic shape, the volume fractions of interfaces may be estimated as $3\Delta/d$ where Δ is the average interface thickness and d is the average grain diameter. In a nanostructure, the volume fraction of the interfacial component is the sum of the volume fractions associated with the grain boundary and the triple junctions [101]. The variation of volume fractions is shown versus grain size in Figure 4.3, which suggests a volume fraction of 70-80 % for intercrystalline region at very small grain size ~ 2-3 nm. It exhibits a wide distribution of interatomic spacing (no average atomic order can be defined) and a reduced density (10 to 30 % less than the polycrystal density). All these observed characteristics have led some scientists to call nanocrystalline materials as a new form of matter [101].

Physical properties. The microstructure of nanocrystalline materials produces unique properties, such as increased strength, improved ductility, higher specific heat, enhanced thermal expansion coefficient, and superior soft magnetic properties compared to conventional coarse-grained and amorphous crystals [104]. Figure 4.4 and Table 4.1 provides some examples of these improved properties. These data show that the heat capacity of nanocrystalline materials is larger than that for the same-compositional amorphous and coarse-grained polycrystalline materials which implies the nanocrystalline state has the highest entropy [104]. Electrical resistivity results (Figure 4.5) are in agreement with the theory of electron scattering. Grain boundary scattering increases with increased disordered material and in particular increases if the grain size is even shorter than the electron mean free path [104].

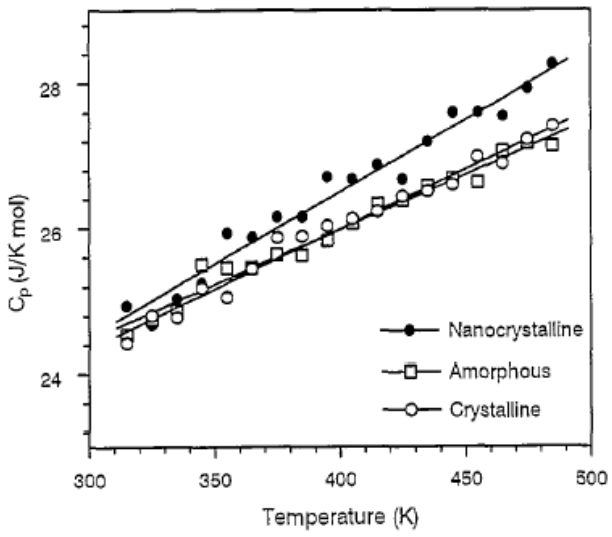

Figure 4.4 Plots of measured heat capacities vs. temperature for three different state of the Ni-P alloy [104].

Material	Nanocrystalline	Amorphous	Coarse-grained polycrystalline
Cu [a] (250 K)	26	–	24
Pd [a] (250 K)	37	27 [d]	24
Ni–P [b] (400 K)	27	26	26
Fe–Si–B [b] (350–450 K)	28	25	24
Ru [c] (250 K)	28	–	23

[a] Samples prepared by means of the UFP consolidation method.
[b] Samples crystallized from amorphous solids.
[c] Samples prepared by ball milling.
[d] Extrapolated to pure Pd based on the values for amorphous $Pd_{72}Si_{18}Fe_{10}$.

Table 4.1 Comparison of heat capacity ($J \cdot mol^{-1} \cdot K^{-1}$) of nanocrystalline, amorphous, and coarse-grained polycrystalline materials prepared by using different methods. The measurement temperatures are given in parentheses [104].

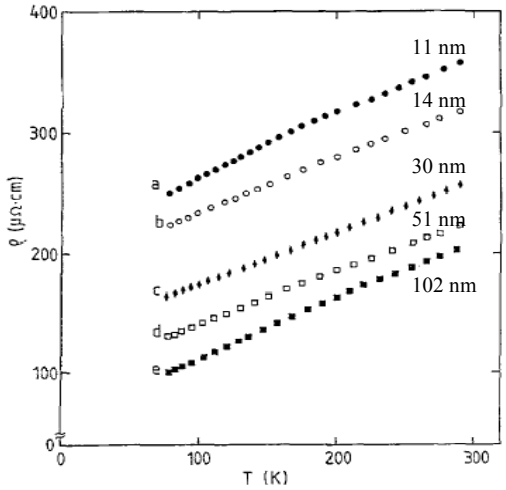

Figure 4.5 Plots of resistivity vs. temperature of the Ni-P nanocrystalline samples with different average grain sizes: 11 nm; 14 nm; 30 nm; 51 nm; 102 nm [104].

4.3 Fabrication routes for nanocrystalline materials

A preliminary classification of nanocrystalline materials together with the typical method of synthesis are given by Table 4.2.

Dimensionality	Designation	Typical methods of synthesis
Three dimensional	crystallite	gas condensation high energy ball milling
Two-dimensional	filamentary	chemical vapour deposition
One-dimensional	layered	vapour deposition electrodeposition

Table 4.2 Classification and typical method of synthesis of nanocrystalline materials [105].

Gas condensation, vapour deposition, electrodeposition, and high energy ball milling are common methods for fabricating nanostructured materials. These methods can

produce bulk materials. This section considers these processing techniques as well as the high-energy ball milling which was used in this thesis work.

4.3.1 Non milling fabrication routes

Gas condensation. The system consists essentially of an ultrahigh vacuum chamber equipped with a turbomolecular pump.

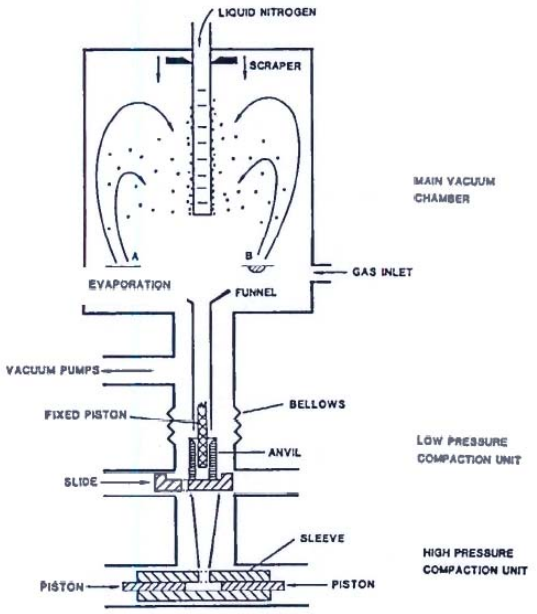

Figure 4.6 Schematic representation of a gas-condensation chamber for the synthesis of nanocrystalline materials [105].

Once the chamber is evacuated to ~ 10^{-7} Pa it is then back filled with an inert gas to a pressure of about 1 KPa. The material to be produced in the nanocrystalline state is then evaporated using conventional methods (i.e. resistive, radius-frequency heating). Because of interatomic collisions with the helium atoms in the chamber, the evaporated metal atoms lose their kinetic energy and condense in the form of nanocrystals onto a liquid nitrogen-filled cold finger. After restoring the high vacuum, the powder is removed down the length of the tube into a compaction device. Compaction is carried out initially at low pressure to produce a compacted pellet. Eventually the sample is then transferred to a high-pressure unit for a further compaction at 5 GPa using a tungsten carbide piston. The scraping and compaction process are both performed under UHV conditions to keep the surface clean and to avoid any gaseous impurities. The particle size in this method is dependent upon inert gas pressure, evaporation rate and gas composition. Very fine particles can be produced by decreasing the gas pressure in

the chamber or the evaporation rate. The control of the inert gas pressure affects both particle size and the resulting phase [105].

Vapour deposition. A relevant structural design for the vapour deposition is given by Figure 4.7. The vapour is condensed onto a polished surface of a temperature-controlled aluminium alloy collector which rotates on a vertical axis. Layered nanocrystalline material of adequate diameter can be achieved with this device achieving rates of 1 to 3 mm/h [105].

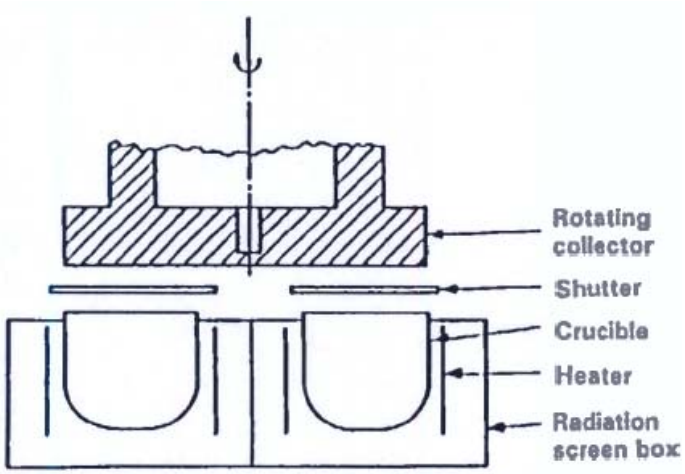

Figure 4.7 Cross-sectional representation of a rotating collector vapour deposition apparatus [105].

Electrodeposition. Multilayered nanocrystals with specific texture can be fabricated by electrodeposition. Deposition rates (with control on the scale at about the 10 nm layer level) are about 0.05 mm/h. Also 3D nanostructures can be prepared. The size of the particles can be controlled via the concentration of the solution species, the deposition voltage current and bath agitation modulation. A schematic cell for electrodeposition is given by Figure 4.8.

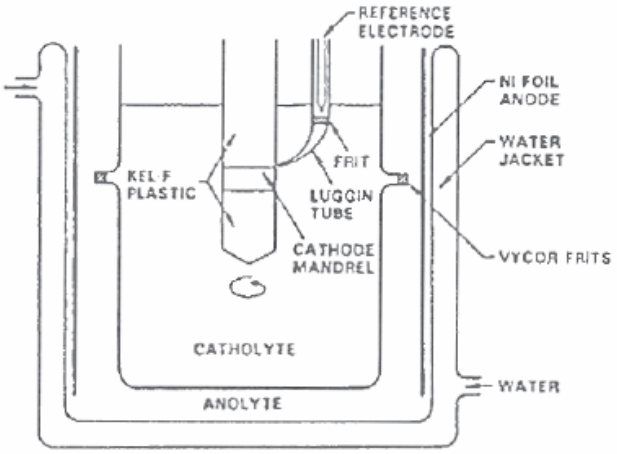

Figure 4.8 Schematic representation of a cell for electro deposition [105].

4.3.2 Milling fabrication routes

In the late 1960's high-energy ball milling (HEBM) was first developed as an industrial process to produce new alloys. Conventional ball milling could not provide enough energy to process them [106]. A common application of the HEBM is the conversion of a course-grained crystalline powder (precursor phase) to a nano-granular microstructure through heavy mechanically induced deformation [107]. The central event during milling is the ball-powder-ball collision (Figure 4.9) [96,107].

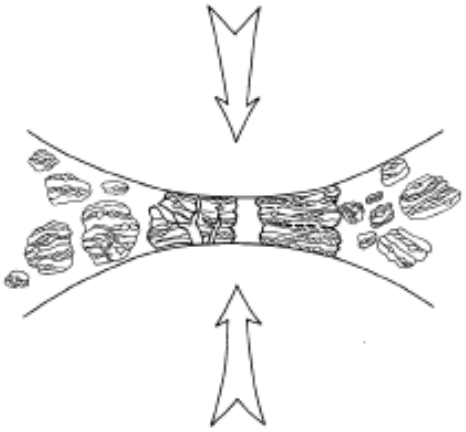

Figure 4.9 Schematic ball-powder-ball collision event [96].

During intensive ball milling the formation of atomically clean surfaces occurs. The contact between clean surfaces produces cold welded particles. The new particle formation consists of high strain-rate deformation and cumulative strain. These events lead to particle fracture. A balance between cold welding and fracturing is eventually achieved in equilibrium during the milling procedure [108,109]. Grain size refinement is approximately a logarithmic function of time and depends on the internal mechanics of the specific mill and on the workability of the materials being processed. Since the kinetic energy of the balls is a function of their mass and velocity, dense materials ($\rho \geq$ 7-8 g·cm^{-3}) are preferred (i.e. copper, niobium, iron, steel, etc) [109]. The HEBM process starts with the powders mixed in the correct proportion. This mix is then milled for a desired length of time. The raw materials used for ball milling are generally powders with particle size in the range 1-200 μm. Ball grinding of a mixture of elemental powders and/or compounds to obtain a homogeneous alloy is commonly named mechanical alloying (MA). We will refer to the ball grinding of a pure element or compound, as mechanical milling (MM). Milling can be carried out with or without an additional process control agent (PCA). The main disadvantage of using a PCA is the

increased contamination of the powder. For this reason, many of the MA/MM operations have been carried out dry and more recently the lower energy jet milling has become particularly important for medical applications where low contamination levels are vital.

4.3.3 Commercial milling systems

Popular high-energy ball mills for laboratory investigations are presented in this section. The milling tools and equipment used in this thesis work are also shown. Jet milling is described first. The wet and dry milling procedures in this thesis were carried out with the Fritsch planetary ball mill and the Spex shaker mill, respectively. The type of mill is an important process variable, which affects the final constituents of the powders.

Jet mill. Jet mills use a fluid energy grinding system to produce particle sizes typically between 1 μm and 10 μm. They are widely used in chemical, pharmaceutical, and mineral industries. Jet mills exhibit various advantages such as the ability to produce micron-sized particle with narrow size distribution, absence of contamination and ability to grind heat sensitive materials [110]. Figure 4.10 and Figure 4.11 show the vortex chamber and other principal components of a jet mill.

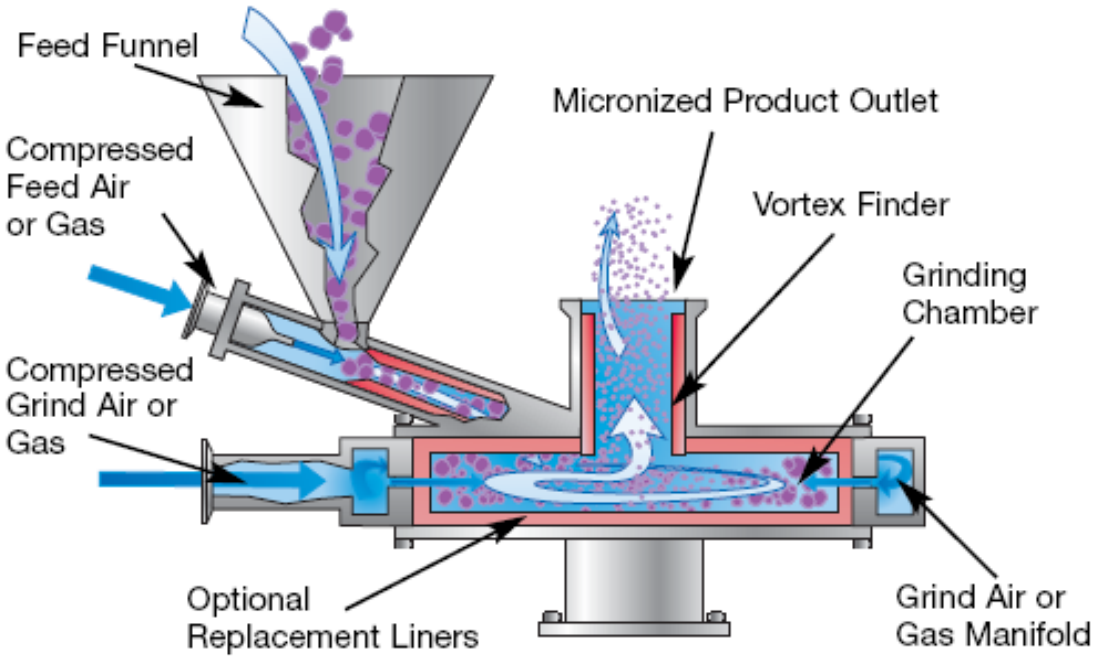

Figure 4.10 Schematic of the vortex chamber in a jet mill [111].

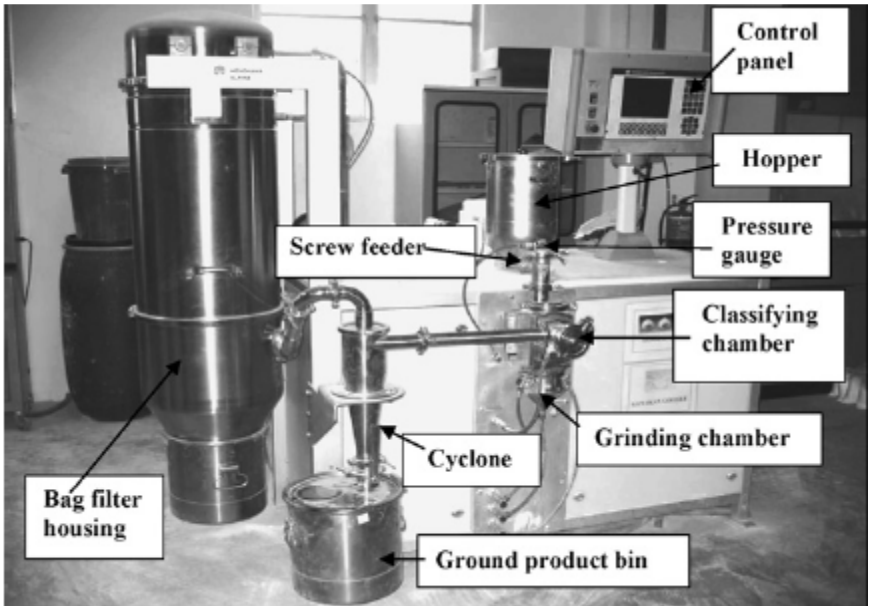

Figure 4.11 Principal components of a jet mill [110].

A gas under pressure is injected tangentially through the nozzle located in the external chamber wall. Particles with small velocities are introduced into the grinding chamber through a feed injector. These solid particles are accelerated by the powerful vortex and fragmented by collision between each other and against the chamber wall. After grinding, the particles are carried by gas flow up to the classifier, which removes the fine particles and returns the coarse ones into the vortex chamber. The ground product is collected in a container below the cyclone [110,112]. In advanced systems (i.e. Micro jet, Fluid Energy Company) the air flow rate, gas pressure and grinding pattern can be adjusted to optimise both the desired particle size and the production rate [113].

Planetary ball mill (Fritsch Pulverisette). These mills can grind a few hundred grams of the powder at time. The milling speed can be controlled up to 600 r.p.m. Fritsch GmbH in Germany manufactures the planetary ball mills. The basic geometry is given by Figure 4.12 [100]. The Fritsch Pulverisette and the corresponding milling tools used during this thesis work are shown in Figure 4.13. The vial rotates in a planetary-like motion as well as around its own axis. The centrifugal forces produced act cyclically in the same and then opposite directions since the vial and the supporting disk rotate in opposite directions. In modern planetary ball mills, the disk and the vial rotation speeds can be independently controlled. The ball-to-ball impact and the ball-to-wall frictional forces produce an effective size reduction in the milled powders. In a single mill one can have one (Pulverisette 6), two (Pulverisette 5 or 7) or four (Pulverisette 5) milling stations.

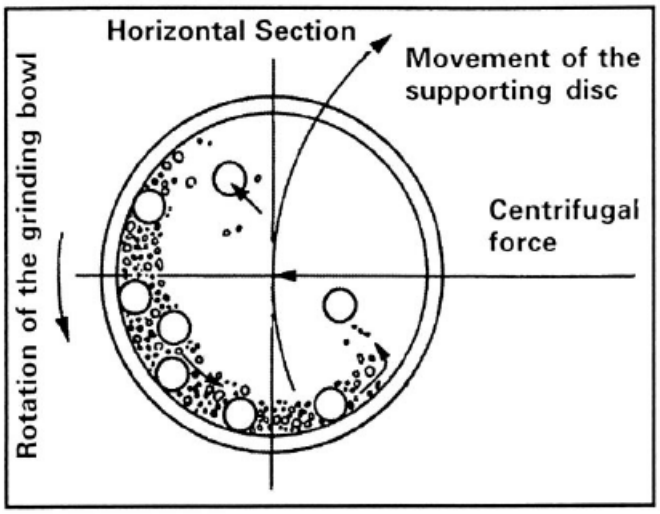

Figure 4.12 Geometry of the planetary ball mill [100].

Figure 4.13 (a) Fritsch planetary mono-mill (Pulverisette 6) in the assembled condition; (b) Copper vial set consisting of the vial, lid, o-ring, and balls (20 and 10 mm diameter).

Shaker mill (SPEX). These mills can grind a 10-20 g of the powder at time. The typical milling speed is 1200 r.p.m. SPEX CertPrep in the USA manufactures them. The SPEX 8000D mixer/mill and the corresponding milling tools used during this thesis work are shown in Figure 4.14. The vial, containing the powder and the grinding balls, is secured in the clamp and swung back and forth. This shaking motion is combined with lateral movements of the ends of the vial, so that the vial appears to be describing an infinity sign all the way through the motion. The amplitude of the vial swing is the same as the internal length of the vial (~ 5 cm). During each swing, the balls impact against the sample and the end of the vial, both milling and mixing the powder.

Figure 4.14 (a) SPEX 8000 D mixer/mill in the assembled condition with a copper vial (b) Copper vial set consisting of the vial, lid, o-ring, and balls (10 mm diameter).

Recent designs of this mill include dual clamps. This feature not only allows twice as many samples to be ground in a given time, but also more balance and less vibration. The internal design of the container is also important. Both flat-ended and round-ended SPEX mill containers have been used in the literature. Alloying was found to occur at a higher rate in flat-ended vials than in the round-ended ones [100].

SPEX vs. FRITSCH. Although the control over milling condition (i.e. milling speed, number of repetitions) is provided exclusively by the Fritsch mill, a higher frequency of ball-to-ball impacts occurs in SPEX mill. For this reason, Fritsch Pulverisette can be considered a lower energy mill than the SPEX. In Durham, both milling apparatus configurations have dedicated seals to minimize the air contamination during milling. Depending on the type, the quantity, and the final constitution of powder required, the most convenient ball mill can be chosen.

4.4 Optimising the ball milling process

HEBM is a complex process that involves the optimisation of many variables to achieve the desired microstructure. The main process parameters are classified as follows: milling tools, milling speed, milling temperature, milling atmosphere, ball to powder weight ratio (BPR), milling time, and process control agent. All these process variables

are not completely independent. The nature of the final product depends on their combined application [100,108].

Milling tools. The material used for the milling tools is important since it can contaminate the powder and alter the chemistry of the reactions. Hardened steel, tool steel, hardened chromium steel, tempered steel, stainless-steel, WC-Co and bearing steel are the most common type of milling container and grinding media. Different materials (i.e. copper, titanium, sintered corundum, agate) are chosen for specialised purposes. The final constitution of the powder depends on the size and density of the grinding medium. Some investigations on Ti-Al elemental powder mixture leads to a Ti-Al solid solution, mixture of Ti and Al separate phases and also amorphous phase using 15 mm, 20-25 mm, 5-8 mm balls diameter, respectively [114,115]. The highest collision energy and a random motion of the ball is expected using balls of different diameter. However, it is common practice to carry out the ball milling using only one size of balls [100,116].

Milling speed. The energy input into the powder increases with the milling speed. The maximum possible speed depends on the design of the mill. Above a critical speed (or intensity of milling), the inner wall of the vial will pin the balls. This effect leads to a reduction of the maximum number and the energy of collisions. The optimal speed should be just below the critical speed. Another consequence of a high speed is the temperature increase of the vial. This effect can be useful where atomic diffusion is required to facilitate homogenisation and/or alloying. In other circumstances, the increase of temperature produces rapid phase transformation, decomposition of supersaturated solid solution and metastable phases formed during milling. High milling intensity can also lead to an increase of the average crystal size and a decrease of the internal strain [100,117].

Milling temperature. The temperature of the milling is another important parameter in deciding the constitution of the milled powders. The temperature of milling has a significant effect on the atomic diffusion processes that can occur. There are only a few investigations reported where the milling of temperature has been varied intentionally. These investigations were undertaken to study the effect of milling temperature on the variation in solid solubility level, or to determine whether an amorphous phase or a nanocrystalline structure forms at different temperatures. The extent of solid solubility

was reported to decrease and the grain size to be larger at high milling temperature [100,118].

Milling atmosphere. The major effect of the milling atmosphere is on the contamination of the powder. Generally, the powder is milled in a vial that has been either evacuated or filled with an inert gas such as argon or helium. High purity argon is the most common environment to prevent oxidation and/or contamination of the powder. Normally, the loading and unloading of the powders into the vial is carried out inside an atmosphere-controlled glove box. The glove-box is cyclically evacuated and refilled with the argon gas. Different atmospheres have been used during for specific purposes. Nitrogen or ammonia atmosphere, which have been found to react with metal powder, are used to produce nitrides [100,119]. Hydrogen is used to produce hydrides [100,120]. The presence of air in the vial leads to the formation of oxides and nitrides in the powder.

Ball-to-powder ratio. The ratio of the weight of the balls to the powder (BPR), referred also as a charge ratio (CR), is an important variable in the milling process. The BPR has a significant effect on the time required to achieve a particular phase in the powder being milled. The higher the BPR ratio, the shorter is the time required. Alloying occurs faster when the number of collision per unit time increases and consequently more energy is transferred to the powder particles [100,105].

Milling time. The milling time is a relevant parameter that depends on the type of mill used, the intensity of milling, the ball-to-powder ratio and the temperature of milling. The proper milling time must be decided for the particular combination of the above-mentioned parameters and for the powder to mill. A side effect of prolonged milling time is an increase in the level of contamination and additional undesired phases. Powders must be ground for the proper milling time to provide a convenient balance between size-reduction and contamination pick-up [100,121].

Process control agents. For many material systems, the balance between cold welding and fracturing required for optimal materials production is not optimal. The balance has to be controlled by the addition of surface additive, called a process control agent. The application of PCA enables a reduction in cold welding and promotes fracturing. The PCAs can be solids, liquids, or gases. The addition of PCA modifies the surface

condition of the deformed particles by reducing the clean metal-to-metal contact necessary for cold welding. The energy required for the size reduction E is given by:

$$E = \gamma \Delta S \tag{4.1}$$

where γ is the specific surface energy and ΔS is the increase of the surface area. A reduction in surface energy results in the use of shorter milling times. The PCA is usually added into the powder mixture prior to milling. The amount of PCA generally used is 1-5 wt. % of the total powder weight. The most important types of PCAs are: stearic acid, hexane, methanol and ethanol. Generally, ball milling of soft materials requires more PCA than brittle ones. A side effect associated with PCA use is its decomposition, interaction, and incorporation with the powder during milling. It has been reported that PCAs affect the final phase formation, changing the solid solubility levels and altering contamination level. The nature and quantity of PCA determines the final size, shape, purity and yield of the milled powder [100,122].

Combating contamination. Contamination sources are generally introduced by impurities present in the original powders (native impurities), milling tools and atmosphere. During milling, foreign elements are broken down and uniformly distributed in the matrix [123]. Owing to the increase of active surface [124], prolonged milling time increases contamination pick-up from the atmosphere. If the contamination process is competitive with the formation of the desired compound it can have also a dramatic effect on its local electronic properties [34,43,46,123]. For instance, oxide formation can affect the atomic ratio of the required stoichiometry, the crystal symmetry and occupy interstitial sites [125,126]. Typically, impurities from atmosphere are quantified by chemical methods [127]. They can be limited using a high purity inert gas, a good quality of vacuum, or a reducing atmosphere such as hydrogen.

4.5 Nanocrystalline and amorphous ball milled metals and intermetallics

Materials scientists characterise HEBM as a “nonequilibrium processing tool” [128] or a “far from equilibrium processing” technique [96]. Indeed high energy ball milling leads towards a considerable flexibility in the production of novel composition and microstructural effects and open a wide range of operations [96]. The high volume

fraction of interfaces in ball-milled material provides a high density of short-route paths for atomic diffusion which in turn allows the fabrication of nanostructured intermetallic phases crystalline phases and amorphous alloys together with an extension of the solid solubility and a high degree of disorder. Consequently, nanocrystalline metals exhibit an enhanced diffusivity in comparison to single crystals or conventional coarse-grained polycrystalline materials with the same chemical composition. The increased diffusivity and reactivity leads also to the formation of intermetallic phases at temperatures much lower than those required for coarse-grained materials and synthesis of alloy phases in immiscible metals.

Extension of solid solubility. The extension of solid solubility has been achieved in many alloy systems by non-equilibrium processing methods. During MA, interdiffusion between the components takes place with the formation of a solid solution. Figure 4.15 and Figure 4.16 show the variation of solid solubility and lattice parameter, respectively. When the equilibrium is reached, a homogeneous solid solution with a lattice parameter in between those of the precursor powder is formed. It is possible to synthesize both stable (equilibrium) and metastable (non-equilibrium) solid solutions. The solid solubility limit is expected to increase with the milling time as diffusion progresses and to reach a saturation level (constant lattice parameter). It is natural to expect that a change in solid solubility should lead to a change in the lattice parameter. However if the atomic radii of unalloyed metals are very similar, the change of the solid solution lattice parameter is expected to be small [93] and closest to that of the major component.

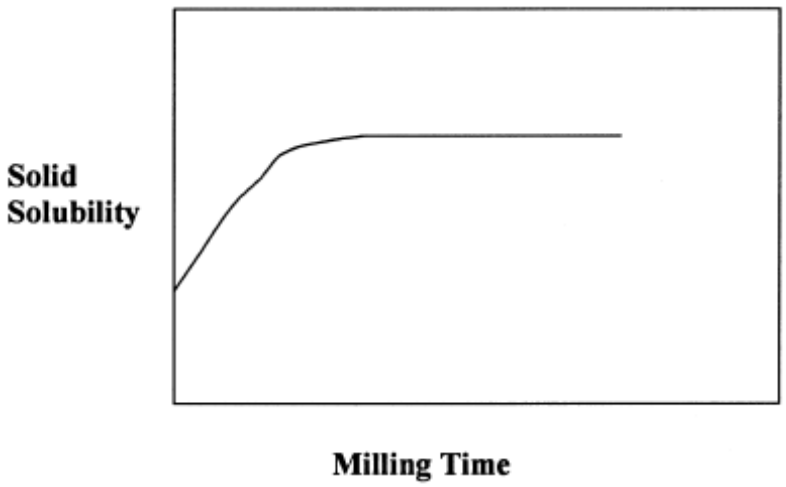

Figure 4.15 Schematic diagram showing the variation of the solid solubility with time during MA of a mixture of powder [100].

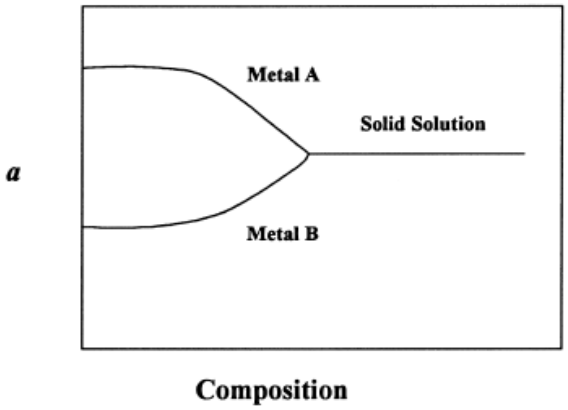

Figure 4.16 Schematic diagram showing the variation of lattice parameter (solid solubility) of the individual powders processed by MA [100].

There are some difficulties in determining the solid solubility of MA'ed powders using X-ray diffraction. Indeed the heavy mechanical deformation decreases the grain size and the increases lattice strain. These two effects lead to a broadening of the X-ray diffraction peaks. The formation of nanocrystalline solid solutions can significantly broaden the X-ray diffraction peaks. Consequently, even if a reflection is present the broadening makes the location of the peak position difficult and consequently the lattice parameters calculated are inaccurate. Often the solid solubility levels are determined by extrapolating data of lattice parameter versus solute content [91,100]. Another difficulty associated with small particle size is their detectability by the technique of the X-ray diffraction. It has been shown that 2 wt. % of Ti can be easily detected if the particle size falls in the range 26 – 38 μm. If the particle size is in the range 0.05 – 1.0 μm a much larger amount of Ti (~ 25 wt. %) is required [100,129]. Nanocrystalline materials have particle size in the latter range (< 1 μm). Consequently, all phases cannot be easily detected by X-ray diffraction techniques. Table 4.3 compares the solid solubility and the phase extension for microcrystalline and nanocrystalline samples.

Solid solutions		**Microcrystalline samples**			**Nanocrystalline samples**		
Solvent	**Solute**	**Solubility**	**Extension**	**Ref**	**Solubility**	**Extension**	**Ref**
Nb	Al	9 at. % at 1000 ^{o}C	~ 21.5 at.% at 2060 ^{o}C	[56]	Not measured	60 at. %	[93]
Nb	Ge	4 at. % at 1000 ^{o}C	11.5 at.% at 1900 ^{o}C	[50]	8.6 at. %	25 at. %	[88]

Table 4.3 Solid solubility and phase extension for Nb-based solid solutions. Microcrystalline and nanocrystalline samples were fabricated by arc-melting (AM) and mechanical alloying, respectively.

Data from the phase diagram indicates the Al solubility of < 10 at.% in Nb at temperatures below 1000 ^{o}C [51]. Mechanically alloyed powders were found to produce very high solid solubility values without using heat treatments – only otherwise found in the phase diagram at much higher temperatures. Hellstern at al. [90] found that the solid solution of Nb and Al, $(Nb)_{ss}$, is extended to at least 30 at. % Al by mechanical alloying. The highest extension for $(Nb)_{ss}$ is about 60 at.% Al and was obtained by Peng et al. [93,100]. This value was attributed to the high energy milling performed with the SPEX 8000 shaker mill whereas Hellstern at al. used a planetary mill [93] (section 3.4.4). Similar extensions of the composition were found in several mechanically alloyed systems [90,100].

Intermetallic phase formation. The HEBM produces a reduction in grain size, disordering of the lattice and modification of a crystal structure. The achievement of all these simultaneous effects makes the HEBM a widely used processing tool to produce intermetallics. The types of intermetallics synthesized by HEBM include quasicrystalline and crystalline intermetallic phases. Crystalline intermetallic phases processed by HEBM can have different degrees of disorder and can be found in both equilibrium and metastable phases. A summary of the Nb-Al intermetallic phases including the relevant processing condition and corresponding enthalpy of formation are reported in Table 4.4. More information about the specific phases developed during Nb-Al MA can be found in chapter 3 (paragraph 3.4.4).

System	Phase	Condition (BPR 10 :1)	ΔH_f (J · g^{-1})
Al – 25 at % Nb	Al_3Nb	Direct MA/15 h	-190
Al – 75 at % Nb	Nb_3Al	MA/5 h + 825 ^{o}C/2 h	-63
Nb – 33.3 at % Al	Nb_2Al	MA/5 h + 825 ^{o}C/2 h	-117

Table 4.4 Formation of intermetallic phases by mechanical alloying [96].

Disordering of intermetallics. The crystalline order of metallic powders processed by HEBM is destroyed under heavy plastic deformation. This leads towards the formation of a variety of structural defects like dislocations, atomic disorder, vacancies, stacking faults, grain boundaries and so on. All these effects destabilise the order of the lattice cell leading to the formation of a disordered phase [130,131]. HEBM can put large amount of energy into the material all the way through the process. The total free energy stored (ΔG) during MM is usually expressed by the sum of the free energies of the

atomic disordering ($\Delta G^{disorder}$) and the grain boundaries ($\Delta G^{grain\ boundary}$) [131,132]. The atomic disorder can be considered in three different ways: anti-site atomic disorder (substitution of the atoms on each other's sublattice), triple defects (formation of X anti-site atoms in combination with the formation of vacancies on X sublattice) and redistribution of interstitials (an A interstitial atom occupies a B interstitial site). The grain refinement increases the grain boundary area and consequently the free energy of the system. Some of the types of changes that can occur on milling an intermetallic compound are summarized by Figure 4.7 [100].

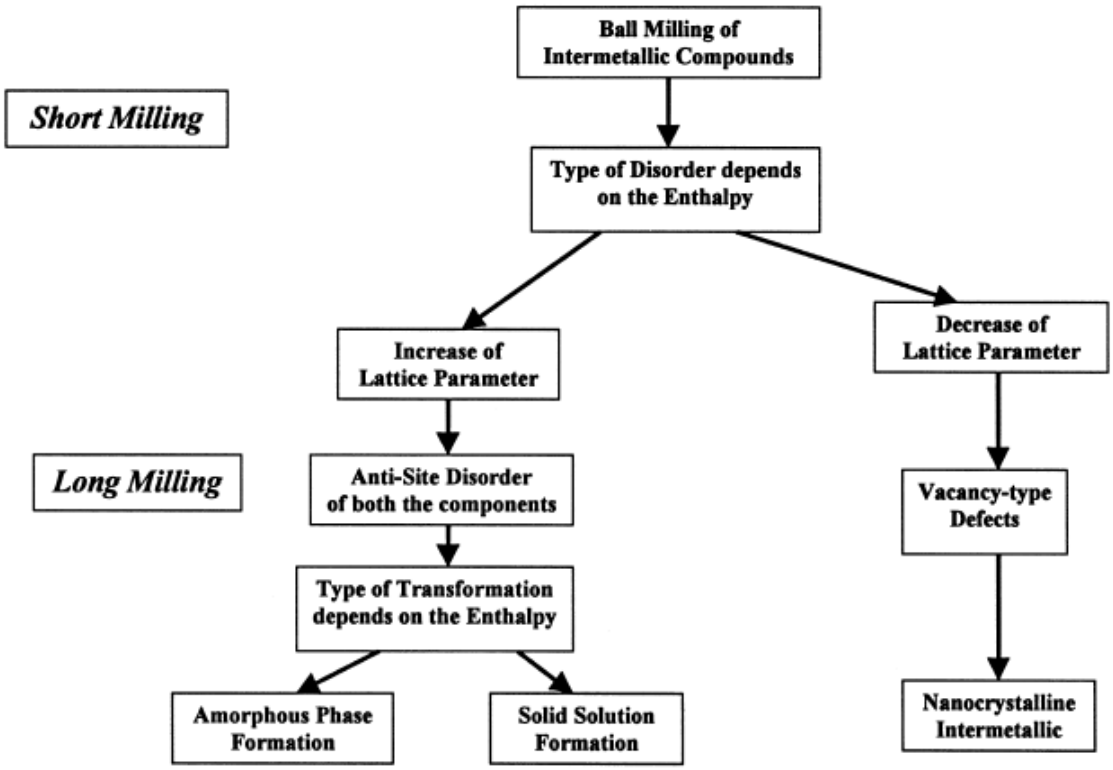

Figure 4.17 Schematic diagram of the expected situation of HEBM of an intermetallic compound [100].

The relative increase in the lattice parameter, $(a - a_0)/a_0$, where a_0 is the lattice parameter prior to milling, is relatively large (e.g. $\leq$ 4 %) [90,133] in the disordered state if the disordering occurs by anti-site disorder, whereas the lattice parameter decreases if disordering occurs by the triple defect disorder [45,100]. The disordered phase precedes the transition to the amorphous state [128,134].

Amorphisation by MM and MA. A solid alloy with a liquid-like atomic arrangement is called a metallic glass or an amorphous (metallic) alloy. The amorphous state lacks long-range order. Amorphisation has been obtained by MM of intermetallics or by MA of elemental powders. The mechanisms for amorphisation have not yet been fully

explained and are believed to be different for MM and MA. Schwartz's often cited investigation [135] on MM of $NiTi_2$ reported that during milling the mechanical impact decreases the crystallite size and eventually prolonged milling eliminates all the crystalline remnants. The DSC data show a broad peak associated with points and lattice defects and a large peak associated with crystallisation - confirmed by XRD analysis below and above the crystallisation temperature [135]. The crystallisation temperature increases as milling time increases because the density of remnant crystallites decreases and there are fewer nucleation centres. For MA of elemental Ni + 2Ti, there is an additional process at lower temperatures, which is attributed to a solid-state amorphisation reaction (SSAR) where there is diffusion of one element into the other which forms an amorphous alloy. A large negative heat of mixing is believed to provide the thermodynamic driving force for the SSAR [128]. During MM the occurrence, or not, of the amorphization is consistent with the relation $\Delta G^{\text{disorder}} + \Delta G^{\text{grain boundary}} \geq \Delta G^{\text{a-c}}$, where $\Delta G^{\text{a-c}}$ is the difference in free energy between the amorphous and crystalline state [131]. If $\Delta G \leq \Delta G^{\text{a-c}}$ a solid solution forms. The amorphisation seems to follow the general sequence:

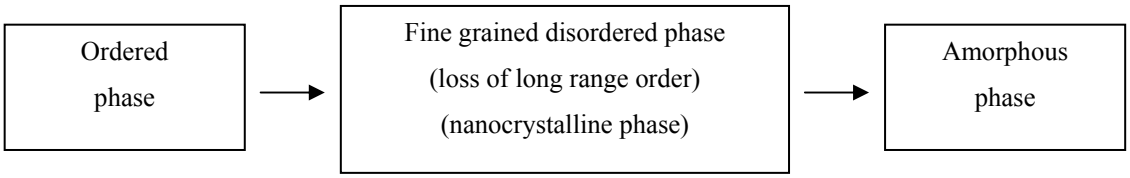

Figure 4.18 Typical sequence for the amorphisation to happen [100].

In general the end product is the same irrespective of whether the starting material is a mixture of elements or intermetallics although as we will see in later chapters, this is only true in the ideal case where there is no contamination and very long milling times can be used. The formation of an amorphous phase depends principally on the energy and contamination during HEBM process. Increased milling energy is expected to lead to a faster amorphisation. We note that prolonged milling of an amorphous phase can also produce more heat, which can cause crystallization of the amorphous phase.

Post nanocrystallisation heat-treatments. The metastable microstructure of high-energy ball milled powders can be crystallized into more stable states under appropriate circumstances [104,133]. The degree of ordering in the intermetallic is a balance between the disorder resulting from HEBM and the tendency for thermally activated reordering. The crystallisation of a solid into a nanometre-sized crystalline

phase is named nanocrystallisation. A heat treatment is commonly used to recover the crystalline order in amorphous precursor materials. In this thesis, we use a combination of temperature and pressure to influence the morphology and structures of the nanocrystallised products. A side effect of the heat treatment is the grain size growth. The grain size limit d^* is provided by:

$$d^* = \alpha \frac{\Delta G^{\mathrm{i}}}{\Delta G^{\mathrm{a}}} \tag{4.2}$$

where ΔG^{i} and ΔG^{a} are the Gibbs free energies for the interface and amorphous phase related to the corresponding crystalline phase, respectively. The above equation means that the higher the degree of amorphicity in the precursor material, the finer will be the final grain size obtained. Differential scanning calorimetry (DSC) enables measurement and classification of reaction enthalpies involved during nanocrystallization of microstructures [135].

4.6 Summary

Nanostructured materials have properties different from, and often superior to, conventional coarse-grained materials. High-energy ball milling is now well established for synthesizing nanocrystalline compounds with a metastable microstructure and composition. Manipulation of materials microstructure allows a wide variety of microstructures, properties and the potential for industrial applications [35]. The severe plastic deformation produces disordered and amorphous nanocrystalline materials characterised by large strains, high concentration of defects, numerous grain boundaries and therefore an enhanced atomic diffusivity (and reactivity).

The major side effect of the HEBM procedure is the increase of the reactive surfaces. This can lead to contamination. Indeed new atoms and gaseous impurities can have a dramatic effect on the local electronic structure of the nanocrystallised alloy. If the correlation between properties and microstructure is well understood, nanocrystalline materials with controlled superconducting properties can be fabricated in a reproducible way. In this thesis, the approach adopted has been first the fabrication of a highly disordered nanophase using ball-milling and second the crystallisation of the A15 phase using a novel procedure to obtain an optimised microstructure.

Chapter 5

Experimental procedures performed in Durham

5.1 Introduction

Chapter 5 provides a description of the experimental equipments and procedures used in this thesis. Section 5.2 reports on the fabrication of nanocrystalline samples. The differential scanning calorimetric (DSC) equipment is reported in section 5.3. The X-ray diffraction (XRD) technique and analysis are introduced in section 5.4. Basic principles of the inductively coupled plasma atomic emission spectroscopy (ICP-AES) and mass spectroscopy (ICP-MS) for compositional analysis are introduced in section 5.5. The resistive measurement technique is shown in section 5.6. The four-probe method was used to collect resistivity data both at room temperature and at low temperature in high magnetic fields. Magnetic moment measurements were performed with a superconducting quantum interference device (SQUID) and an alternating current measurement system (ACMS). Both techniques will be presented in section 5.7 on magnetic techniques. The scanning electron microscopy (SEM) technique is reported in section 5.8.

5.2 Fabrication of nanocrystalline samples

Disordered nanocrystalline powders. Disordered nanocrystalline powders were fabricated using wet and dry ball milling. The millers used were described in chapter 4.

Copper as a milling media. We chose copper as milling media because of its high density (8.93 $g \cdot cc^{-1}$ at 300 K) and high thermal conductivity (401 $W \cdot m^{-1} \cdot K^{-1}$ at 300 K) [78]. These properties improve the highly efficiency of the milling since during energetic impacts, they reduce temperature increases. Furthermore, the binary alloy phase diagram [55] shows that no compound formation or intermediate phases occur between Cu and Nb. More recent investigations carried out using mechanical alloying [166] also confirm there is very little niobium dissolved in the copper (or vice versa). Furthermore, in studies of the formation of the A15 phases Nb_3Sn and Nb_3Sn + Cu, the effect of copper additions reduced the temperature necessary for the A15 phase to form

and hence increased the critical temperature/volume of superconducting phase for similar annealed samples [167].

Fabrication of nanocrystalline bulk materials. Mechanical alloyed and mechanical milled powders were processed using a hot isostatic press (HIP) operating at 0.2 GPa in a temperature range of 500 ^{o}C to 1200 ^{o}C to produce superconducting nanocrystalline bulk materials. The hot isostatic press provides the mean to produce bulk high density and fine grain material. The isostatic pressure is applied by compressing high purity (99.998 %) argon gas. Indeed, under pressure the argon has a large thermal expansion, low density, and viscosity. These properties drastically improve the convection inside the HIP furnace compared to an ordinary electronic furnace. The structure of a furnace for heating under high pressure is provided in Figure 5.1.

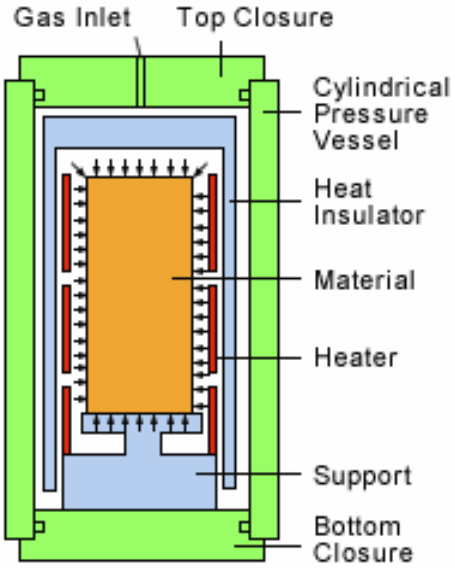

Figure 5.1 Schematic furnace for heating under high pressure [136].

The characteristic pieces of a HIP furnace are the (graphite) heater and the thermal barrier, which insulates the inside of the furnace and protects the pressure vessel wall from experiencing internal high temperatures. The HIP console controls the pressure-temperature cycle. The action of a gas compressor and intensifier is combined to provide high pressure. The temperature is controlled manually to reach the chosen processing temperature when the pressure is 0.2 GPa. The temperature measurements are made using thermocouples located at the top and at the bottom of the sample space. The parameters can be adjusted during the experiment by the console. Typically, the temperature and the pressure were kept constant for processing time of 5 h. The specific HIP'ing temperature used in this work will be reported in chapter 6 and 7.

Billet preparation. Before powder samples could be reacted in the HIP, they were sealed in billets. Inside the glove-box, a few grams of powder were wrapped in a cylinder of niobium foil (0.025 μm thick, purity 99.8%, Alfa Aesar) and put into a stainless steel tube which had one end TIG (Tungsten inert gas) welded. The argon environment is sealed inside the tube by a home-made apparatus which includes an O-ring seal, isolation tap and a vacuum fitting. Subsequently the tube was taken out of the glove-box and evacuated using a vacuum pump. A fly-press was then used to compress a section of tube and a spot welder sealed the encapsulation so the steel could be cut to length. Before HIP'ing the spot-welded end of the billet was TIG welded to ensure a good seal. Different stages of the bulk material fabrication are shown in Figure 5.2. After HIP'ing, the bulk sample was then recovered by cutting open the billet.

Figure 5.2 Different stages of the billet preparation (a) Powder wrapped in niobium foil; (b) Sealed billet before consolidation; (c) HIP'ed billet; (d) Bulk sample recovery [137].

5.3 Differential scanning calorimetry

The thermal response that occurred during the heating of milled powders was characterized by differential scanning calorimetry (DSC). The machine used in this investigation was a STA 499C/6/G Jupiter NETZSCH. This apparatus can simultaneously make DSC and thermogravimetric analysis (TGA) at a temperature between -120 ^{o}C and 1650 ^{o}C. These simultaneous measurements are known as simultaneous thermogravimetric analysis (STA). The system provides a measure of the heat exchanged between a sample pan which contains the sample and a reference pan which is either empty or contains a reference materials. Figure 5.3 gives a schematic of the equipment is given.

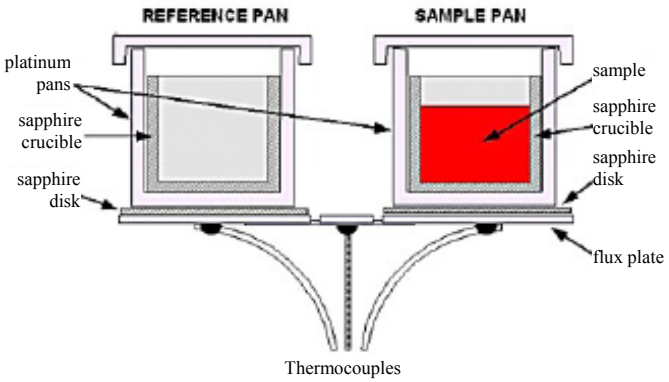

Figure 5.3 Schematic of the simultaneous thermal analysis (STA) equipment [137].

A single furnace is used to heat the chamber in which both the sample and reference pans are housed. As heat is input into the sample chamber, thermocouples read the differences in temperature of the two pans. The difference in heat flow is then calculated to produce the DSC signal. A high precision balance (± 0.01 mg) allows TGA to be simultaneously performed with DSC.

DSC calibration and measurement. The instrument was calibrated measuring the melting points of standards samples (i.e. gold, bismuth, zinc). Alumina pans and lids were used and conditioned under vacuum prior to use. Each test was carried out using a pellet of ~ 20 mg. The measurement was conducted in a protective argon gas flowing at 20 $cm^3 \cdot min^{-1}$. Before starting a test, the calorimeter was purged with cycles of vacuum (10^{-4} mbar) and argon (50 $cm^3 \cdot min^{-1}$) at a room temperature. This facilitated the removal of vapour and other gases after sample handling outside the glove box. A previously prepared buoyancy correction file was chosen to drive the temperature program. Measurements were made while increasing the temperature at 10 $^oC \cdot min^{-1}$ from 40 ^oC to 1000-1100 ^oC and during the dwell of 10 minutes at the highest temperature followed by a ramp down to 20 ^oC at cooling rate of 10 $^oC \cdot min^{-1}$. Two successive runs of the same powder sample were performed. The analysis of the TG and DSC traces was performed using the software Proteus Analysis.

5.4 X-ray Diffraction

Bragg's law, derived by W.H. Bragg and his son W.L. Bragg in 1912, is the physical law governing X-Ray diffraction (XRD) and is given by:

$$n\lambda = 2d \sin \vartheta_B \tag{5.1}$$

This law shows that peaks are present in the diffraction pattern whenever the sine of the scattering angle ϑ_B (Bragg angle) for reflection from a crystal plane is equal to the ratio of an integer number of wavelengths of radiation ($n\lambda$) to twice the spacing of atomic planes ($2d$). X-Ray diffraction is an essential technique to characterise the formation of new compounds and to calculate crystallographic parameters. Powder X-ray diffraction measurements were performed on a Siemens D5000 diffractometer. In this device a copper source generates the X-ray beam from the Cu-*K* shell with lines K_α (λ = 0.1540568 nm) and K_β (λ = 0.1544390 nm). A graphite monochromator is installed in the reflected beam path, in front of the detector in order to filter out the K_β-line. The diffractometer is interfaced to the PC by the software Diffract Act that is able to execute the scan. A background correction is provided by Eva software, which also includes the data processing (i.e. evaluation of FWHM, peak angle). The device is based on the Bragg Brentano geometry (Figure 5.4).

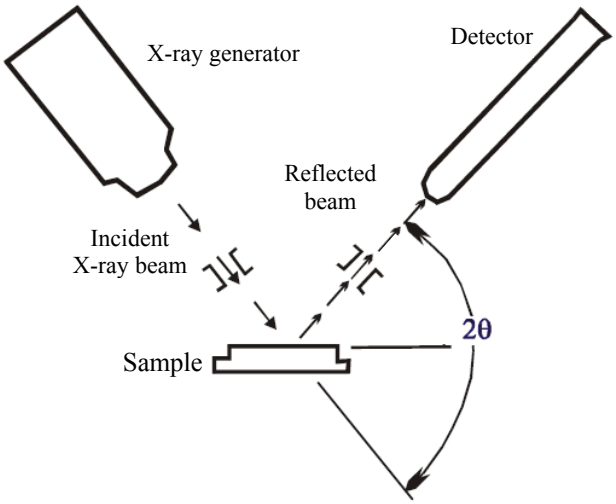

Figure 5.4 Schematic of the Bragg-Brentano geometry.

The scan angle 2θ was varied from 2 to 140° with a angular step of 0.01°. Sample preparation typically consisted of uniformly spreading powders over a ~ 10 mm diameter and 0.25 mm thick circularly recessed sample holder. Powders were held together in the sample holder using a small amount of petroleum jelly.

5.4.1 Analysis methods

The techniques employed for analyzing XRD patterns to evaluate grain size and strain are now described. The Scherrer formula [138], used to determine the particle size, is given by:

$$B(2\vartheta) = \frac{0.94\lambda}{D\cos\vartheta_B} \tag{5.2}$$

where $B(2\vartheta)$ is the angular difference between the FWHM of the diffraction peaks for a sample of the milled material and that of a sample of the same material that has not been milled. $B(2\vartheta)$ is quantified as below:

$$B(2\vartheta) = \sqrt{\Delta(2\vartheta)^2_{raw} - \Delta(2\vartheta)^2_{mw}} \tag{5.3}$$

where $\Delta(2\vartheta)_{raw}$ is the broadening due to the reduction of the grain size and $\Delta(2\vartheta)^2_{mw}$ is that associated with the finite size of the aperture from where the X-ray are emitted. Another method of extracting values from strain and grain size for XRD data is the Hall-Williamson analysis [139]. It takes into consideration broadening effects resulting from both grain size and strain into the crystalline material. The Hall-Williamson equation is:

$$\frac{B(2\vartheta)\cos\vartheta_B}{\lambda} = \frac{1}{D} + \frac{2\varepsilon\sin\vartheta_B}{\lambda} \tag{5.4}$$

where D is the grain size and ε is the strain. Equation (5.4) can be used to form a linear plot whose gradient is the average strain and the reciprocal of the y-intercept is the average grain size. Eva (Bruker, Academic version) was the program used to define the full width at a half maximum (FWHM) and ϑ_B for each peak at a time from the raw data. Rietveld refinement is a more elaborate method and powerful technique for analyzing XRD data because it provides a global fit to all the angular data. A least square approach is used to fit the measured data to a reasonable degree of accuracy. Topas (Bruker, Academic version) was used to do the Rietveld refinement of the XRD patterns. The modelling of the experimental profile $Y(2\vartheta)$ is a convolution of peak shape functions (PSF). $Y(2\vartheta)$ is written in terms of the instrumental correction and the physical properties of the sample in the fundamental parameters approach (FPA). X-ray patterns were modelled by a Voigt function to calculate the grain size and lattice parameters of nanocrystalline samples. The XRD diffraction peaks were labelled using

the software PowderCell. The crystallographic information files (cif) were taken from the Daresbury Chemical Database Service [78].

5.5 Inductively coupled plasma atomic emission spectroscopy and mass spectrometer

The copper contamination introduced by the milling tools material were characterised by an inductively coupled plasma atomic emission spectroscopy (ICP-AES, Perkin Elmer Optima 3100RL) and an inductively coupled plasma mass spectrometer (ICP-MS, Perkin Elmer-Sciex Elan 6000). The schematic of an ICP torch is provided by Figure 5.5. The ICP-AES device is composed of two parts: the ICP torch and the optical spectrometer. The torch heats the sample until it becomes a plasma prior to mass spectroscopy analysis. The ICP torch consists of a circular quartz tube with separate gas inlets. The gas routinely used is argon. A radio frequency (RF) generator produces an intense a.c. magnetic field through an induction coil, which partly surrounds the torch. The induced a.c. magnetic field creates electric currents in the gas, leading to the plasma formation at about 6000 - 7000 ^{o}C.

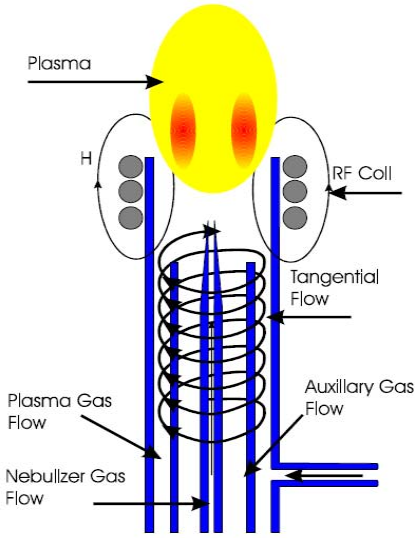

Figure 5.5 Schematic of a typical ICP torch [140].

The sample is dissolved in a suitable acid solution and subsequently introduced into the plasma flame where the various compounds/molecules are atomised and the atoms are ionised through the collisions with charged particles of the plasma. Two possibilities are now available: (i) detection of characteristics wavelengths and (ii) detection of isotopes of the elements involved. In case (i) an optical spectrometer (Figure 6) detects the

wavelength and a photomultiplier counts the light intensity at the specific wavelength(s) for the element(s) of interest. In case (ii) the mass spectrometer (Figure 5.7) deflects the isotopes trajectory by magnetic fields. Lighter isotopes are deflected more than heavier ions. The detector records the abundance of the isotope(s) of the selected element(s). Both in ICP-AES and ICP-MS the intensity of each reading is then compared to previous measured intensities of known concentrations of the element and its concentration is then computed by extrapolation along the calibration line. Homogeneous samples must be measured to provide correct contamination content.

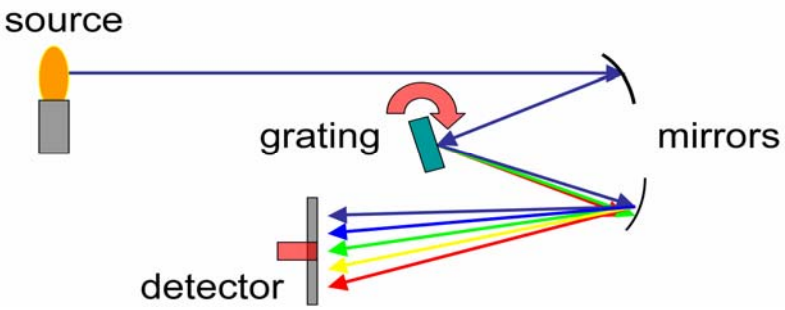

Figure 5.6 Schematic of a simple spectrometer [141]

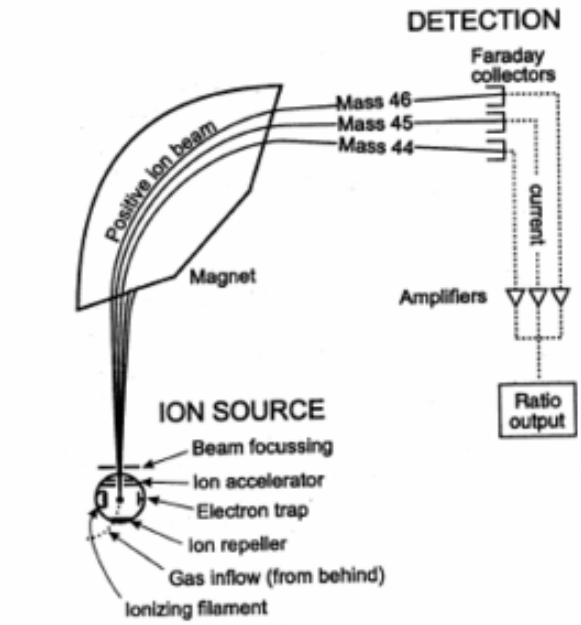

Figure 5.7 Schematics of a simple mass spectrometer [142].

5.6 Resistivity measurements

Rectangular shape samples of about 10 × 1 × 1 mm were cut from the HIP'ed materials. Four electrical contacts were fixed on the sample surface using a conductive paste. The flowing current was injected by the outside contacts and the potential difference across

the specimen monitored by the inner probes and measured for different applied currents. This four-probe method was used to obtain both resistive data at room temperature and at low temperature and in high magnetic fields. Typical currents were used from 1 to 100 mA in both forward and reverse direction. High magnetic field resistivity measurements were carried out in the Grenoble High Field Magnetic Laboratory. The resistivity was measured in function of the temperature for several applied magnetic fields up to 22.5 T (resistive magnet). In Grenoble, three samples were mounted in a home-made probe perpendicular to the applied field and a current of 30 mA was used. A Cernox^{TM} thermometer was used and its field dependence corrected following the work of Brandt [143]. LabView software was programmed to run the experiment.

5.7 Magnetic measurements - DC and AC magnetometry

The Magnetic Property Measurement System (MPMS) and the Physical Property Measurement System (PPMS) are two primary research tools used in the study of the magnetic properties of superconductors. These systems offer very high detection sensitivities over a broad range of temperature and in high-applied magnetic fields. Superconductivity is the enabling technology that provides the production of large, stable magnetic fields and the ability to detect very small signals. MPMS and PPMS represent the state-of-the-art in superconducting technologies. Magnetic moment measurements were performed in the Superconducting Quantum Interference device (SQUID, MPMS XL Quantum Design) and the Alternate Current Measurement System (ACSM, Model 6000 PPMS).

5.7.1 Superconducting quantum interference device

The DC magnetic moment of superconducting samples were measured in field up to 5 T at low temperatures (MPMS XL). The main MPMS components are shown in Figure 5.8 [144]. A measurement is performed in the MPMS by moving a sample through the superconducting detection coils. The detection coils, the connecting wires and the SQUID input coil form a closed superconducting loop. Since the SQUID (Josephson junction) works as a linear current-to-voltage converter, the induced current variations in the coils are converted in the SQUID to an output voltage variation. The calibrated system converts the SQUID output voltage in a highly accurate measurement of the magnetic moment.

Superconducting loop. The detection coils is a piece of superconducting wire wound in a set of three coils configured as shown Figure 5.9. This configuration minimises the noise in the signal detection caused by fluctuation and relaxation in the large magnetic field of the superconducting magnet. Indeed the flux change in the central coils is cancelled by the flux change in the top and bottom coils. A stepper-motor-controlled device is used to drive the sample through the detection coils in a series of discrete steps. It is possible to use discrete steps because the detection coil, SQUID input coil and connecting wires form a complete superconducting loop. A change in the sample position changes the current in the superconducting circuit. This current does not experience decay as it would do in a normal conductor. During the measurement, the sample is stopped at a number of positions and several readings of the SQUID voltage are collected and averaged.

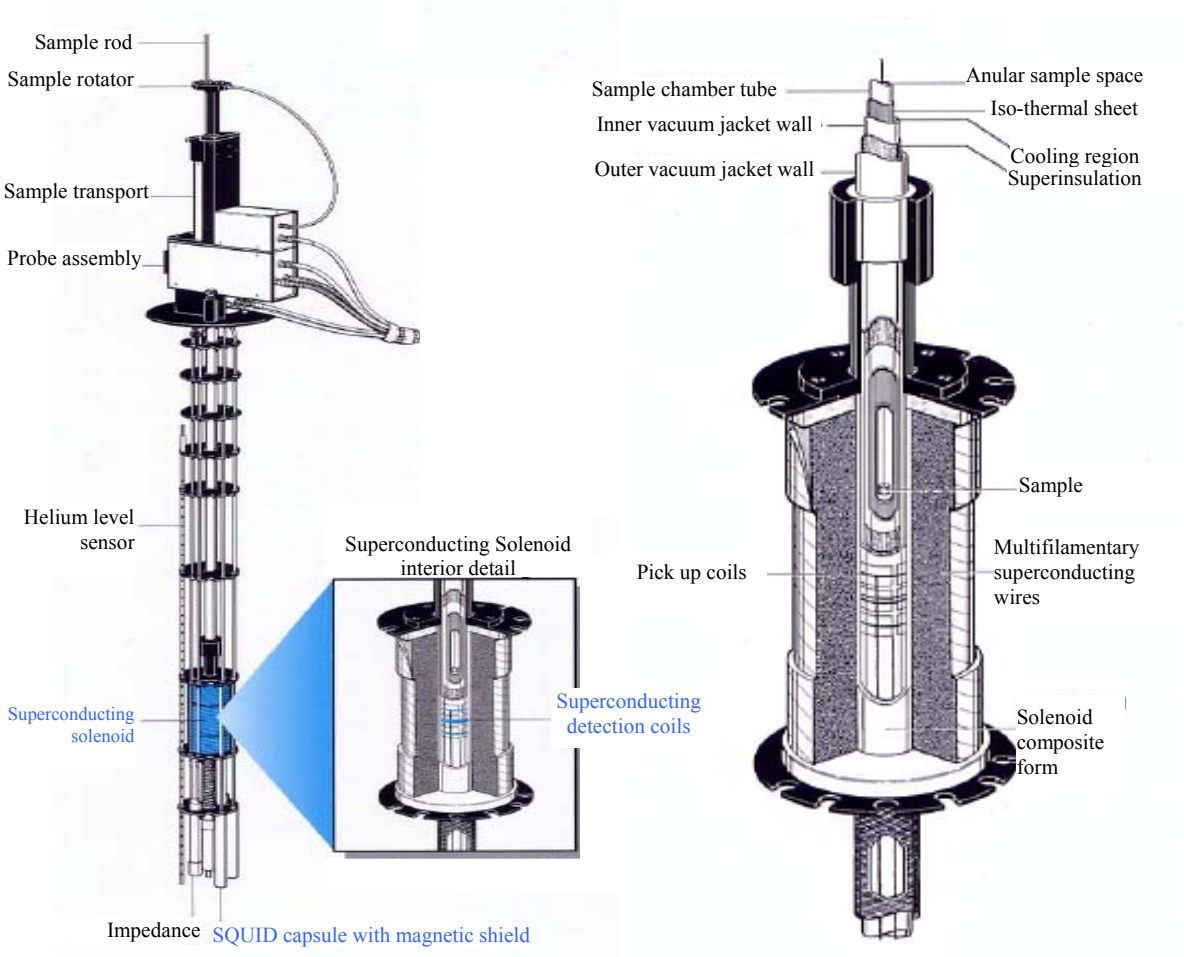

Figure 5.8 Major component of the MPMS SQUID probe [144].

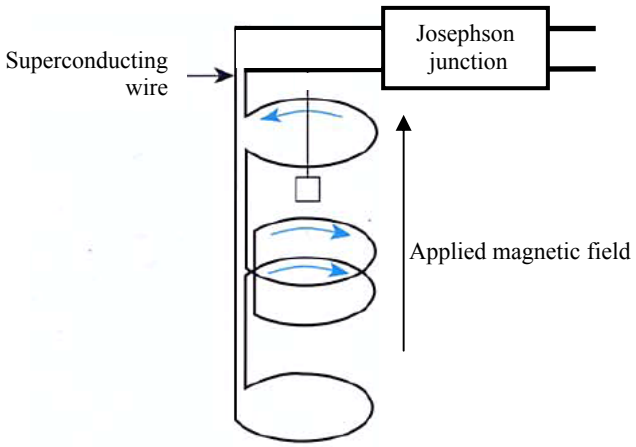

Figure 5.9 Schematic of the SQUID superconducting loop[144].

Sample transport and temperature control. The sample space is made from a 9 mm diameter tube and is maintained at a low pressure with static helium gas. At the top of the sample space there is an airlock. This can be cyclically evacuated and purged with helium gas from the dewar. During measurement, the airlock is a continuous part of the sample space. The lower part (~ 30 cm) of the sample space is lined with copper to provide a region of high thermal uniformity. Two thermometers calibrated for high field provide the temperature control.

Sample centring and output signal. The spatial dependence of the ideal SQUID signal from a point-source magnetic dipole is shown in Figure 5.10.

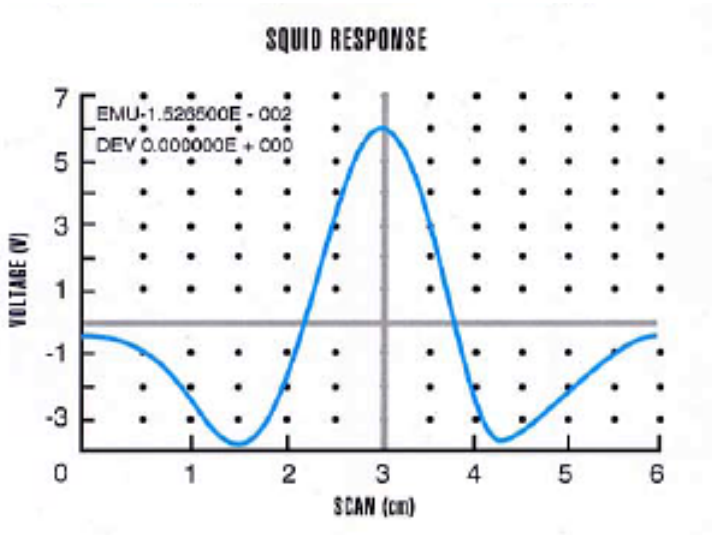

Figure 5.10 SQUID output vs. position in the detection coil space.

In order to observe this signal the sample must be uniformly magnetised and much smaller than the detection coils. Uniform magnetisation is often not encountered in high

critical current density superconductors. In addition, the shape and the size of the sample require special attention. The best procedure for calibration, recommended by Quantum Design is to use a standard sample similar in form and sample to the samples to be measured.

Computer fits are used to analyse the SQUID output signal. The full scan (the integrated area under the SQUID voltage is proportional to the magnetic moment) and the linear regression method (a linear regression algorithm fits the SQUID signal with a theoretical SQUID signal) needs accurate sample centring. The interactive regression method can accommodate the position offsets using additional variables in the computer program.

Superconducting magnet. The MPMS employs a superconducting magnet wound in a solenoidal configuration, which is a closed superconducting loop. The superconducting magnet network is shown in Figure 5.11.

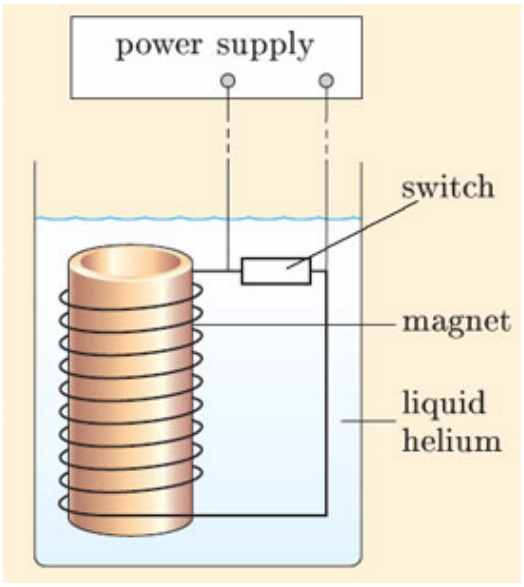

Figure 5.11 Schematic of the superconducting magnet network [145].

To charge the magnet or change the current in a magnet, the switch is opened. In this device, the switch is formed by wrapping a small heater around a short segment of the superconducting wire. Indeed the segment of wire within the heater loses the superconducting state and opens the closed superconducting loop. By attaching a power supply to each side of the switch, it becomes possible to change the current in the superconducting magnet. If the current from the power supply is different from that flowing in the magnet there is a chance that the magnet will quench. This means that a

portion of the magnet becomes normal and the resistive loss is transformed into heat. The resulting heat causes an even large portion of the magnet to become normal. The entire magnet eventually becomes normal. The trapped fields in the superconducting magnet are eliminated by a controlled quench to warm the magnet above its superconducting temperature for a short time. The possible MPMS persistent modes (i.e. stable superconducting current) of magnet operation are: no-overshoot (rapid rate near the desired field and slow change to avoid overshooting the target value) and oscillate (alternate overshoot and undershoot the target value with amplitude decreasing in every cycle). The magnet is not in persistent mode when the current supply is constantly part of the magnet circuit. This is the hysteresis operation mode. The liquid helium boil off rate is higher in the hysteresis operation mode.

5.7.2 Alternate current measurement system

The ACMS option for the PPMS is a versatile DC magnetometer and AC susceptometer. The magnetic response of samples was investigated with AC measurements in field up to 9 T at low temperatures. The hardware overview is given by Figure 5.12. The AC option adds a small alternating field (max ± 10 Oe) to the large applied field from the superconducting magnet. In our measurement, we used a 77 Hz frequency for the alternating magnetic field. The amplitude and the phase of the magnetic sample response are measured by the PPMS. The amplitude of the signal is the amplitude of the change in the magnetic moment dM due to the alternating field of dH amplitude. Hence, the real part of the signal gives the real part of the susceptibility and was used to determine the critical temperature and the upper critical field of the nanocrystalline superconducting samples.

ACSM insert. Figure 5.13 shows the relevant part of the ACSM insert. The insert fits directly in the PPMS sample chamber and contains a sample space that occupies the uniform magnetic field region of the host PPMS. It includes the drive and detection coils, thermometer, and electrical connections for the ACMS. The sample is held within the insert coil set within the insert coil on an end of a thin, rigid sample rod.

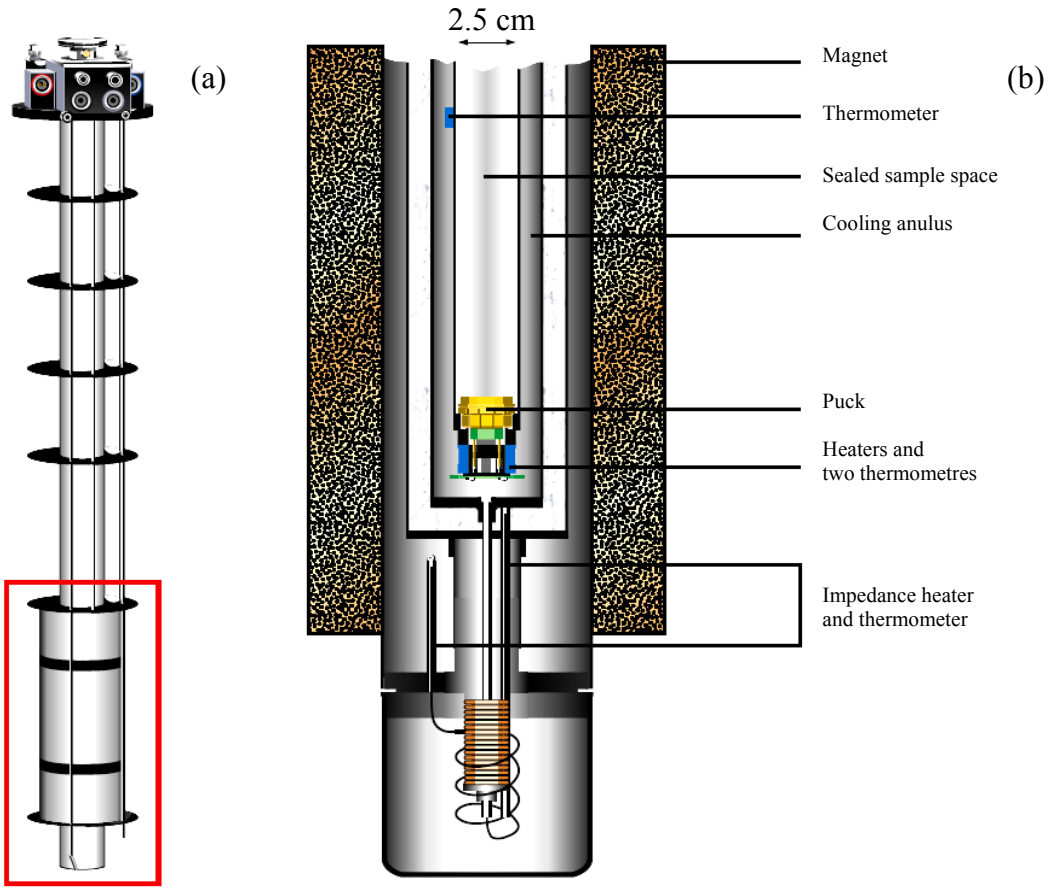

Figure 5.12 Main components of the PPMS hardware; (a) ACSM insert and (b) ACSM host [146].

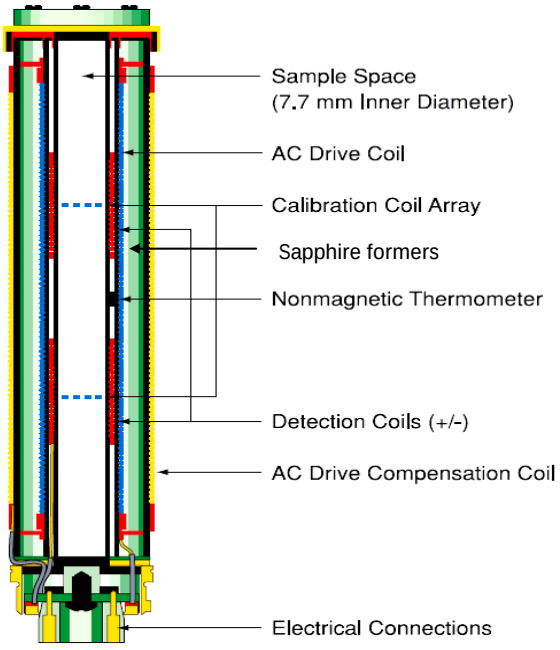

Figure 5.13 Bottom of the ACMS insert [146] .

ACMS coil set. The ACMS contains an AC-drive coil set that provides an alternating excitation field and a detection coil set that inductively responds to the combined sample moment and excitation field. Both sets of copper coils are wound on sapphire coil formers, which provide excellent thermal properties and are situated within the ACMS insert concentric with the superconducting DC magnet of the PPMS. At any temperature the drive coil can generate alternating field in a frequency range of 10 Hz to 10 kHz. At temperatures below 25 K, large amplitude field can warm the PPMS sample chamber and the ACSM insert. A compensation coil is located outside the AC drive coil. The drive coil and compensation coil are connected in series so that they receive the same excitation signal. This confines the excitation fields to the volume of the coil set and actively reduces the environmental noise during AC measurements. Two detection coils are arranged in a first order gradiometer configuration. Their function is to indicate how the applied field is altered by the presence of the sample. Each detection coil contains in the centre a calibration coil, which improves the measurement accuracy. Specifically, the low-inductance calibration coils determine the instrument-dependent phase shift. Indeed all alternate current instruments have a background phase shift between the drive signal and the measured signal due to time constants in the electronics and in the coil set that depend on temperature, frequency, and magnetic field. The ACMS raw data are corrected for this background by measuring the instrumental phase shift throughout each measurement. The ACMS coils are connected to the PPMS electronics through the 12-pin connector located at the base of the PPMS chamber. This configuration eliminates the need for additional wiring and connectors. The AC board incorporates a digital signal processor (DSP) to generate the excitation waveforms, record the detected response signal and improves the signal-to-noise ratio without removing part of the wanted signal.

AC measurement. A signal is applied to the drive coil and the sample is centred in one of the two detection coils. The DSP records the voltage across the detection coils for a predetermined amount of time. Thereafter multiple AC signals are averaged to reduce the noise of the final output signal. Successively the sample is positioned in the second detection coil and the response is again measured. The default measurement mode is based on a five point data acquisition including three readings in the centre of each coil and two readings in the centre of coil array. The difference in these signals is the sample

signal without environmental and instrumental factors. The magnetic sample response is provided as in-phase and out-of-phase signals.

5.8 Scanning Electron Microscopy

In this thesis work, the microstructure and composition of superconducting nanocrystalline samples was investigated using a Scanning Electron Microscope with an energy dispersive X-ray (EDX) system. In Durham, SEM analysis was carried out using a Hitachi SU70 Analytical Ultra High Resolution Scanning Electron Microscopy (SEM). The system is equipped with an Oxford Instruments INCA Energy EDX system with an extended software option of 'QuantMap'. The calibration was performed for the EDX system using a cobalt standard (Microanalysis Consultants Ldt, registered standard number: 7574) at 20 KeV. The beam current was measured using the Oxford instrument wave analysis system (~ 6.71 nA). The main components of a scanning electron microscope are given by Figure 5.14.

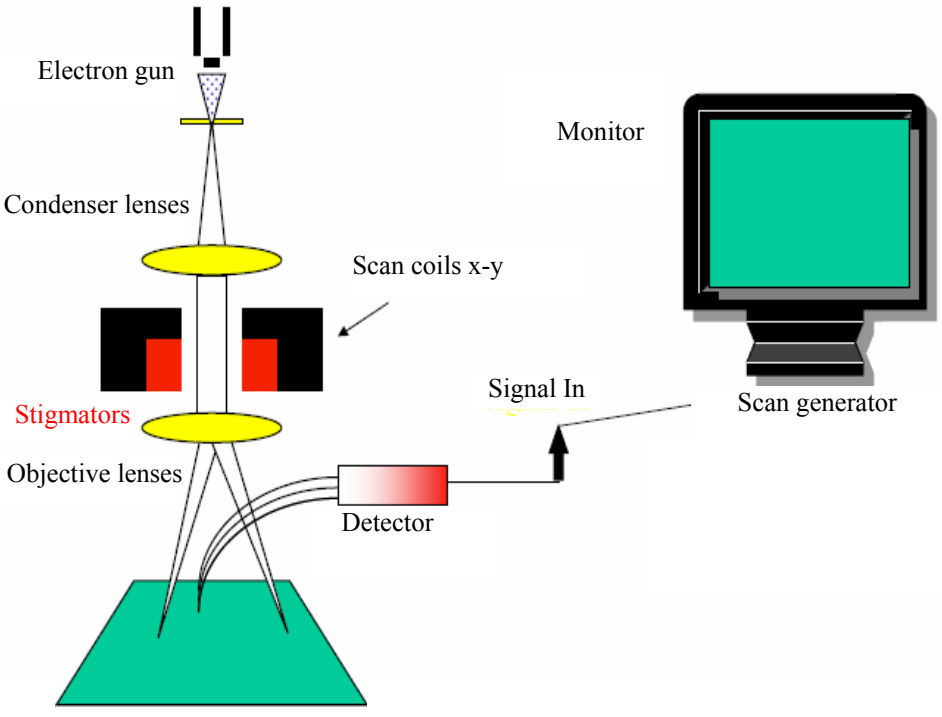

Figure 5.14 Schematic diagram of a scanning electron microscope [147].

The electron source is usually a thermally assisted Schottky cathode where electrons tunnel through the tip resulting in emission. The electrons are accelerated to an energy, which is typically between 1 KeV and 30 KeV. Condenser lenses fine focus the electron

beam to a diameter of 1.9 – 10 nm before it hits the specimen. The beam position on the sample is digitally controlled and the resultant image is displayed on a computer screen.

Image formation process. In a digital SEM, the electron beam and the framestore are both scanned synchronously in a rectangular set of straight lines. Figure 5.15(a) shows the correspondence between the raster on the sample specimen and the raster on the framestore. Figure 5.15(b) shows that the image is built sequentially pixel by pixel during the scan. The size of the specimen pixel cannot be less than:

$$p = \frac{100}{M}\ \mu\text{m} \tag{5.5}$$

where M is the magnification [148,149].

The optimum resolution is only achieved if the diameter of the electron beam is no larger than p (Figure 5.23). The ultimate resolution is the smallest probe, which can provide an adequate signal for the specimen.

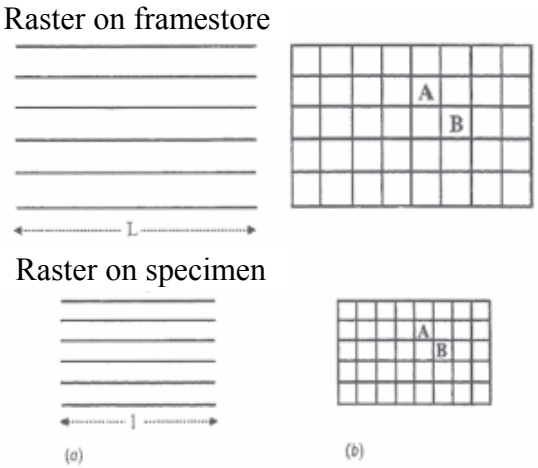

Figure 5.15 Digital SEM data acquisition (a) The electron beam scans a raster of side l in the specimen whilst a raster of side L is scanned on the framestore (b) Raster as array of pixel [148].

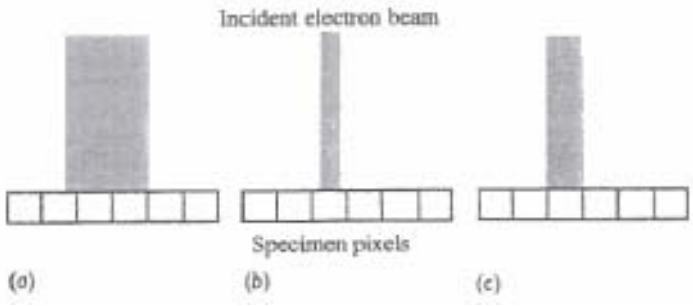

Figure 5.16 The resolution depends on the relationship between beam diameter and size of the specimen: (a) The signal is merged; (b) The signal is weak with noise; (c) Good resolution [148];

Electron beam and solid interaction. The range of the image types available from the SEM depends on the electron beam interaction with the solid. The region into which the beam electron penetrates is known as the interaction volume. The interaction volume and the regions from which secondary electrons, backscattered electrons and X-ray may be detected are shown in Figure 5.17. The level of penetration of the beam into the sample is dependent on the accelerating voltage and atomic density of the sample. Figure 5.18 shows that the higher the accelerating voltage is the greater is the depth of penetration achieved. The beam-sample interaction depends also on the density and the composition of the specimen. As the atomic weight increases, the interaction volume decreases. Therefore, light elements like aluminium have a large interaction volume compared to iron and gold (Figure 5.19). Inelastic scattering causes electron energy loss via the formation of Auger electrons, other ionised electrons (called secondary electrons), cathodoluminescence and X-ray. Figure 5.20 shows an ideal energy spectrum for the emitted electrons. Figure 5.21(a) provides a model for secondary and backscattered electrons trajectories. The spatial distribution of secondary electrons is shown by Figure 5.21(b). The volume of the material contributing to the signal is known as the sampling volume. The sampling volume depends on the signal being used. A small sampling volume produces a better image resolution [148].

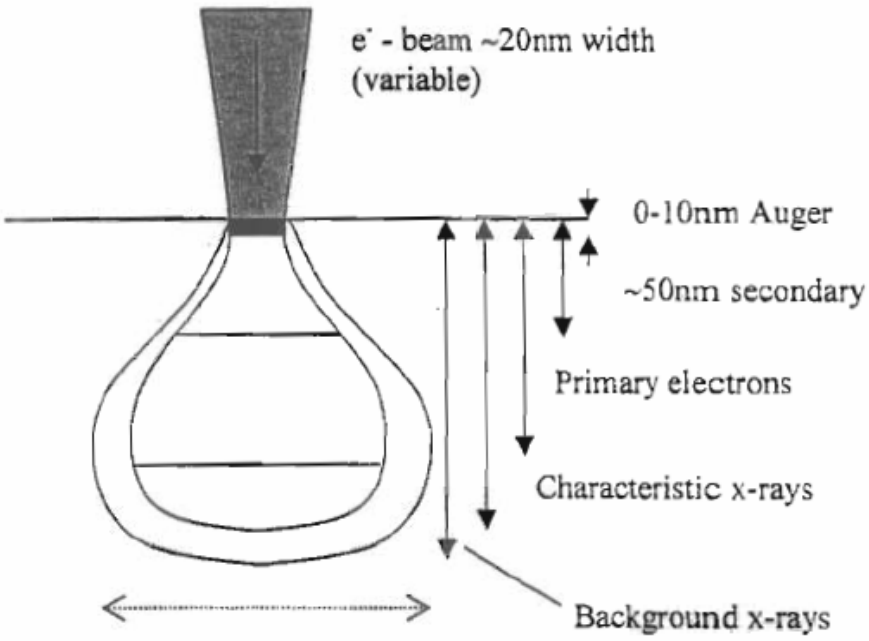

Figure 5.17 Interaction volume and regions from which the various signals may be detected [150].

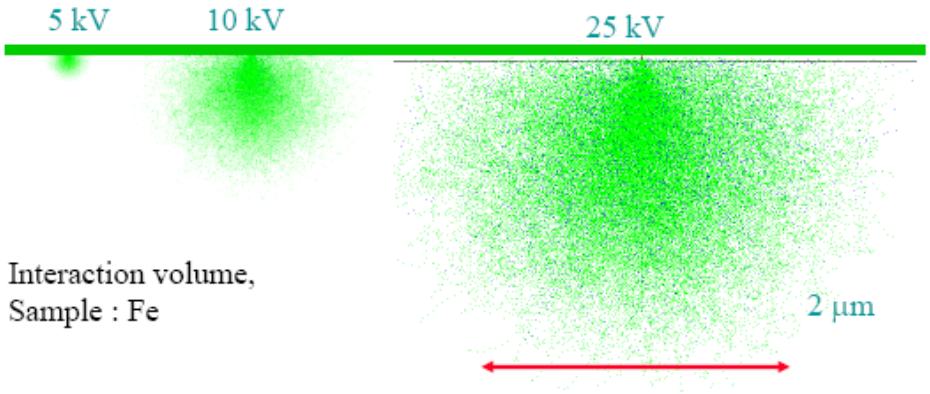

Figure 5.18 Simulation of the depth of penetration for different accelerating electron voltage [147].

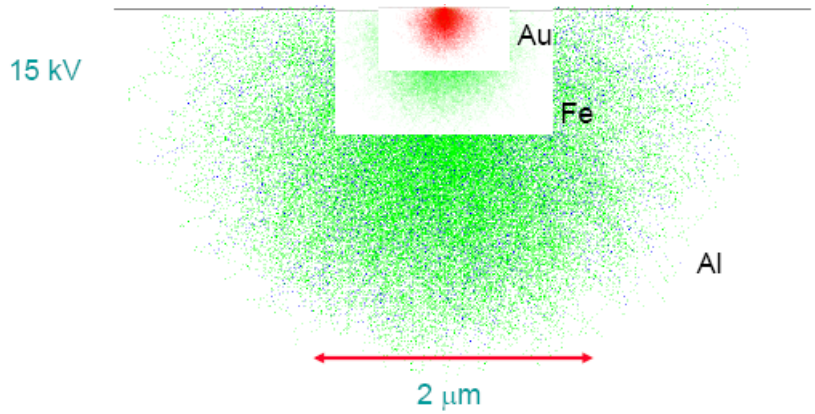

Figure 5.19 Simulations of the interaction volume in Au, Fe and Al at 15 KV electron beam energy [147].

Backscattered and secondary electrons. Backscattered electrons have a broad energy spectrum (Figure 5.20). The backscattered electrons with the highest energy (close to the primary beam energy E_0) have been scattered only a few times and originate near the incident beam (A in Figure 5.21(a)). The backscattered electrons, which have experienced multiple scattering, lose more energy and get across a larger area (B in Figure 5.21(a)). Their information has a worse spatial resolution since they experience a large sampling volume. The secondary electrons have a limited energy spectrum and a small sampling volume. Indeed they originate mainly from a region which is little larger than the diameter of the incident beam. They are generated by the ionisation of atoms through primary and backscattered electrons.

The numbers of secondary and backscattered electrons emitted from the specimen are known as the secondary electron coefficient (δ) and the backscattered electron coefficient (η), respectively. Figure 5.22(a) and (b) shows the dependence of the electron yield as a function of the atomic number (Z) and the accelerating voltage,

respectively. The secondary electron coefficient is approximately constant with the sample composition, but is sensitive to the surface condition and electronic structure. Therefore, the images produced by the secondary electrons are mainly used to study the sample topology and to produce high resolution images. The backscattered coefficient varies monotonically with *Z* and depends on the orientation of a crystal with respect to the incident beam (electron channelling). Therefore, the images produced by the backscattered electrons provide information on chemical composition variation and study of the grain microstructure. However channelling contrast is generally much weaker than the atomic number contrast [148].

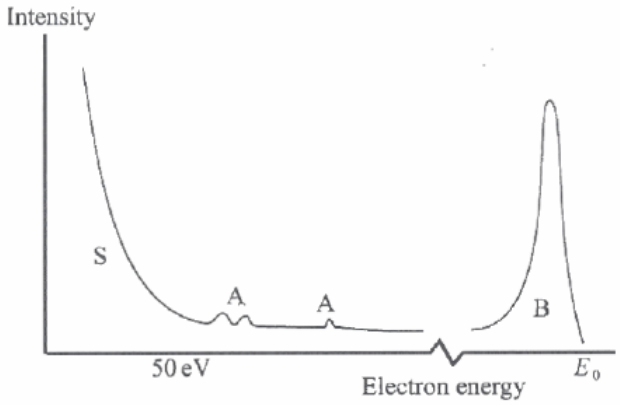

Figure 5.20 Energy spectrum for secondary (S), Auger (A) and backscattered electrons (B). The primary beam E_0 energy is typically >> 50 eV [148].

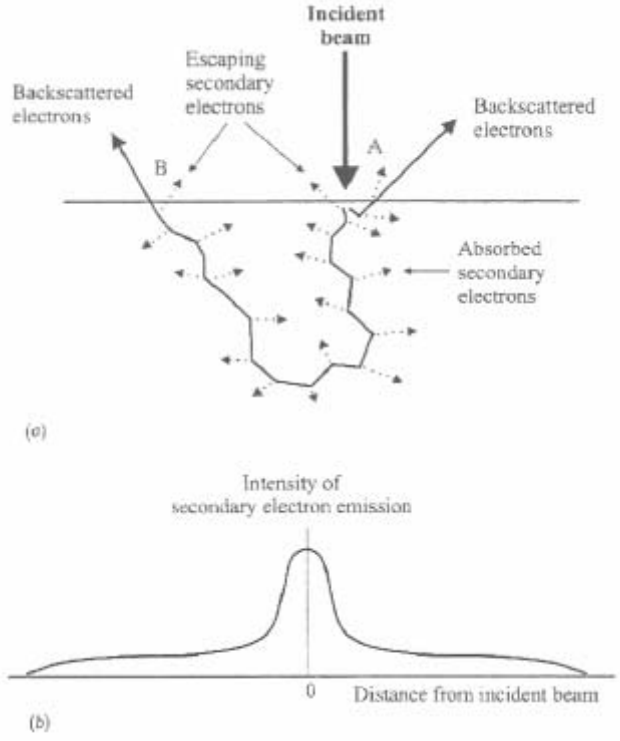

Figure 5.21 (a) Electrons scattering trajectories; (b) Spatial resolution of secondary electrons [148].

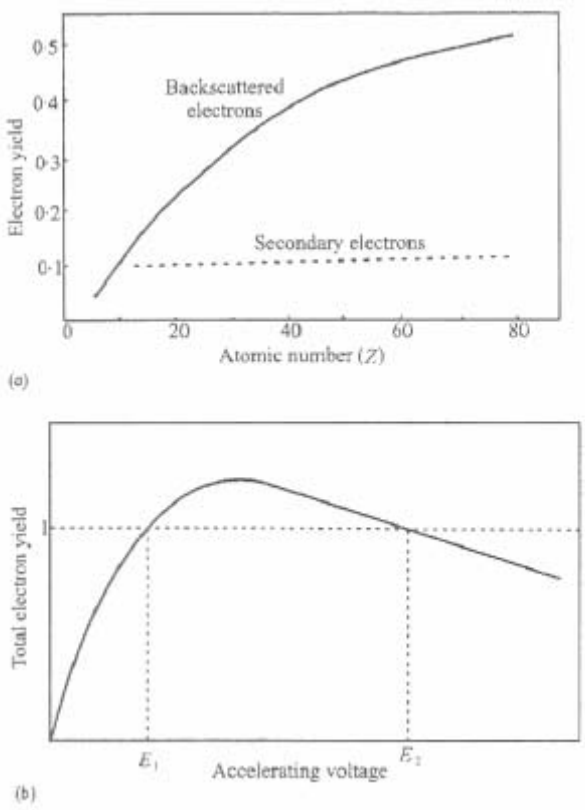

Figure 5.22 (a) The effect of atomic number on the number of backscattered electrons (η) and secondary electrons (δ); (b) total electronic yield ($\eta + \delta$) versus the accelerating voltage of the primary beam [148].

X-ray analysis. X-rays have large sampling volumes, which are comparable with the total interaction volume. X-rays characteristic of the sample are produced when a high voltage accelerates electrons. The measurements of the characteristic X-ray energy enable one to find out which elements are in the sample (qualitative analysis). This method is named energy dispersion X-ray (EDX) analysis. The measurement of the number of characteristic X-ray emitted per second provides a measurement of how much of the element is present (quantitative analysis) and to estimate the stoichiometry. The SEM output signal is an average of compositional information from nanosized pixels. However, the complexity of this measurement makes accurate analysis extremely difficult. The fraction of the detected X-ray depends on their energy and the average atomic weight of the specimen. For instance, soft X-rays (low energy) are readily absorbed and a few of them will escape from the surface; hard X-rays (high energy) penetrate many micrometers into most solids. In conclusion the sampling volume and the fraction of the X-rays which are emitted from the specimen depends strictly on the energy of the electron beam, the energy of the X-ray being studied and the local atomic weight of the specimen. Figure 5.23 shows a basic energy dispersive

X-ray detector with analysis system (EDS). The detector is usually a semiconductor that produces a current proportional to the energy of the incident X-ray. The protective window absorbs a significant proportion of low energy X-rays and makes light element particularly difficult to detect. The EDS is controlled by a software, which stores the energies of all elements present.

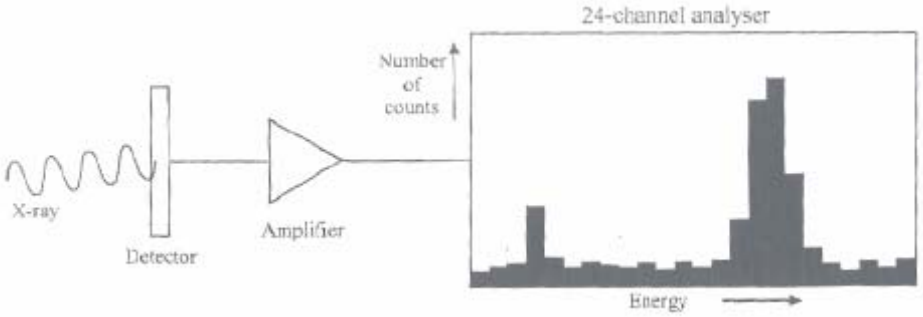

Figure 5.23 A simplified energy dispersive analysis system [148].

Quantitative X-ray mapping. Quantitative maps are images in which the concentration of elements present is calculated at every pixel. Quantitative X-ray mapping (XRM) has become a very powerful method to understand the distribution of elements and to provide necessary compositional information in nanophase materials. The advent of spectral imaging enables one to perform separately the EDX elemental mapping on the microscope and the data processing for quantification analysis. These quantification maps provide the concentration for each element in atomic or weight percent, which can be used to classify the phases present in the material.

Sample preparation and measurement. Bulk samples were incorporated into an epoxy resin mould prior to sub-micron mechanical polishing. Flat surfaces are required to ensure the beam is perpendicular to the surface and hence ideal for electron collection. The epoxy resin mould was carbon coated (~ 40 nm) prior to measurement. This is required to avoid negative charge built-up on the non-conductive epoxy resin surface and consequent deviation/distortion of the images. Maps of multiphase nanocrystalline superconductors were collected at 20 KeV. For the resulting spectrum image, maps for Nb, Al, Ge and Cu were extracted and quantified by using INCA software. The magnification used was 256 × 192. This means that the image was displayed on a framestore of 49152 pixels. The state-of-the-art X-ray detector provided a total X-ray count of about 16-18 millions for all EDX maps, which provides accurate statistics for the element concentration estimation (subsection 7.4.2 and 8.4.2).

5.9 Summary

Chapters 5 reports on the various methods performed to investigate the various nanocrystalline material produced. The basic principles behind the experimental techniques were discussed jointly with the corresponding device geometry. Description of the performed experimental procedure, technical data, and processing software were reported. Several techniques were used to investigate the correlation between superconductivity, microstructure, and composition in nanophase samples. Specific experimental procedures/details (e.g. heat treatment times) are presented in the following chapters.

Chapter 6

Properties of wet mechanically alloyed Nb-Al-Ge

6.1 Introduction

Chapter 6 reports on the properties of wet milled Nb-Al-Ge elemental powders. This investigation has been a preliminary attempt to fabricate nanocrystalline A15 materials, to improve their superconducting properties and to get some experience with the standard milling procedure and tools. Wet milling was found to produce high levels of contamination in milled powders including high copper contamination from the milling tools. It was clear that the high level of impurities would mitigate against nucleating the A15 phase, but although the volume percent of A15 material would be low, the intention was to use wet milling as a means to providing an idea of what upper critical fields were possible in nanocrystalline forms of A15 Nb-Al-Ge compounds. This piece of work has been published in the EUCAS 2007 proceedings [151]. Section 6.2 is an overview of fabrication of powders and bulk samples. A comprehensive description of the data for milled powders and nanocrystalline bulk materials is reported by section 6.3 and 6.4, respectively. The comprehensive data include: yield data associated with milling, ICP-AES; simultaneous thermogravimetric analysis DSC/TG, X-ray diffraction, resistivity and dc magnetometry. Finally, we discuss the role of PCA in fabricating superconducting materials and summarise our results in section 6.5.

6.2 Overview of fabrication of powders and bulk materials

In this work, we report on the use of ball milling with a process control agent (PCA) to fabricate three sets of nanocrystalline materials. It is known that using a PCA can increase yield, minimize powder agglomeration, and produce finer powders in shorter milling times. The specific procedures carried out to mill and compact the powder are now presented.

Starting materials. The starting materials were niobium powder (- 60 mesh, purity 99.8 %) from Alfa Aesar, aluminium powder (- 325 mesh, purity 99.97 %) and germanium powder (- 100 mesh, purity 99.999 %). A stoichiometric mix of elemental

powders was produced in the form 3 Nb + (1 - x) Al + (x) Ge with x = 0, 0.3 and 1 with the intention of producing Nb_3Al, $Nb_3Al_{0.7}Ge_{0.3}$ and Nb_3Ge, respectively.

Wet milling procedure. A Fritch planetary mono mill (pulverisette 6) was used to grind up the mix of elemental powders (10 g). A ball-to-powder ratio of 15:1 was chosen. Seven 10 mm and two 20 mm diameter balls were used. In this experiment, distilled water was chosen as a PCA because water is a relatively small molecule and thus does not break apart as easily as do significantly larger organic molecules [100,152]. However, the hydrogen bonds in water make it polar which gives it a strong affinity for the exposed metallic surfaces produced during milling. High energy ball milling was completed (in air) using distilled water in the quantities of 2000, 20, 10 and 5% of the initial powder mass [100] at a rotational speed of 300 rpm for up to 20 hours. To simplify the notation, the amount of PCA will be hereafter given as the percentage of the initial mass of the powder. During all milling processes after every hour, the apparatus stopped milling for five minutes and thereafter a reversal in the direction of rotation followed. Such rest period was necessary to reduce the temperature of the vial contents and to promote alloy and intermetallic compound formation through mechanical processes rather than as result of the melting. The change in direction of rotation increased the homogenisation of the powder produced. After every five hours of milling, the inside wall of the vial was scraped using a copper rod. Eighteen samples were produced in total – six of each composition as specified in Table 6.1. In order to remove all the PCA, heat treatments of 250 ^{o}C × 4 h and 350 ^{o}C × 4 h were carried out on PCA5% milled powders in a furnace under argon. These procedures are summarised in Table 6.1. Three series of wet mechanically alloyed powders milled for up to 20 h were given a heat treatment at 350 ^{o}C × 4 h prior to HIP'ing.

Starting materials	**M.T. (h)**	**PCA**	**Post-milling annealing**
3 Nb + Al 3 Nb + 0.7 Al + 0.3 Ge 3 Nb + Ge	20 h	2000%	-
		20%	-
		10%	-
		5%	-
		5%	250 ^{o}C × 4 h
		5%	350 ^{o}C × 4 h

Table 6.1 Processing conditions for wet milled nanocrystalline powders prior to HIP'ing: milling time (M.T.), PCA expressed as percentage of the initial powder weight; isochronal annealing given to powders after milling.

HIP'ed samples. Twenty-one hot isostatically pressed samples were produced – seven for each of the three compositions. Table 6.2 summarises the processing conditions for Nb-Al, Nb-Al-Ge and Nb-Ge powders for both wet mechanically alloyed powders and unmilled powders. The hot isostatic press was operated at a constant pressure of 0.2 GPa and at temperatures of 450, 550, 650 and 750 ^{o}C × 5 h. The powders for the unmilled samples were mixed in the ball milling vial without the presence of any milling balls.

Nomenclature. We characterise the processing conditions for all the samples presented in Chapter 6 using the general nomenclature: PCAXXXX + AYYY + HIPZZZ where XXXX, YYY and ZZZ indicate, the water amount expressed as percentage of the initial powder weight, the temperature of the annealing prior to HIP'ing and HIP'ing temperature respectively.

Starting materials	**M.T. (h), PCA**	**Annealing prior to HIP'ing**	**HIP'ing pressure and temperature**
3 Nb + Al 3 Nb + 0.7 Al + 0.3 Ge 3 Nb + Ge	Not milled	No heat treatment	0.2 GPa, 750 ^{o}C × 5 h
			0.2 GPa, 650 ^{o}C × 5 h
			0.2 GPa, 550 ^{o}C × 5 h
	20 h, PCA5%	350 ^{o}C × 4 h	0.2 GPa, 750 ^{o}C × 5 h
			0.2 GPa, 650 ^{o}C × 5 h
			0.2 GPa, 550 ^{o}C × 5 h
			0.2 GPa, 450 ^{o}C × 5 h

Table 6.2 Processing conditions for Nb-Al, Nb-Al-Ge and Nb-Ge bulk materials fabricated in Durham. The water amount is expressed as percentage of the initial powder weight. Heat treatment are isochronal. M.T. is the milling time.

6.3 Properties of milled powders

Powder changes and contamination effects, which occurred during wet mechanical milling were investigated by simultaneous DSC/TG, ICP-AES and yield for all three sets of starting powders. In this preliminary chapter, we only report X-ray diffraction measurements on the Nb-Al powders. Each set of results will be discussed in turn. Finally, the properties of wet milled powders are summarised in section 6.3.5.

6.3.1 Simultaneous DSC/TG properties

Simultaneous DSC/TG measurements were performed on Nb-Al, Nb-Al-Ge and Nb-Ge powders milled for up to 20 h with different PCA percentages before and after isochronal annealing. Not all data are presented on all the samples fabricated – we have chosen representative data for inclusion typically including samples with high PCA content and those with low PCA content before and after annealing.

Figure 6.1, Figure 6.2 and Figure 6.3 show data for wet milled Nb-Al samples with PCA2000%, PCA5% and PCA5% + A350, respectively. Figure 6.4 and Figure 6.6 show the thermal response for wet milled Nb-Al-Ge with PCA20% and PCA5% + A350, respectively. Figure 6.7 and Figure 6.8 show equivalent data for wet milled Nb-Ge with PCA20% and PCA5% + A350, respectively. Tables are also reported which give the analysis of the DSC peaks that characterise the microstructural evolution for the Nb-Al (Table 6.3), Nb-Al-Ge (Table 6.4) and Nb-Ge (Table 6.4) final powders. Characteristic mass changes for wet milled powders occur below ~ 400 ^{o}C. Annealing the samples at 250 ^{o}C and 350 ^{o}C removes all the low temperature exothermic peaks and minimises the changes observed in the TGA measurements. The peaks below ~ 400 ^{o}C can be mainly associated with the PCA trapped in the milled powders whereas the peaks above ~ 400 ^{o}C are predominantly due to the nano-structure (i.e. grain boundary, ordering) and compound formation. There are peaks that occur at the same temperature in different compositions (e.g. ~ 660 ^{o}C for Nb-Al and Nb-Al-Ge; ~ 420 ^{o}C for Nb-Al-Ge; ~ 540 ^{o}C for Nb-Ge) for materials milled with different PCA contents. These can often be associated with new compound formation (identified in the phase diagrams) and with microstructural changes.

The interpretation of the data is complex because of the mutual effect of the concurrent microstructural changes and compound formation. Peak identification was carried out using the archival literature on wet milled powder mixtures [153,154], phase diagrams (see the appendix) and thermochemical data from the Daresbury database. A detailed analysis of TG/DSC traces, enthalpies of reaction, and the different types of peaks within one/across different materials follows the presentation of the figures and tables.

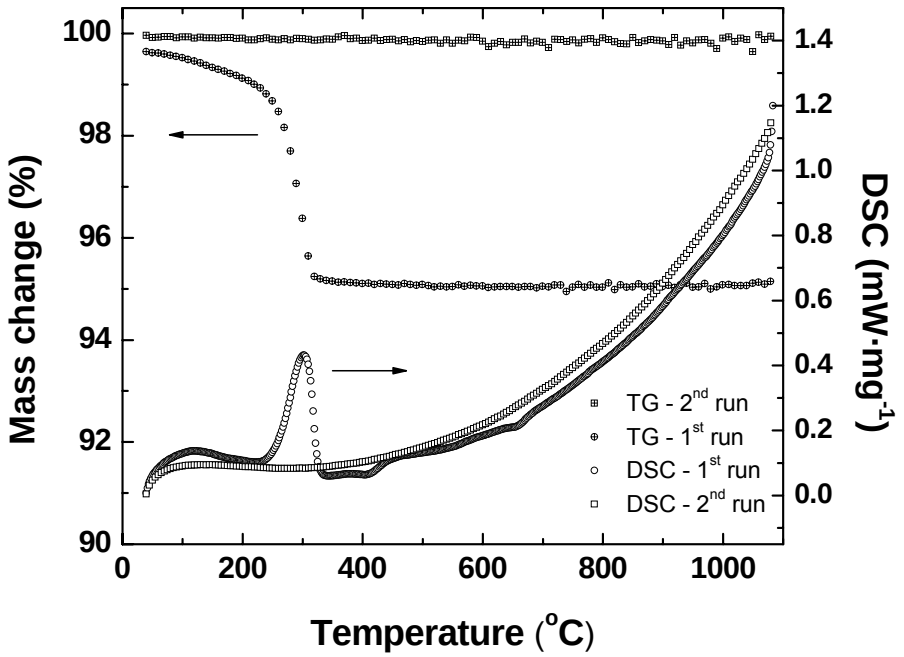

Figure 6.1 TG and DSC traces for Nb-Al powders milled for up to 20 h with PCA2000%. The two runs up are successive tests on the same powder at a heating rate of 10 K·min^{-1}. The two sets of data provided for each milled sample were both obtained while increasing temperature during the first half of two successive cycles obtained at a heating rate of 10 K·min^{-1}.

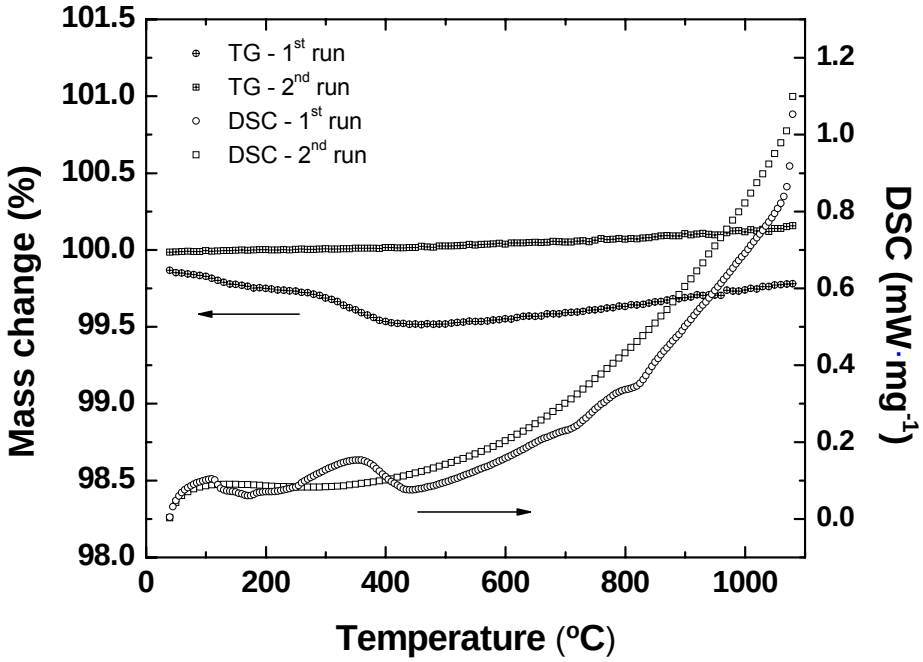

Figure 6.2 TG and DSC traces for Nb-Al powders milled for up to 20 h with PCA5%. The two runs up are successive tests on the same powder at a heating rate of 10 K·min^{-1}. The two sets of data provided for each milled sample were both obtained while increasing temperature during the first half of two successive cycles obtained at a heating rate of 10 K·min^{-1}.

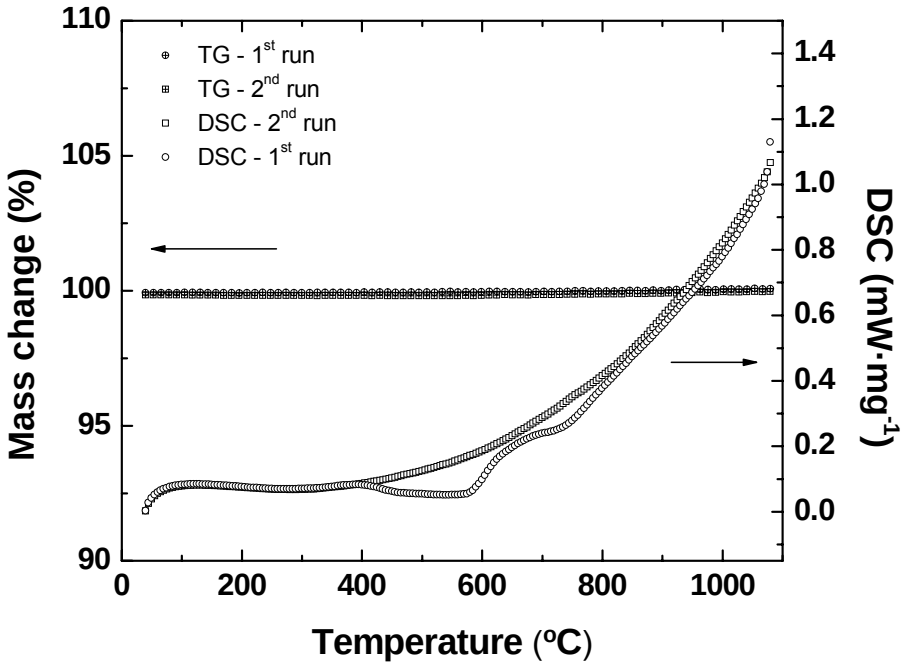

Figure 6.3 TG and DSC traces for Nb-Al powders milled for up to 20 h with PCA5% + A350 in an Ar furnace. The two runs up are successive tests on the same powder at a heating rate of 10 K·min^{-1}. The two sets of data provided for each milled sample were both obtained while increasing temperature during the first half of two successive cycles obtained at a heating rate of 10 K·min^{-1}.

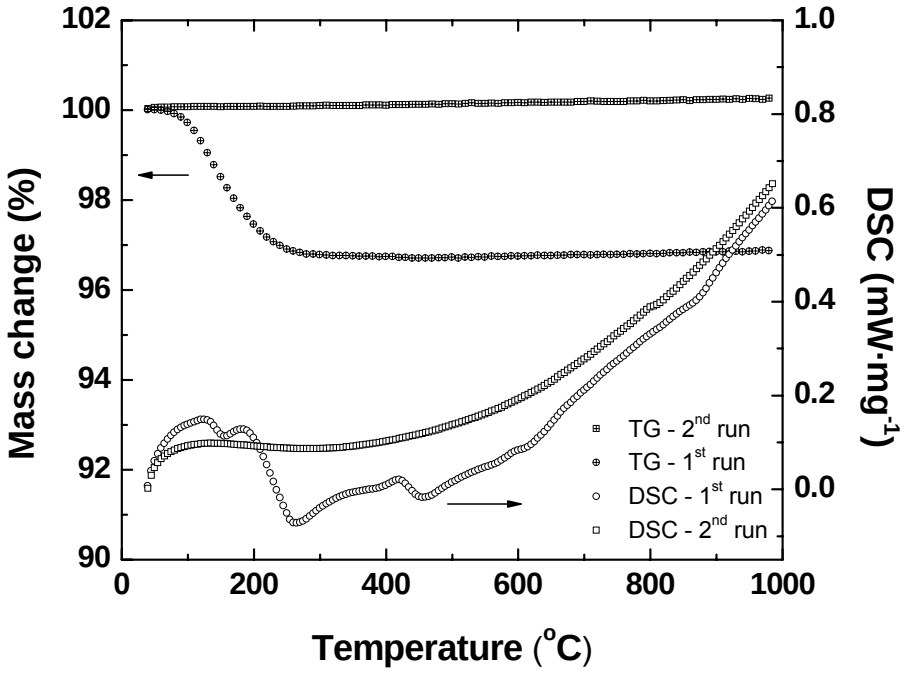

Figure 6.4 TG and DSC traces for Nb-Al-Ge powders milled for up to 20 h with PCA20%. The two runs up are successive tests on the same powder at a heating rate of 10 K·min^{-1}. The two sets of data provided for each milled sample were both obtained while increasing temperature during the first half of two successive cycles obtained at a heating rate of 10 K·min^{-1}.

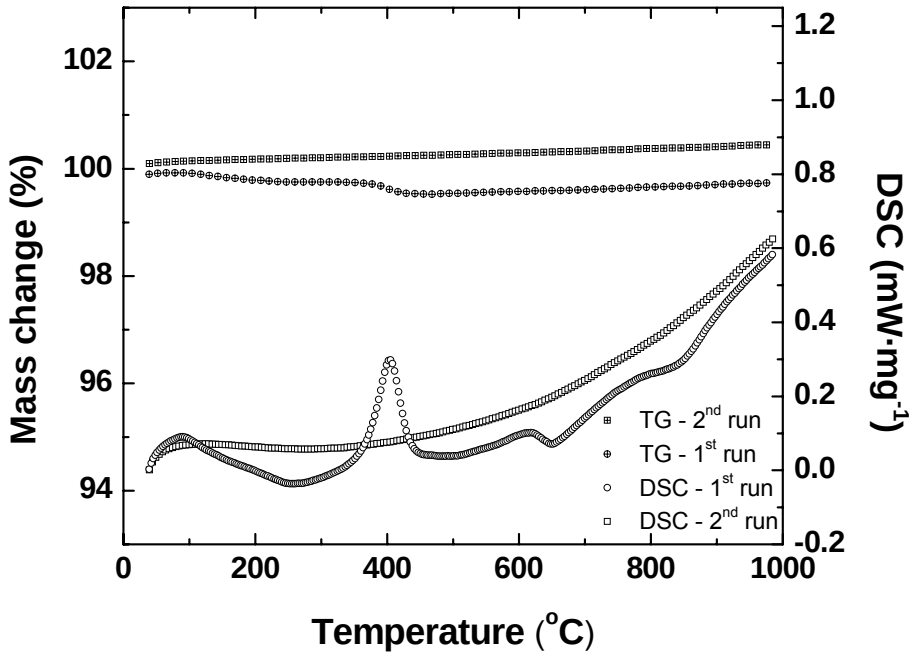

Figure 6.5 TG and DSC traces for Nb-Al-Ge powders milled for up to 20 h with PCA5%. The two runs up are successive tests on the same powder at a heating rate of 10 K·min^{-1}. The two sets of data provided for each milled sample were both obtained while increasing temperature during the first half of two successive cycles obtained at a heating rate of 10 K·min^{-1}.

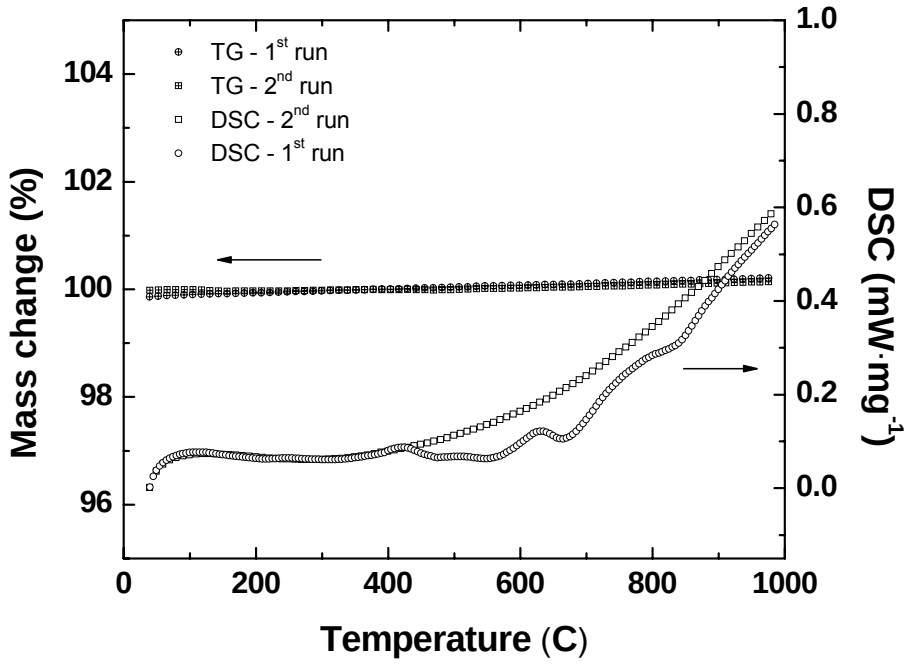

Figure 6.6 TG and DSC traces for Nb-Al-Ge powders milled for up to 20 h with 5% + A350 in an Ar furnace. The two runs up are successive tests on the same powder at a heating rate of 10 K·min^{-1}. The two sets of data provided for each milled sample were both obtained while increasing temperature during the first half of two successive cycles obtained at a heating rate of 10 K·min^{-1}.

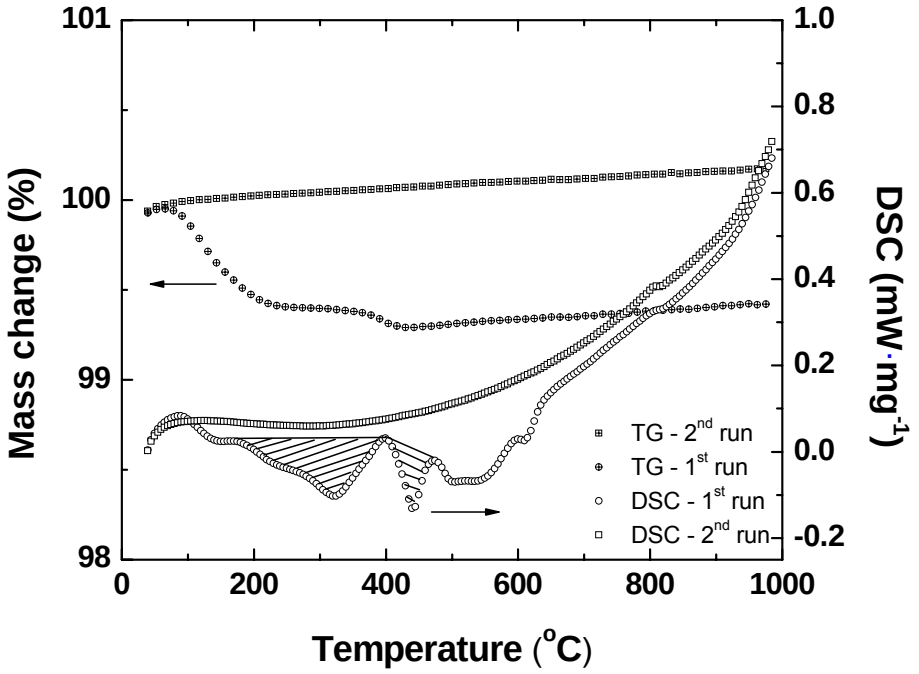

Figure 6.7 TG and DSC traces for Nb-Ge powders milled for up to 20 h with PCA20%. The two runs up are successive tests on the same powder at a heating rate of 10 K·min^{-1}. The two sets of data provided for each milled sample were both obtained while increasing temperature during the first half of two successive cycles obtained at a heating rate of 10 K·min^{-1}.

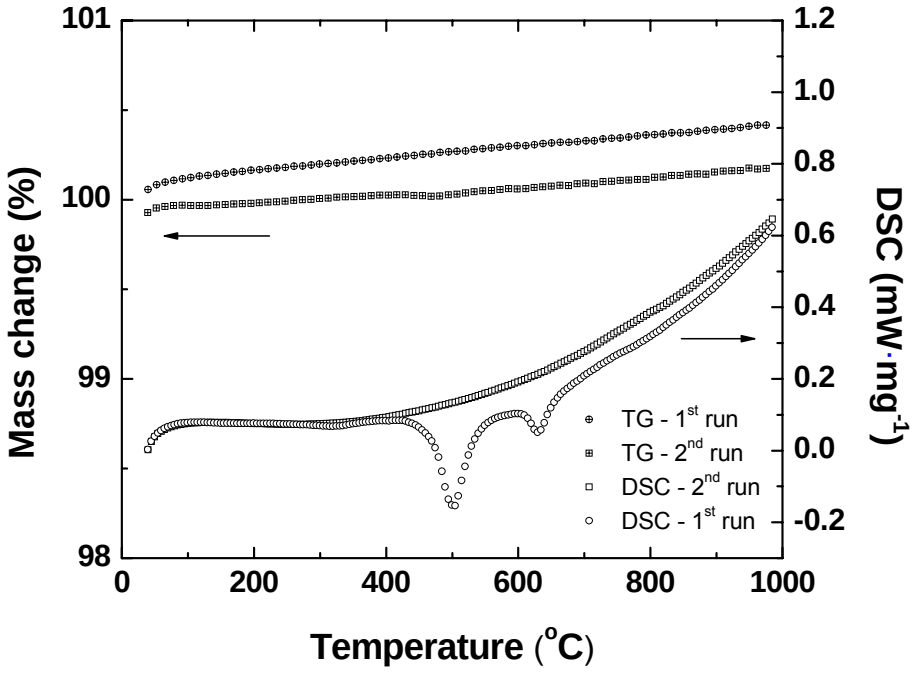

Figure 6.8 TG and DSC traces for Nb-Ge powders milled for up to 20 h with the PCA5% + A350 in an Ar furnace. The two runs up are successive tests on the same powder at a heating rate of 10 K·min^{-1}. The two sets of data provided for each milled sample were both obtained while increasing temperature during the first half of two successive cycles obtained at a heating rate of 10 K·min^{-1}.

Sample	Peak area ($J \cdot g^{-1}$)						
	~ 120 °C	~ 300 °C	~ 350 °C	~ 400 °C	~ 570 °C	~ 660 °C	~ 730 °C
PCA2000%	13	94	-	-7	-	-4	-
PCA20%	78	-115	-	-9	-	-7	-
PCA10%	60	-114	22	-	-	-17	-
PCA5%	-	-	48	-	-	-	-7
PCA5% + A250	-	-	-	31	-22	-	-24
PCA5% + A350	-	-	-	-	-86	-	-23

Table 6.3 Enthalpy of reaction for Nb-Al milled for up to 20 h with different amount of H_2O before and after heat treatments. The peak temperature is indicative for the peak position. Positive and negative peaks areas are for endothermic (e.g. melting peaks) and exothermic (e.g. crystallisation) reactions, respectively. The error for the enthalpy is ± 3 %.

Sample	Peak area ($J \cdot g^{-1}$)						
	~ 90 °C	~ 120 °C	~ 250 °C	~ 350 °C	~ 420 °C	~ 660 °C	~ 850 °C
PCA2000%	-	-76	- 71	-103	-	- 10	-
PCA20%	-	- 12	- 69	-	5	-3	-2
PCA10%	8	-	- 63	-	61	-15	-14
PCA5%	12	-	-	-	66	-11	-11
PCA5% + A250	13	-	-	-	63	-16	-14
PCA5% + A350		-	-	-	5	-17	-8

Table 6.4 Enthalpy of reaction ($J \cdot g^{-1}$) for Nb-Al-Ge milled for up to 20 h with different amount of H_2O before and after heat treatments. The peak temperature is indicative for the peak position. Positive and negative peaks areas are for endothermic (e.g. melting peaks) and exothermic (e.g. crystallisation) reactions, respectively. The error for the enthalpy is ± 3 %.

Sample	Peak area ($J \cdot g^{-1}$)				
	~ 300 °C	~ 440 °C	~ 500 °C	~ 540 °C	~ 630 °C
PCA2000%	- 36	-	-	-	-131
PCA20%	- 85	- 25	-	- 34	-
PCA10%	- 104	- 24	-	- 96	- 0.2
PCA5%	- 80	- 15	-	- 44	- 0.8
PCA5% + A250	- 30	-	- 69	- 55	-17
PCA5% + A350	-	-	- 68	-	-16

Table 6.5 Enthalpy of reaction for enthalpy ($J \cdot g^{-1}$) for Nb-Ge milled for 20 h with different amount of H_2O before and after heat treatments. The peak temperature is indicative for the peak position Positive and negative peaks areas are for endothermic (e.g. melting peaks) and exothermic (e.g. crystallisation) reactions, respectively. The error for the enthalpy is ± 3 %.

TG analysis. TG curves of wet milled powders show a marked mass variation up to 4.5 % during the 1st heating run for powders milled with PCA2000%. In contrast, they are relatively constant during the 2nd run. Most large mass changes for each type of mixture occur below ~ 400 °C which has been reported in other wet milled systems (including epoxy composites) and predominantly attributed to the PCA [153,154] although eventually one can produce the decomposition of hydroxide and carbonates due to the milling in air [155,156]. We conclude, consistently with the literature, that that mass changes below ~ 400 °C are due mainly to removing the process control agent (section 4.4). For these reason we chose to anneal the wet milled powder at 350 ^{o}C × 4 h, prior to HIP'ing.

DSC analysis. In the standard DSC analysis for increasing temperature peaks are positive if an endothermic heat change takes place (e.g. melting) whereas peaks are negative if an exothermic heat change occurs (e.g. crystallisation of amorphous material). The peak area is a measure of the enthalpy which occurs during thermally activated reactions [104,135]. Enthalpy changes can be attributed to several factors like microstructure (i.e. decrease of interfaces) [104], formation of new compounds [157], amorphisation [135] and crystallisation [87,158].

Change of enthalpy. All DSC traces include several peaks in the 1st run that completely disappear in the 2nd run indicating they are crystallisation peaks The systematic behavior of the peak areas is reported in Table 6.3, Table 6.4 and Table 6.5 for Nb-Al, Nb-Al-Ge and Nb-Ge respectively. The area was evaluated in a systematic way considering a reasonably smooth baseline for all data sets using Proteous Analysis software as shown in Figure 6.7. The baselines are clearly not unique but nevertheless give a means to obtain approximate values for the enthalpy of the peaks. Heat of formation is an important factor in the preparation of intermetallic compounds [159]. Tabulated values of the heat of formation, ΔH_f, for undesired metals oxides (i.e. AlO, CuO, Al_2O_3), carbides (i.e. AlC, NbC), nitrates (i.e. AlN, NbN) and hydroxides (i.e. Al(OH)) are available in the literature [157]. For comparison purposes, standard heats of formation, ΔH_f^o, for Nb, Al and Ge oxides in the solid state are given by Table 6.6. Nb_2O_5 and Al_2O_3 oxides are known to be very stable structures [160,161]. Indeed their strongly negative heat of formation shows that there is a relatively high probability that a number of those oxides will exist in the system [159,162]. This clearly indicates that

the oxide formation has also an elevated potential to compete with the formation of the A15 phase.

Oxide	ΔH_f^o (J · g^{-1})
NbO	-3722.9
NbO_2	-6369.6
Nb_2O_5	-7141.0
Al_2O_3	- 16428.4
GeO	-2976.1
GeO_2	-5523.8

Table 6.6 Standard heats of formation (25 ^oC, 1 atm) for Nb, Al, Ge oxides [163].

Discussion of the DSC peaks. The Nb-Al data reported in Table 6.3 show how important the role of the PCA is and how difficult it is to interpret these data. For example very large peaks appear in Nb-Al materials that have been annealed prior to the DSC measurement that are not in the materials that were not subjected to an annealing heat treatment. We can interpret some of the peaks with reference to dry-milled samples that appear in chapters 7 and 8 but delay detailed consideration until those chapters. The group of peaks at ~ 420 ^oC for Nb-Al-Ge (cf table 6.4) are also observed in dry Nb-Al-Ge mixtures at the same temperature (section 8.3.1) can be attributed to the eutectic reaction L ↔ $(Al)_{ss}$ + $(Ge)_{ss}$ (420 ^oC). This endothermic reaction occurs at 30 at.% Ge [55]. We attribute the exothermic reaction that appears at 660 ^oC in Nb-Al and Nb-Al-Ge, but not in Nb-Ge, to the formation of Al_2O_3 oxide. This peak does not appear in dry-milled powders so we suggest the source of the oxygen is from the PCA. The most important high temperature peaks for Nb-Ge are 540 ^oC and 630 ^oC (c.f. table 6.5). Following Schwartz et al. [135], the low temperature peak is due to the formation of the amorphous Nb-Ge alloy, which is formed following diffusion between the amorphous elements. The high temperature peak is due to the crystallisation of the A15 intermetallic Nb_3Ge.

6.3.2 ICP-AES results

These measurements were carried out by Dr. Ottley (Earth Science Department, Durham University) on powders ball milled for up 20h with PCA5% (Table 6.7). They were done to quantify the atomic percent of the elements such as Nb, Al, Ge and in particular the level of Cu contamination in the Nb-Al, Nb-Al-Ge and Nb-Ge mixtures .

Sample	Nb (at. %)	Al (at. %)	Ge (at. %)	Cu (at. %)
Nb-Al	58.1	18.9	0	23.0
Nb- Al- Ge	74.7	4.8	5.0	13.9
Nb-Ge	63.3	0	15.6	18.0

Table 6.7 ICP-AES results for powder mixtures ball milled for up to 20 h with PCA5%. The error is ± 5 %.

The most notable feature of these AES data is the high Cu content because of the Cu milling media. These values are consistent with the Cu peaks found in the XRD data shown in section 6.4.1.

6.3.3 Yield results

A measure of the tendency of the powder to become cold welded to the milling balls and vial wall is described by the yield. Yield is defined as follows:

$$Yield\ (\%) = \frac{\text{mass of powder obtained after milling}}{\text{initial mass of powder before milling}} \times 100 \qquad (6.1)$$

The yield data versus milling times are presented for the various Nb-Al (Figure 6.9), Nb-Al-Ge (Figure 6.10) and Nb-Ge (Figure 6.11) mixtures. The values are tabulated for each milling procedure.

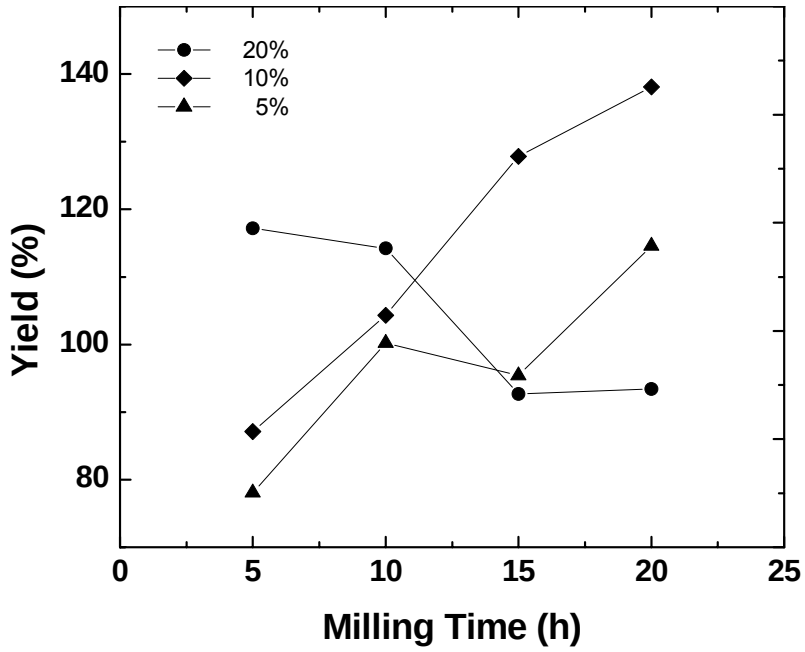

Figure 6.9 Yield data vs. milling time for wet milled Nb-Al mixtures.

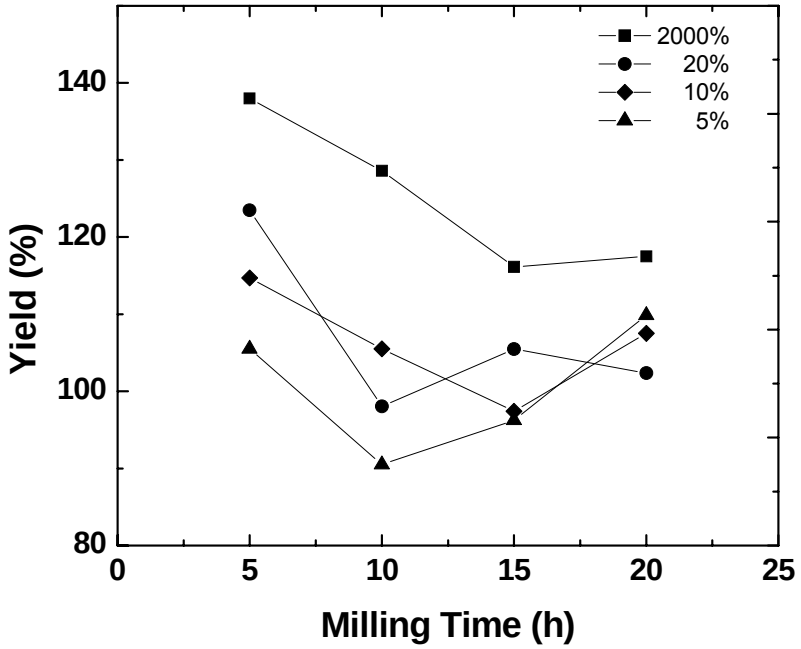

Figure 6.10 Yield data vs. milling time for wet milled Nb-Al-Ge mixtures [151].

M.T. (h)	PCA2000%		PCA20%		PCA10%		PCA5%	
	Yield (%)	BPR	Yield (%)	BPR	Yield (%)	BPR	Yield (%)	BPR
5	138	14	124	14	115	15	106	15
10	129	10	98	12	106	13	91	15
15	116	9	106	12	97	13	96	17
20	118	8	102	12	108	13	110	19

Table 6.8 Yield data and BPR ratio vs. milling time for wet milled Nb-Al-Ge mixtures.

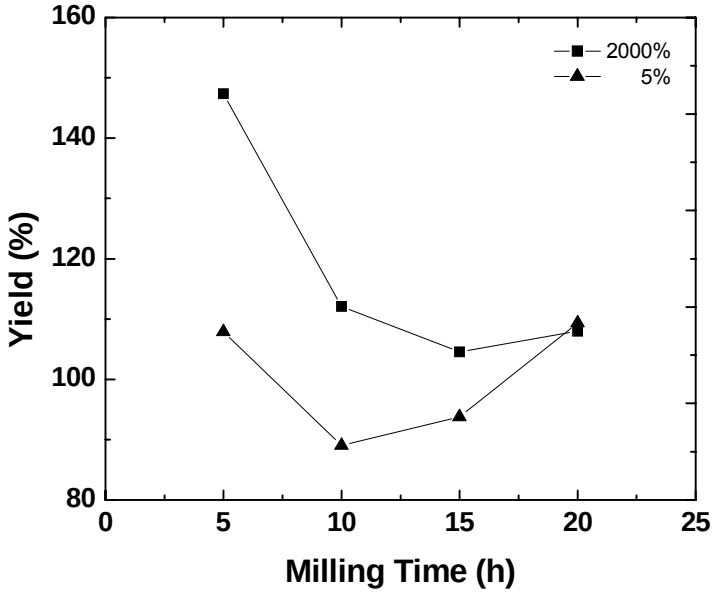

Figure 6.11 Yield data vs. milling time for wet milled Nb-Ge mixtures.

M.T. (h)	PCA2000%		PCA5%	
	Yield (%)	BPR	Yield (%)	BPR
5	147	14	108	15
10	112	10	89	14
15	105	9	99	17
20	108	9	109	19

Table 6.9 Yield data and BPR ratio vs. milling time for wet milled Nb-Ge mixtures.

It is important to record the mass variations of all components in order to have a complete picture of the system during milling. The powder-vial-balls group is a system that needs an accurate characterization by yield and BPR parameters. All plots and tables show that the wet milling process for Nb-based powder mixture produces a final yield of approximately 110%. The high yield is a result of the PCA trapped during mechanical alloying and contamination by copper from the milling tools. However, it is also consistent with the intention to prevent or at least reduce the cold welding during milling. In this work, the BPR value started at ~ 15:1. Low values such as 8:1 were shown only for the powder milled with the PCA2000%. We suggest that milling with high PCA content caused more Cu fragments to chip away from the surface of the milling balls and the pot.

6.3.4 X-ray diffraction

The XRD properties are presented for Nb-Al milled powders alone. The grain size was calculated for milled powders using the Scherrer formula and the Williamson-Hall plot.

Milled powders. The evolution and the main compositional phases for Nb-Al mechanically milled with PCA2000%, PCA20%, PCA10% and PCA5%, are in turn illustrated by Figure 6.12, Figure 6.13, Figure 6.14 and Figure 6.15. The variation of crystallite size with milling time is tabulated for each X-ray analysis. Figure 6.16 compares the grain size derived using the Hall-Williamson XRD analysis. In general, the wet milling procedure performed in this work broadened and shifted all crystalline peaks. In particular, the XRD data from wet powders milled with PCA10% (Figure 6.14) and PCA5% (Figure 6.15) show after 10 h milling a peak shift that is larger than that associated with powders milled with higher water content. The reader can follow these complex microstuctural changes produced via wet ball milling by taking into account the strongest $(Nb)_{ss}$ XRD peaks: (110) at ~ 40°, (211) at ~ 70°, and (321) at ~ 120 °. The fact that the majority of peaks did not disappear indicates that wet milled powders are far from being amorphous.

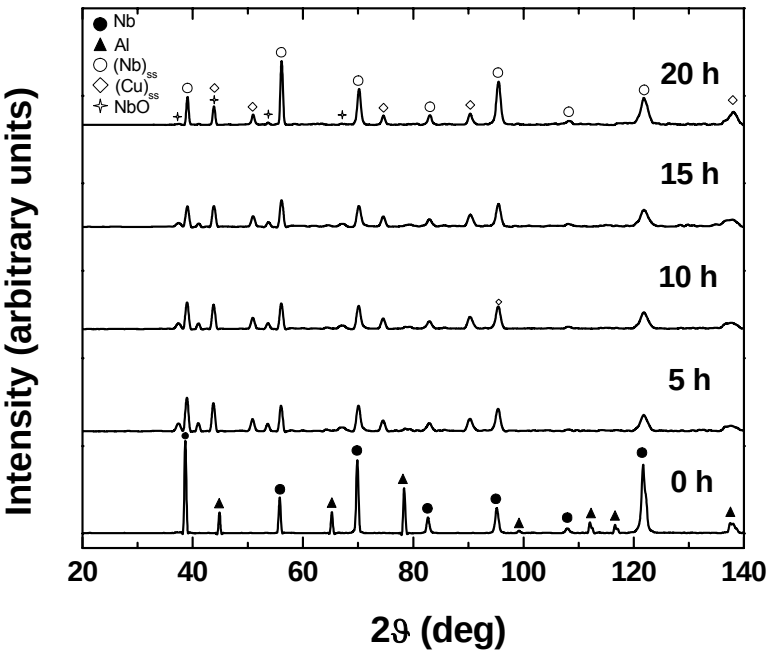

Figure 6.12 Evolution of XRD patterns of Nb-Al powder mechanically milled for up to 20 h with PCA2000%.

M.T. (h)	GS_S (nm)	W-H Linear fit	$GS_{W\text{-}H}$ (nm)	$\varepsilon_{W\text{-}H}$ (%)
5	7.86(2)	y = 0.02152x - 0.12394	8.07(3)	2.15(3)
10	4.70(2)	y = 0.01867x - 0.21108	4.74(3)	1.87(3)
15	3.38(2)	y = 0.016x - 0.31648	3.16(3)	1.60(3)
20	3.29(2)	y = 0.01953x - 0.30484	3.28(3)	1.95(3)

Table 6.10 Grain size (GS_S) evaluated using the Scherrer formula, average grain size ($GS_{W\text{-}H}$) and lattice strain ($\varepsilon_{W\text{-}H}$) calculated using and the Williamson-Hall method reported for Nb-Al powder mechanically milled for up to 20 h with PCA2000%.

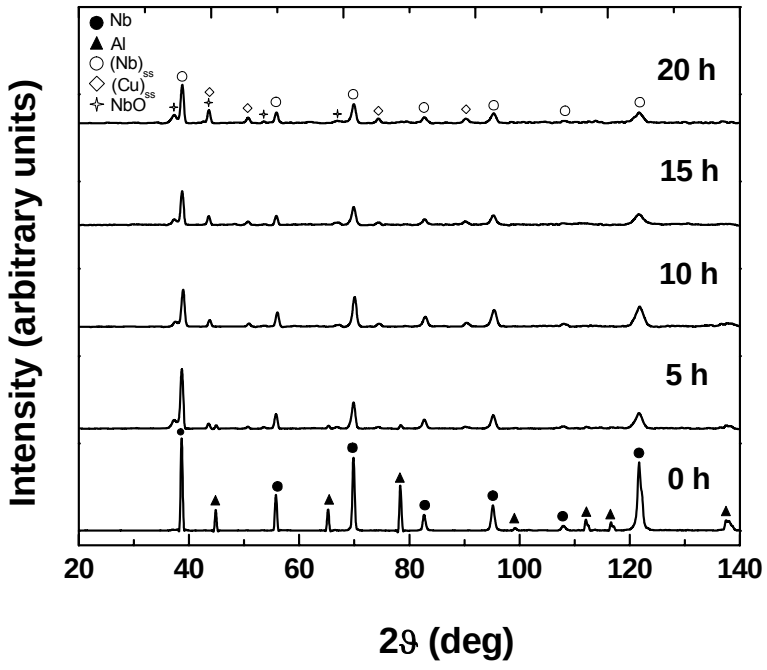

Figure 6.13 Evolution of XRD patterns of Nb-Al powder mechanically milled for up to 20 h with PCA20%.

M.T. (h)	GS_S **(nm)**	**W-H Linear fit**	$GS_{W\text{-}H}$ **(nm)**	$\varepsilon_{W\text{-}H}$ **(%)**
5	4.14(2)	y = 0.01997x - 0.23691	4.22(3)	1.98(3)
10	2.64(2)	y = 0.01396x - 0.38595	2.61(3)	1.40(3)
15	2.31(2)	y = 0.01537x - 0.43361	2.31(3)	1.50(3)
20	2.10(2)	y = 0.03434x - 0.45136	2.22(3)	3.43(3)

Table 6.11 Grain size (GS_S) evaluated using the Scherrer formula, average grain size ($GS_{W\text{-}H}$) and lattice strain ($\varepsilon_{W\text{-}H}$) calculated using and the Williamson-Hall method reported for Nb-Al powder mechanically milled for up to 20 h with PCA20%.

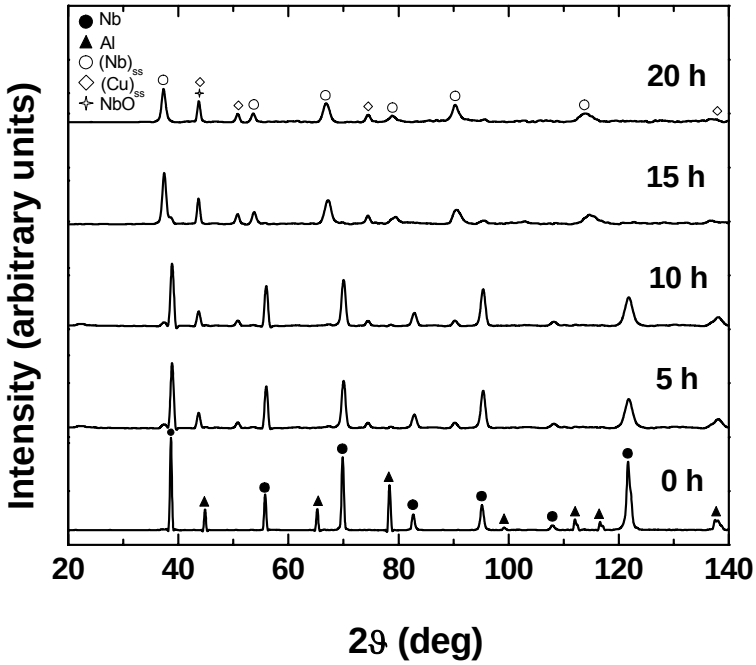

Figure 6.14 Evolution of XRD patterns of Nb-Al powder mechanically milled for up to 20 h with PCA10%.

M.T. (h)	GS_S (nm)	W-H Linear fit	$GS_{W\text{-}H}$ (nm)	$\varepsilon_{W\text{-}H}$ (%)
5	3.21(2)	y = 0.02531x - 0.28965	3.45(3)	2.53(3)
10	2.83(2)	y = 0.02093x - 0.3362	2.97(3)	2.09(3)
15	2.59(2)	y = 0.00172x - 0.38114	2.62(3)	1.72(3)
20	2.36(2)	y = 0.01542x - 0.37099	2.70(3)	1.54(3)

Table 6.12 Grain size (GS_S) evaluated using the Scherrer formula, average grain size ($GS_{W\text{-}H}$) and lattice strain ($\varepsilon_{W\text{-}H}$) calculated using and the Williamson-Hall method reported for Nb-Al powder mechanically milled for up to 20 h with PCA10%.

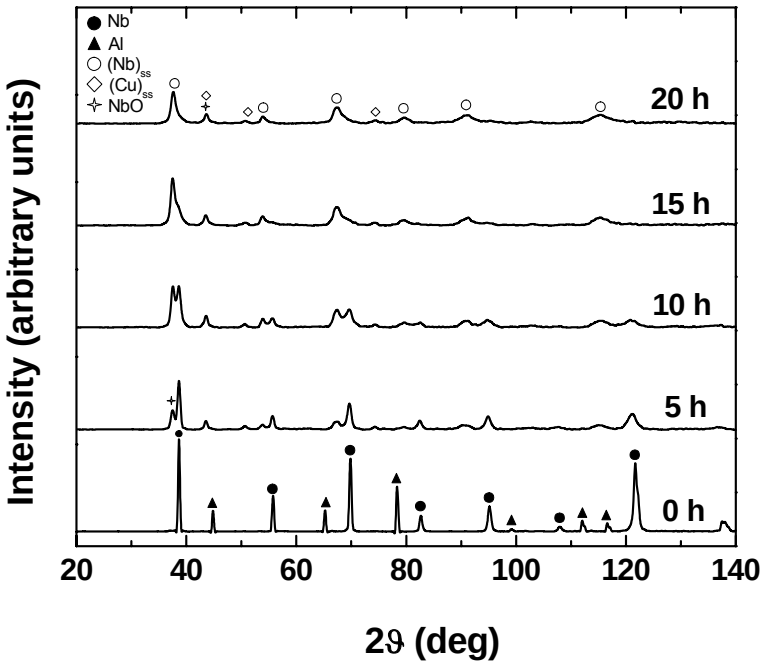

Figure 6.15 Evolution of XRD patterns of Nb-Al powder mechanically milled for up to 20 h with PCA5%.

M.T. (h)	GS_S (nm)	W-H Linear fit	$GS_{W\text{-}H}$ (nm)	$\varepsilon_{W\text{-}H}$ (%)
5	2.03(2)	y = 0.00848x – 0.48501	2.09(3)	0.08(3)
10	1.85(2)	y = 0.0213x - 0.60578	1.65(3)	0.21(3)
15	1.27(2)	y = 0.03215x + 0.74583	1.34(3)	0.32(3)
20	1.15(2)	y = 0.09984x - 0.94436	1.06(3)	0.99(3)

Table 6.13 Grain size (GS_S) evaluated using the Scherrer formula, average grain size ($GS_{W\text{-}H}$) and lattice strain ($\varepsilon_{W\text{-}H}$) calculated using and the Williamson-Hall method reported for Nb-Al powder mechanically milled for up to 20 h with PCA5%.

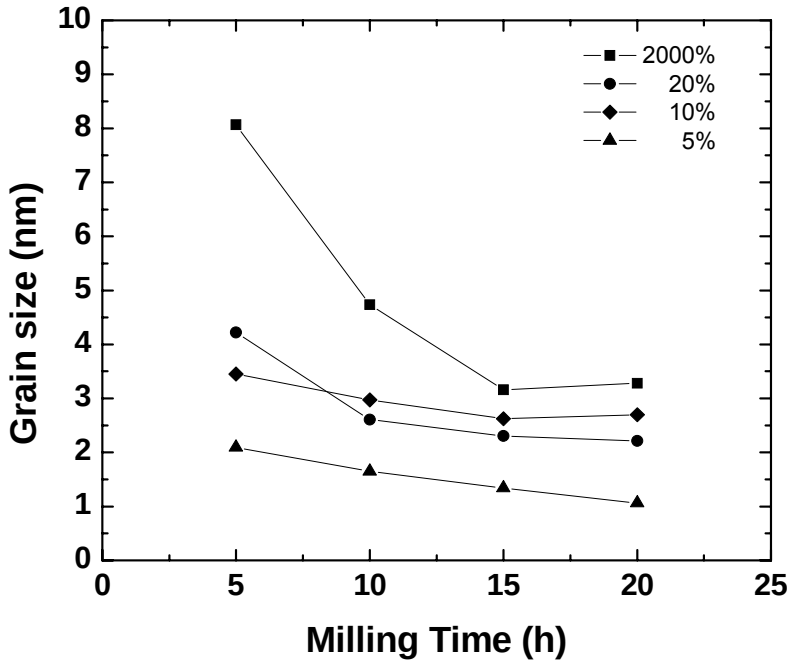

Figure 6.16 Variation of grain size of the wet milled Nb-Al mixture with milling time derived from the Hall-Williamson XRD analysis.

Grain sizes (*GS*) less than 8 nm were achieved after just 5 h, but milling for longer periods only decreases the *GS* slightly. Figure 6.16 shows that reducing the PCA content produces a systematic decrease of grain size. The minimum grain sizes were achieved in milled Nb-Al powder using PCA5% so we chose this PCA content for producing all HIP'ed samples.

6.3.5 Summary

The refinement of the grain size down to the nanometre level, simultaneous microstructural changes and high contamination level were investigated using different techniques. XRD patterns do show significant changes in term of FWHM and intensity, the DSC/TG properties indicate specific systematic changes eventually due to the nanocrystalline microstructure, compound formation, atomic ordering, and their concurrent interaction. Yield, XRD and ICP-AES indicated a large amount of contamination from copper and oxygen, which, as shown by next section, has prevailed over the A15 compound formation. These data on wet-milled powders lead us to HIP the PCA5% samples as discussed in the next section.

6.4 Properties of nanocrystalline bulk materials

The structural phases and grain sizes of nanocrystalline bulk samples were investigated using XRD on Nb-Al samples and presented in 6.4.1. The superconducting properties of all the three sets of starting powders were investigated using resistivity measurements and DC magnetometry are presented in subsection 6.4.2 and 6.4.3, respectively.

6.4.1 X-ray diffraction

The evolution of XRD patterns from HIP'ed Nb-Al bulk materials from wet milled and unmilled powders are illustrated in Figure 6.17 and Figure 6.18, respectively. Figure 6.19 and Table 6.14 show the grain size values from Rietveld analysis. These indicate a small *GS* growth of the HIP'ed wet milled powders up to 12 nm. The unmilled samples remain microcrystalline.

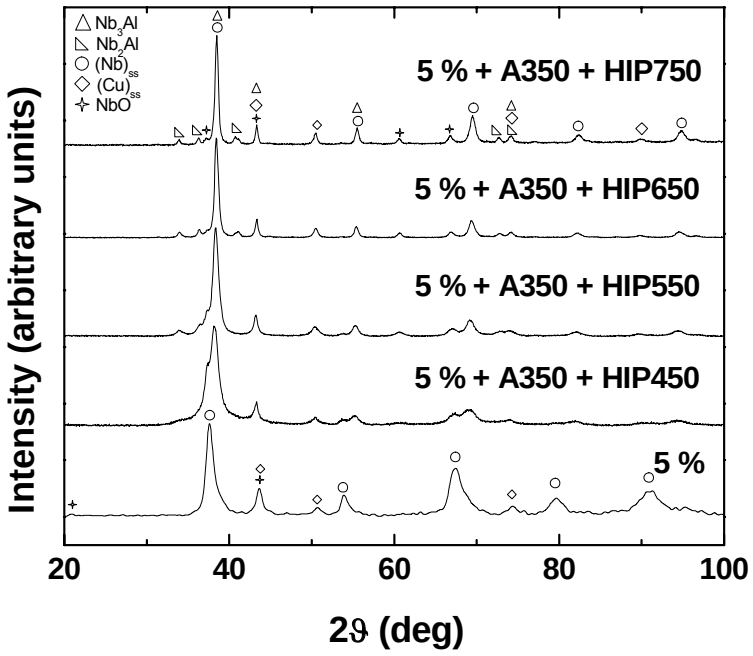

Figure 6.17 Evolution of XRD patterns for PCA5% Nb-Al bulk materials from wet milled powders subsequently annealed and HIP'ed at different temperatures. The main phases are labelled.

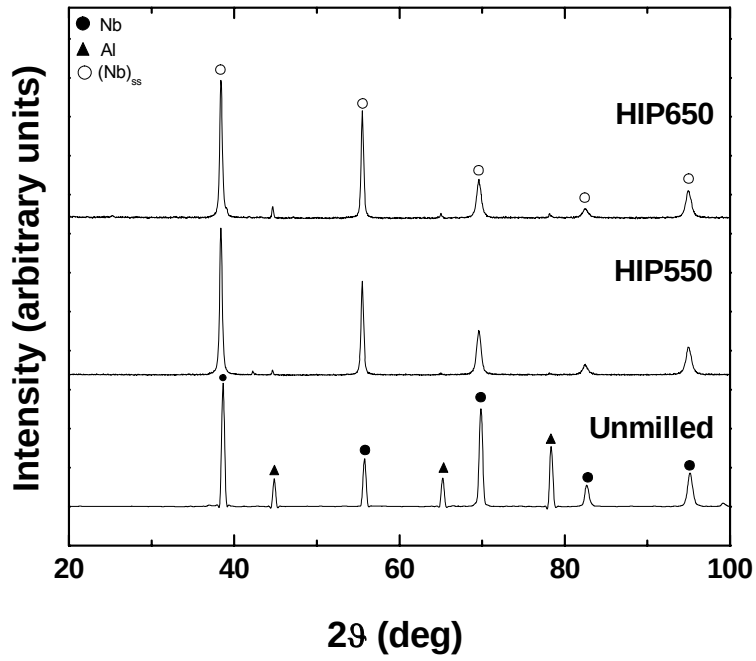

Figure 6.18 Evolution of XRD patterns of the unmilled Nb-Al powder and then HIP'ed at different temperatures.

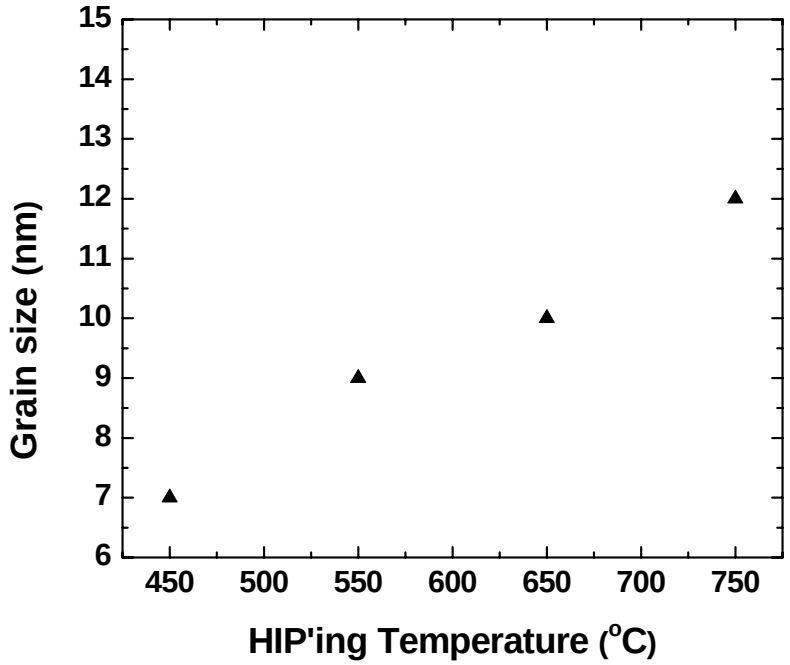

Figure 6.19 Rietveld refinement results for the crystallite size of the wet milled Nb-Al mixture against HIP'ing temperature.

Type	HIP'ing	D_R (nm)	ε_R (%)
Milled	450 °C × 5 h	7(6)	0.013(5)
	550 °C × 5 h	9(5)	0.012(3)
	650 °C × 5 h	10(4)	0.02(1)
	750 °C × 5 h	12(6)	0.021(6)
Unmilled	550 °C × 5 h	2600	-
	650 °C × 5 h	2950	-

Table 6.14 Grain size (D_R) and strain (ε_R) defined by the Rietveld Refinement for HIP'ed powder of the 20h milled Nb-Al with the 5% of PCA.

There are many overlapping XRD peaks for Nb_3Al phase and concurrent secondary phases, oxides. This makes clear identification of which materials are present difficult. Nevertheless the A15 compound has a strong peak close to 25° which is not observed, suggesting no superconducting material has been fabricated at these temperatures and pressures [151].

6.4.2 Resistivity

These section shows resistivity measurements at room temperature and at low temperature in high magnetic field. Transport measurements are relevant to probe the grains size/microstructural disorder in the normal state of a superconductor (see section 2.2). These measurements characterise the connectivity, the fraction, and distribution of the superconducting grains through the material. Indeed, a superior grain connectivity can produce a continuous path for the superconducting current and improved technical performance. The minimum fraction of the superconducting grains at which a continuous superconducting current can still pass across the sample is known as the percolation threshold [164]. Figure 6.20, Figure 6.21 and Figure 6.22 show resistivity values at room temperature respectively for Nb-Al, Nb-Al-Ge and Nb-Ge bars. A summary of the numerical values and relative HIP'ing temperatures are reported in Table 6.15. Resistive data as a function of temperature and applied field (H_a) are given for our best sample in Figure 6.23. For the experimental details, the reader is referred to section 5.6.

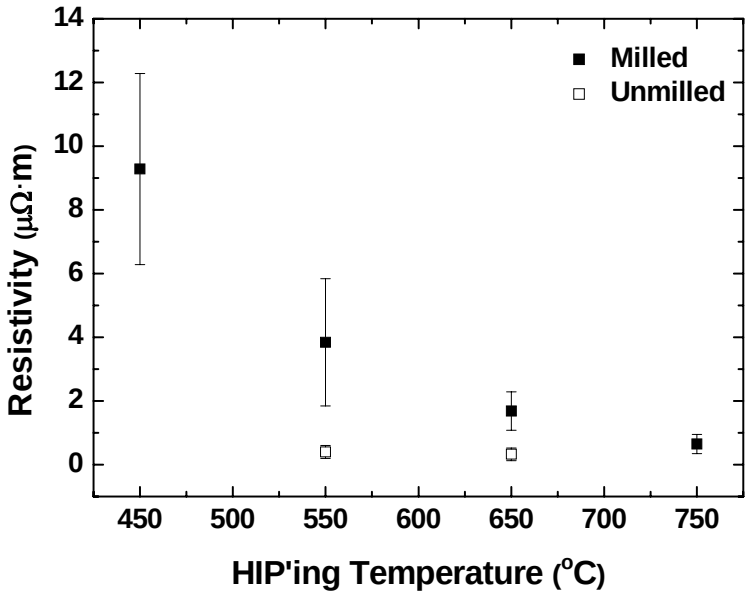

Figure 6.20 Resistivity at room temperature for unmilled and milled Nb-Al samples HIP'ed at different temperatures.

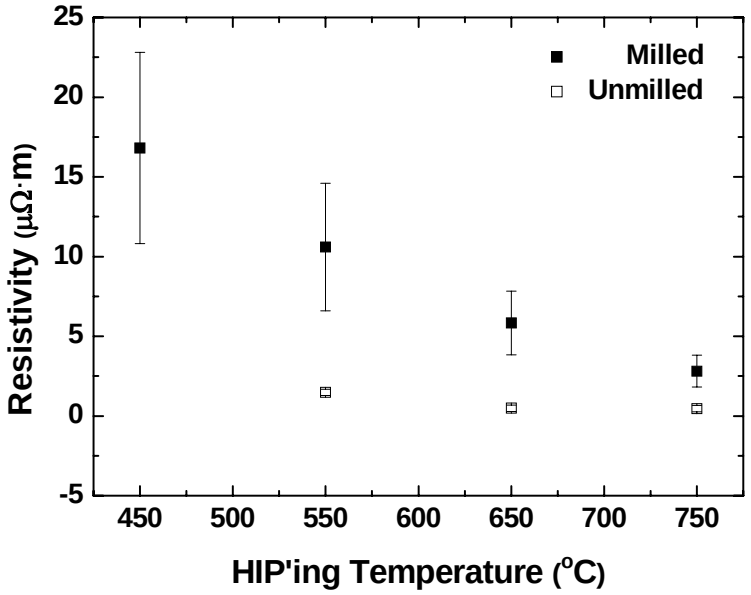

Figure 6.21 Resistivity at room temperature for unmilled and milled Nb-Al-Ge samples HIP'ed at different temperatures.

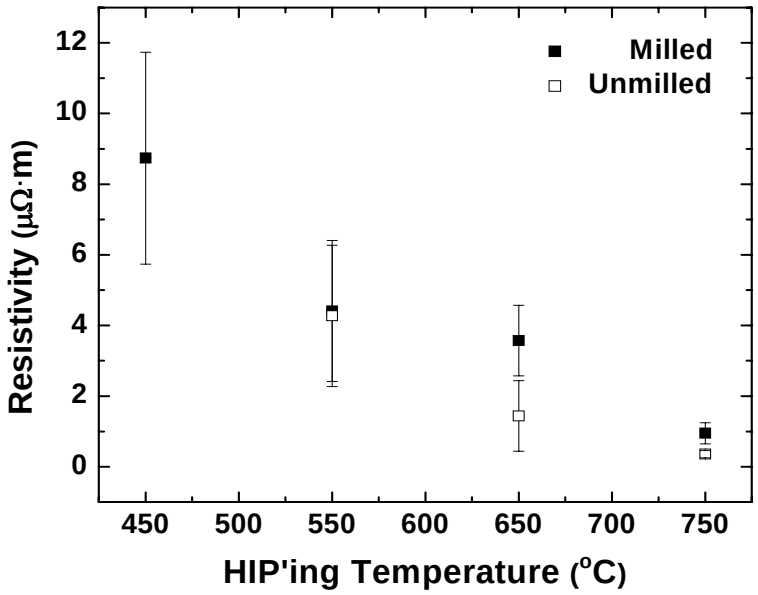

Figure 6.22 Resistivity at room temperature for unmilled and milled Nb-Ge samples HIP'ed at different temperatures.

Type	HIP'ing	ρ_{300K} (10^{-7} Ω·m)		
		Nb -Al	**Nb - Al - Ge**	**Nb - Ge**
Unmilled	750 °C × 5 h	-	4.58	3.58
Unmilled	650 °C × 5 h	3.26	4.80	14.4
Unmilled	550 °C × 5 h	3.98	14.8	57.2
Milled	750 °C × 5 h	6.44	28.1	9.46
Milled	650 °C × 5 h	16.8	58.3	35.7
Milled	550 °C × 5 h	38.4	106	44.1
Milled	450 °C × 5 h	92.8	168	87.4

Table 6.15 Resistivity at room temperature for Nb-Al, Nb-Al-Ge and Nb-Ge and corresponding HIP processing conditions [151].

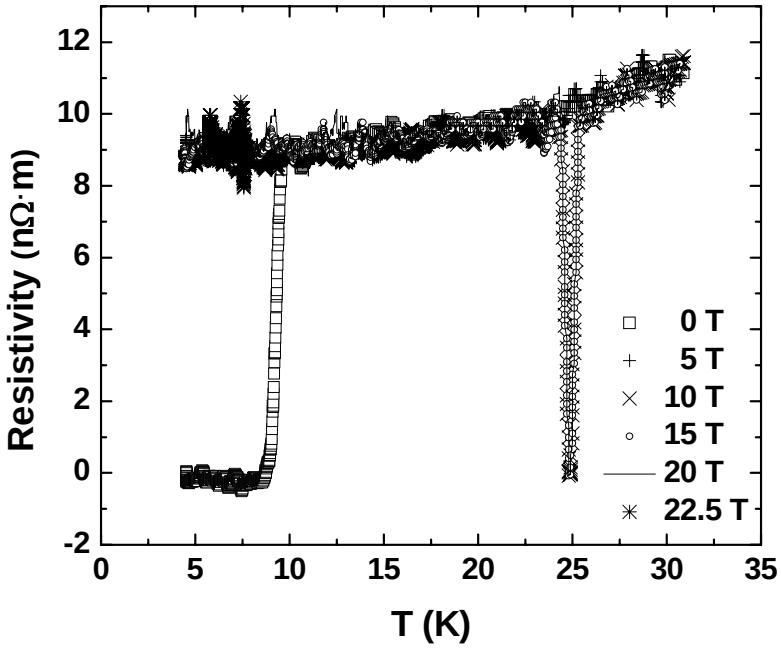

Figure 6.23 Resistive data of the milled Nb-Al sample HIP'ed at 750 °C as a function of T and H_a. The zero field data show the transition for pure Nb. The data for high fields are all offset from zero resistivity and all superimpose [151].

Consistent with the XRD data showing grain growth, Figure 6.20 to Figure 6.22 illustrate the resistivity of the milled samples at room temperature decreases as the HIP temperature increases. Normal state resistivity is higher in milled powder than in the as-received one. This can be explained in term of mean free path. In the case of milled powder, there is smaller grain size with the associated increase in the density of grain boundaries and defects, which reduces the mean free path. Figure 6.23 shows resistive data taken below 30 K in high magnetic fields in Grenoble. At about 8 K one can see the superconducting transition of Nb in zero field. The sharp peak at 25 K occurred when the current through the sample was switched off and demonstrates that the thermal offset voltages during these measurements were negligible. Unfortunately, these high field data show there is no evidence for superconductivity in these samples.

6.4.3 SQUID Magnetometry

SQUID measurements were performed on bulk materials to characterise the superconducting properties in stable magnetic fields at low temperature. In these measurements, the measured signal is produced by a superconducting screening surface rather than a preferential path for the superconducting current, as required by transport measurements. Zero field cooling (ZFC) and field cooling (FC) curves were acquired from 3 to 30 K in magnetic fields up to 9 T. The FC magnetisation curves are shown for unmilled and milled samples. Some of the typical data are shown below. Figure 6.24 and Figure 6.25 are for Nb-Al HIP'ed samples; Figure 6.26 and Figure 6.27 are Nb-Al-Ge and Nb-Ge unmilled mixtures.

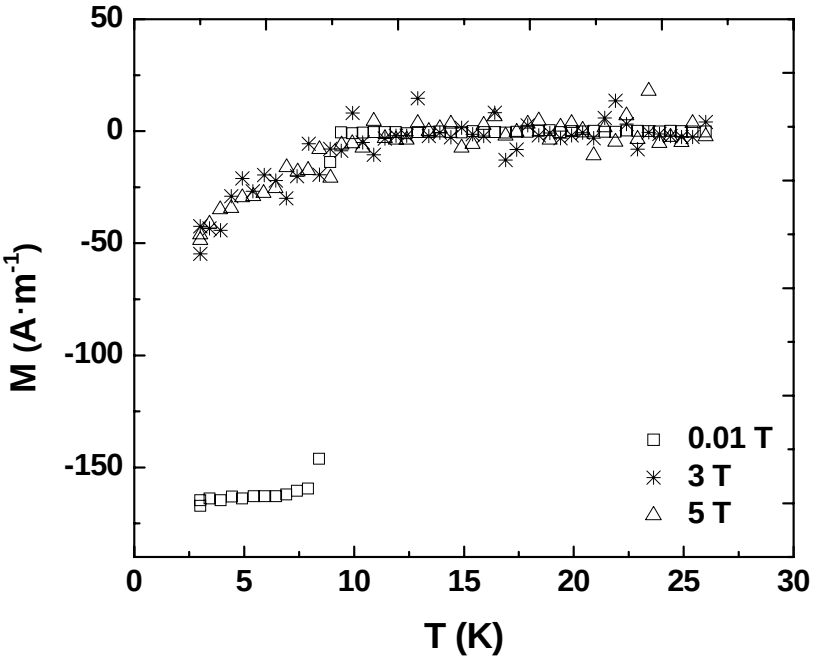

Figure 6.24 FC magnetic moment curves, without background, against temperature for the unmilled Nb-Al sample HIP'ed at 650 °C (0.4 × 0.5 × 0.6 mm, 0.12 mm^3); the first dimension is aligned parallel to the magnetic field.

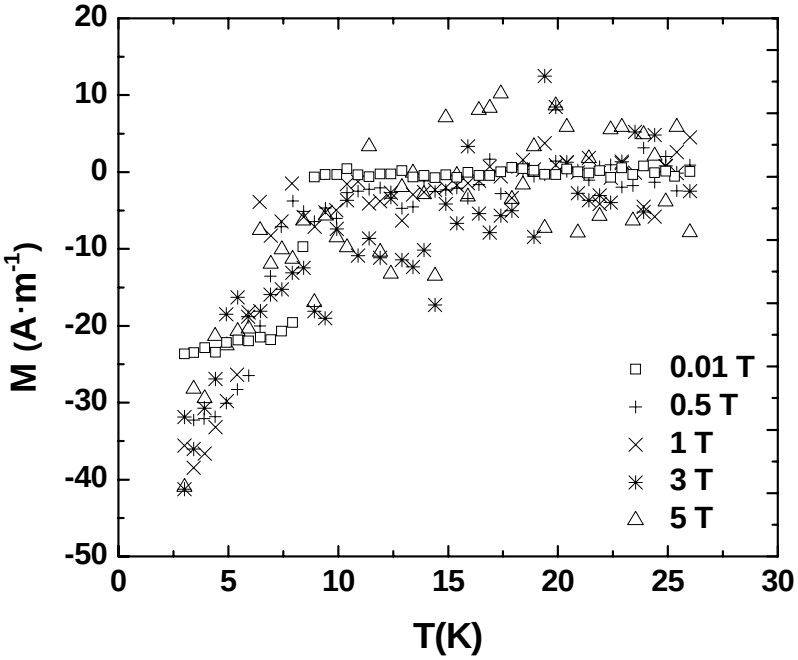

Figure 6.25 FC magnetic moment curves, without background, against temperature for the milled Nb-Al sample HIP'ed at 750 °C (0.4 × 0.4 × 0.4 mm, 0.064 mm^3); the first dimension is aligned parallel to the magnetic field.

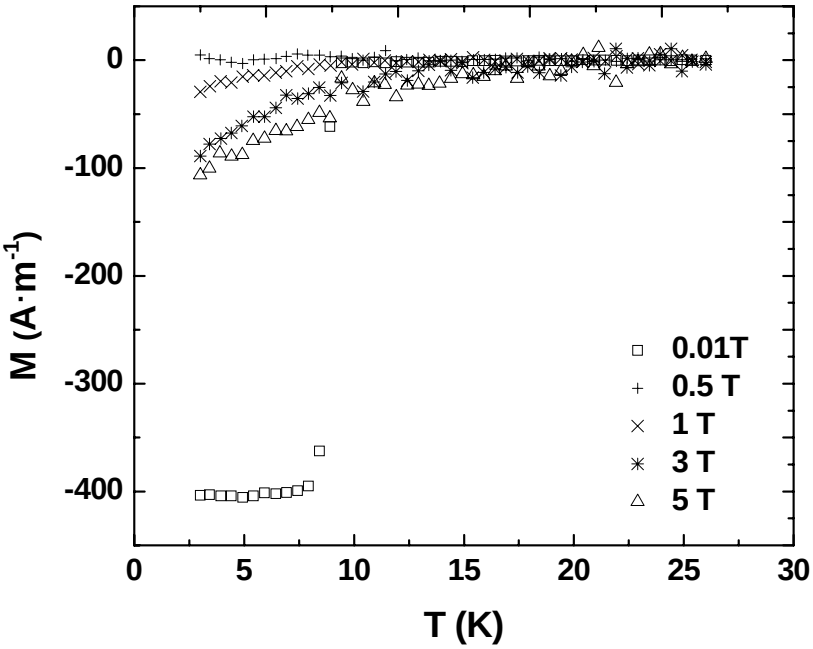

Figure 6.26 FC magnetic moment curves, without background, against temperature for the unmilled Nb-Al-Ge sample HIP'ed at 750 ^{o}C (0.4 × 0.5 × 0.5 mm, 0.10 mm^3); the first dimension is aligned parallel to the magnetic field.

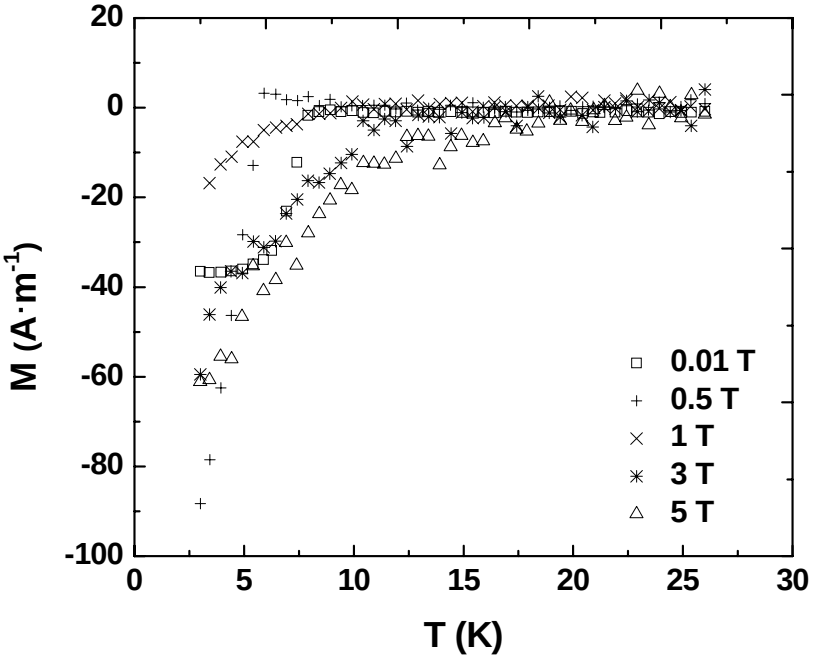

Figure 6.27 FC magnetic moment curves, without background, against temperature for the unmilled Nb-Ge sample HIP'ed at 750 ^{o}C (0.5 × 0.7×0.4 mm, 0.14 mm^3) ; the first dimension is aligned parallel to the magnetic field.

In general, unmilled samples show the superconducting response of Nb whereas the milled samples produce no signal beyond the noise of the experiment and uncertainties associated with the temperature dependent background. Unfortunately, there was no evidence in any of the SQUID measurements for superconducting material with the A15 structure [151].

6.4.4 Discussion

The microstructure and superconducting properties of wet milled bulk materials were investigated using X-ray diffraction, resistivity measurements and SQUID magnetometry. These data confirm that no superconducting properties due to the A15 compounds were found. Nevertheless this, the decrease of normal state resistivity and the simultaneous increase of grain size indicate that this fabrication process based on milling and subsequent HIP'ing has the potential to produce superconducting samples with properties relevant to understand superconductivity at nanometre level. Furthermore, this research on materials fabricated using PCA in air shows that the high reactivity of precursor materials (i.e. Al) eliminated the ability to fabricate nanocrystalline A15 materials.

6.5 Conclusion

SQUID, resistive and ac. susceptibility data confirm that no A-15 material has been formed in the Nb-Al, Nb-Al-Ge and Nb-Ge materials fabricated in this work. Different experimental techniques have allowed a thorough investigation of whether any trace nanocrystalline A15 materials were made but none were detected. The high milling media contamination shown by ICP-AES might also contribute to limiting the Nb_3X layer formation. The air in the milling process probably also affected the final materials. The likely development of oxides such as Al-O, Ge-O, Nb-O may also have reduced A15 formation. Certainly, these sources of contamination are important. We had expected that even if the samples fabricated were multiphase, we could have identified the potential of nanocrystalline $Nb_3(Al_{1-x}Ge_x)$ superconductors from the presence of small amounts of material. However, the contrast between the formation of A15 material when dry milling Nb-Al mixtures [12,87,91] and the results presented here for HIP'ed wet milled material is very stark indeed. It is very probable that no A15 material was produced during wet milling because the PCA both stopped the powders welding to

the milling media and passivated the clean metallic surfaces produced during milling - preventing formation of A15 compound. The STA measurements suggest that PCA was trapped inside the metallic powder. Although most of the PCA was removed prior to HIP'ing, we suggest that the PCA is nevertheless incorporated throughout the bulk of the milled powders during milling. This widespread contamination by the PCA prevented A15 material from being produced during HIP'ing. This study confirms that using a PCA with milling does lead to high yields and provides a fast method to decrease the grain size of the materials. However, in the context of fabricating superconductors in which inhomogeneities and second phase material on the scale of the coherence length can destroy the superconductivity, we conclude that fabricating nanocrystalline superconductors is best done in an inert environment and that using distilled water as a PCA during milling A15 compounds is not to be recommended [151].

Chapter 7

Fabrication and properties of nanocrystalline Nb_3Ge produced using dry mechanical alloying with elemental powders

7.1 Introduction

In this chapter, we report on the fabrication of A15 nanocrystalline Nb_3Ge produced by introducing disorder via high-energy ball milling (HEBM) and successively by compaction techniques involving HIP'ing and/or annealing [20]. This technique has produced Nb_3Ge (A15) in bulk form with record T_C and $B_{C2}(0)$ values of ~ 12 K and ~ 13 T, respectively. The chapter focuses on the superconducting properties, composition and microstructure (i.e. grain size, crystallisation) of disordered nanocrystalline A15 Nb_3Ge bulk materials for high magnetic field applications. In section 7.2, an overview of the fabrication processes for all the materials is outlined – the powders produced using milling and the bulk materials produced using HIP'ing and annealing. A comprehensive description of all the structural and superconducting data for milled powders and nanocrystalline bulk materials are reported in section 7.3 and section 7.4, respectively. The comprehensive data include: yield data associated with milling; ICP-MS; differential scanning calorimetry; scanning electron microscopy (SEM) coupled with electron dispersive X-ray (EDX) analysis for Nb_3Ge samples processed using the HIP'ing; ACMS (alternating current measurement system); and XRD to investigate grain size and composition. Finally, section 7.4.4 reports a summary of the data and the conclusions. This work is to be submitted to Applied Physics Letters [165].

7.2 Overview of fabrication of powders and bulk samples

Disordered nanocrystalline powders were produced from elemental powders using dry milling. The various procedures carried out to mill and compact the powder are now presented. For details about the experimental techniques and the starting elemental powders, the reader is referred to Chapter 5 and 6, respectively.

Dry milled powder. A SPEX 8000D mixer/mill was used to grind up a 5 g stoichiometric mix of elemental powders. Specially-designed OFHC copper vials were sealed securely inside the glove box and subsequently placed in the ball mill. The milling was performed under an inert gas atmosphere (argon) at room temperature. A ball-to-powder ratio of 4:1 was chosen. Five balls of 10 mm diameter were used. The operations prior to milling, such as vial and balls coating, and also dislodging the powders from the inner walls and lid of the vial (which was done every 1 h throughout the grinding process) were done inside a glove-box full of argon with an oxygen level less than 10 ppm. A dedicated niobium rod was always used to dislodge the powders. A series of samples milled for 0, 2.5, 5, 10, 15, 20 and 30 h were produced. A short milling time produced a single-phase bcc solid solution of Nb + Ge and was confirmed using XRD for samples milled for ~ 5 - 10 h. These results suggested a convenient milling time of 6 h. Mechanical alloyed powders milled for 6 (bcc) and 20 h (amorphous) were then processed using a hot isostatic press (HIP).

Dry milled powder processed with HIP. Mechanically alloyed powders milled for up to 6 h (bcc) and 20 h (amorphous) were then processed using a hot isostatic press (HIP) operating at 0.2GPa in a temperature range from 600 ^{o}C to 1200 ^{o}C to produce superconducting A15 nanocrystalline bulk materials.

Annealing of HIP'ed samples. The hot isostatic pressed dry milled powders were subsequently given an isochronal heat treatment for 18 h at the following temperatures 600, 700, 800 and 900 ^{o}C. The role of post-HIP heat treatments was investigated for those materials HIP'ed at 600 and 1200 ^{o}C. For comparison purposes, identical heat treatments were also performed on (non-HIP'ed) milled powders. A home-made titanium alloy (Ti-6Al-4V) tube was used to perform the heat treatment on HIP'ed samples and pellets from milled powders (i.e. not-HIP'ed) in high purity argon. Inside the glove box, small pieces of nanocrystalline bulk materials samples were inserted into Nb foil containers. The niobium foil was used as a protective shield between samples and the alumina container.

Nomenclature. The large number of samples presented in this thesis are described using the following nomenclature for processing conditions: MX + HIPYYY + AZZZ where X, YYY and ZZZ indicates the milling times in hours, the HIP'ing temperature (the HIP time was fixed at 5 h) and the annealing temperature (the annealing time was always 18h) in ^{o}C, respectively. This chapter considers the 32 bulk samples that were

milled either for 6 h (series M6) or 20 h (series M20) and processed using the conditions shown in Table 7.1.

No.	Processing condition	Group ID
1	HIP 600 ^{o}C × 5 h	M6 or M20 + HIPYYY
2	HIP 700 ^{o}C × 5 h	
3	HIP 800 ^{o}C × 5 h	
4	HIP 1200 ^{o}C × 5 h	
5	HIP 600 ^{o}C × 5 h + 600 ^{o}C × 18 h	M6 or M20 + HIP600 + AZZZ
6	HIP 600 ^{o}C × 5 h + 700 ^{o}C × 18 h	
7	HIP 600 ^{o}C × 5 h + 800 ^{o}C × 18 h	
8	HIP 600 ^{o}C × 5 h + 900 ^{o}C × 18 h	
9	HIP 1200 ^{o}C × 5 h + 600 ^{o}C × 18 h	M6 or M20 + HIP1200 + AZZZ
10	HIP 1200 ^{o}C × 5 h + 700 ^{o}C × 18 h	
11	HIP 1200 ^{o}C × 5 h + 800 ^{o}C × 18 h	
12	HIP 1200 ^{o}C × 5 h + 900 ^{o}C × 18 h	
13	600 ^{o}C × 18 h	M6 or M20 + AZZZ
14	700 ^{o}C × 18 h	
15	800 ^{o}C × 18 h	
16	900 ^{o}C × 18 h	

Table 7.1 Sample and processing condition ID for Nb-Ge bulk materials based on heat treatment and fabrication method.

7.3 Properties of milled powders

The Nb-Ge powder changes that occurred during high-energy ball milling were investigated by the differential scanning calorimetry, yield, AC magnetometry and XRD results. Each set of results will be described in turn. Finally, the properties of milled powders are discussed in section 7.3.6.

7.3.1 Differential scanning calorimetry

The differential scanning calorimetry measurements were taken on powders milled for up to 30 h. The differential scanning calorimetry data are shown in Figure 7.1, Figure 7.2 and Table 7.2.

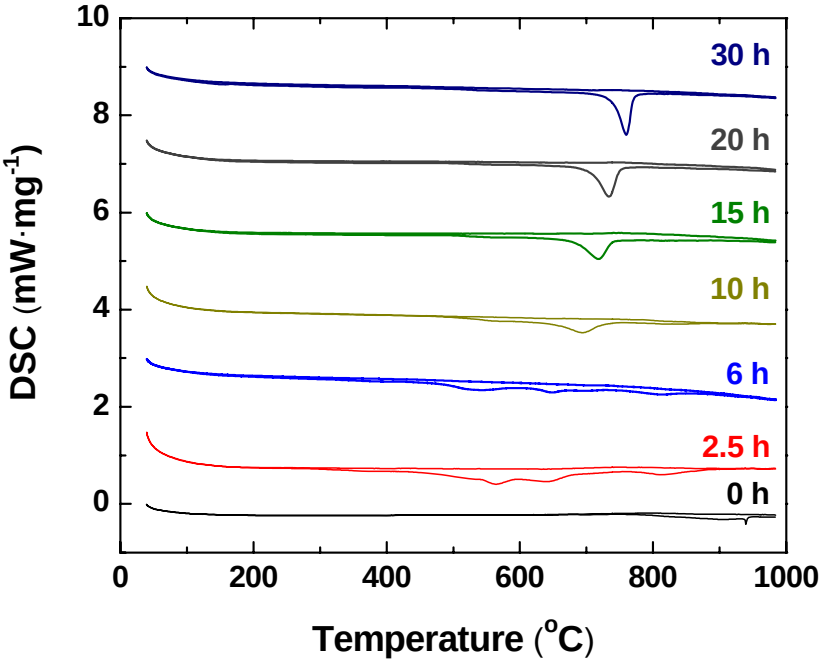

Figure 7.1 DSC traces for Nb-Ge milled for up to 30 h. The data shown for milled powders have been sequentially offset by 1.5 $mW \cdot mg^{-1}$ from the 0 h data for clarity. The two sets of data provided for each milled sample were both obtained while increasing temperature during the first half of two successive cycles obtained at a heating rate of 10 $K \cdot min^{-1}$.

M.T. (h)	T_a (°C)	ΔH_a ($J \cdot g^{-1}$)	T_x (°C)	ΔH_x ($J \cdot g^{-1}$)	T_x (°C)	ΔH_x ($J \cdot g^{-1}$)	T_x (°C)	ΔH_x ($J \cdot g^{-1}$)
2.5	564.5	-16	639.4	-26	-	-	813.8	-28
5	542.0	-40	643.2	-2	704.4	-2	804.1	-13
6	542.0	-38	647.3	-9	703.8	-2	809.2	-13
10	559.5	-5	695.2	-71	-	-	-	-
15	559.8	-3	718.0	-90	-	-	-	-
20	565.4	-1	733.9	-111	-	-	-	-
30	541.5	-3	759.8	-114	-	-	-	-

Table 7.2 Temperature and enthalpy of reaction for amorphisation (T_a, ΔH_a) and crystallisation (T_x, ΔH_x) versus milling times for Nb-Ge milled up 30 h. The error on the enthalpy is ± 3 %.

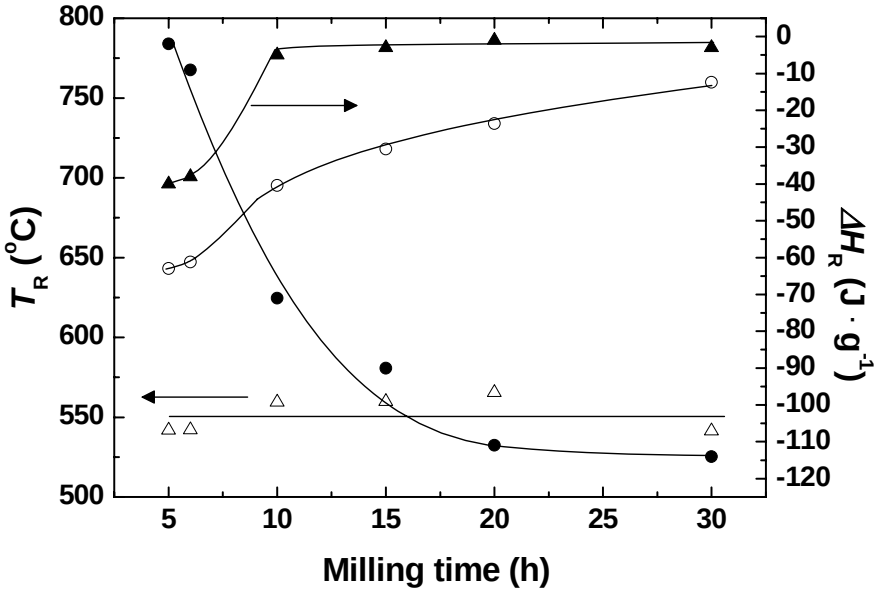

Figure 7.2 Temperature (empty symbols) and enthalpy of reaction (full symbols) for the amorphisation (triangle) and the lowest temperature crystallisation (circle) peaks versus milling times for Nb-Ge milled up 30 h.

Figure 7.1 shows two traces corresponding to each of two consecutive heating runs for the same powder sample. The upper traces (from the second heating run) provide a baseline for the reactions that take place during the first heating run. All samples in Figure 7.1 show exothermic reactions. The DSC data consists of two types of peaks T_a and T_x – the lower temperature peak is an amorphisation peak and the higher temperature peak is a crystallisation peak (cf chapter 4). We follow a similar explanation to that provided by Schwartz's et al. [135]: (i) the lower temperature peak is an amorphisation peak produced by amorphisation at the Nb/Ge interfaces whose rate of formation decreases throughout milling; (ii) the crystallisation peak is produced by the crystallisation of the amorphous Nb-Ge alloy whose rate of formation increases during milling. The area between each pair of traces defines the reaction enthalpy. The temperature and enthalpy of reaction has been calculated for each peak and is shown in Figure 7.2. Initially at 2.5 h milling, there are three peaks at 540, 650 and 800 ^{o}C. For longer milling times (< 10 h) there are four peaks that appear at temperatures of about 540, 650, 700 and 800 ^{o}C. DSC peaks at 540 ^{o}C and 650 ^{o}C can be reasonably attributed to the formation of an amorphous alloy from amorphous elemental powders and to the A15 crystallisation, respectively. There is similar behaviour to that observed by Schwarz where there is an overall increase in the absolute value of the enthalpy and temperature for the crystallisation peak whereas in contrast, for the amorphisation peak the magnitude of the enthalpy decreases and the temperature is reasonably constant.

Considering our X-ray results on milled powders (Figure 7.6), we can reasonably suggest that the peaks at higher temperatures (700 ^{o}C and 800 ^{o}C) are due to the crystallisation of a Ge-rich solid solution, $(Ge)_{ss}$, and a Nb-rich solid solution, $(Nb)_{ss}$, respectively. After 2.5 h milling that the DSC peak at 700 ^{o}C is missing possibly indicating that only a small amount of $(Ge)_{ss}$ has been alloyed compared to that achieved at higher milling times. The disappearance of the crystallisation peaks at 700 ^{o}C and 800 ^{o}C beyond 10 h milling indicates that the milling has basically consumed the elemental powders to form an amorphous alloy. This interpretation for milling times greater than 10 h is consistent with XRD data considered below.

7.3.2 ICM-MS results

These measurements were performed by Dr. Ottley (Earth Science department, Durham University) on powders dry milled for up to 20 and 30 h.

M.T. (h)	Cu (at. %)
20	0.8 ± 0.1
30	2.1 ± 0.1

Table 7.3 ICP-MS results for Nb-Ge powder mixture ball milled for up to 20 and 30 h.

Copper has two stable isotopes, ^{63}Cu and ^{65}Cu, and numerous radioisotopes. Isotopes ^{63}Cu and ^{65}Cu were measured. The estimate for the total copper concentration is given by the sum of the concentration of the detected isotopes. Therefore, the uncertainty of the sum is given by the sum of the uncertainties in ^{63}Cu and ^{65}Cu [168]. The error for each reading was nominally ± 0.05 at. %. Some measurements were repeated and found to be reproducible, which ensured the data were representative of our inhomogeneous materials. Unlike the atomic emission spectroscopy (ICP-AES) of chapter 6, we think that the mass spectroscopy values (ICP-MS) shown in Table 7.3 do not correctly represent the copper contamination because they are in disagreement both with the XRD data and electron microscopy data. Indeed, the appearance of the Cu peaks in the XRD data at 30 h milling is not explained if the Cu amount is only 2 at.%. This value is below the XRD detection limit. A consistent estimation of the Cu content is presented below using only yield (section 7.3.3) and SEM (section 7.4.2) data.

7.3.3 Yield results

The yield was calculated as shown in section 6.4. The yield was measured after repeated 5 h ball milling periods and is reported in Figure 7.3. The yield was found to increase during milling. The value of yield below 100 % at 5 h means that initially, some powder welding took place. For further milling times, the yield slightly increases and eventually increases above 100 %. These data suggest that during dry milling the contamination from the copper milling tools is ~ 7 %.

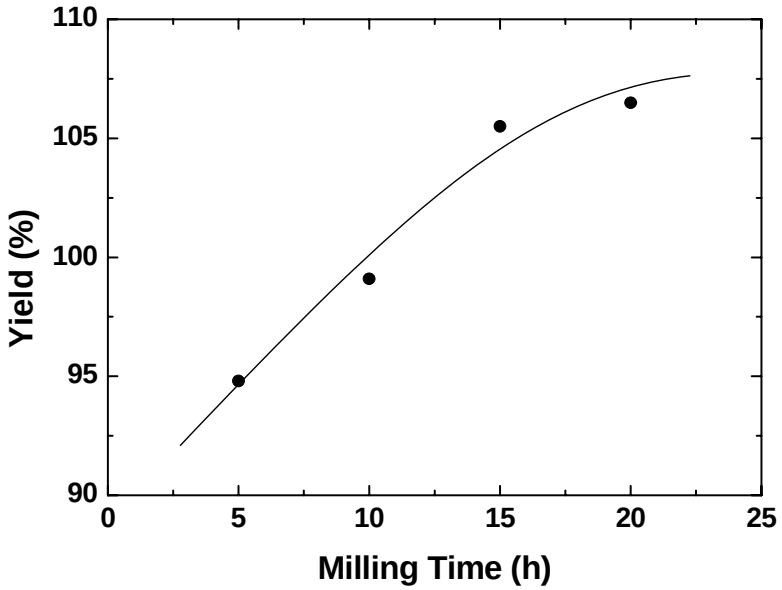

Figure 7.3 Average yield of Nb-Ge powders milled up to 20 h. The line is a guide to the eye.

7.3.4 AC magnetometry

The atomic disorder created by high-energy ball milling was investigated by zero field AC magnetometry in the temperature range 20 - 3 K. These measurements were performed on ~ 10 mg pellets of similar shape and dimensions (~ 3 mm diameter, ~ 0.5 mm thickness). Figure 7.4 shows the zero field AC magnetometry curves and Figure 7.5 the extracted value of the magnetization at 4.2 K.

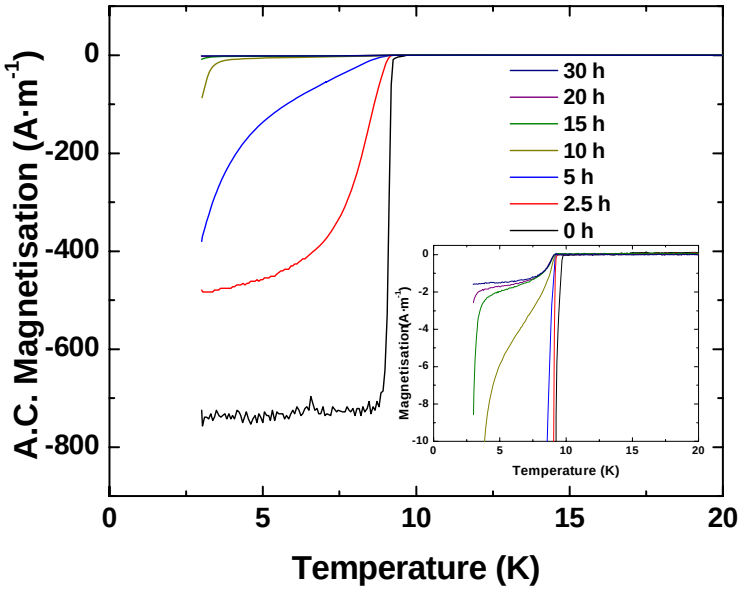

Figure 7.4 Zero field AC magnetometry curves for Nb-Ge milled up to 30 h.

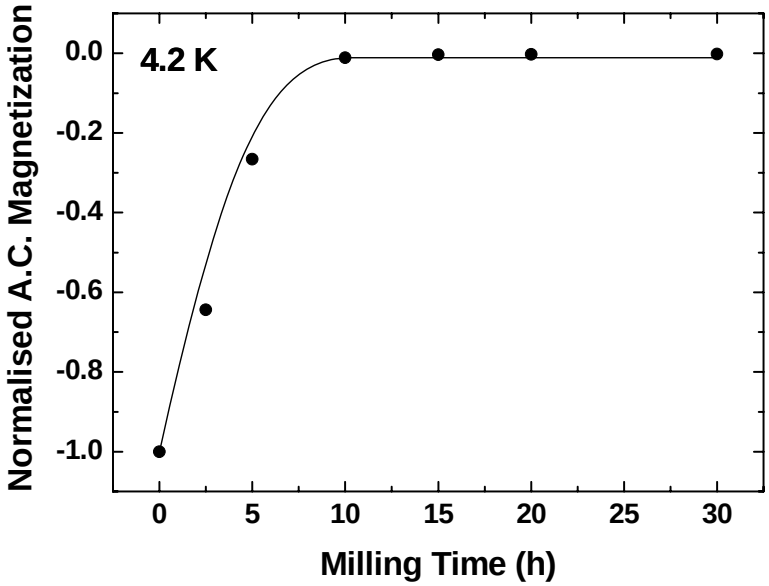

Figure 7.5 Normalised zero field AC magnetization for Nb-Ge milled for up to 30 h at 4.2 K.

Description and explanation of AC magnetometry results. Figure 7.4 shows the superconductivity transition of Nb-Ge powders during milling. The onset transition temperature was found to be approximately 9 K because of the elemental niobium. Thereafter the large signal transition was reduced to less than 5 K. This means that the fraction of the superconducting volume (screening effect) decreases continuously through the milling and is highlighted by Figure 7.5 which shows the normalised AC magnetization moment at 4.2 K against milling time [169]. However, very sensitive measurements show a general feature of the work in this thesis. Namely milled powders

produced by mechanical alloying and mechanical milling show a similar behaviour both in terms of onset temperature and in terms of saturation magnetisation (the reader is referred to section 8.3.4) - in particular there is always a very small signal with an onset temperature of 9 K. This suggests that even during protracted ball milling there are always some remnant nanocrystalline Nb grains, which provide some screening. Double superconducting transitions at ~ 9 K and ~ 5 K were often observed for powders MA'ed for 10, 15 and 20 h. We suggest that if Nb-Ge milling had been carried out using materials harder than copper, such as niobium [30] or hardened steel [134] this may eliminate the remnants of nanocrystalline Nb.

7.3.5 X-ray diffraction

The structural changes of Nb-Ge ball milled powders were investigated by X-ray diffraction. Figure 7.6 shows the XRD evolution of Nb-Ge milled powders. Figure 7.7 provides the grain size and the variation of the lattice parameters versus milling time. Figure 7.8 shows the lattice changes of the Nb and Ge. Table 7.4 gives numerical value for the structural changes involved during high-energy ball milling (Figure 7.7).

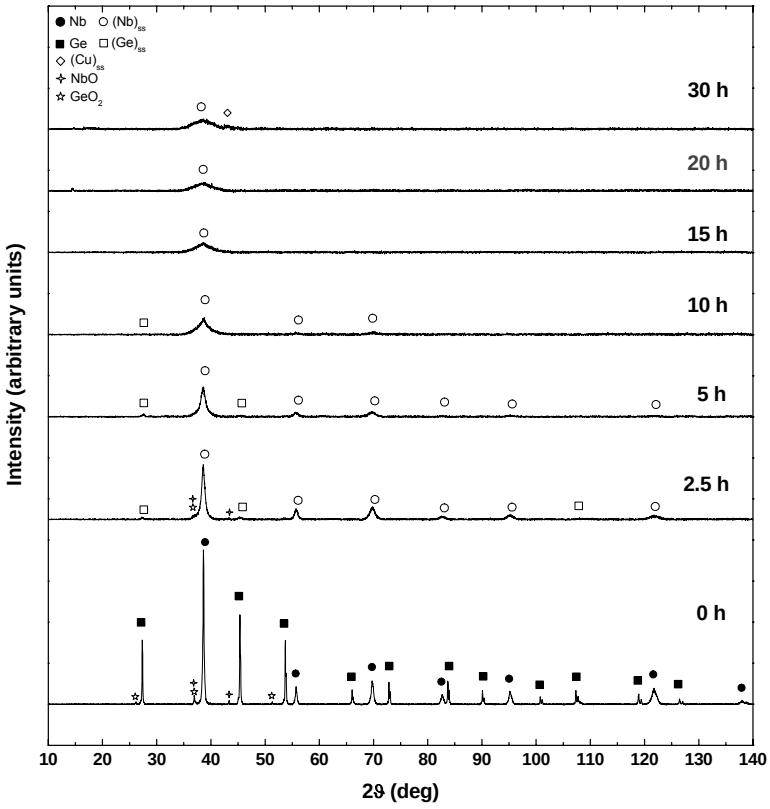

Figure 7.6 XRD evolution for Nb-Ge milled powders. The dominant phases Nb and Ge have the bcc and fcc (diamond) structure, respectively.

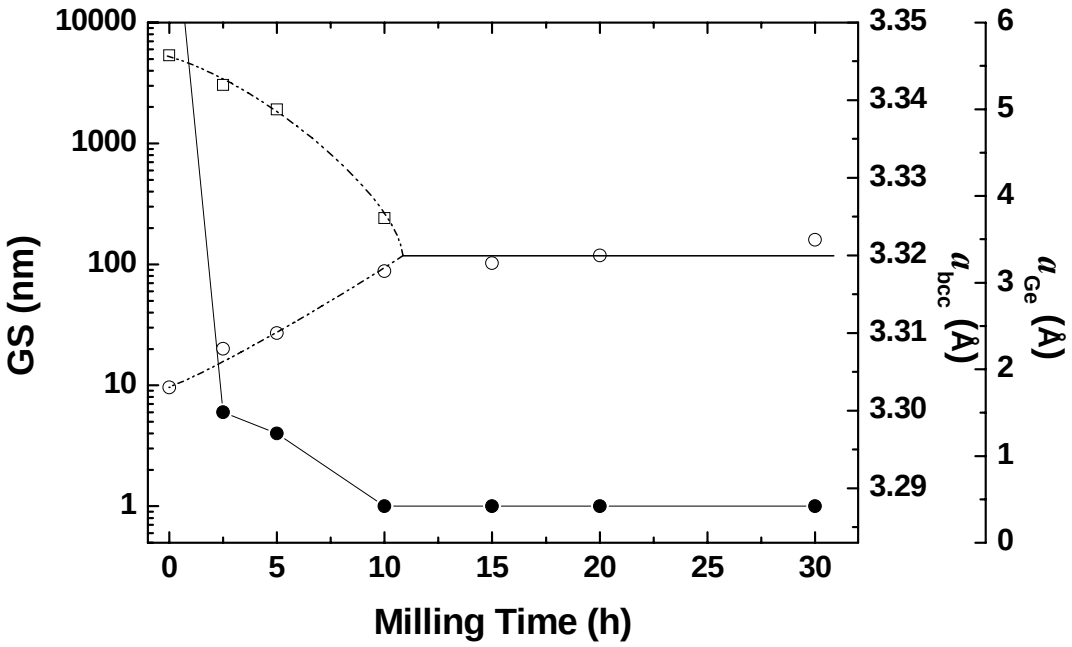

Figure 7.7 Variation of the grain size (circle) and lattice parameters of the Nb-bcc (triangle) and Ge-fcc (circle) powders during milling. The solid solution at the equilibrium is represented by a continuous line starting at ~ 11 h milling.

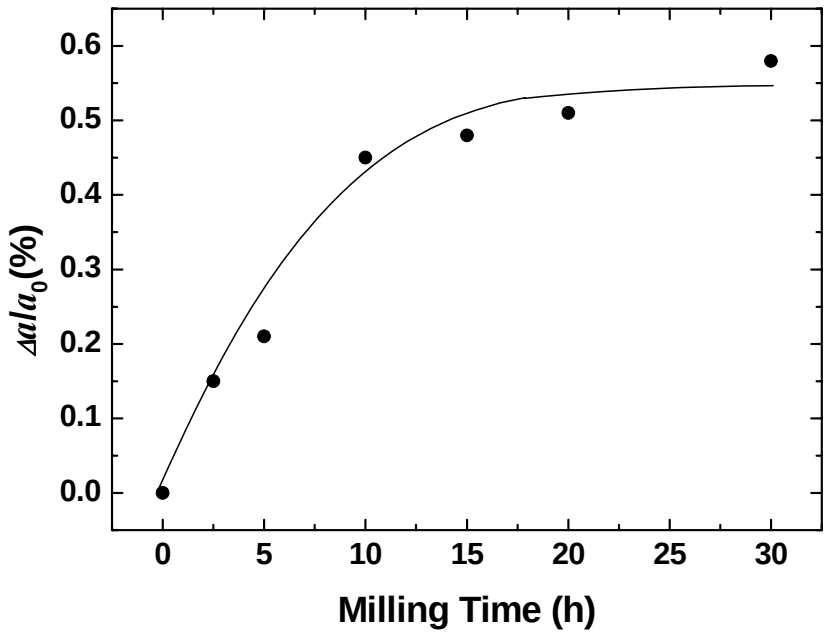

Figure 7.8 The relative increase of the bcc lattice parameter versus milling time for Nb-Ge powders.

M.T. (h)	***GS* (nm)**	a_{bcc} **(Å)**	$\Delta a_{bcc}/a_0$ **(%)**	a_{Ge} **(Å)**
0	200 μm	3.303	0	5.621
2.5	6	3.308	0.15	5.286
5	3	3.310	0.21	4.935
10	1	3.318	0.45	3.743
15	1	3.319	0.48	-
20	1	3.320	0.51	-
30	1	3.322	0.58	-

Table 7.4 Grain size (*GS*), lattice constants and relative lattice increase for bcc-Nb solid solution. The lattice parameter of pure Nb and Ge were taken from the scientific literature [78].

Figure 7.6 shows the formation of a nanostructured bcc-Nb(Ge) solid solution, hereafter indicated as $(Nb)_{ss}$, the formation of a germanium-rich solid solution, $(Ge)_{ss}$, and a gradual disappearance and broadening of crystalline peaks. We found in a detailed analysis of our XRD data using Rietveld refinement that, consistent with the literature (subsection 3.4.4), during milling there is concurrent formation of the compositional phases $(Nb)_{ss}$, Nb_3Ge, Nb_5Ge_3 and $NbGe_2$ found in the phase diagram [88]. For clarity figure 7.6 only includes the dominant phases. Figure 7.7 shows simultaneous structural changes as the grain size (GS) is refined down to a few nanometres and the formation of a nanophase $(Nb)_{ss}$ occurs. The grain size was found to decrease very rapidly in a roughly logarithmic way. The lattice parameter of $(Ge)_{ss}$ decreases and merge approximately after 10 h milling with that of $(Nb)_{ss}$. The equilibrium state for $(Nb)_{ss}$ occurs after ~ 11 h milling with a lattice constant of about 3.320 Å. The decrease of the Ge lattice parameter under high energetic deformation can be explained in terms of vacancy type defects (i.e. triple disorder) [100,132] whereas the increase of the Nb lattice parameter can be interpreted by anti-site disorder [134] (section 4.5). Therefore, Ge atoms leave their original sites and occupy the sites in the Nb cell. The lattice expansion for the bcc-Nb extends up to ~ 0.6 %. This value is smaller that that found by Hellstern. et al. (~ 1.2 %) for MA'ed Nb-Al [90] probably due to the smaller atomic radius of Ge (152 pm) compared to that of Al (182 pm). Nevertheless, the properties of MA'ed Nb-Ge powders fall into the schematic proposed by Suryanaryana (section 4.5). Table 7.4 reports the numerical values for all the relevant structural changes, which occur during heavy mechanical deformation.

Comparison with Nb-Ge microcrystalline BCC materials. The investigation carried out by Jorda et al. [50] shows that the bcc structure, $(Nb)_{ss}$, for Nb-Ge microcrystalline materials has a solid solubility which varies from 4 to 11.5 at.% Ge at high temperature ($1600 \leq T \leq 1900$ ^{o}C) while the corresponding lattice parameter slightly decreases due to major Ge content in the unit cell (section 3.3). Our results on nanocrystalline MA'ed Nb-Ge powders present a saturation behaviour of the $(Nb)_{ss}$ lattice parameter, whose lattice expansion were found to extend up to ~ 0.6 % at the equilibrium.

7.3.6 Summary

High-energy ball milled Nb-Ge elemental powders were investigated using several techniques. After prolonged milling, we find a single crystallisation peak in our DSC data consistent with highly amorphous material. We will find that that this crystallisation temperature determines that important boundary between the low temperature range where materials remain broadly amorphous from high temperatures where the material crystallises and hence provides important information about where the optimum HIP or annealing heat treatments may be found as described in section 7.4 on bulk materials. Yield values above 100 % suggest that during dry milling large contamination from the milling media occurred. The large yield increase (~ 7 %) is in agreement with the Cu amount (~ 9 %) found by EDX measurements (subsection 7.4.3) performed on Nb_3Ge bulk materials. The zero field ac magnetometry of Nb-Ge MA'ed powders indicates that the material is broadly amorphous with a critical temperature below 5 K although some remnants remain with T_C of ~ 9 K. The X-ray diffraction peaks indicate the formation of all phases indicated in the phase diagram during milling and also of two Ge-rich and a Nb-rich solid solution, which merge after 10 h milling to form a dominant $(Nb)_{ss}$ phase. The analysis of crystalline phase and yield results indicate a large amount of copper contamination from the milling media.

7.4 Properties of nanocrystalline bulk samples

Superconductivity in A15 Nb-Ge nanocrystalline bulk samples was investigated via AC magnetometry in conjunction with compositional and structural information. The Nb-Ge metastable powders milled for 6 h and 20 h were processed using three different routes to produce bulk materials: HIP'ing, HIP'ing and subsequent annealing and annealing. For the processing conditions, the reader is referred to Table 7.1. Four groups of data:

HIPYYY, HIP600 + AZZZ, HIP1200 + AZZZ and AZZZ are discussed in the various parts of this section. The XRD results are presented in subsection 7.4.1. Subsection 7.4.2 reports the SEM coupled with EDX images and data analysis. The AC magnetometry curves are reported in subsection 7.4.3. A summary of data is discussed in subsection 7.4.4.

7.4.1 X-ray diffraction

X-ray diffraction was used to investigate the crystalline structure and compositional changes. XRD scans are given for Nb_3Ge bulk materials produced from powders milled for up to 6 and 20 h. The XRD results are indicated for the four groups: HIPYYY, HIP600 + AZZZ, HIP1200 + AZZZ and AZZZ. The XRD labelling was based on the major phases found by SEM coupled with EDX: Nb_3Ge, Nb_5Ge_3, $(Nb)_{ss}$ and $(Cu)_{ss}$. Traces of niobium and germanium oxides are also indicated. Unfortunately, analysis of the XRD peaks is complicated by overlapping peaks, the presence of many phases and the changing lattice parameters with milling. We have completed an extensive Rietveld refinement of these data using the software Topas and it was not possible to find a unique description of the amount of phases present. Nevertheless, XRD scans are analysed to find typical grain size (*GS*) and A15 lattice parameter ($a_{\text{Nb-Ge}}$) ($T_{\text{C,onset}}$ data are also tabulated). More general arguments are used to evaluate the effect of heat treatment on the phase content of the materials fabricated.

Group 1: M6 + HIPYYY and M20 + HIPYYY. XRD of HIP'ed samples are shown in Figure 7.9 and Figure 7.10 for M6 and M20 HIP'ed at different temperatures, respectively. Results are tabulated in Table 7.5. The increase of HIP'ing temperature produces increased grain size in our nanocrystalline samples. Figure 7.11 shows as expected that the grain size increases against HIP'ing temperature.

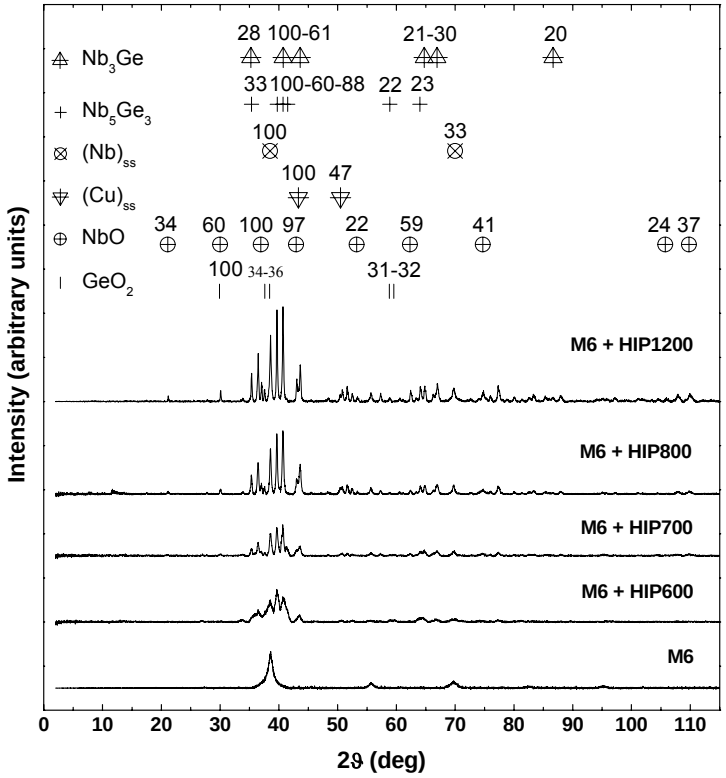

Figure 7.9 XRD scans for M6 + HIPYYY at different HIP temperatures and precursor powder prior to HIP'ing. The peaks specified above, for the important phases, are only those which are greater than 20 % of the largest peak for the structure.

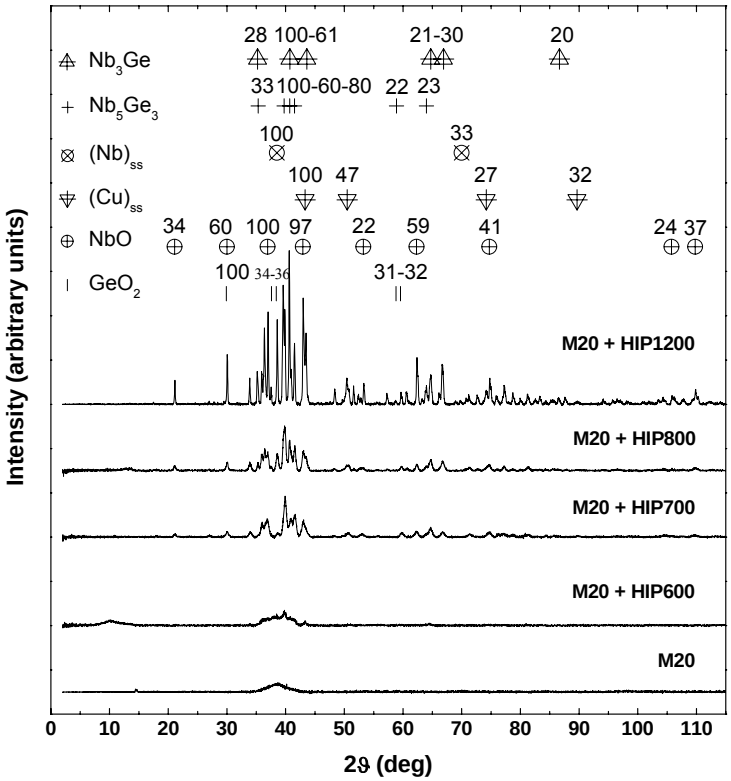

Figure 7.10 XRD scans for M20 + HIPYYY at different HIP temperatures and precursor powder prior to HIP'ing. The peaks specified above, for the important phases, are only those which are greater than 20 % of the largest peak for the structure.

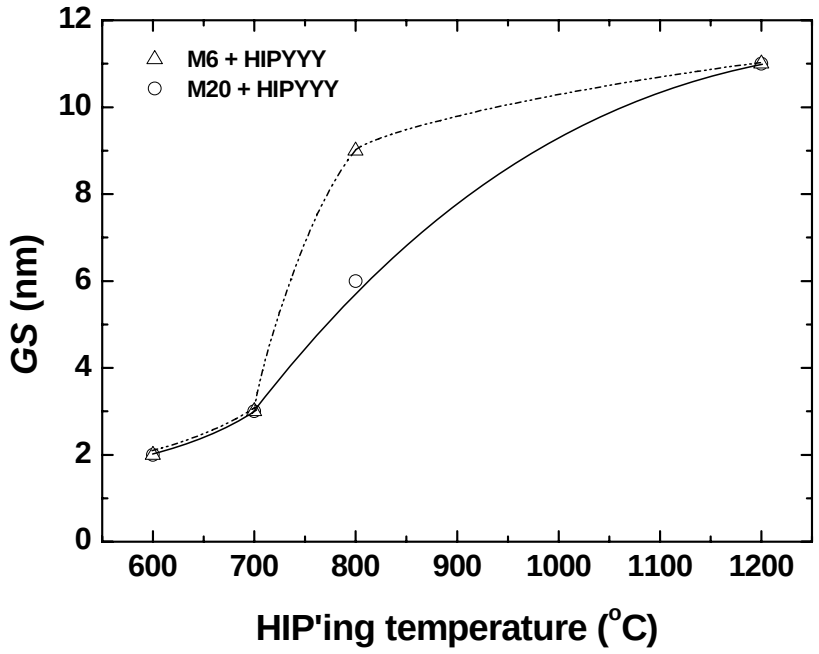

Figure 7.11 Grain size (*GS*) for M6 (triangle) and M20 (circle) processed using HIPYYY.

HIPYYY	Series M6			Series M20		
	GS **(nm)**	$a_{\text{Nb-Ge}}$ **(Å)**	$T_{\text{C,onset}}$ **(K)**	***GS*** **(nm)**	$a_{\text{Nb-Ge}}$ **(Å)**	$T_{\text{C,onset}}$ **(K)**
HIP600	2(1)	5.154(4)	8.44	2(1)	5.16(1)	7.38
HIP700	3(1)	5.155(2)	7.76	3(2)	5.154(2)	9.01 {4.46}
HIP800	9(4)	5.155(2)	7.61	6(3)	5.156(1)	8.61
HIP1200	11(6)	5.156(2)	7.11	11(4)	5.158(3)	8.22

Table 7.5 Typical average grain size (*GS*), A15 lattice parameter (*a*) and $T_{\text{C,onset}}$ for M6 and M20 processed using HIPYYY. In curly brackets, the second transition temperature is recorded. The relatively large error (± 0.01) on the A15 lattice constant for sample M20 + HIP600 is due to the broad peak at 10 ^{o} (Figure 7.9).

Group 2: M6 + HIP600 + AZZZ and M20 + HIP600 + AZZZ. XRD of samples HIP'ed at 600 ^{o}C and subsequently isochronally annealed are shown in Figure 7.12 and Figure 7.13 for group M6 and M20, respectively. Results are tabulated in Table 7.6. The precursor phase (HIP600) has small grains, which gradually increase with high

temperature heat treatment characterised by an increase of the number of XRD peaks, intensity and a progressive reduction of the peak width due to the GS growth. One can broadly track the growth of the A15 and the various secondary phases and contamination oxides for our best sample (Figure 7.12) by considering the non-overlapping peaks: (110) at ~ 30 ^{o} and (220) at ~ 62.4 ^{o} for NbO; (213) at ~ 64 ^{o} for Nb_5Ge_3; (320) at ~ 65 ^{o} and (321) at ~ 66.8 ^{o} for Nb_3Ge. The NbO first crystallises approximately at an annealing temperature of 700 ^{o}C with strong XRD peaks at 900 ^{o}C. In contrast, the Nb_3Ge and Nb_5Ge_3 progressively crystallise as the annealing temperature increases from as low as 600 ^{o}C. Precursor samples (HIP600) after annealing at 600 ^{o}C × 18 h show an unexpected strong peak intensity at ~ 25 ^{o}, which is found in Nb_3Al at this angle and might indicate different possibilities: a preferred orientation, an improved atomic ordering or a slight structural difference between our samples and those found in the (CDS – Chemical database service) literature. In this group of samples, this peak is only found in samples with some component of high T_C material. Figure 7.14 shows an increase in grain size against HIP'ing temperature.

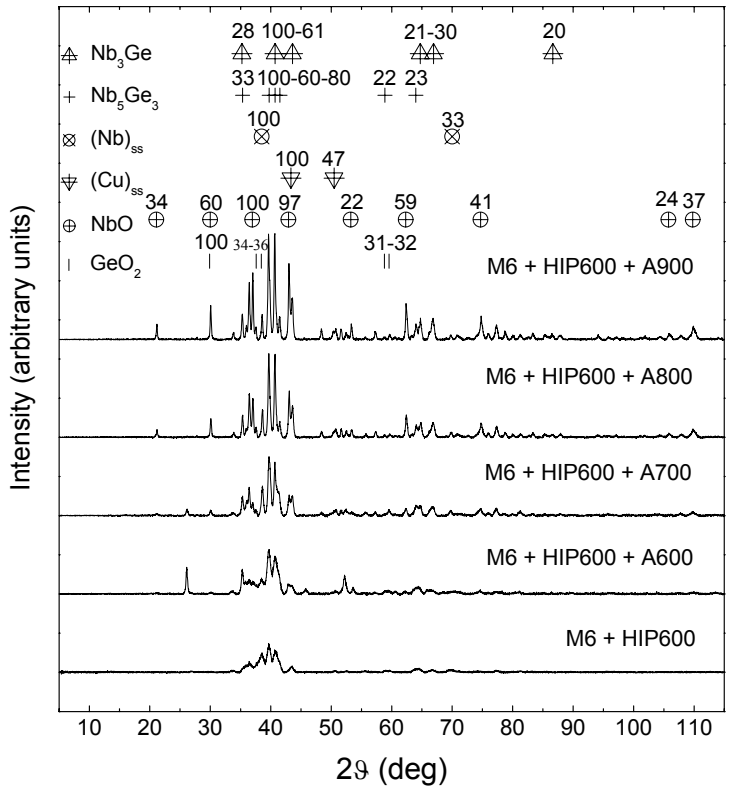

Figure 7.12 XRD scans for M6 + HIP600 + AZZZ at different annealing temperatures and precursor powder prior to HIP'ing. The peaks specified above, for the important phases, are only those which are greater than 20 % of the largest peak for the structure.

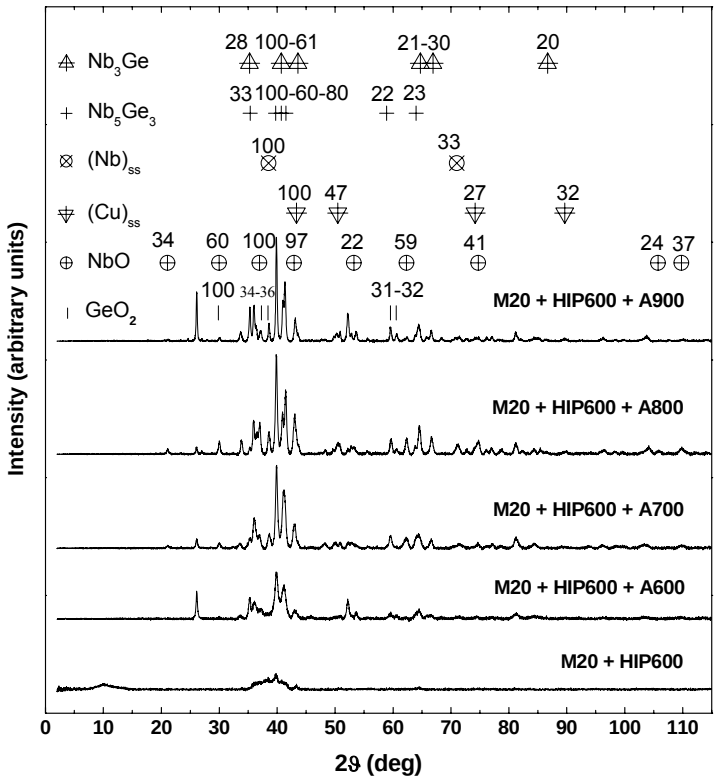

Figure 7.13 XRD scans for M20 + HIP600 + AZZZ at different annealing temperatures and precursor powder prior to HIP'ing. The peaks specified above, for the important phases, are only those which are greater than 20 % of the largest peak for the structure

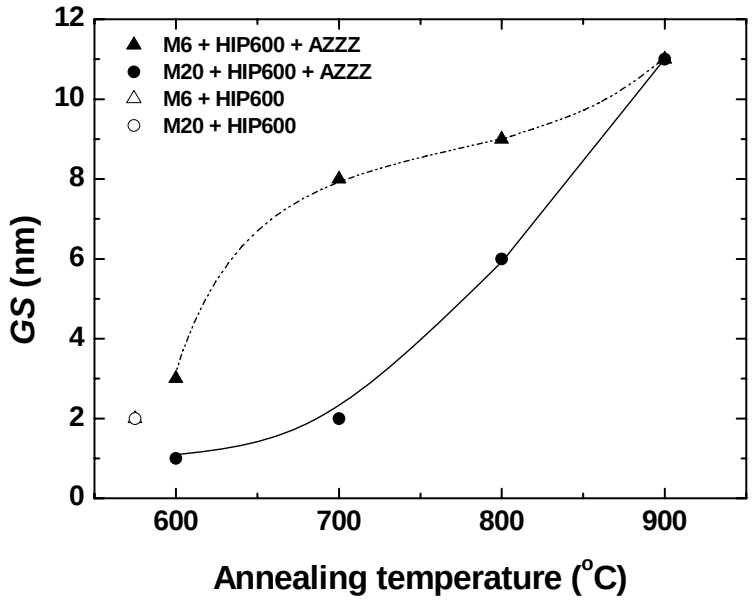

Figure 7.14 Grain size (*GS*) for M6 (triangle) and M20 (circle) processed using HIP600 + AZZZ. The empty symbol represents the precursor state prior to annealing.

HIP600 + AZZZ	Series M6			Series M20		
	GS **(nm)**	$a_{\text{Nb-Ge}}$ **(Å)**	$T_{\text{C,onset}}$ **(K)**	***GS*** **(nm)**	$a_{\text{Nb-Ge}}$ **(Å)**	$T_{\text{C,onset}}$ **(K)**
HIP600	2(1)	5.154(4)	8.44	2(1)	5.16(1)	7.38
HIP600 + A600	1(2)	5.155(2)	7.18 {17.01}	3(4)	5.157(4)	7.61 {16.43}
HIP600 + A700	2(7)	5.153(2)	12.02	8(6)	5.154(1)	10.77
HIP600 + A800	6(2)	5.154(2)	8.12	9(6)	5.154(2)	8.71
HIP600 + A900	11(5)	5.157(1)	7.85	11(8)	5.157(1)	8.11

Table 7.6 Grain size (*GS*), A15 lattice parameter (a) and $T_{\text{C,onset}}$ for M6 and M20 processed using HIP600 + AZZZ and precursor material prior to annealing. In curly brackets, the second transition temperature is recorded.

Group 3: M6 + HIP1200 + AZZZ and M20 + HIP1200 + AZZZ. XRD of samples HIP'ed at 1200 ^{o}C and isochronally annealed are shown in Figure 7.15 and Figure 7.16 for M6 and M20, respectively. Figure 7.17 reports the grain size vs. HIP'ing temperature and is tabulated in Table 7.7. The apparent decrease in grain size observed in these samples is probably due to the associated error bars but may result when new material crystallises with very small grains thus reducing the average. We conclude that broadly the annealing does not significantly change the intensity or the number of the XRD peaks. This indicates that the crystalline structure of samples M6 + HIP1200 and M20 + HIP1200 is in a metastable equilibrium state. Therefore post-HIP annealing introduced additional energy which triggered small structural changes as indicated by XRD patterns. It is likely that prolonged heat treatment leads to the stable equilibrium condition.

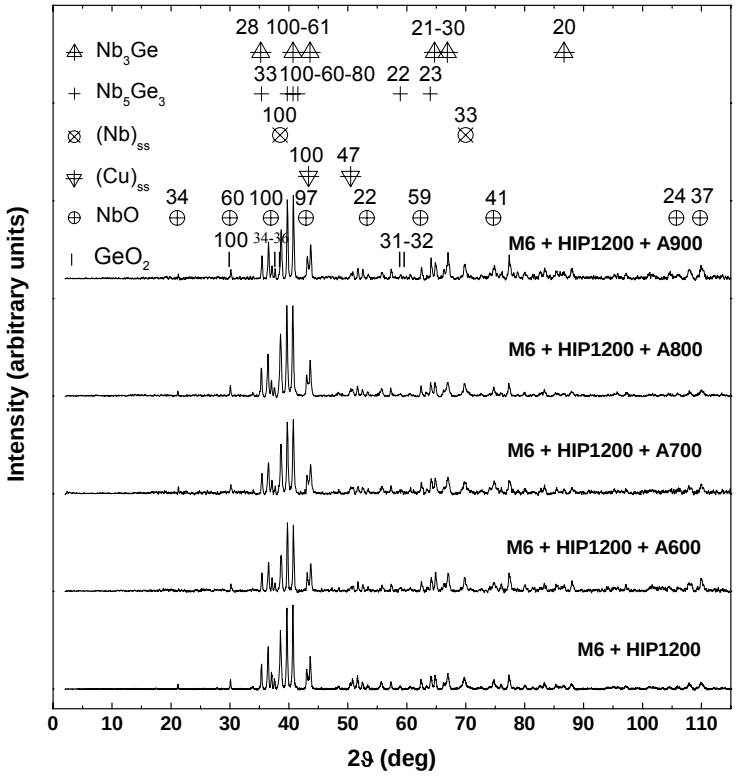

Figure 7.15 XRD scans for M6 + HIP1200 + AZZZ at different annealing temperatures and precursor powder prior to annealing. The peaks specified above, for the important phases, are only those which are greater than 20 % of the largest peak for the structure.

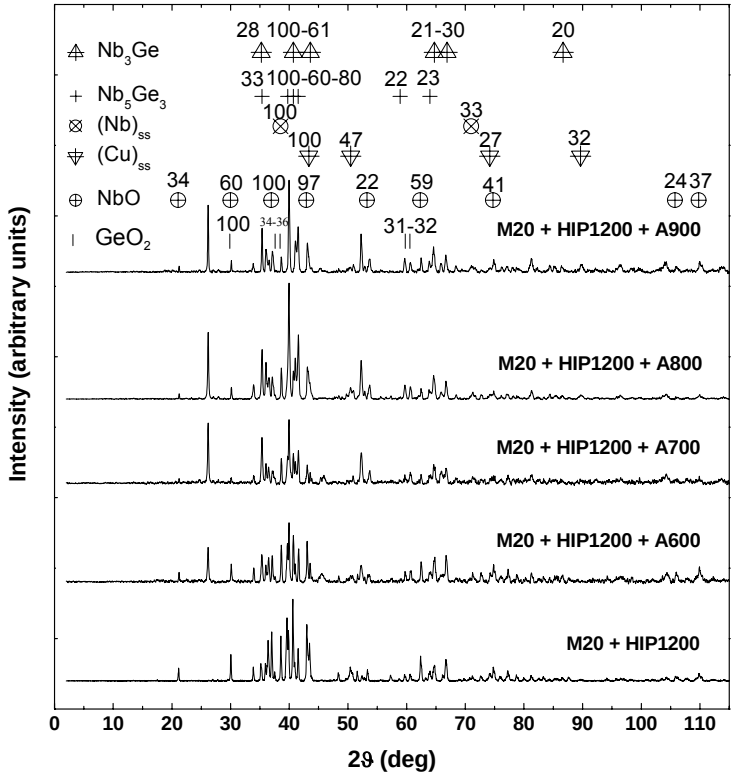

Figure 7.16 XRD scans for M20 + HIP1200 + AZZZ at different annealing temperatures and precursor powder prior to annealing. The peaks specified above, for the important phases, are only those which are greater than 20 % of the largest peak for the structure .

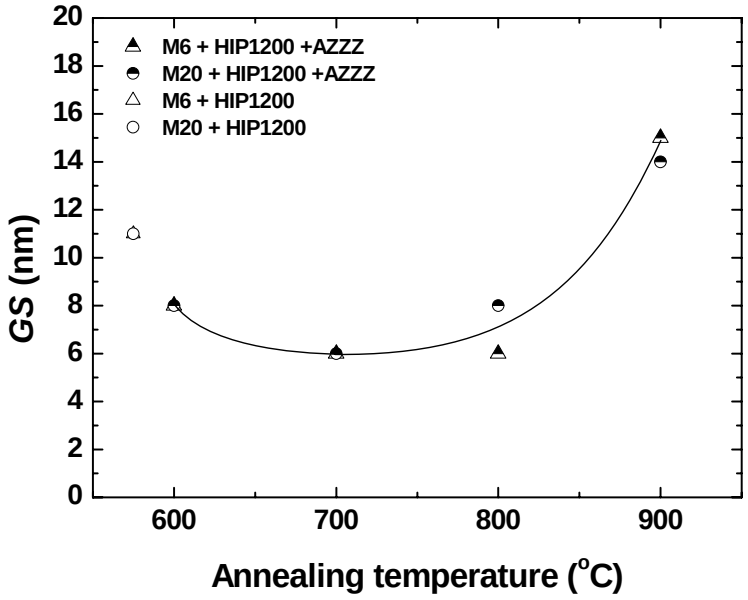

Figure 7.17 Grain size (*GS*) for M6 (triangle) and M20 (circle) processed using HIP1200 + AZZZ. The empty symbol represents the precursor state prior to annealing.

HIP1200 + AZZZ	Series M6			Series M20		
	GS **(nm)**	$a_{\text{Nb-Ge}}$ **(Å)**	$T_{\text{C,onset}}$ **(K)**	***GS*** **(nm)**	$a_{\text{Nb-Ge}}$ **(Å)**	$T_{\text{C,onset}}$ **(K)**
HIP1200	11(6)	5.156(2)	7.11	11(4)	5.158(3)	8.22
HIP1200 + A600	8(9)	5.160(2)	7.81	8(2)	5.160(2)	7.82
HIP1200 + A700	6(3)	5.160(2)	7.61 {16.17}	6(5)	5.160(2)	7.95
HIP1200 + A800	6(1)	5.159(1)	7.60	8(6)	5.160(2)	7.64
HIP1200 + A900	15(3)	5.160(2)	7.71	14(4)	5.159(2)	7.72

Table 7.7 Grain size (*GS*), A15 lattice parameter (a) and $T_{\text{C,onset}}$ for M6 and M20 processed using HIP1200 + AZZZ and precursor material prior to annealing. In curly brackets, the second transition temperature is recorded.

Group 4: M6 + AZZZ and M20 + AZZZ. XRD patterns of samples milled for M6 and M20 and then isochronally annealed are shown in Figure 7.18 and Figure 7.19, respectively. For this set of samples, again we find that the heat treatment produces an increase of the number and the intensity of peaks. Figure 7.20 reports the grain size vs. annealing temperature. Data are tabulated in Table 7.8.

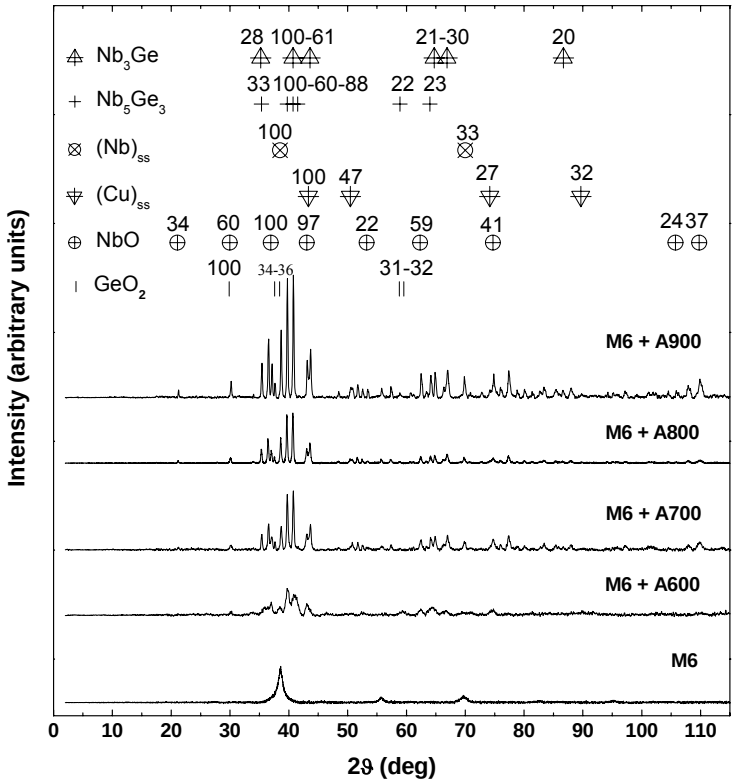

Figure 7.18 XRD scans for M6 + AZZZ at different annealing temperatures and precursor powder prior to annealing. The peaks specified above, for the important phases, are only those which are greater than 20 % of the largest peak for the structure.

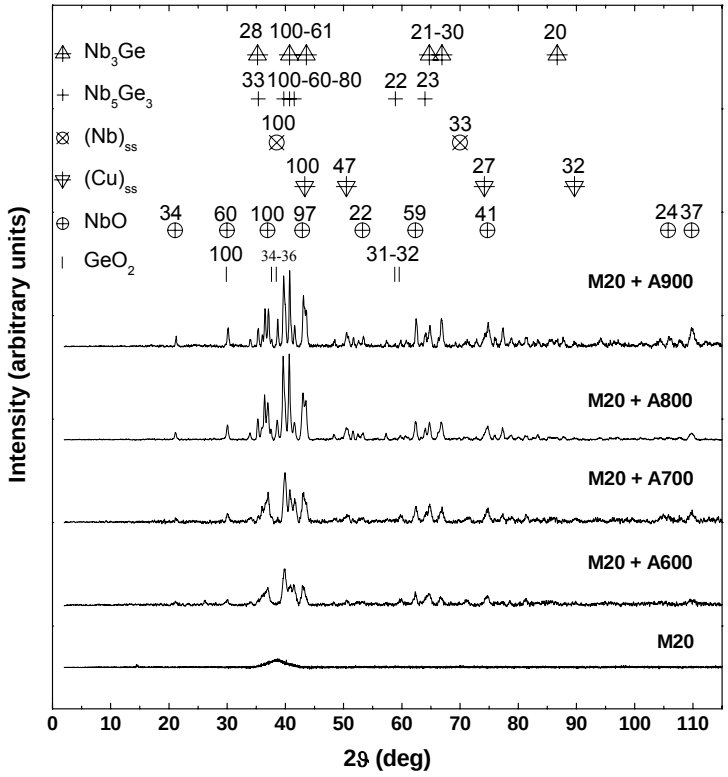

Figure 7.19 XRD scans for M20 + AZZZ at different annealing temperatures and precursor powder prior to annealing. The peaks specified above, for the important phases, are only those which are greater than 20 % of the largest peak for the structure.

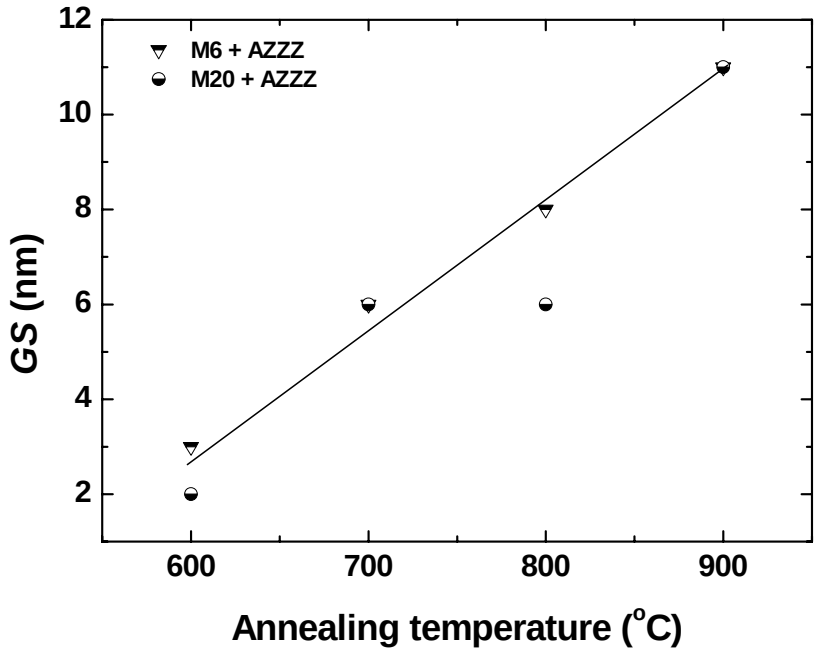

Figure 7.20 Grain size (*GS*) for M6 (triangle) and M20 (circle) processed using AZZZ.

AZZZ	Series M6			Series M20		
	GS **(nm)**	$a_{\text{Nb-Ge}}$ **(Å)**	$T_{\text{C,onset}}$ **(K)**	***GS*** **(nm)**	$a_{\text{Nb-Ge}}$ **(Å)**	$T_{\text{C,onset}}$ **(K)**
A600	3(3)	5.160(2)	8.40	2(1)	5.159(3)	8.21
A700	6(2)	5.160(2)	8.53	6(7)	5.157(2)	8.23
A800	8(4)	5.159(2)	8.09 {16.91}	6(5)	5.157(2)	8.22 {16.09}
A900	11(6)	5.159(2)	8.06	11(11)	5.159(2)	8.26 {16.52}

Table 7.8 Grain size (*GS*), A15 lattice parameter (a) and $T_{\text{C,onset}}$ for M6 and M20 processed using AZZZ. In curly brackets, the second transition temperature is recorded.

Summary for XRD. In agreement with the literature (section 3.2 and 3.3.4), the crystallite size was found to increase with increasingly aggressive heat treatments - annealing and/or HIP from 2-3 nm up to 15 nm. In contrast, in groups 1 and 2 there is a general trend that T_C increases as the lattice parameter decreases (and hence the Ge content increases) consistent with thin film results. The phases Nb_3Ge, Nb_5Ge_3 were found to progressively crystallise with isochronal heat treatment. The oxides only crystallise at high temperature, which we shall see occurs beyond the optimum T_C, which opens the possibility of NbO competing with the superconducting phase.

7.4.2 Scanning electron microscopy

The compositions and spatial distribution of the phases in these samples were investigated by means of the SEM coupled with energy dispersive X-ray and X-ray quantification maps (XQM). Only two samples were investigated in this section - M6 + HIP600 and sample M6 + HIP1200. Firstly, the compositional results from the energy dispersive X-ray spectroscopy are presented. Secondly, the SEM images and X-ray quantification maps (XQM) are presented for these two samples. In the end, the results are discussed. Well-known phase diagrams were used to produce educated guesses of the various phases and their volume percent.

Compositional results from Energy Dispersive X-ray Spectroscopy (Macroscopic spatial averages). The stoichiometry (chemical formula of a compound) of HIP'ed samples was estimated using the SEM coupled with the EDX. We performed this analysis on these multiphase samples to verify whether the average atomic ratio is different from the starting nominal ratio (3:1). Table 7.9 reports the normalised atomic percentages of Nb, Ge and Cu, the resulting Nb/Ge atomic ratio and the stoichiometry for both samples. The small error bars of the atomic percentages (≤ 0.3 at.%) indicate that the atomic composition is approximately constant. The copper contamination from milling media is the same in both samples, as expected for samples fabricated from the same milled powders. Furthermore, the copper contamination results are close to that estimated from the yield measurements (subsection 7.3.3). Figure 7.21 is a typical EDX spectrum. It shows the X-ray emission lines of Nb and Ge, but also contamination from the Cu milling media and the presence of the oxygen. The EDX analysis performed does not include the evaluation of gas impurities (i.e O_2, N_2) because it is known to be inaccurate owing to the X-ray absorption produced by light elements.

Sample	Nb (at. %)	Ge (at. %)	Cu (at. %)	Nb/Ge	Stoichiometry
M6 + HIP600	69.9 (2)	21.3 (1)	8.8 (1)	3.3(1)	$Nb_3Ge_{0.9}$
M6 + HIP1200	70.5 (3)	20.6 (3)	8.9 (1)	3.4(2)	$Nb_3Ge_{0.9}$

Table 7.9 Normalised atomic percentages, Nb/Ge atomic ratio and stoichiometry for M6 processed using HIP600 and HIP1200. Errors are reported in bracket.

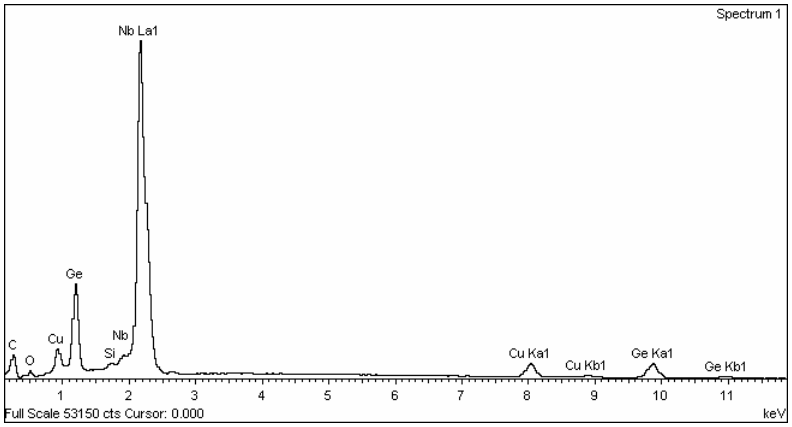

Figure 7.21 Typical EDX spectrum for M6 + HIP600. Undesired atoms are also present: Cu is from the milling procedure; C and Si are introduced during polishing; O is from the various oxides formed.

X-ray Quantification Maps for M6 + HIP600 (Local compositions and structures). Figure 7.22 and Figure 7.23 are the SE and BSE images representative for the topology of the surface and the element distributions, respectively. Both images show porous material. The well-known low workability of Ge produces a porous microstructure, which degrades the overall connectivity. The dark regions shown by SE are due to porosity and the BSE images with corresponding quantification maps confirm that these regions include Cu-Ge segregation. We associate the segregation with the eutectic Ge-Cu alloy that melts at 644 ^{o}C. The distribution of these elements is not uniform and the HIP'ing temperature is below the melting points of both Ge (938.25 ^{o}C) and Cu (1084.72 ^{o}C)

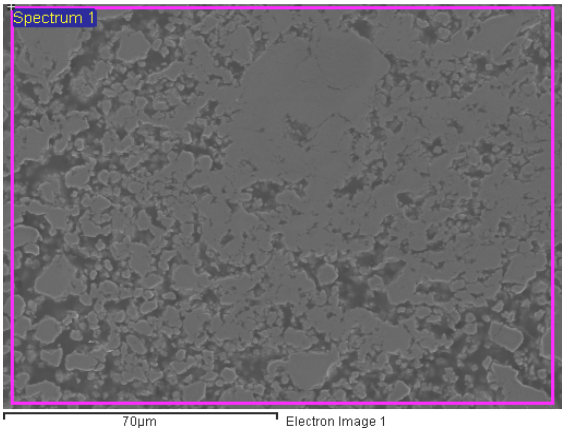

Figure 7.22 Typical SE image for M6 + HIP600.

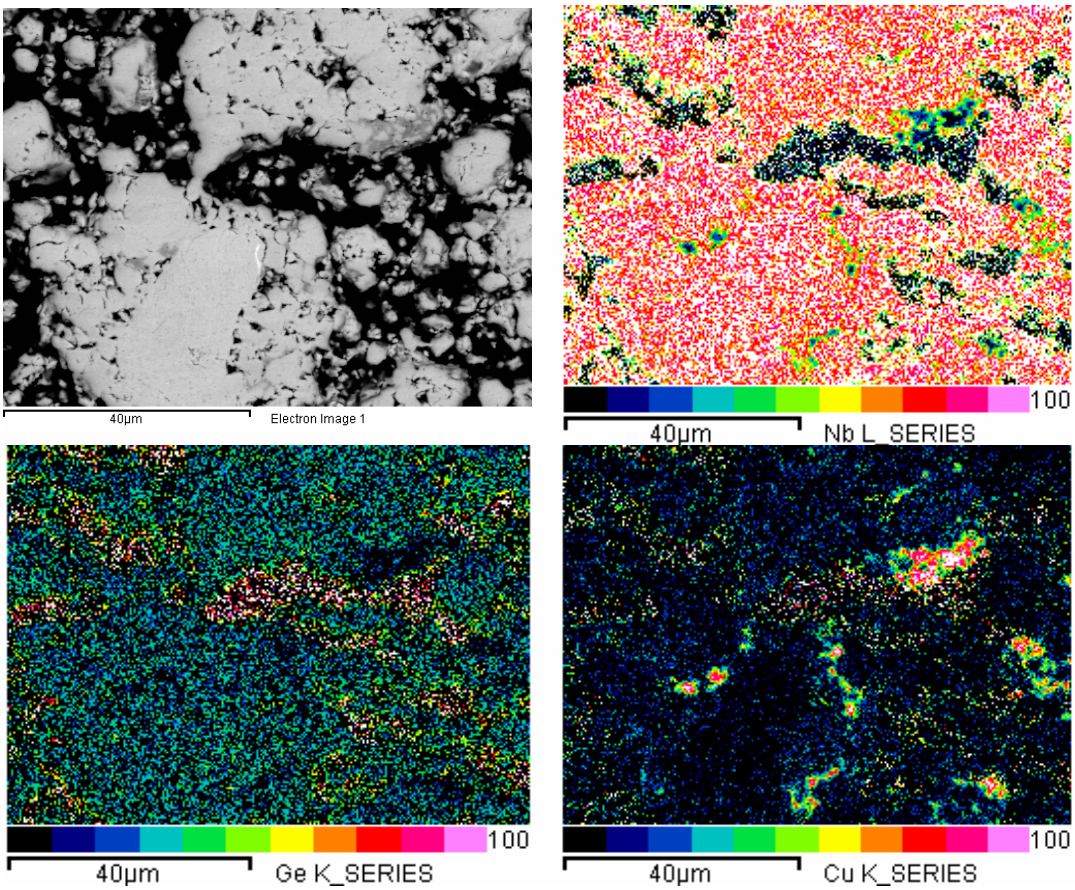

Figure 7.23 BSE image and corresponding X-ray quantification maps for M6 + HIP600. The distribution of niobium, germanium and copper is not uniform throughout the material.

In this thesis work, the phase identification and the volume phase percent are educated guesses based on the phase diagram. Indeed, even when a pixel includes material in the composition associated with the A15 strucure, we cannot exclude that each pixel volume (~ 0.15 μm^3) contains unreacted elements and/or their terminal solid solution.

A local analysis on phase type and volume was carried out in three different regions of sample M6 + HIP600: a low copper content (Table 7.10), a typical copper content (Table 7.11) and a high copper content region (Table 7.12). 50 pixels were taken in each region to determine the local composition. Phase diagrams [50,55,67] were used to interpret the compositional phases and to estimate the volume percent of the phases present. The tables provide phase diagram data, in particular the range(s) of compositions including the terminal compositions. The average composition and its standard deviation were calculated for groups of compositional points, which are included in the same region of the phase diagram. The fact that standard deviations cover a few atomic percent (≤ 4 at. %), indicates that at the micron level the material consists of a limited number of phases with specific compositions. Nb_3Ge is found to form in the compositional range: (28 ± 4) at.% Ge, which includes the nominal composition 25 at.% Ge (section 7.2) and is also located in the double-phase region $Nb_3Ge + Nb_5Ge_3$ (figure 3.5).

Low copper region				
Elements	**Composition (at. %)**	**n**	**Volume (%)**	**Phase diagram data**
Cu K Ge K Nb L	0 27 (± 4) 73 (± 4)	24	48	$Nb_3Ge + Nb_5Ge_3$ 20 < Ge < 38 at. %
Cu K Ge K Nb L	0 0 100	23	46	Nb
Cu K Ge K Nb L	14 (± 2) 21.61(± 0.01) 65 (± 2)	2	4	$(Nb)_{ss} + Nb_5(Ge,Cu)_3 + (Cu)_{ss}$ $Nb_5(Ge,Cu)_3$ with Nb = 50 at. %
Cu K Ge K Nb L	0 38.43 61.57	1	2	Nb_5Ge_3 38 ≤ Nb ≤ 41.5 at. %

Table 7.10 The average compositional points (at. %) in the low copper content region for M6 + HIP600. 50 pixels were used to estimate the crystalline phases and the corresponding volume percent (n/50). Phase diagrams from the literature [50,55,67] were used to identify the resulting phases. Also provided is the associated range of composition within the relevant region of the phase diagram.

Typical copper region				
Elements	**Composition (at. %)**	**n**	**Volume (%)**	**Phase diagram data**
Cu K Ge K Nb L	0 0 100	23	46	Nb
Cu K Ge K Nb L	0 29 (± 3) 71 (± 3)	15	30	$Nb_3Ge + Nb_5Ge_3$ $20 < Ge < 38$ at. %
Cu K Ge K Nb L	21 (± 2) 0 79 (± 2)	4	8	$(Nb)_{ss} + (Cu)_{ss}$ $0 < Nb < 100$ at. %
Cu K Ge K Nb L	0 40 (± 1) 60 (± 1)	3	6	Nb_5Ge_3 $38 \leq Ge \leq 41.2$ at. %
Cu K Ge K Nb L	17 (± 4) 21 (± 1) 62 (± 5)	3	6	$(Nb)_{ss} + Nb_5(Ge,Cu)_3 + (Cu)_{ss}$ $Nb_5(Ge,Cu)_3$ with Nb = 50 at. %
Cu K Ge K Nb L	12 (± 1) 29 (± 2) 59 (± 3)	2	4	$(Nb)_{ss} + Nb_5(Ge,Cu)_3$ $Nb_5(Ge,Cu)_3$ with $50 \leq Nb \leq 61$ at. %

Table 7.11 The average compositional points (at. %) in the typical copper content region for M6 + HIP600. 50 pixels were used to estimate the crystalline phases and the corresponding volume percent (n/50). Phase diagrams from the literature [50,55,67] were used to identify the resulting phase. Also provided is the associated range of composition within the relevant region of the phase diagram.

High copper region				
Elements	**Composition (at. %)**	**n**	**Volume (%)**	**Phase diagram data**
Cu K Ge K Nb L	74 (± 13) 0 26 (± 13)	31	62	$(Nb)_{ss} + (Cu)_{ss}$ $0 < Nb < 100$ at. %
Cu K Ge K Nb L	0 0 100	10	20	Cu
Cu K Ge K Nb L	66 (± 3) 18 (± 2) 16 (± 2)	5	10	$Nb_5(Ge,Cu)_3 + (Cu)_{ss}$ $Nb_5(Ge,Cu)_3$ with $44 \leq Nb \leq 50$ at. %
Cu K Ge K Nb L	33 (± 3) 23 (± 2) 44 (± 1)	2	4	$(Nb)_{ss} + Nb_5(Ge,Cu)_3 + (Cu)_{ss}$ $Nb_5(Ge,Cu)_3$ Nb = 50 at. %
Cu K Ge K Nb L	57 (± 11) 43(± 11) 0	2	4	$(Ge)_{ss} + Cu_3Ge$ $0 < Ge < 76.9$ at. %

Table 7.12 The average compositional points (at. %) in the high copper content region for M6 + HIP600. 50 pixels were used to estimate the crystalline phases and the corresponding volume percent (n/50). Phase diagrams from the literature [50,55,67] were used to identify the resulting phase. Also provided is the associated range of composition within the relevant region of the phase diagram.

X-ray Quantification Maps (XQM) for M6 + HIP1200 (Local compositions and structures). Figure 7.24 and Figure 7.25 provide SE and BSE images for the second sample. The brightest regions of the BSE (Figure 7.25) image can be attributed to high Nb concentration. In agreement with SE and XQM, the dark grey regions are due to porosity. In contrast to the sample HIP'ed at 600 ^{o}C, this sample shows a more uniform elemental distribution because this HIP'ing temperature was above the Ge (938.25 ^{o}C) and Cu melting point (1084,62 ^{o}C).

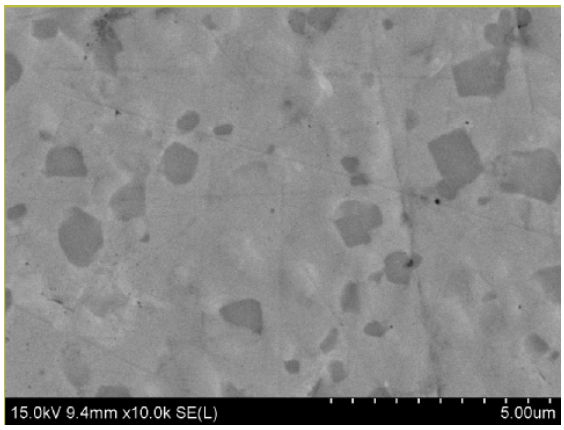

Figure 7.24 Typical SE image for M6 + HIP1200.

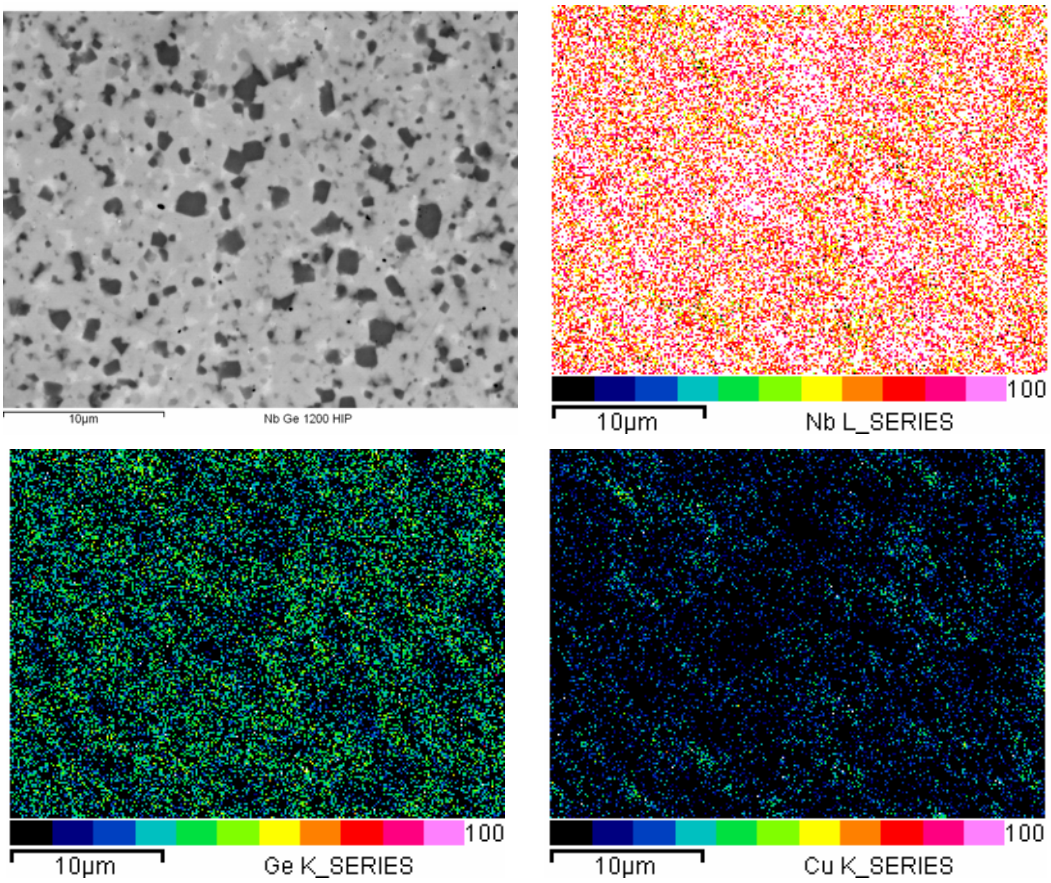

Figure 7.25 BSE image and corresponding X-ray quantification maps for M6 + HIP1200. The distribution of niobium, germanium and copper is not uniform throughout the material.

Figure 7.25 shows the BSE image and the X-ray quantification maps of niobium, germanium and copper for sample M6 + HIP1200. The compositional analysis was carried out using 150 pixels in different areas because the distribution of elements was far more uniform. Table 7.13 reports the phases and their volume percent. Nb_3Ge formed mainly at (29 ± 5) at.% Ge which is similar to M6 + HIP600.

Elements	Composition (at. %)	n	Volume (%)	Phase diagram data
Cu K Ge K Nb L	0 29 (± 5) 71 (± 5)	58	39	$Nb_3Ge + Nb_5Ge_3$ 20 < Ge < 38 at. %
Cu K Ge K Nb L	0 0 100	42	28	Nb
Cu K Ge K Nb L	21 (± 8) 79 (± 8) 0	25	16	$(Nb)_{ss} + (Cu)_{ss}$ 0 < Nb < 100 at. %
Cu K Ge K Nb L	17 (± 5) 15 (± 4) 68 (± 7)	8	6	$(Nb)_{ss} + Nb_5(Ge,Cu)_3 + (Cu)_{ss}$ $Nb_5(Ge,Cu)_3$ with Nb = 50 at. %
Cu K Ge K Nb L	0 44 (± 2) 56 (± 2)	4	3	$Nb_5Ge_3 + NbGe_2$ 41.2 < Ge < 65 at. %
Cu K Ge K Nb L	0 39 (± 2) 61 (± 2)	4	3	Nb_5Ge_3 38 ≤ Ge ≤ 41.2 at. %
Cu K Ge K Nb L	0 14 (± 2) 86 (± 2)	3	2	$(Nb)_{ss} + Nb_3Ge$ 4 < Ge < 18.5 at. %
Cu K Ge K Nb L	12 (± 2) 33.9 (± 0.4) 54 (± 2)	3	2	$Nb_5(Ge,Cu)_3$ 44 ≤ Nb ≤ 61 at. %
Cu K Ge K Nb L	8 (± 1) 28 (± 3) 64 (± 1)	3	2	$(Nb)_{ss} + Nb_5(Ge,Cu)_3$ $Nb_5(Ge,Cu)_3$ with 50 ≤ Nb ≤ 61 at. %

Table 7.13 The average compositional points (at. %) for M6 + HIP1200. 150 pixels were used to estimate the crystalline phases and the corresponding volume percent (n/50). Phase diagrams from the literature [50,55,67] were used to identify the resulting phase. Also provided is the associated range of composition within the relevant region of the phase diagram.

Discussion. SEM data are discussed in two parts: the average composition using EDX and the local compositional information (XQM) for samples M6 + HIP600 and M6 + HIP1200.

EDX. The overall Nb:Ge ratio for sample M6 + HIP600 and for M6 + HIP1200 is (3.4 ± 0.2). These results indicate a lower Ge content than the nominal content independently of the HIP'ing temperatures. We suggest either the error in composition from the EDX measurements alone is ~ 20 % (rather than ~ 6 %) or during milling, loss of germanium occured. Hence, Ge loss does not necessarily occur at very high temperatures where volatility becomes an issue (i.e. $1700 \leq T \leq 2200$ ^{o}C) [52].

XQMs. Table 7.14 shows the compositions extracted from tables 7.10 to 7.13 associated with those regions that include the A15 phase and corresponding phase diagram compositional data for samples M6 + HIP600 and M6 + 1200, respectively. Table 7.15 uses the Lever rule to calculate the volume phase percentage of the phases present for samples M6 + HIP600 and M6 + HIP1200, respectively.

Sample	Composition	Phase diagram data
M6 + HIP600	(28 ± 4) at.% Ge	$Nb_3Ge + Nb_5Ge_3$ 20 < Ge < 38 at. %
M6 + HIP1200	(14 ± 2) at.% Ge	$(Nb)_{ss} + Nb_3Ge$ 4 < Ge < 18.5 at. %
	(29 ± 5) at.% Ge	$Nb_3Ge + Nb_5Ge_3$ 20 < Ge < 38 at. %

Table 7.14 The average composition (at.%) and the regions of the A15 phase for samples M6 processed via HIP600 and HIP1200. The lever rule was used to estimate the A15 weight fraction.

Phase	M6 + HIP600			M6 + HIP1200
	Cu low	Cu average	Cu high	
Nb	46 %	46 %	-	28 %
$(Nb)_{ss}$	1 %	8 %	19 %	11 %
Nb_3Ge	46 %	12 %	-	29 %
Nb_5Ge_3	4 %	24 %	-	15%
$Nb_5(Ge,Cu)_3$	2 %	4 %	8 %	7 %
$(Cu)_{ss}$	1 %	1 %	49 %	9 %
Cu	-	-	20%	-
Cu_3Ge	-	-	2 %	-
$(Ge)_{ss}$	-	-	2 %	-
$NbGe_2$	-	-	-	1 %

Table 7.15 Indicative phases and their volume percentages for M6 processed using M6 + HIP600 and M6 + HIP1200.

As shown in Table 7.14, Nb_3Ge (A15) forms in the two-phase region $Nb_3Ge + Nb_5Ge_3$ in samples M6 + HIP600 whereas sample M6 + HIP1200 shows in addition the formation of $(Nb)_{ss} + Nb_3Ge$. However most of the A15 phase is formed predominantly in the two-phase region $Nb_3Ge + Nb_5Ge_3$ at approximately the same compositional point for both samples.

Table 7.15 shows volume percentages for the A15 phase and secondary phases. For sample M6 + HIP600 the A15 phase content is 46 % and 12 % in the low and typical copper content region, respectively. This indicates that the copper limits severely the A15 phase formation. The Nb + $(Nb)_{ss}$ volume percentages are ~ 40 - 50 % in all regions. The total volume of Cu + $(Cu)_{ss}$ was found to be ~ 70 % in the copper high region. For sample M6 + HIP1200 the volume percentages of the A15 phase, the bcc Nb + $(Nb)_{ss}$ phase and the fcc Cu + $(Cu)_{ss}$ phase are ~ 30 % and ~ 40 % and ~ 10 %, respectively.

Summary. The EDX results indicate large contamination from milling media of (8.9 ± 0.1) at.% Cu, which is in agreement with the yield increase (subsection 7.3.3). The Nb/Ge ratios for both samples M6 + HIP600 and M6 + HIP1200 indicate that the Ge loss does not necessarily occur at very high temperatures where volatility becomes an issue. The XQMs for Nb_3Ge bulk materials indicates that Nb_3Ge formed mostly in the double phase regions $Nb_3Ge + Nb_5Ge_3$ at approximately the same composition (29 ± 5) at.% Ge. The formation of A15 material on the Ge-rich side of the phase diagram is consistent with the relatively small lattice parameters we have observed and the enhanced superconducting properties described in the next section.

7.4.3 AC magnetometry

The superconducting properties were investigated using ac magnetometry. The superconducting parameters derived from these measurements are $T_{C,onset}$ and $B_{C2}(0)$. Zero-field and in-field data are measured on the four groups of samples shown in Figure 7.1: HIPYYY, HIP600 + AZZZ, HIP1200 + AZZZ and AZZZ. Data were obtained for both series M6 and M20. We report AC magnetisation data for all samples in zero field and typical data for one sample in field. A summary plot of $T_{C,onset}$ vs. processing temperature and corresponding table is also provided. $T_{C,onset}$, $B_{C2}(0)$ and background signal will be discussed in turn.

Group 1: M6 + HIPYYY and M20 + HIPYYY. The zero-field data are shown for M6 + HIPYYY in Figure 7.26 and the in-field data for one sample in Figure 7.27. Equivalent data for series M20 + HIPYYY are shown in Figure 7.28 and Figure 7.29. Figure 7.30 and Table 7.16 reports the superconducting properties of both series. In this group, all ac magnetisation in zero-field T_C values were found to vary in the range 7-9 K with two different behaviours for M6 and M20. In series M6, the transition temperature decreases monotonically from ~ 8 to ~ 7 K with increasing HIP'ing temperature. In series M20, T_Cs first increases to reach a maximum value of 9 K when HIP'ed at 700 °C. This sample M20 + HIP700 also shows a second transition at 4.46 K (Figure 7.29). These two transitions have associated $B_{C2}(0)$ values of 1.61 and 1.68 T, respectively. All HIP'ed samples show a small $B_{C2}(0)$ of ~ 1- 2 T. In absence of magnetic field, the normal state magnetisation above T_C is, within the noise, zero for samples M6 + HIP700, M6 + HIP800 and M6 + HIP1200. All samples from series M20 and M6 + HIP600 show a paramagnetic response in zero field whereas for higher fields the background magnetic moment is slightly diamagnetic. The paramagnetic background/normal state magnetisation depends on the sample considered and was found to be ~10 $A \cdot m^{-1}$ for sample M6 + HIP600 and ~ 2 - 5 $A \cdot m^{-1}$ for series M20.

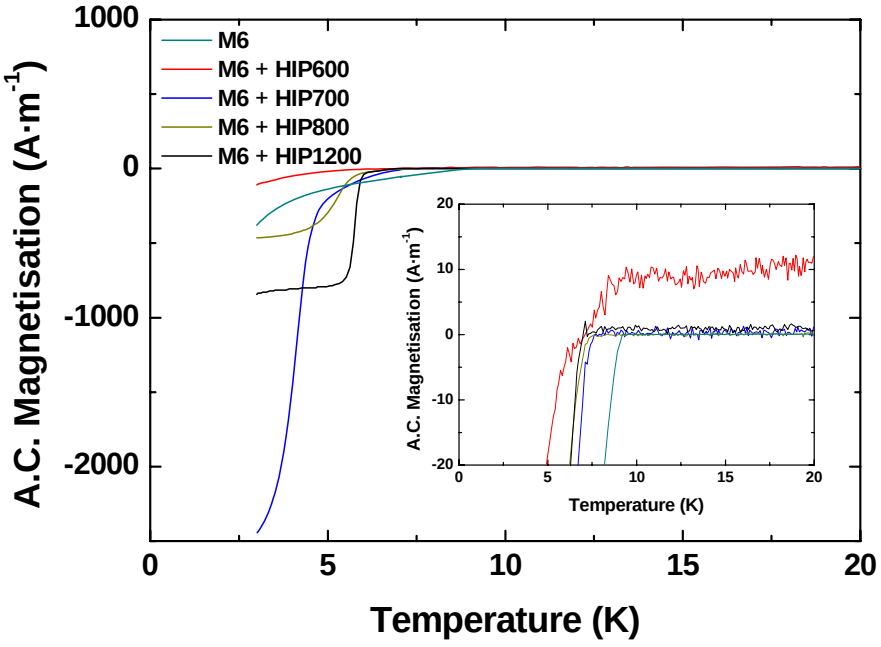

Figure 7.26 Zero field a.c. magnetization for M6 + HIPYYY and precursor powder prior to HIP'ing.

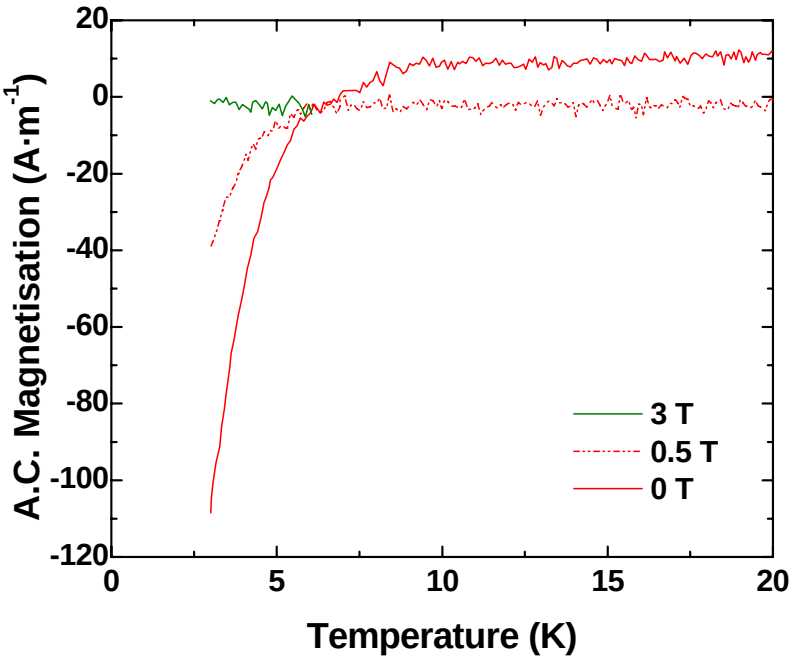

Figure 7.27 AC magnetization versus temperature for M6 + HIP600.

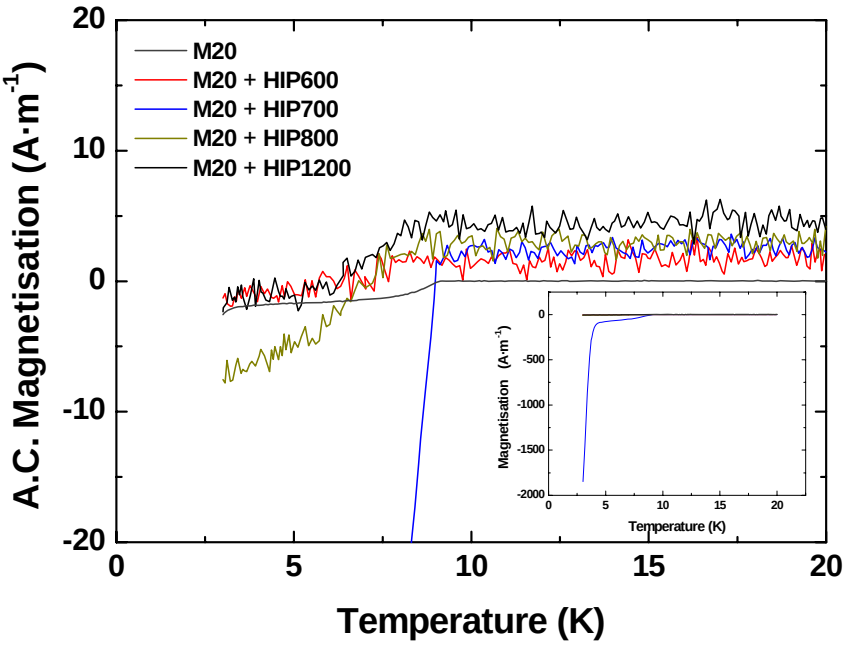

Figure 7.28 Zero field A.C. magnetization for M20 + HIPYYY and precursor powder prior to HIP'ing.

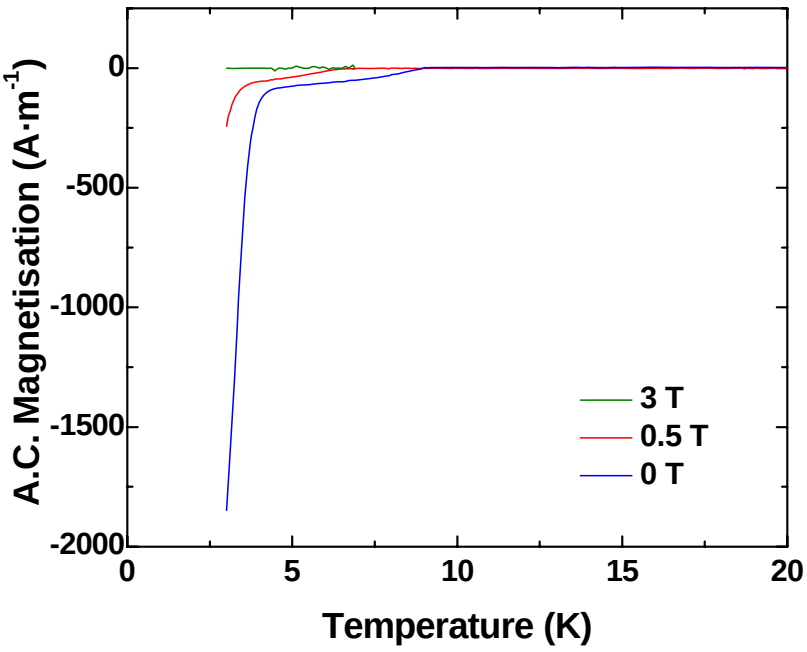

Figure 7.29 A.C. magnetization versus temperature for M20 + HIP700.

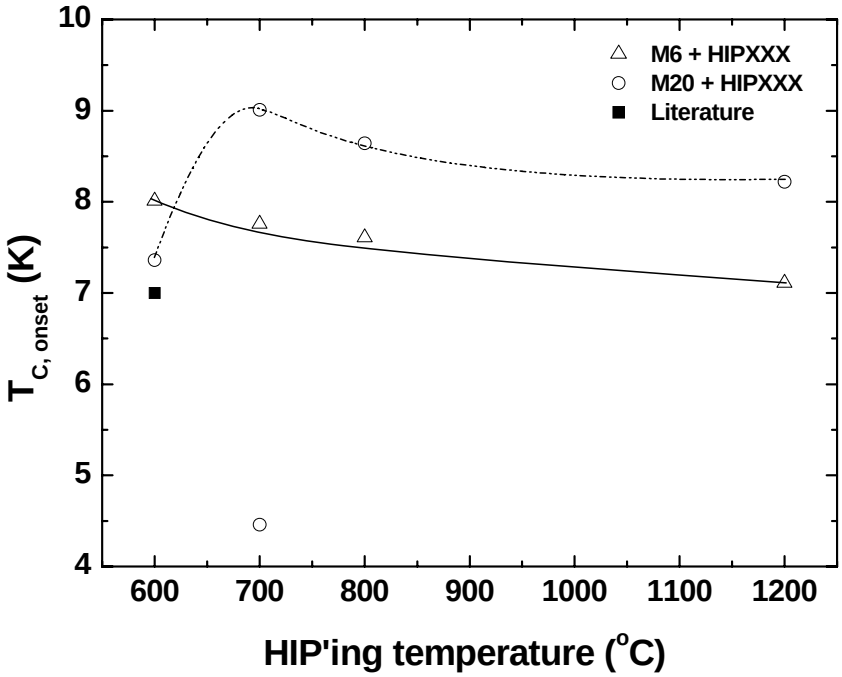

Figure 7.30 $T_{C,onset}$ for M6 (triangle) and M20 (circle) processed using HIPYYY. Typical T_C for Nb_3Ge in bulk form from literature (full squares) is also reported [46,50].

HIPYYY	Series M6		Series M20	
	$T_{C,onset}$ (K)	$B_{C2}(0)$ (T)	$T_{C,onset}$ (K)	$B_{C2}(0)$ (T)
HIP600	8.01	1.13	7.36	0.74
HIP700	7.76	1.55	9.01 {4.46}	1.61 {1.68}
HIP800	7.61	1.80	8.61	1.42
HIP1200	7.11	1.47	8.22	1.23

Table 7.16 $T_{C,onset}$ and B_{C2} for M6 and M20 processed using HIPYYY. In curly brackets, the second transition temperature is recorded.

Group 2: M6 + HIP600 + AZZZ and M20 + HIP600 + AZZZ. Data from samples HIP'ed at 600 ^{o}C and subsequently annealed are shown for series M6 + HIP600 +AZZZ in Figure 7.31 and Figure 3.32 and for series M20 + HIP600 + AZZZ in Figure 7.33 and Figure 7.34. Figure 7.35 and Table 7.18 report their superconducting properties. T_Cs were found for these materials vary in the range 7 – 12 K with similar in-field behaviour. T_Cs reach a maximum value of 12.02 and 10.77 K for samples M6 + HIP600 + A700 and M20 + HIP600 + A700, respectively. The upper critical field was found to be dramatically improved from ~ 1 Tesla up to 13.10 T and 12.63 T. Sample M6 + HIP600 + A700 shows better superconducting properties than the equivalent one milled for 20 h. This might be attributed to a smaller contamination from the milling media and atmosphere. Samples M6 + HIP600 + A600 and M20 + HIP600 + A600 show a double transition with high T_Cs of 17.01 and 16.43 K and lower T_Cs of 7.18 K and 7.61 K, respectively. This indicates that the sample is not homogeneous and that there is a small amount of highly ordered A15 phase. Unfortunately, this phase does not produce a superconducting transition in field (at 0.5 T, cf Figure 7.32 and Figure 7.34) indicating that the evaluated B_{C2} is produced by the low T_C phase. Indeed the high quality A15 grain distribution does not significantly screen the sample in any applied magnetic field. The background is zero, within the noise, for all M6 + HIP600 + AZZZ samples (except the precursor M6 + HIP600) and sample M20 + HIP600 + A600, M20 + HIP600 + A700 and M20 + HIP600 + A800. We note that sample M6 + HIP600 and the precursor sample M20 + HIP600 have a similar paramagnetic magnetisation in the

normal state (~ 2 $A \cdot m^{-1}$). The additional annealing removes the paramagnetic response in the normal state.

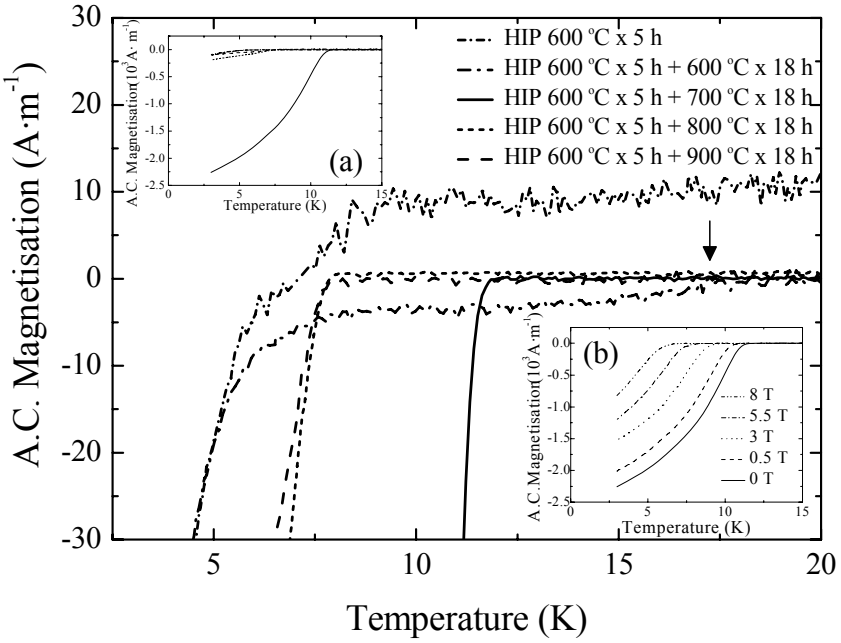

Figure 7.31 Zero field A.C. magnetisation versus temperature for M6 + HIP600 + AZZZ and precursor material prior to annealing. The remnant high T_C at 17.01 K is shown more clearly in Figure 7.32. Inset a: full-scale y-axis for zero field A.C magnetisation. Inset b: In-field A.C. magnetisation versus temperature for M6 + HIP600 + A700.

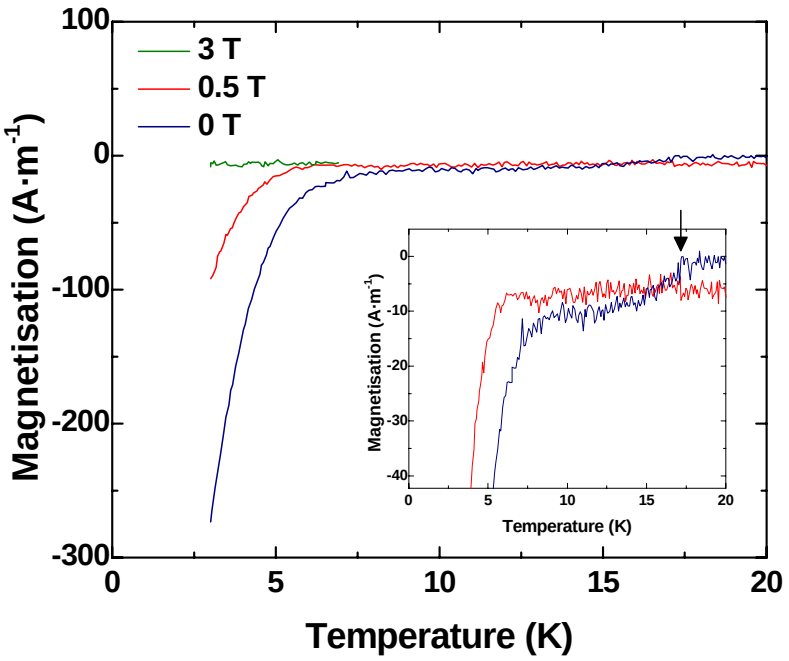

Figure 7.32 A.C. magnetization versus temperature for M6 + HIP600 + A600. The arrow shows remnant high T_C at 17.01 K.

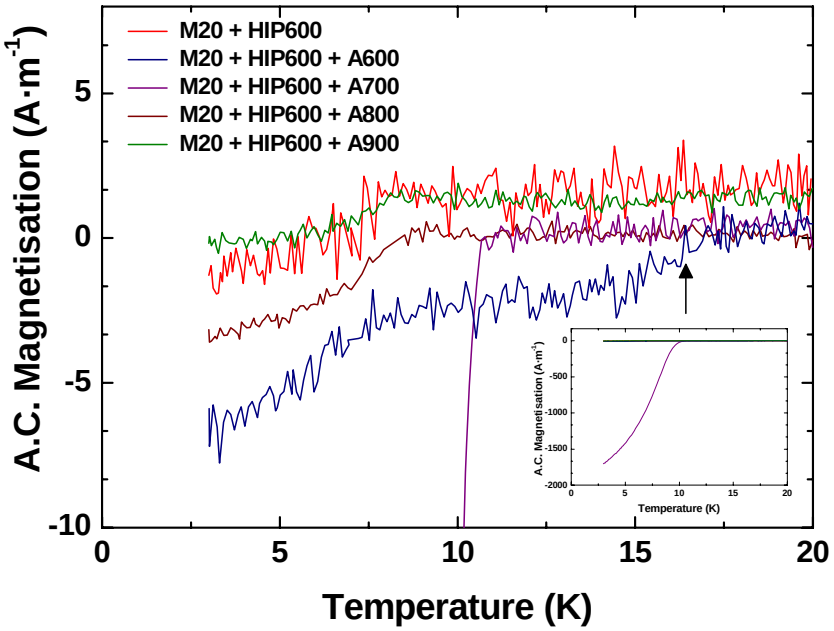

Figure 7.33 Zero field a.c. magnetisation versus temperature for M20 + HIP600 + AZZZ. The remnant high T_C at 16.43 K is shown more clearly in Figure 7.34.

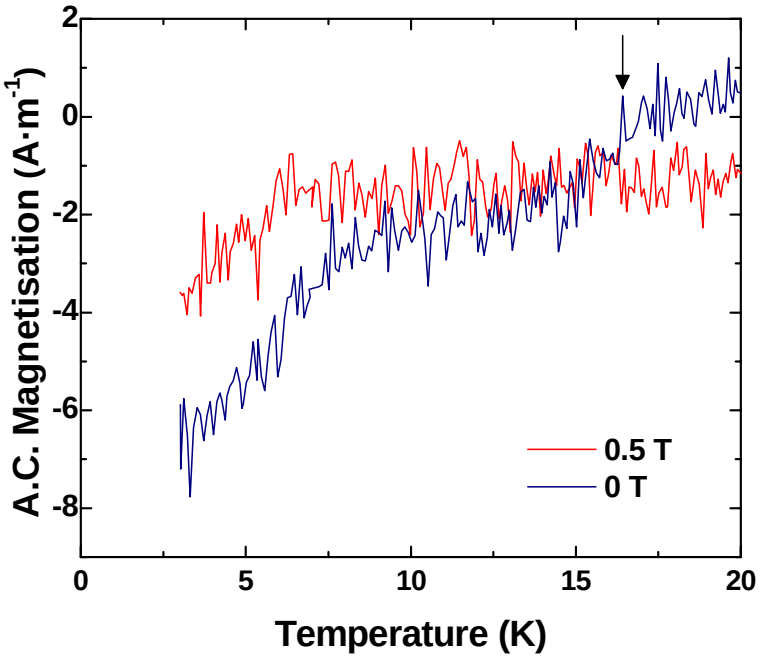

Figure 7.34 A.C. magnetization versus temperature for M20 + HIP600 + A600. The arrow shows remnant high T_C at 16.43 K.

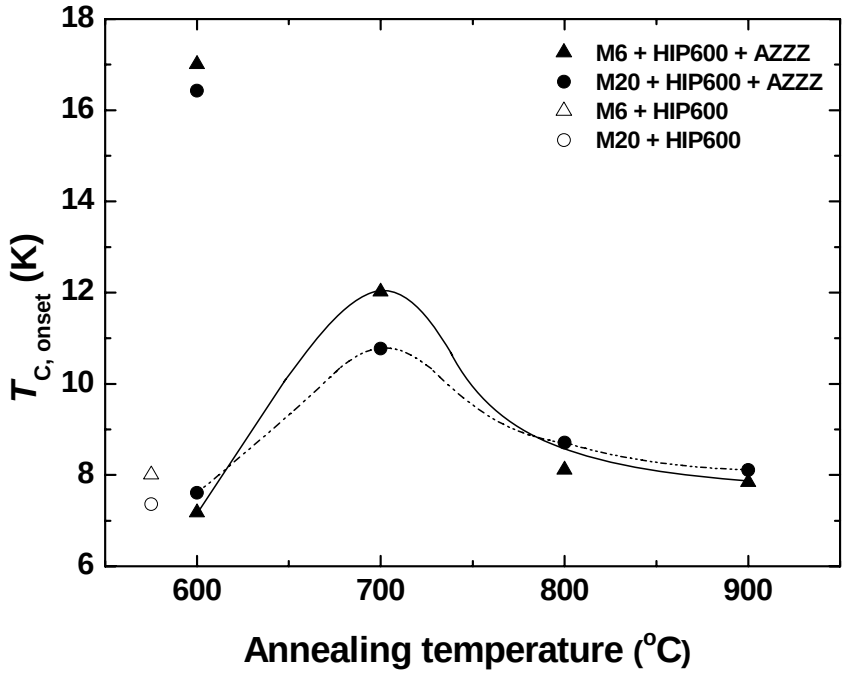

Figure 7.35 $T_{C,onset}$ for M6 (triangle) and M20 (circle) processed using HIP600 + AZZZ. The empty symbol represents the precursor state (HIP600) prior to annealing.

HIP600 + AZZZ	**Series M6**		**Series M20**	
	$T_{C,onset}$ **(K)**	$B_{C2}(0)$ **(T)**	$T_{C,onset}$ **(K)**	$B_{C2}(0)$ **(T)**
HIP600	8.01	1.13	7.36	0.74
HIP600 + A600	7.18 {17.01}	2.39	7.61 {16.43}	2.16
HIP 600C + A700	12.02	13.10	10.77	12.63
HIP600 + A800	8.12	1.61	8.71	1.25
HIP600 + A900	7.85	1.63	8.11	1.47

Table 7.17 $T_{C,onset}$ and B_{C2} for M6 and M20 processed using HIP600 + AZZZ and precursor material prior to annealing. In curly brackets, the second transition temperature is recorded.

Group 3: M6 + HIP1200 + AZZZ and M20 + HIP1200 + AZZZ. Zero-field data for samples HIP'ed at 1200 ^{o}C and subsequently annealed are shown by Figure 7.36 and Figure 7.37 for series M6 and M20, respectively. Figure 7.38 and Table 7.18 compare the superconducting properties of these samples. T_Cs and B_{C2} for both series were found to be ~ 7.5 K and ~ 1-2 T, respectively. Only sample M6 + HIP1200 + A700 shows two superconducting transitions with T_C of 16.17 and 7.61 K. The background is ~1 A·m^{-1} for both groups M6 + HIP1200 + AZZZ and M20 + HIP1200 + AZZZ. This value is slightly lower than that of samples M6 + HIP1200 and M20 + HIP1200. Samples M20 + HIP1200, M20 + HIP1200 + A700/A800/A900 show similar saturation magnetisations/superconducting volume. The lack of any change in superconducting properties for these samples is consistent with the similarities observed in the XRD data.

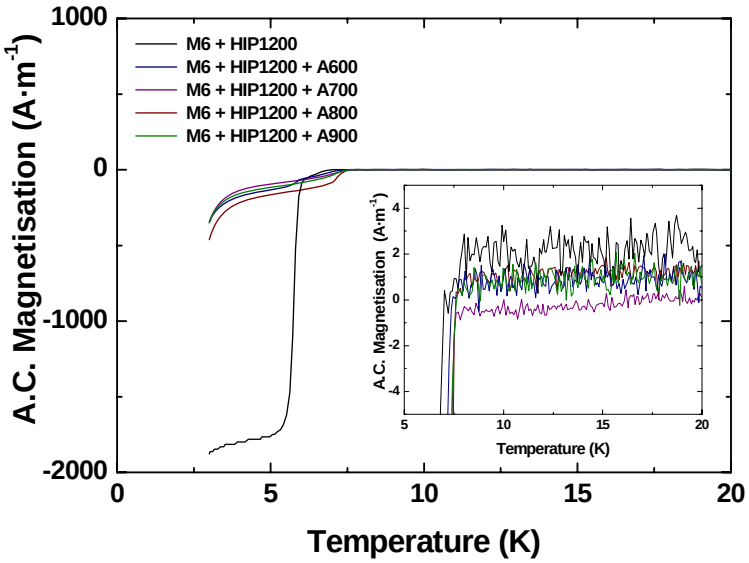

Figure 7.36 Zero field a.c. magnetisation versus temperature for M6 + HIP1200 + AZZZ.

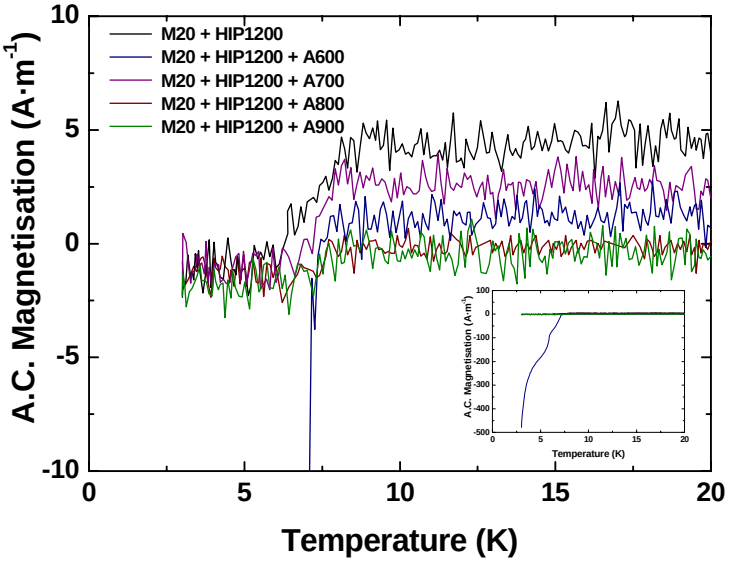

Figure 7.37 Zero field a.c. magnetisation versus temperature for M20 + HIP1200 + AZZZ.

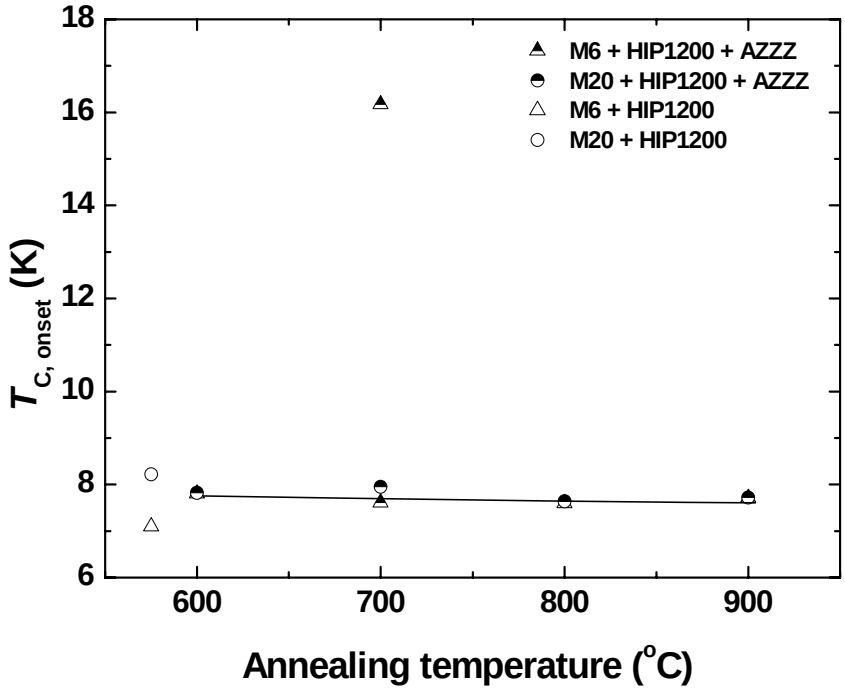

Figure 7.38 $T_{C,onset}$ for M6 (triangle) and M20 (circle) processed using HIP1200 + AZZZ. The empty symbol represents the precursor state (HIP1200) prior to annealing.

HIP1200 + AZZZ	Series M6		Series M20	
	$T_{C,onset}$ (K)	$B_{C2}(0)$ (T)	$T_{C,onset}$ (K)	$B_{C2}(0)$ (T)
HIP1200	7.11	1.47	8.22	1.23
HIP1200 + A600	7.81	1.36	7.82	1.87
HIP 1200C + A700	7.61 {16.17}	1.57	7.95	1.20
HIP1200 + A800	7.60	1.44	7.64	1.54
HIP1200 + A900	7.71	1.51	7.72	1.44

Table 7.18 $T_{C,onset}$ and B_{C2} for M6 and M20 processed using HIP1200 + AZZZ and precursor material prior to annealing. In curly brackets, the second transition temperature is recorded.

Group 4: M6 + AZZZ and M20 + AZZZ. Data for the milled and annealed samples (group AZZZ) are shown in Figure 7.39 and Figure 7.40 for M6 and M20, respectively. Figure 7.41 and Table 7.19 compare the superconducting properties of annealed samples. T_Cs and B_{C2} were found for group M6 + AZZZ and M20 + AZZZ to be approximately constant with values ~ 8 K and ~1-2 T, respectively. Double phase samples are samples: M6 + A800 (T_C = 16.91 and 8.9 K), M20 + A800 (T_C = 16.09 and 8.22 K) and M20 + A900 (T_C = 16.52 and 8.26 K).

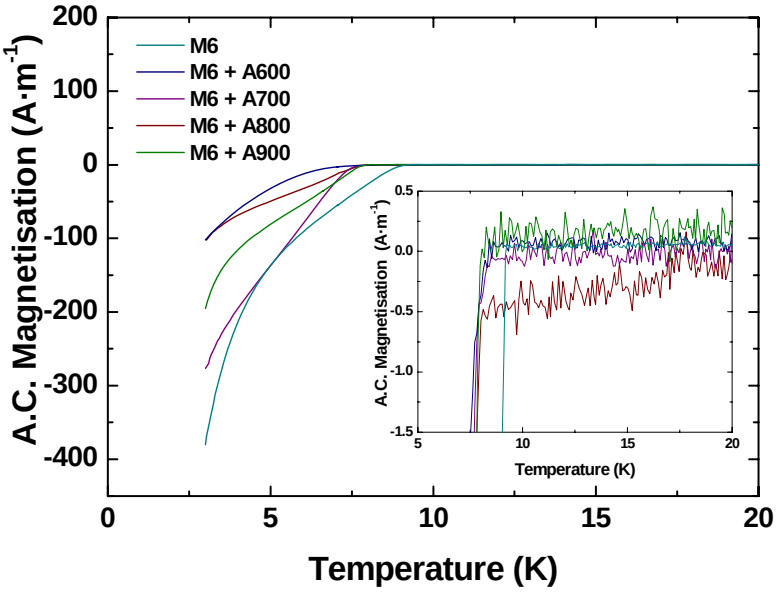

Figure 7.39 Zero field a.c. magnetisation versus temperature for M6 + AZZZ.

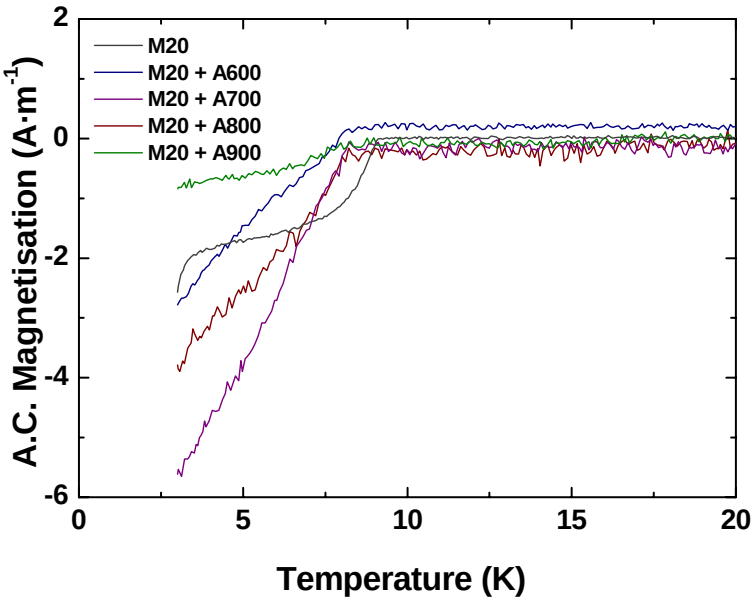

Figure 7.40 Zero field a.c. magnetisation versus temperature for M20 + AZZZ.

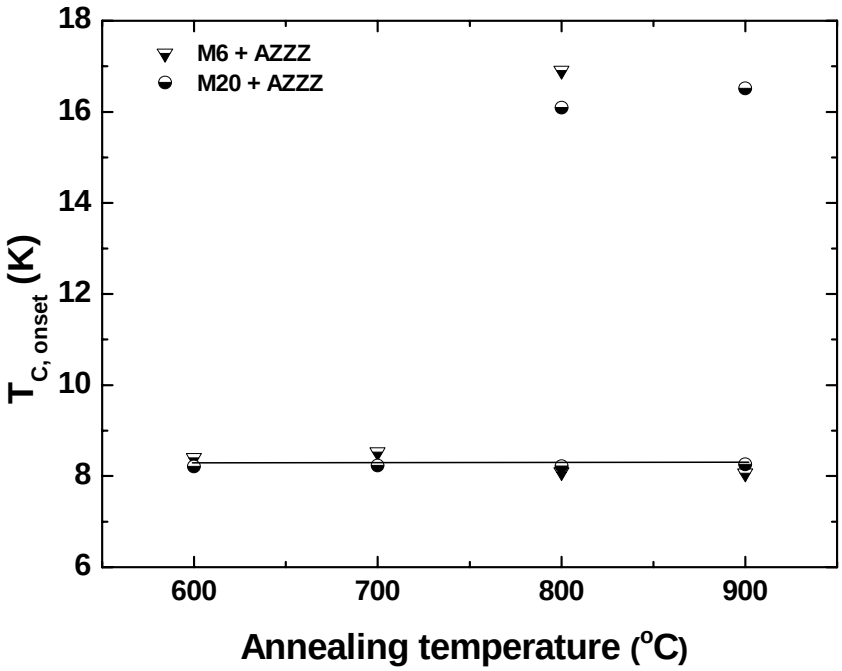

Figure 7.41 $T_{C,onset}$ for M6 (triangle) and M20 (circle) processed using AZZZ.

AZZZ	Series M6		Series M20	
	$T_{C,onset}$ (K)	$B_{C2}(0)$ (T)	$T_{C,onset}$ (K)	$B_{C2}(0)$ (T)
A600	8.40	1.35	8.21	1.36
A700	8.53	1.30	8.23	1.79
A800	8.09 {16.91}	1.34	8.22 {16.09}	1.39
A900	8.06	1.49	8.26 {16.52}	1.44

Table 7.19 $T_{C,onset}$ and B_{C2} for M6 and M20 processed using AZZZ and precursor material prior to annealing. In curly brackets, the second transition temperature is recorded.

Summary of conclusion for ac magnetometry. The combination of HIP'ing and subsequent annealing has produced state-of-the-art Nb_3Ge A15 samples with record values for T_C and B_{C2} of ~ 12 K and ~ 13 T, respectively. A.c. magnetisation measurements show that the superconducting properties of nanocrystalline materials are drastically improved, as shown by samples M6 + HIP600 + A700 and M20 + HIP600 + A700. Better superconducting properties were found in HIP'ed bulk materials fabricated from powders previously milled for up to 6 h rather than 20 h. We suggest that short

milling time can be used to produce both lower contamination and small GS. Almost all the a.c. magnetisation curves show broad superconducting transitions, which indicate that our samples are multiphase, in agreement with XRD (subsection 7.4.1) and EDX (subsection 7.4.2). Our results show that both HIP'ing and annealing are both required to produce high T_C. This implies that good grain connectivity and density obtained by milling and HIP'ing in conjunction with some crystallisation of material with high Ge content improves the superconducting properties.

7.4.4 Discussion and conclusion

Finally, we review superconducting properties, composition and microstructure shown in nanocrystalline Nb_3Ge (A15) bulk superconductors. Data presentation and discussion are structured around the four groups of materials: MX + HIPYYY, MX + HIP600 + AZZZ, MX + HIP1200 + AZZZ and MX + AZZ. Summary plots Figure 7.44 and Figure 7.45 show the $T_{C,onset}$ versus $a_{Nb\text{-}Ge}$ for different thermal processings. The XRD properties are also given together with $T_{C,onset}$ and B_{C2} by Table 7.20. Table 7.21 reports the lattice parameter for our best Nb_3Ge nanocrystalline bulk materials, the corresponding Ge solid solubility (obtained from figure 3.5(b)) and the expected T_C (obtained from figure 3.36). The interpretation of these new materials is based on the various measurements performed and on a relevant comparison with the literature.

Groups 1 and 2: MX + HIP YYY and MX + HIP600 + AZZZ. Figure 7.42 and Figure 7.43 show $T_{C,onset}$ against $a_{Nb\text{-}Ge}$ for group 1 and group 2, respectively. Figure 7.44 reports $a_{Nb\text{-}Ge}$ together with $T_{C,onset}$ (second y-axis) versus the HIP'ing temperature. The lattice parameter decreases while T_C increases for M6 + HIPYYY and M20 + HIPYYY. Figure 7.45 gives $a_{Nb\text{-}Ge}$ and $T_{C,onset}$ (second y-axis) against each annealing temperature for group 2. In the same figure, $T_{C,onset}$ shows a maximum improvement of ~ 4 K and ~ 3 K starting from the precursor HIP'ed state in series M6 + HIP600 + AZZZ and M20 + HIP600 + AZZZ, respectively. The lattice parameters show an increase after A700. The increase in T_C with Ge content observed in group 1 and group 2 is a trend observed in films [83] although the absolute values are very different (cf Figure 7.46). Figure 7.46 reports $T_{C,onset}$ against $a_{Nb\text{-}Ge}$ for samples M6/M20 + HIPXXX and M6/M20 + HIP600 + AZZZ. For comparison purposes, the data from Nb_3Ge films are also reported. The high-T_C data associated with the remnant

material are in agreement with data from thin films of Nb_3Ge [50], as shown by Figure 7.46. We suggest that the A15 phase with high T_Cs of ~ 17 K and ~ 16.5 K, which formed in the M6 + HIP600 + A600 and M20 + HIP600 + A600 samples is possibly produced by a small volume fraction of highly ordered Nb_3Ge. The XRD patterns for M6/M20 + HIP600 + A700 (Figure 7.12 and Figure 7.13) suggest the oxides compete with good superconducting properties. The lattice parameter for the best Nb_3Ge bulk materials are reported in Table 7.21 with the corresponding solid solubility taken from sputtered materials [50]. We conclude that the 'best' Nb_3Ge bulk materials with the highest T_C and $B_{C2}(0)$ have a larger Ge content in the A15 structure.

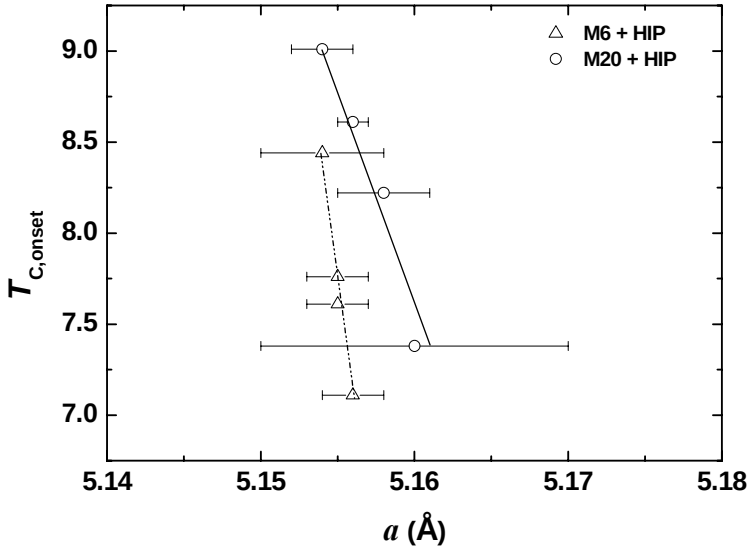

Figure 7.42 $T_{C,onset}$ and lattice constant of the A15 phase for M6 + HIP (triangle) and M20 + HIP (circle) processed using milling and HIP'ing alone.

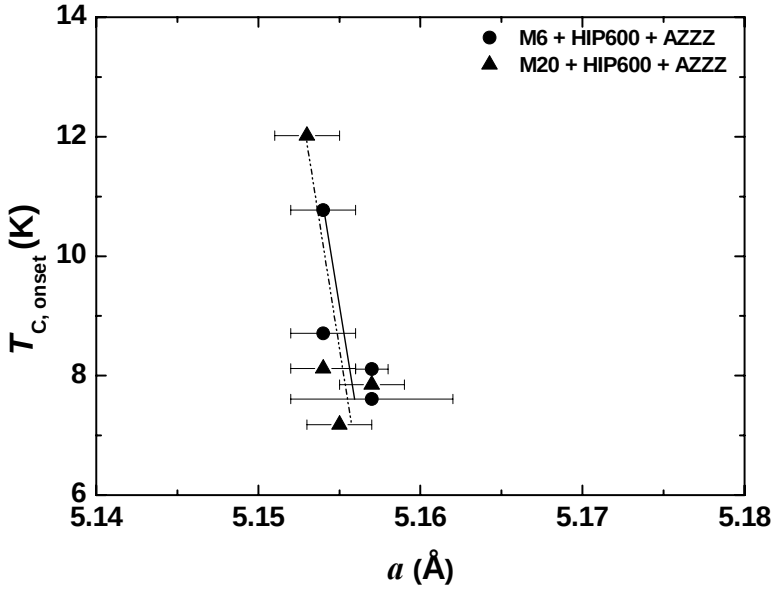

Figure 7.43 $T_{C,onset}$ and lattice constant of the A15 phase for M6 + HIP600 + AZZZ (triangle) and M20 + HIP600 + AZZZ (circle) processed using milling and HIP'ing alone.

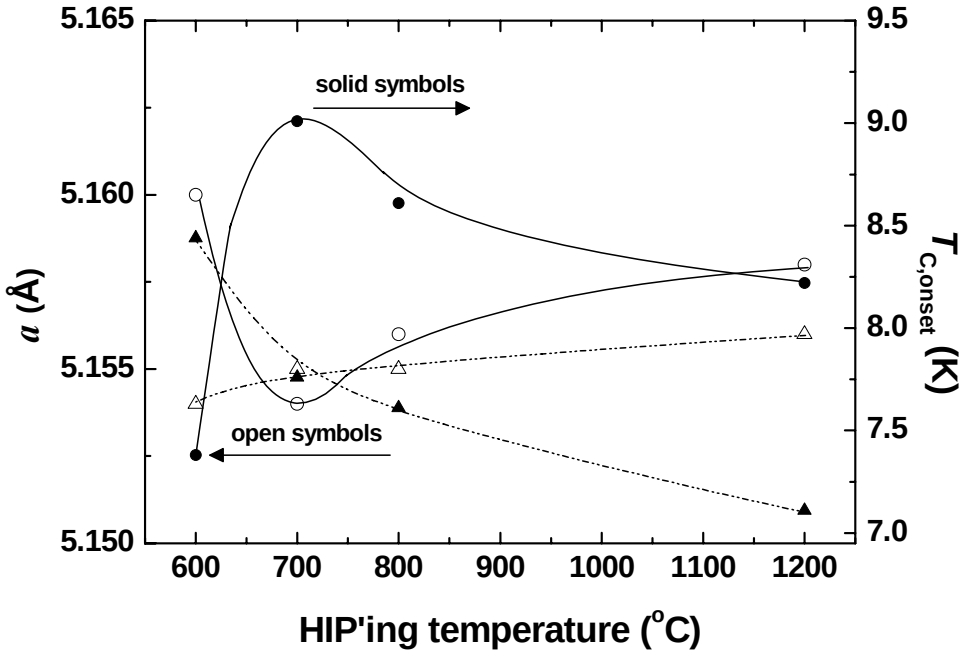

Figure 7.44 Lattice constant (open symbols) and $T_{C,onset}$ (full symbols) for M6 + HIPYYY (triangle) and M20 + HIPYYY (circle) processed using milling and HIP'ing alone.

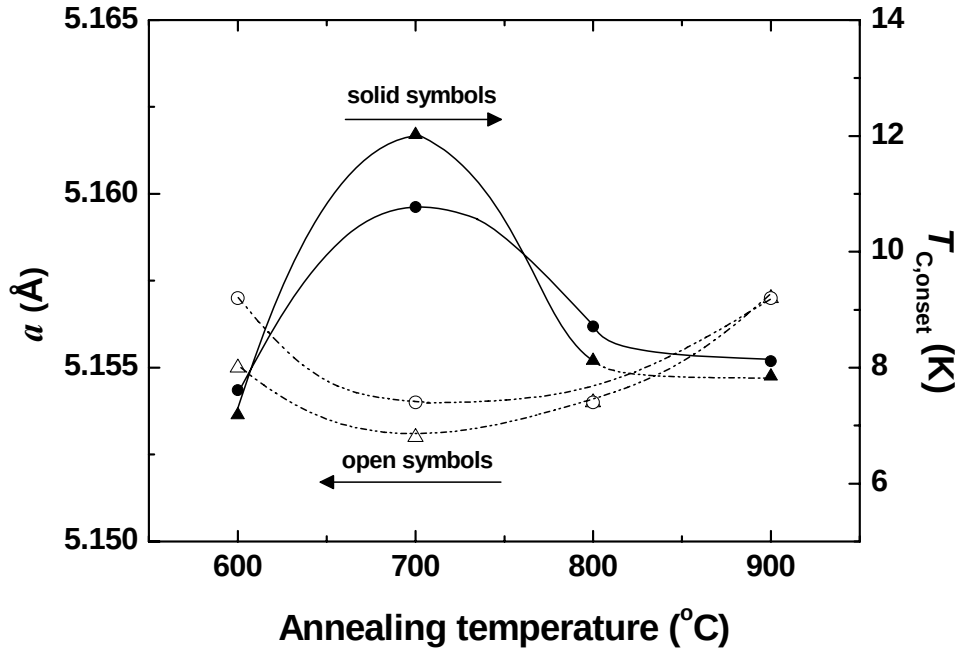

Figure 7.45 Lattice constant (empty symbols) and critical temperature (full symbols) of Nb_3Ge milled for up to 6 h (triangle) and 20 h (circle), HIP'ed at 600 °C × 5 h and subsequently annealed at different temperatures for 18 h.

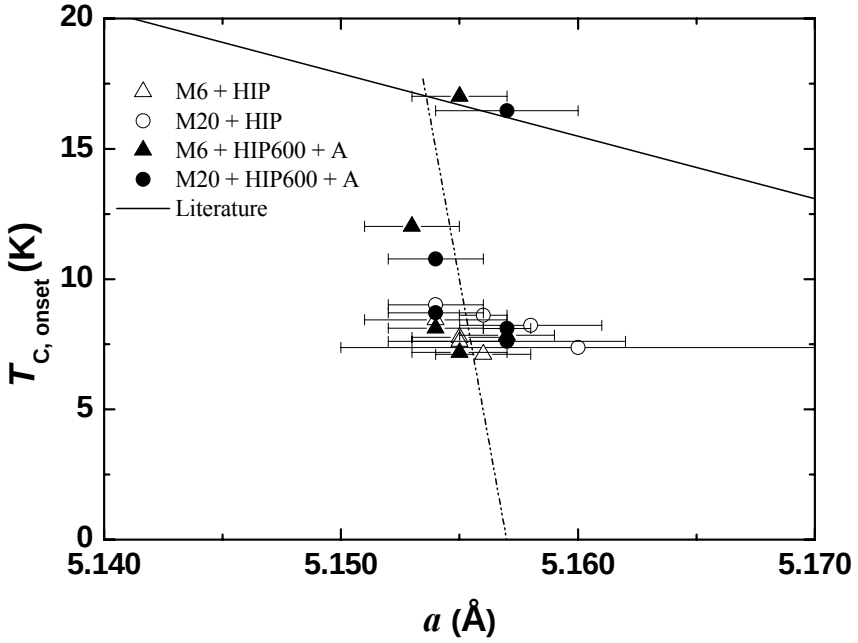

Figure 7.46 Critical temperature versus lattice constant of Nb_3Ge milled for up to 6 h (M6) and 20 h (M20), HIP'ed at different temperatures for 5 h (empty symbols); HIP'ed at 600 ^oC × 5 h and subsequently annealed at different temperatures for 18 h (full symbols). The data from Nb_3Ge films are also reported [83].

Groups 3 and 4: MX + HIP1200 + AZZZ and MX +AZZZ. Figure 7.47 reports $T_{C,onset}$ versus $a_{Nb\text{-}Ge}$ for MX + HIP1200 + AZZZ. Small $T_{C,onset}$ variations (~ 0.6 K) for post annealed samples show that the precursor material (HIP1200) is almost stable for both series. The maximum $T_{C,onset}$ changes for MX +AZZZ are ~ 0.5 and 0.05 K for M6 + AZZZ and M20 + AZZZ, respectively as shown by Figure 7.48. We suggest that T_C values below 9 K might also produced by $(Nb)_{ss}$.

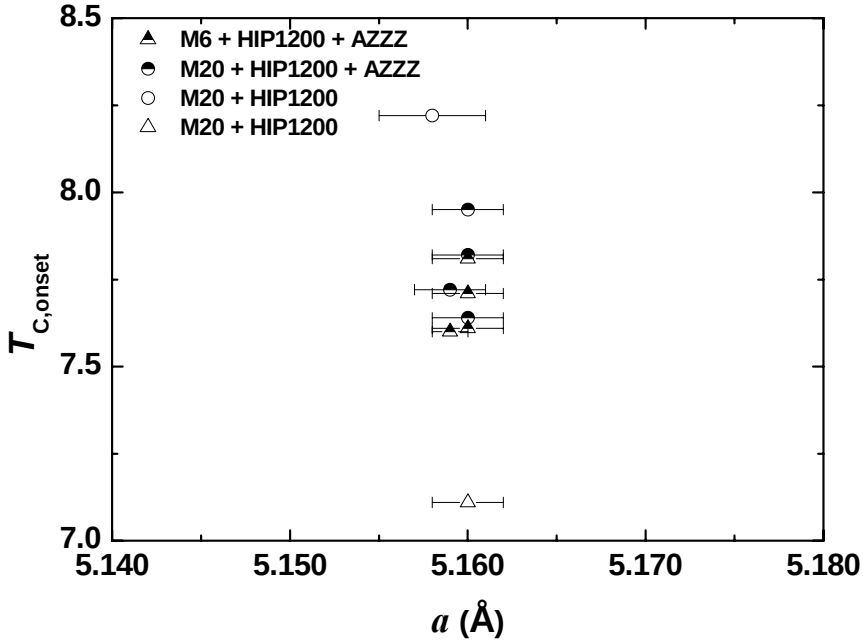

Figure 7.47 $T_{C,onset}$ and lattice constant of the A15 phase for M6 (triangle) and M20 (circle) processed using HIP1200 + AZZZ. The empty symbol represents the precursor state prior to annealing.

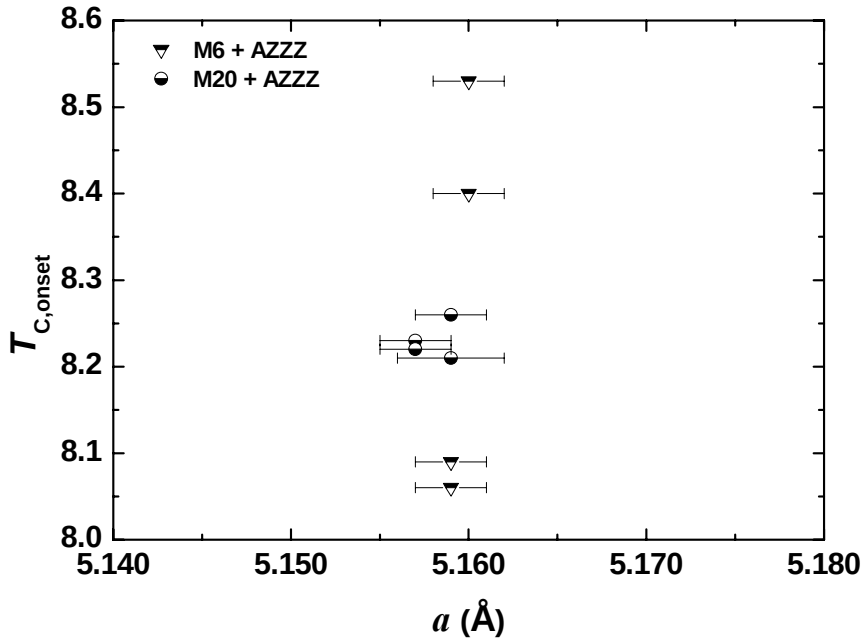

Figure 7.48 $T_{C,onset}$ and lattice constant of the A15 phase for M6 (triangle) and M20 (circle) processed using AZZZ

Group	Series M6				Series M20			
	GS **(nm)**	$a_{\text{Nb-Ge}}$ **(Å)**	$T_{\text{C,onset}}$ **(K)**	$B_{C2}(0)$ **(T)**	***GS*** **(nm)**	$a_{\text{Nb-Ge}}$ **(Å)**	$T_{\text{C,onset}}$ **(K)**	$B_{C2}(0)$ **(T)**
HIP600	2(1)	5.154(3)	8.01	1.13	2(1)	5.16(1)	7.36	0.74
HIP700	3(1)	5.155(2)	7.76	1.55	3(2)	5.154(2)	9.01 {4.46}	1.61 {1.68}
HIP800	9(4)	5.155(2)	7.61	1.80	6(3)	5.156(1)	8.61	1.42
HIP1200	11(6)	5.156(2)	7.11	1.47	11(4)	5.158(3)	8.22	1.23
HIP600 + A600	1(2)	5.155(2)	7.18 {17.01}	2.39	3(4)	5.157(3)	7.61 {16.43}	2.16
HIP600 + A700	2(7)	5.153(2)	12.02	13.10	8(6)	5.154(1)	10.77	12.63
HIP600 + A800	6(2)	5.154(2)	8.12	1.61	9(6)	5.154(2)	8.71	1.25
HIP600 + A900	11(5)	5.157(1)	7.85	1.63	11(8)	5.157(1)	8.11	1.47
HIP1200 + A600	8(9)	5.160(2)	7.81	1.36	8(2)	5.160(2)	7.82	1.87
HIP1200 + A700	6(3)	5.160(2)	7.61 {16.17}	1.57	6(5)	5.160(2)	7.95	1.20
HIP1200 + A800	6(1)	5.159(1)	7.60	1.44	8(6)	5.160(2)	7.64	1.54
HIP1200 + A900	15(3)	5.160(2)	7.71	1.51	14(4)	5.159(2)	7.72	1.44
A600	3(3)	5.160(2)	8.40	1.35	2(1)	5.159(3)	8.21	1.36
A700	6(2)	5.160(2)	8.53	1.30	6(7)	5.157(2)	8.23	1.79
A800	8(4)	5.159(2)	8.09 {16.91}	1.34	6(5)	5.157(2)	8.22 {16.09}	1.39
A900	11(6)	5.159(2)	8.06	1.49	11(11)	5.159(2)	8.26 {16.52}	1.44

Table 7.20 Grain size (*GS*), lattice constant of the A15 phase and $T_{\text{C,onset}}$ for M6 and M20 processed using different technique. In curly brackets, the second transition temperature is recorded.

Sample	Phase	Lattice constant (Å)	Solid.Sol. (Ge at.%)	Expected T_C (K)
M20 + HIP600 + AZZZ	Nb_3Ge	5.153 ± 0.002	22.0 ± 0.5	17.1 ± 0.5
M20 + HIP600 + AZZZ	Nb_3Ge	5.154 ± 0.002	21.8 ± 0.5	16.9 ± 0.5

Table 7.21 A15 lattice constant representative for Nb_3Ge M6/M20 + HIP600 + AZZZ bulk materials and corresponding solid solubility from literature [50,83]. The expected T_C is from microcrystalline samples.

In summary, we conclude that milling and subsequent annealing HIP600 + A700 produces the crystallisation of the A15 phase without the oxides that occur at higher temperature and compete with superconductivity. At higher temperatures, milling and subsequent HIP'ing and annealing do not produce the highest T_C values in Nb_3Ge bulk materials although higher temperatures increase the amount of A15 material and the grain size. We attribute this to also the increased Ge content of the A15 at these higher temperatures. In the literature (cf chapter 3 [12,47]) annealing has been performed on arc-melted microcrystalline A15 superconductors as a way to improve the atomic ordering.

In this work, post-HIP annealing has produced state-of-the-art Nb_3Ge in bulk form with record T_C and B_{C2} of ~ 12 K and ~ 13 T. Previously used conventional techniques (i.e. annealing) produced a typical T_C of 6-7 K for Nb_3Ge in bulk form [37,50]. So far, only thin-film or splat-cooled deposition have produced higher T_C Nb_3Ge superconductors which set a target limit for bulk materials with T_C and $B_{C2}(0)$ values of ~ 23 K and ~ 37 T, respectively [80].

Chapter 8

Fabrication and properties of nanocrystalline $Nb_3Al_{1-x}Ge_x$ with x = 0 and x = 0.3 produced using dry mechanical alloying and milling

8.1 Introduction

Chapter 8 reports on the properties of nanocrystalline A15 $Nb_3Al_{1-x}Ge_x$ with $0 \leq x \leq 0.3$ superconductors fabricated using dry mechanical alloying and milling. We will use the term mechanical alloying (MA) only in connection with the processing of elemental powders (3Nb + 0.7Al + 0.3Ge) to obtain a homogeneous alloy and also for milling the compounds ($0.7Nb_3Al$ + $0.3Nb_3Ge$). We will refer to the processing of a pure intermetallic (Nb_3Al) as mechanical milling (MM), even though the milling processes were identical (same milling machine, milling media and number of balls). This chapter is structured similarly to chapter 7. The overview of the nanocrystalline fabrication process is reported by section 8.2. Section 8.3 and 8.1 present comprehensively the properties of milled powder prior to consolidation and the properties of nanocrystalline bulk materials, respectively. The comprehensive data include: yield data associated with milling; ICP-MS; differential scanning calorimetry; scanning electron microscopy (SEM) coupled with electron dispersive X-ray (EDX) analysis and XQM (X-ray quantification maps); ACMS (alternate current measurement system); and XRD to investigate microstructure and composition. For more details about the experimental techniques, the reader is referred to Chapter 5. Finally, section 8.4.4 reports a summary of the data and the conclusions. This work is to be submitted to Journal of Applied Physics [170].

8.2 Overview of fabrication of powders and bulk samples

The A15 $Nb_3(Al_{0.7}Ge_{0.3})$ ternary compound has the optimal combination of high critical temperature T_C and extremely high upper critical field B_{C2} of 41 T at 4.2 K [36,62,171]. In this work, we fabricated disordered nanocrystalline powders using dry milling of elemental powders and compounds to produce $Nb_3Al_{1-x}Ge_x$ with x = 0 and 0.3 superconductors. For details about the dry milling, the reader is referred to section 7.2. For details about the starting elemental powders, the reader is referred to chapter 6. The

mechanical alloying was carried out using Nb_3Al (- 100 mesh, 99.5%) and Nb_3Ge (- 100 mesh, 99.5%) from CERAC. The mechanical milling was performed on Nb_3Al alone. There are three different starting powders investigated: 3Nb + 0.7Al + 0.3Ge from elemental powders (E) mixed to produce the ternary compound (T) - denoted with ET; $0.7(Nb_3Al) + 0.3(Nb_3Ge)$ from powders of compounds (C) mixed to produce the ternary (T) compound - denoted with CT; and Nb_3Al - denoted with Nb_3Al.Table 8.1 and Table 8.2 report the processing conditions and nomenclature for precursor powders and bulk materials, respectively. In the text we will use the shorthand ET and CT. In figures, tables and titles, we use ET (3Nb + 0.7Al + 0.3Ge) and CT ($0.7Nb_3Al + 0.3Nb_3Ge$).

Stoichiometric mixes	M.T. (h)	ID Components
3 Nb + 0.7 Al + 0.3 Ge	6	ET M6
3 Nb + 0.7 Al + 0.3 Ge	20	ET M20
0.7 (Nb_3Al) + 0.3 (Nb_3Ge)	20	CT M20
Nb_3Al	20	Nb_3Al M20

Table 8.1 Stoichiometric mixes, milling time (M.T.) and nomenclature for milled powders.

No.	Processing condition	Group ID
1	HIP 600 ^oC × 5 h	Series ID + HIPYYY
2	HIP 700 ^oC × 5 h	
3	HIP 800 ^oC × 5 h	
4	HIP 1200 ^oC × 5 h	
5	HIP 600 ^oC × 5 h + 600 ^oC × 18 h	Series ID + HIP600 + AZZZ
6	HIP 600 ^oC × 5 h + 700 ^oC × 18 h	
7	HIP 600 ^oC × 5 h + 800 ^oC × 18 h	
8	HIP 600 ^oC × 5 h + 900 ^oC × 18 h	
9	HIP 1200 ^oC × 5 h + 600 ^oC × 18 h	Series ID + HIP1200 + AZZZ
10	HIP 1200 ^oC × 5 h + 700 ^oC × 18 h	
11	HIP 1200 ^oC × 5 h + 800 ^oC × 18 h	
12	HIP 1200 ^oC × 5 h + 900 ^oC × 18 h	
13	600 ^oC × 18 h	Series ID + AZZZ
14	700 ^oC × 18 h	
15	800 ^oC × 18 h	
16	900 ^oC × 18 h	

Table 8.2 Processing conditions for Nb-Al-Ge bulk materials based on heat treatment and fabrication method.

The sample identification is based on the forementioned tables and given by: ID components + MX + HIPYYY + AZZZ, where X, YYY and ZZZ are the milling time, and the processing temperature for isochronal HIP'ing and annealing, correspondingly.

8.3 Properties of nanocrystalline powders

The powder changes during high-energy ball milling were investigated by the differential scanning calorimetry, yield, AC magnetometry and XRD results. Each set of results will be discussed in turn for ET, CT, and Nb_3Al. Finally, the properties of milled powders are discussed in section 8.3.6.

8.3.1 Differential scanning calorimetry

The differential scanning calorimetry measurements were taken after sequentially increasing the ball milling time up to 30 h. Figure 8.1, Figure 8.3 and Figure 8.5 show two traces corresponding to two consecutive heating runs at different milling stages for ET, CT and Nb_3Al, correspondingly. The upper traces (from the second heating run) provide a baseline for the reactions which take place during the first heating run. The reaction enthalpy (ΔH_R) and the corresponding peak area (T_R) versus milling time are reported in Figure 8.2, Figure 8.4 and Figure 8.6 for each powder. Table 8.3 summarises the systematic behaviour shown by milled powder. The relevant references which helped with a reasonable interpretation of our DSC traces are from previous investigations, which cover calorimetric investigation and processing of powder particles with ball milling [55,100,135,158]. Exothermic reactions are shown by all DSC traces. The only endothermic peak is shown by unmilled sample ET. In agreement with the Al-Ge phase diagram, an eutectic reaction at ~ 420 ^{o}C occurs at the composition (30 at.% Ge) [55]. The DSC traces are now given and discussed for each material group.

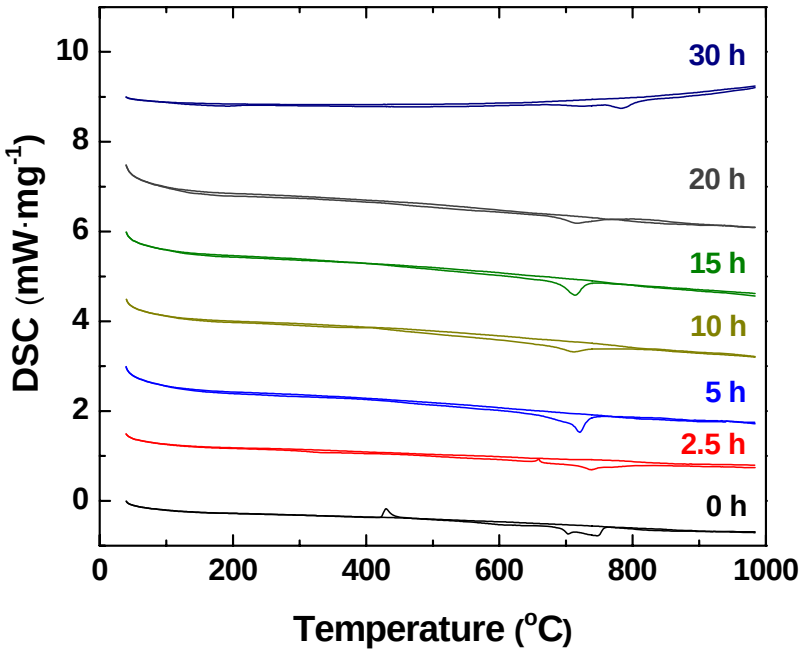

Figure 8.1 DSC traces for ET (3Nb + 0.7Al + 0.3Ge) milled for up to 30 h. The data shown for milled powders have been sequentially offset by 1.5 mW·mg^{-1} from the 0 h data for clarity. The two sets of data provided for each milled sample are both obtained while increasing temperature during the first half of two successive cycles obtained at a heating rate of 10 K·min^{-1}.

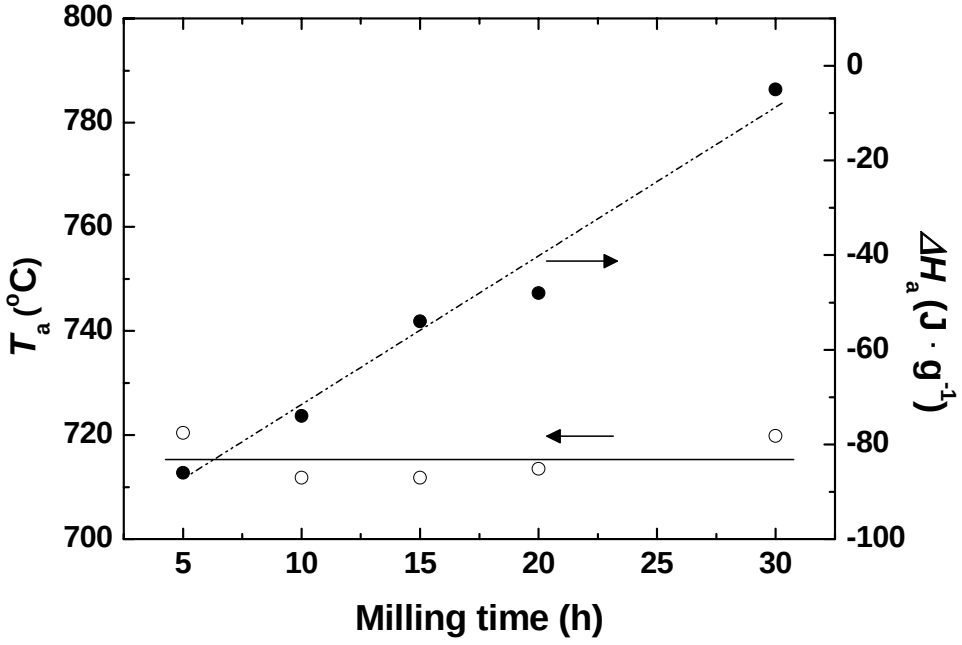

Figure 8.2 DSC peak temperature T_a (full symbols) and enthalpy of amorphisation ΔH_a (open symbols) versus milling times for ET (3Nb + 0.7Al + 0.3Ge) milled for up to 30 h.

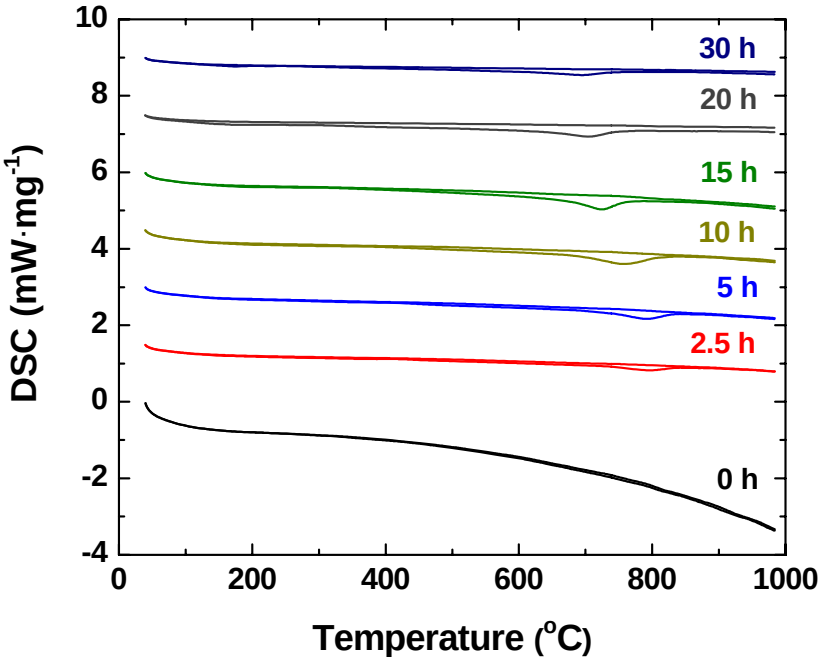

Figure 8.3 DSC traces for CT ($0.7Nb_3Al + 0.3Nb_3Ge$) milled for up to 30 h. The data shown for milled powders have been sequentially offset by 1.5 $mW \cdot mg^{-1}$ from the 0 h data for clarity. The two sets of data provided for each milled sample are both obtained while increasing temperature during the first half of two successive cycles obtained at a heating rate of 10 $K \cdot min^{-1}$.

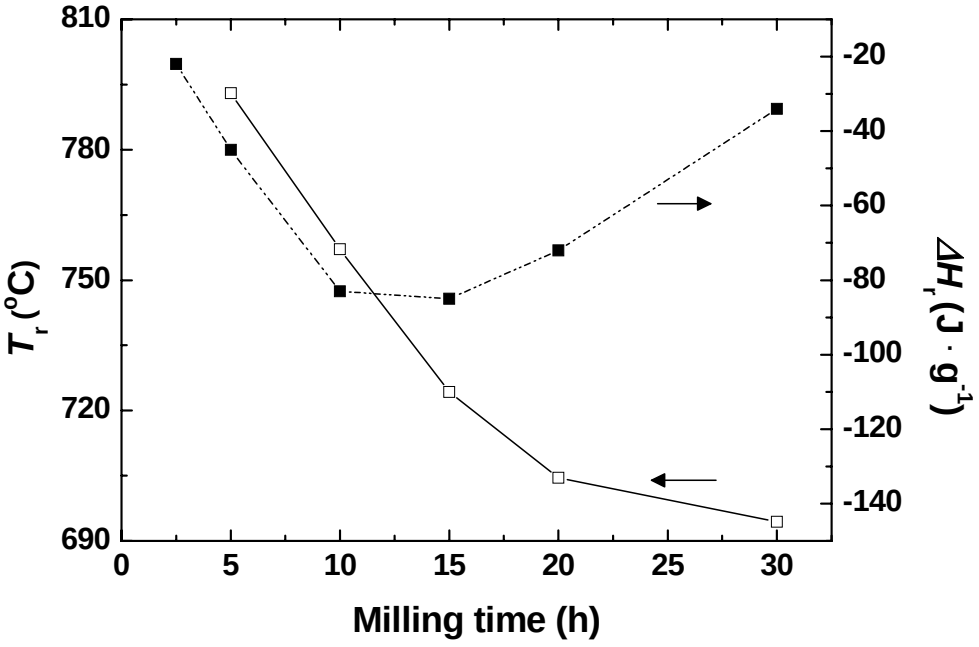

Figure 8.4 DSC peak temperature T_r (open symbols) and enthalpy of reaction ΔH_r (full symbols) versus milling times for CT ($0.7Nb_3Al + 0.3Nb_3Ge$) milled for up 30 h.

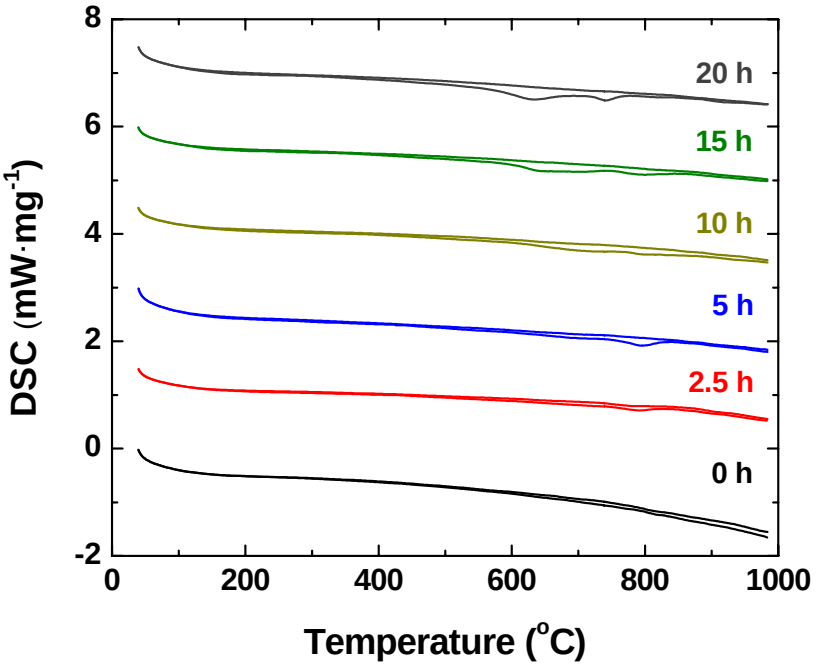

Figure 8.5 DSC traces for Nb_3Al milled for up to 30 h. The data shown for milled powders have been sequentially offset by 1.5 $mW \cdot mg^{-1}$ from the 0 h data for clarity. The two sets of data provided for each milled sample are both obtained while increasing temperature during the first half of two successive cycles obtained at a heating rate of 10 $K \cdot min^{-1}$.

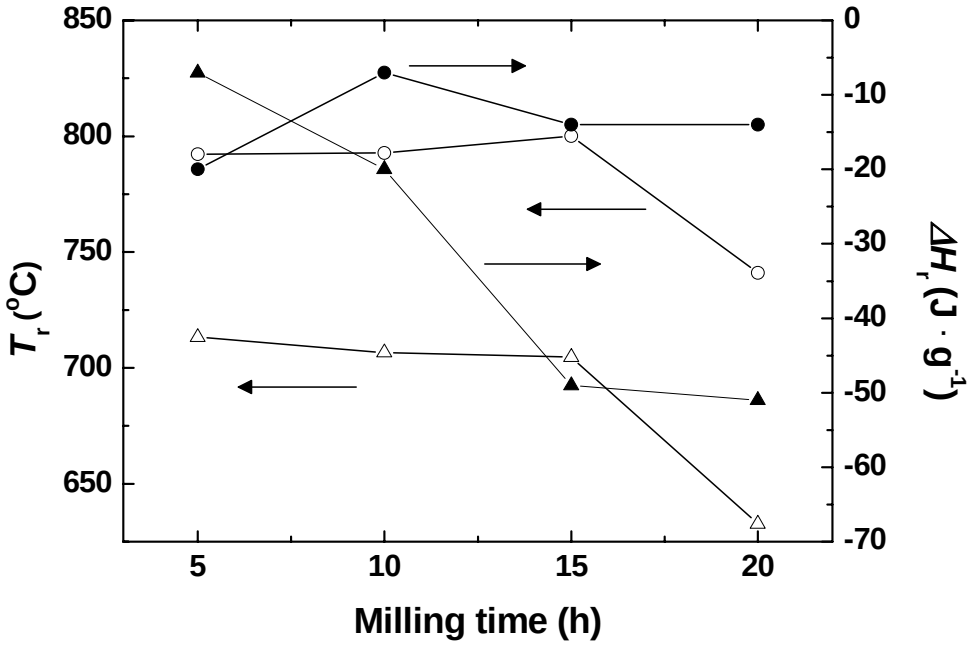

Figure 8.6 Temperatures (open symbols) for double exothermic peaks (full triangles and circles) for Nb_3Al milled for up 30 h. See the text for details

M.T. (h)	ET (3Nb + 0.7Al + 0.3Ge)				CT ($0.7Nb_3Al + 0.3Nb_3Ge$)		Nb_3Al			
	T_a (^oC)	ΔH_a ($J \cdot g^{-1}$)	T_x (^oC)	ΔH_x ($J \cdot g^{-1}$)	T_r (^oC)	ΔH_r ($J \cdot g^{-1}$)	T_x (^oC)	ΔH_x ($J \cdot g^{-1}$)	T_r (^oC)	ΔH_r ($J \cdot g^{-1}$)
2.5	738.0	-34	-	-	793.2	-22	-	-	790	-11
5	720.4	-86	-	-	793.0	- 45	713.3	-7	792.3	-20
10	711.8	-74	-	-	757.1	-83	706.7	-20	792.8	-7
15	713.5	-54	-	-	724.3	-85	704.7	-49	800.1	-14
20	716.8	-48	-	-	704.5	- 72	632.7	-51	741.0	-14
30	719.8	-5	783.5	-17	694.4	-34	-		-	

Table 8.3 Enthalpy and temperature of reaction for powders milled for up to 30 h. The subscripts a, x and r stand for amorphisation, crystallization and an unknown reaction, respectively.

ET (3Nb + 0.7Al + 0.3Ge). The Nb-Al-Ge DSC traces show a reduction of the peak area and an approximately constant reaction temperature. This behaviour indicates the formation of amorphous phases at constant temperature (~ 710 ^oC) similarly to that found for amorphous Nb-Ge milled powder (section 7.2). As previously found by Schwartz et al. [135], the exothermic peaks in Figure 8.1 at 30 h milling might indicate that amorphisation (ΔH_a) and crystallisation (ΔH_x) occurred in turn. The negative sign of the enthalpy indicates that both the amorphisation and crystallisation reactions are exothermic, therefore the powder mixture releases heating during each transformation. The fact that the T_a does not depend on the milling time might be connected with the process of amorphisation. As suggested by Schwartz et al. [135], a constant T_a might represent the onset temperature for the Ge diffusion in the amorphous Nb-Ge alloy. Indeed in agreement with our XRD results (figure 8.12), the amorphous phase forms mostly by Ge diffusion into crystalline Nb and the final amorphous Nb-Ge alloy is expected to be rich in Nb(bcc). Politis [87] investigated the calorimetric response of ball milled Nb-Ge and Nb-Al-Ge powder and found that they crystallised in turn at 581 ^oC and 504 ^oC (cf subsection 3.4.4). We think that the use of tungsten carbide or hardened tool steel leads to a more homogeneous and finer microstructure, which crystallises at low temperatures (< 600 ^oC). The fact that our Nb-Al-Ge samples form an amorphous alloy at ~ 710 ^oC and crystallise at ~ 780 ^oC show that a soft milling media strongly delays crystallisation. A study of compositional and structural phases (i.e. XRD) obtained as a function of the temperature could clarify the thermal response of Nb-Al-Ge milled powder during heating.

CT (Nb_3Al + Nb_3Ge) and Nb_3Al. The $Nb_3Al + Nb_3Ge$ traces in Figure 8.3 show a saturation of the reaction temperature T_r whereas ΔH_r presents a parabolic-like behaviour. It is reasonably to associate ΔH_r tending to zero to imply an amorphisation, however given the broadening of the peak and the starting compounds materials, in these complex materials one can consider structural, composional changes and/or contamination that are more pronounced at higher milling times. The Nb_3Al traces have double exothermic peaks. Indeed for CT, the material transfer/alloying might somewhat be possible whereas for Nb_3Al the homogenisation does not require a previous alloying. Thus, Nb_3Al experiences the destruction of long-range order and the crystallisation starts from earlier milling time (< 5 h). Figure 8.6 shows the total reaction enthalpy, which is the sum of the areas of the double exothermic peaks (Table 8.3).

Summary. Systematic behaviour of the DSC traces was found for all milled powders produced in this work. Our samples experienced mainly exothermic heat changes as shown by the literature [87]. Even though the milling parameters were identical, this study shows that three different behaviours were found for ET, CT, and Nb_3Al. Specifically, DSC traces for ET show a reduction of the peak area and an approximately constant amorphisation temperature. The DSC traces for CT show a saturation of the reaction temperature T_r whereas ΔH_r present a parabolic-like behaviour. The calorimetric traces for Nb_3Al show double exothermic peaks with a crystallisation peak and an unknown reaction peak. These results show that the thermal response depends on starting materials, milling procedure and copper contamination.

8.3.2 ICP-MS results

These measurements were performed by Dr. Ottley (Earth Science department, Durham University) on powders dry milled for up to 20 and 30 h. Isotopes ^{63}Cu and ^{65}Cu were found. The error for each reading was ± 5 at. %.

M.T (h)	ET (3Nb + 0.7Al + 0.3Ge) (at. % Cu)	CT (0.7Nb_3Al + 0.3Nb_3Ge) (at. % Cu)	Nb_3Al (at. % Cu)
20	1.6 ± 0.1	4.2 ± 0.1	5.6 ± 0.1
30	3.0 ± 0.1	4.9 ± 0.1	-

Table 8.4 ICP-MS results for ET (3Nb + 0.7Al + 0.3Ge), CT (0.7Nb_3Al + 0.3Nb_3Ge) and Nb_3Al yield data milled for up 30 h.

As already discussed in section 7.3.2, we think that the mass spectroscopy values (ICP-MS) shown in Table 8.4 do not correctly represent the copper contamination because they are in disagreement both with electron microscopy data. A consistent estimation of the Cu content is presented below using only yield (section 8.3.3) and SEM (section 8.4.2) data.

8.3.3 Yield results

The yield was calculated as shown in section 6.4. The yield was measured after sequential 5 h milling periods. Data are shown by Figure 8.7. The relatively low yield at 5 h milling for ET means that initially, powder welding took place. For further milling times the yield slightly increases and eventually increases above 100 %. This suggests that during dry milling the contamination from the copper milling tools occurred and is ~ 10 %.

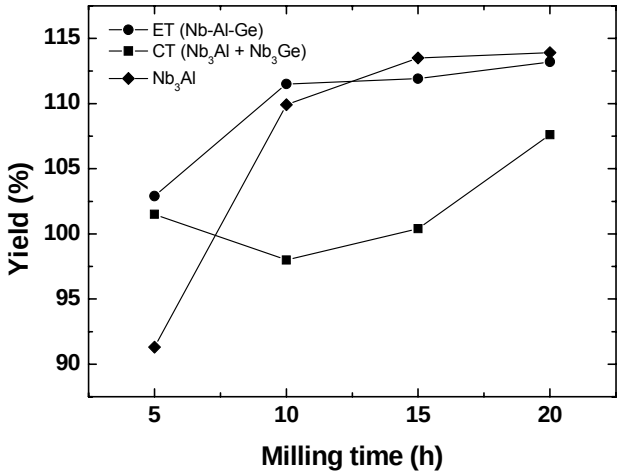

Figure 8.7 Average yield for ET (3Nb + 0.7Al + 0.3Ge), CT ($0.7Nb_3Al + 0.3Nb_3Ge$) and Nb_3Al milled up for to 20 h.

8.3.4 AC Magnetometry

The atomic disorder created by high-energy ball milling was investigated by zero field AC magnetometry in the temperature range 20 – 3 K. These measurements were performed on ~ 10 mg pellets of similar shape and dimensions. Figure 8.8, Figure 8.9 and Figure 8.10 report the zero field AC magnetometry curves for ET, CT and Nb_3Al. Figure 8.11 reports the residual magnetization at 4.2 K versus milling time.

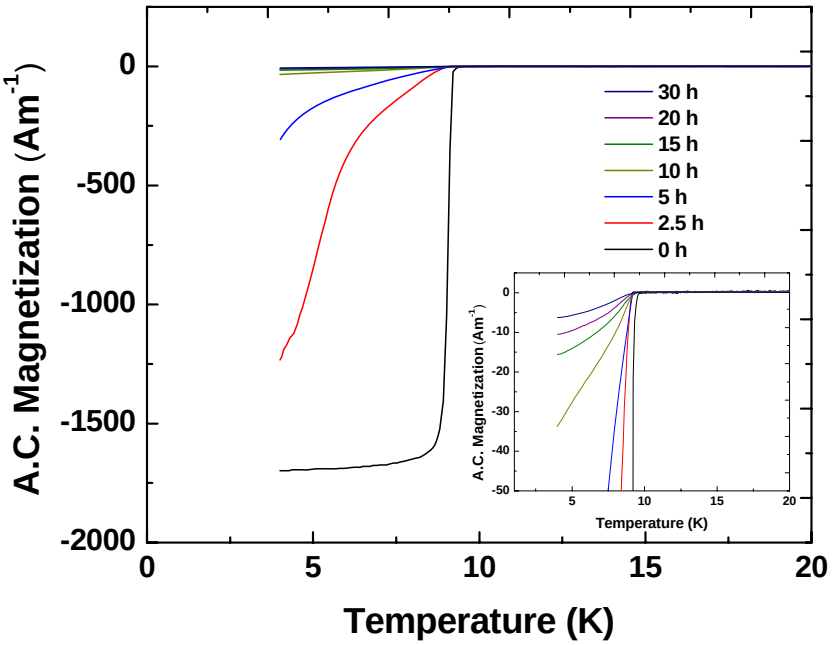

Figure 8.8 Zero field a.c. magnetisation for ET (3Nb + 0.7Al + 0.3Ge) milled up for to 30 h. The inset highlights the superconducting transition at different milling times.

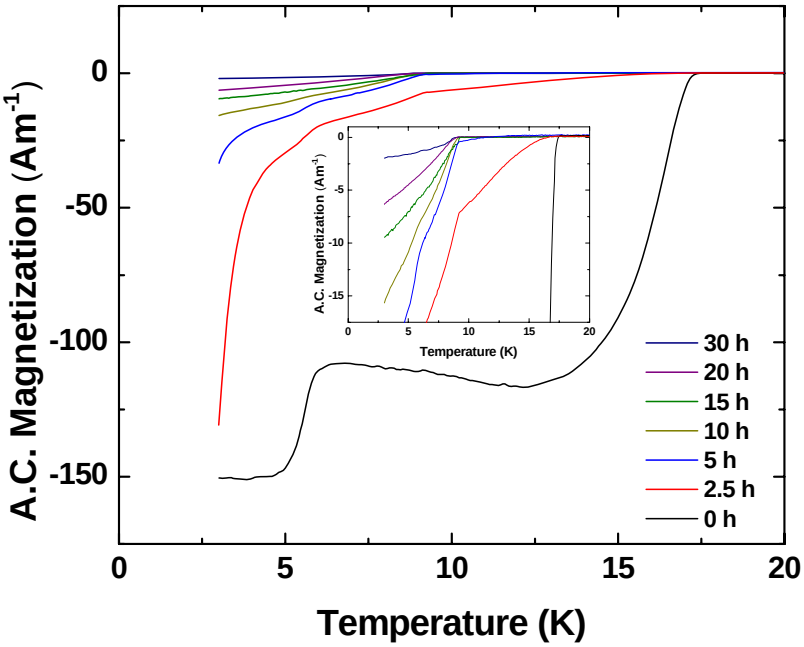

Figure 8.9 Zero field a.c. magnetisation for CT ($0.7Nb_3Al + 0.3Nb_3Ge$) milled up for to 30 h. The inset highlights the superconducting transitions of Nb_3Al (~ 17 K) and Nb_3Ge (~ 6 K) at different milling times. The transition due to Nb (~ 9 K) appears at early milling stages.

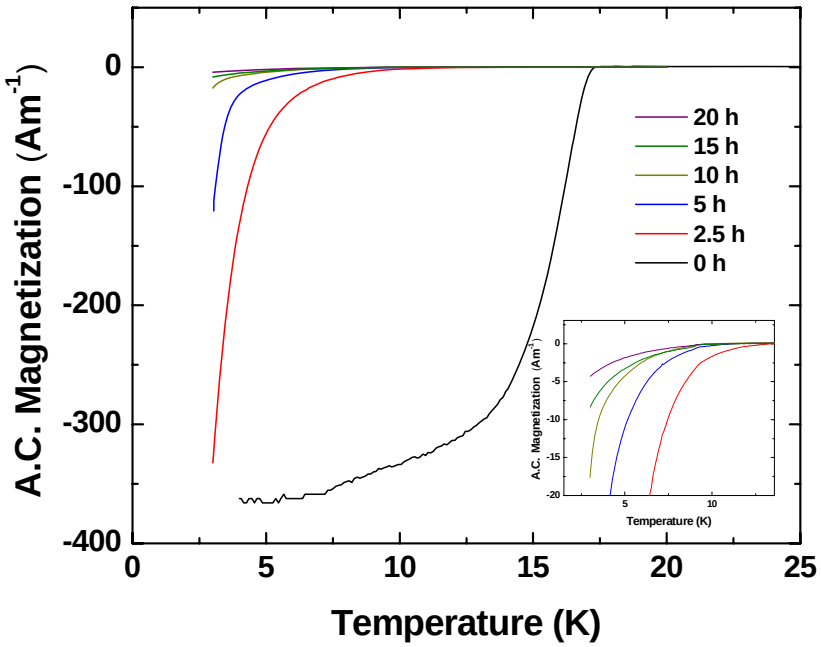

Figure 8.10 Zero field a.c. magnetization curves for Nb_3Al milled up for to 20 h. The inset highlights the superconducting transitions of Nb_3Al (~ 17 K) and Nb (~9 K) at different milling times.

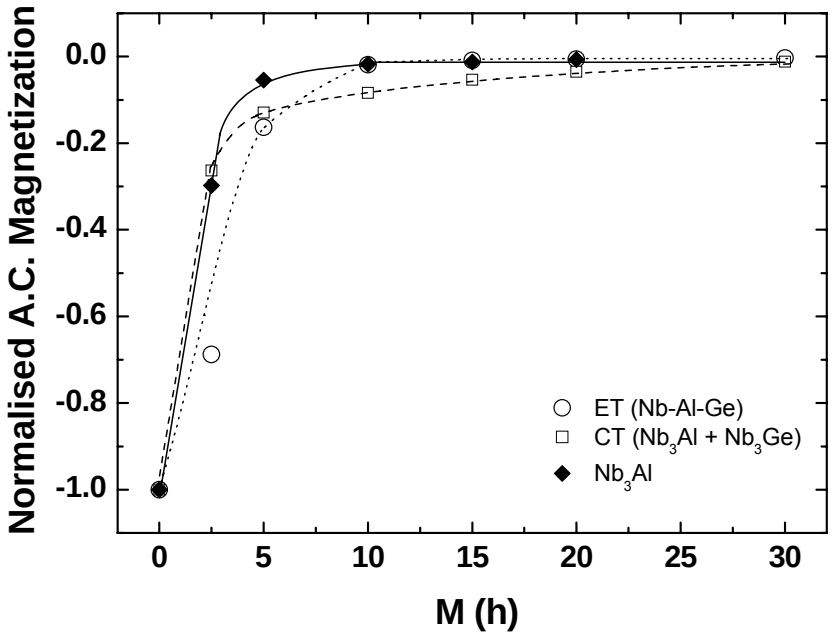

Figure 8.11 Normalised zero field a.c. magnetization at 4.2 K for ET (3Nb + 0.7Al + 0.3Ge), CT ($0.7Nb_3Al + 0.3Nb_3Ge$) processed using MA (broken line) and Nb_3Al (continuous line) milled for up to 30 h.

In this thesis work, the ac curves of mechanically alloyed and milled powders fabricated during this thesis show a similar behaviour in terms of onset temperature and in terms of saturation magnetisation. The onset transition temperature for ET was found to be approximately 9 K all the way through milling, as shown by the inset of Figure 8.8. CT has three superconducting transitions up to 5 h milling at temperatures ~ 17 K, ~ 9 K and ~ 6 K due to Nb_3Al, Nb and Nb_3Ge phases, respectively. Similarly to CT, Nb_3Al shows a dramatic decrease of temperature from ~ 17 K to ~ 10 K within 5 h milling. Both CT and Nb_3Al show a small superconducting transition of ~ 9 K starting from 10 h milling. This suggests that during ball milling there are some nanocrystalline Nb grains, which screen the response from other eventual disordered nanocrystalline A15 grains. It seems that the overall magnetic response is linked to the microstructure at nanometre scale. Probably, if the milling procedure had been carried out using materials harder than copper, like niobium [30] or hardened steel there will be a pronounced degradation of the critical temperature all the way through HEBM as shown by Nb_3Sn [134] and Nb_3Au [172]. The atomic disorder created by HEBM decreases the magnitude of the magnetisation during milling as previously observed for Nb-Ge (Chapter 7) and in other systems [169]. Figure 8.11 shows the normalised zero field a.c. magnetization against milling time for powders processed with MA and MM. A saturation magnetisation is shown exclusively in unmilled powders.

8.3.5 XRD Results

The structural changes of HEBM'ed powders were investigated by X-ray diffraction. Figure 8.12 and Figure 8.14 and show labelled XRD peaks and their evolution with milling for ET and CT, respectively. Figure 8.13 and Figure 8.15 provide the grain size and the variation of the lattice parameters versus milling time. Table 8.5 summarises the relevant structural changes involved during milling.

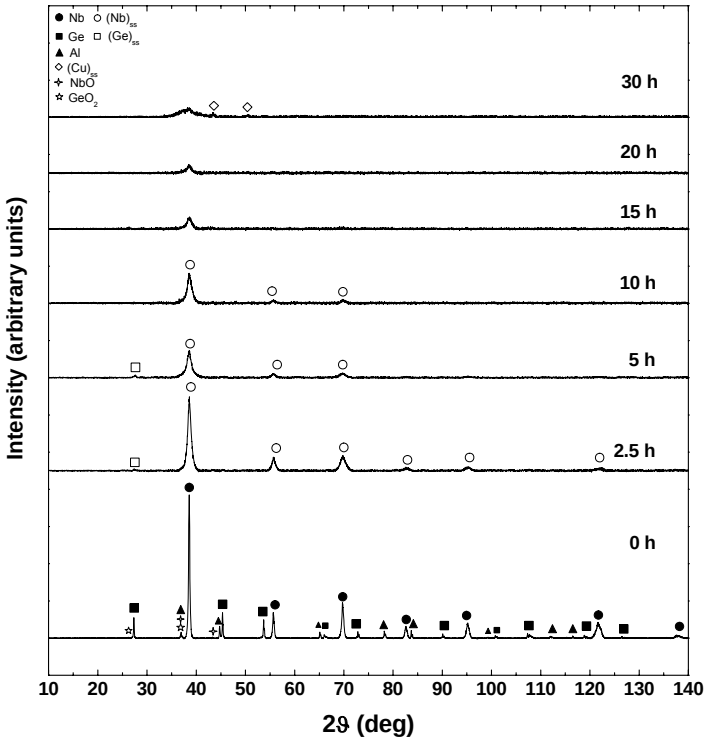

Figure 8.12 XRD evolution for ET (3Nb + 0.7Al + 0.3Ge) during milling. Nb, Ge and Al have the bcc, fcc (diamond) and fcc structure, respectively.

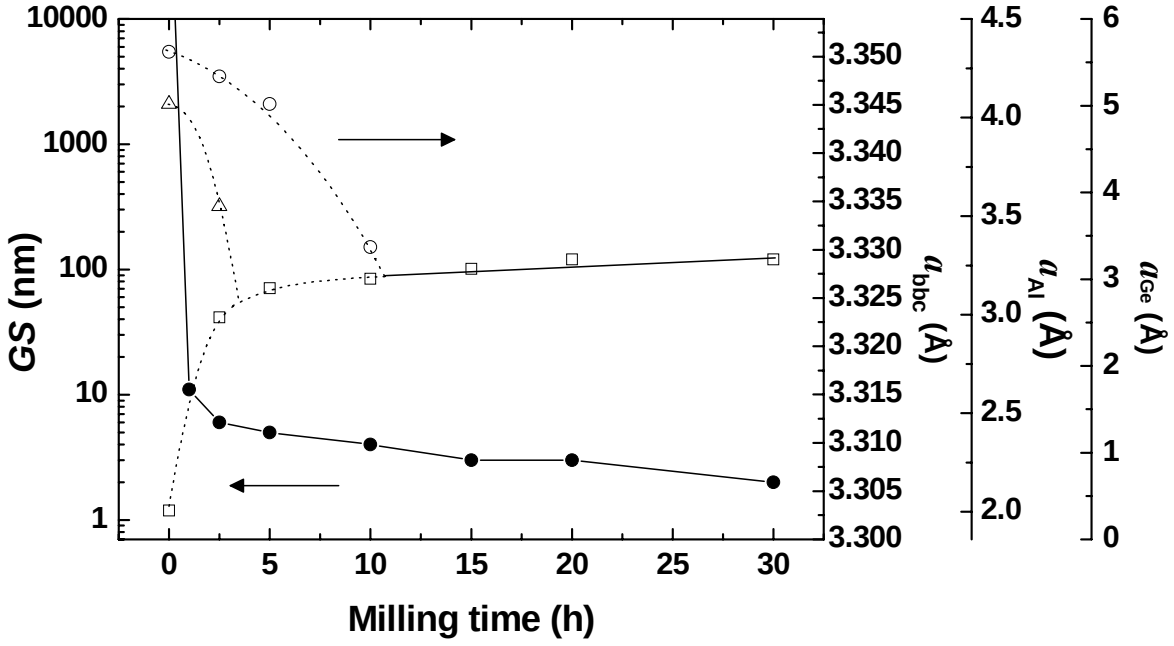

Figure 8.13 Grain size (*GS*) (full circle) and lattice constant (*a*) of Nb-bcc (square), Al-fcc (triangle), Ge-fcc (empty circle) solid solutions for ET (3Nb + 0.7Al + 0.3Ge) milled for up to 30 h. The solid solution at the equilibrium is represented by a continuous line starting at ~ 11 h.

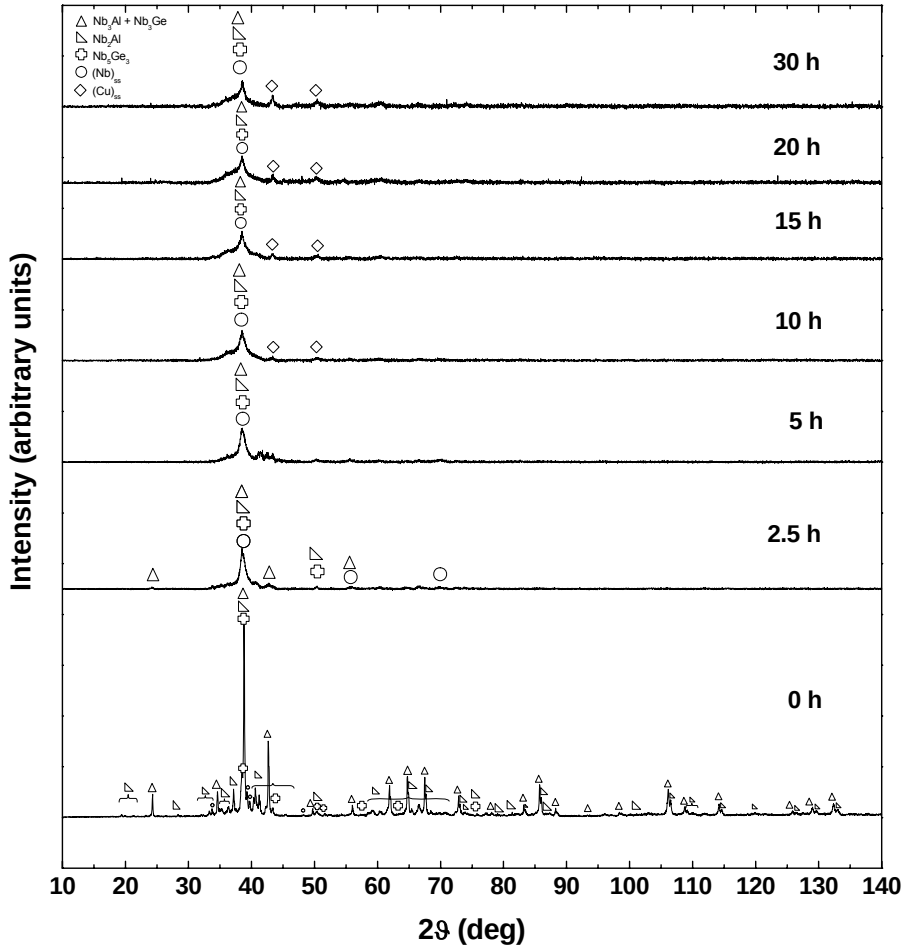

Figure 8.14 XRD evolution for CT ($0.7Nb_3Al + 0.3Nb_3Ge$) during milling.

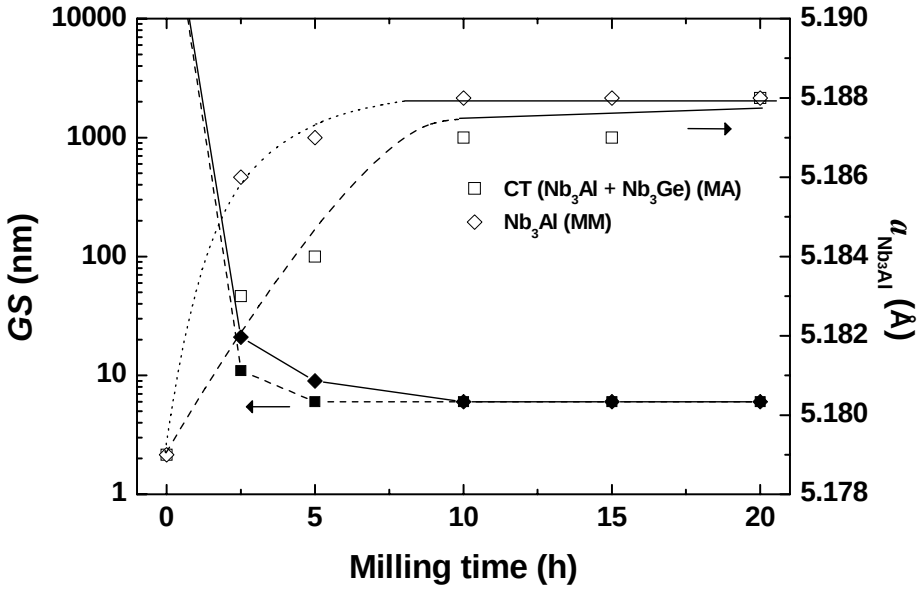

Figure 8.15 Grain size (*GS*) (full symbol) and Nb_3Al lattice constant (empty symbol) for CT ($Nb_3Al + Nb_3Ge$) (squares, dotted line) and Nb_3Al (rhombus, dashed line) during milling. The equilibrium is indicated by a continuous line.

M.T. (h)	ET (3Nb + 0.7Al + 0.3Ge)			CT (0.7Nb_3Al + 0.3Nb_3Ge)				Nb_3Al		
	GS **(nm)**	a_{bcc} **(Å)**	$\Delta a_{bcc}/a_o$ **(%)**	***GS*** **(nm)**	a_{Nb3Al} **(Å)**	$\Delta a_{Nb3Al}/a_o$ **(%)**	a_{Nb3Ge} **(Å)**	***GS*** **(nm)**	a_{Nb3Al} **(Å)**	$\Delta a_{Nb3Al}/a_o$ **(%)**
0	-	3.303	0	-	5.179	0	5.166	-	5.179	0
2.5	11	3.323	0.61	11	5.183	0.08	5.167	21	5.186	0.14
5	6	3.326	0.70	6	5.184	0.10	5.167	9	5.187	0.15
10	5	3.327	0.73	6	5.187	0.15	5.168	6	5.188	0.15
15	4	3.328	0.76	6	5.187	0.17	5.168	6	5.188	0.17
20	3	3.328	0.76	6	5.188	0.17	5.169	6	5.188	0.17
30	3	3.329	0.79	6	5.188	0.17	5.169	-		

Table 8.5 Grain size (GS), lattice constant and the corresponding relative increase for lattice parameters. The lattice parameter of unmilled powders was taken from the scientific literature [51,78,173].

Figure 8.12 shows the formation of a nanostructured bcc-Nb(Al,Ge) solid solution, hereafter indicated as $(Nb)_{ss}$, and a gradual disappearance of the Al and Ge peaks for ET. Figure 8.13 summarises simultaneous structural changes as the grain size (GS) refinement down to a few nanometres and the formation of $(Nb)_{ss}$. The lattice parameters of both fcc-structured Al-rich and Ge-rich solid solutions decrease and merge approximately at 2.5 h and 10 h with that of $(Nb)_{ss}$, respectively. The equilibrium state for $(Nb)_{ss}$ is reached at ~ 10 h with a lattice constant of about 3.330 Å. The lattice expansion for the bcc-Nb extends up to ~ 0.8 %. This value is smaller that that found by Hellstern. et al. [90] (~ 1.2 %) for MA'ed Nb-Al eventually due to the reduced atomic radius of Ge (152 pm) compared to that of Al (182 pm) and different milling. The decrease of Al and Ge lattice parameters during HEBM can be explained in terms of vacancy type defects (i.e. triple disorder) whereas the increase of the Nb lattice parameter can be interpreted by anti-site disorder [100].

The ball milling of CT (Figure 8.14) and Nb_3Al produced weak $(Nb)_{ss}$ peaks up to 5 h milling. Accordingly with the mechanical milling dynamics, Figure 8.15 shows that Nb_3Al reached the disordered state faster that MA'ed Nb_3Al + Nb_3Ge powders. In the literature, the microcrystalline-to-nanocrystalline bcc phase transformation has been previously observed during milling of MA'ed and MM'ed powders (for more details the reader is referred to section 3.4.4).

Summary. Table 8.5 summarises the changes of grain size and lattice parameter during HEBM. All sets of data show a fast decrease of GS down to a few nanometres. The lattice expansion for the bcc-Nb extends up to ~ 0.8 %. This value is smaller that that found by Hellstern. et al. [90] (~ 1.2 %) for MA'ed Nb-Al eventually due to the reduced atomic radius of Ge (152 pm) compared to that of Al (182 pm). The lattice parameter of the intermetallic compounds Nb_3Al shows a small relative increase, $\Delta a/a_o$, of ~ 0.2 %, which is close to previous results on Nb_3Sn and Nb_3Au milling [134,172]. The lattice expansion of the major phase indicates that the ball milling produces anti-site disorder. MA'ed (ET and CT) and MM'ed (Nb_3Al) powders reach the equilibrium at ~ 10 h and ~ 7.5 h, respectively. This result indicates that the time required to produce homogeneous nanophase materials is shorter in pre-processed materials.

8.3.6 Discussion

Grain size refinement and atomic disorder produced by HEBM were studied by differential scanning calorimetry, magnetic measurements and X-ray diffraction. The reaction enthalpy shows a systematic behaviour with milling time. This indicates a wide range of microstructural changes like crystallization, amorphisation and atomic reordering process. Some of these reactions occur simultaneously or sequentially during heat treatment and are distinctive feature of the processed material. After a relatively short milling time (~ 10 h), the value of lattice parameters tend to become constant and a saturation behaviour was observed at ~ 10 h milling both in the AC magnetisation data (Figure 8.11) and in the lattice parameters of the major compositional phases (Figure 8.13 and Figure 8.15). The saturation behaviour is consistent with previous investigations of ball milled powders [134,135,169]. The HEBM generated an expansion of the unit cell due mainly to anti-site disorder. The monitoring of the atomic disorder is relevant for understanding superconductivity in nanocrystalline bulk materials formed from highly disordered powders.

8.4 Properties of nanocrystalline bulk samples

We investigated the properties of nanocrystalline bulk materials. A selection of representative data is given below for the processed powders ET M6, ET M20, CT M20 and Nb_3Al M20. As with Nb_3Ge in Chapter 7, the powders were processed using four routes: HIPYYY, HIP600 + AZZZ, HIP1200 + AZZZ and AZZZ. For the sample nomenclature the reader is referred to Table 8.2. Subsection 8.4.1 reports on the XRD properties. The SEM images and the compositional results from the energy dispersive X-ray are given by subsection 8.4.2. The data and analysis of the AC magnetometry curves are shown by 8.4.3. A summary of data is discussed in subsection 8.4.4.

8.4.1 X-ray diffraction

The X-ray diffraction was used to investigate the crystalline phases and compositional changes of our nanocrystalline samples. We provide XRD scans representative of the bulk materials fabricated using HIPYYY, HIP600 + AZZZ, HIP1200 + AZZZ and AZZZ for each group of materials. The XRD scans are presented in turn for ET M6, ET M20, CT M20 and Nb_3Al M20. The main phases were the A15 phase $Nb_3(Al_{1-x}Ge_x)$, the secondary phases $Nb_2(Al_{1-x}Ge_x)$, $Nb_5(Al_{1-x}Ge_x)_3$ and the terminal solid solutions $(Nb)_{ss}$ and $(Cu)_{ss}$. Traces of various oxides (i.e. NbO, Al_2O_3) are also indicated. The effect of thermal processing on the crystalline structure is described throughout the text. The XRD scans were processed using the Rietveld refinement to estimate the grain size (*GS*) and the lattice parameters for the A15 phases Nb_3Al, Nb_3Ge and $Nb_3(Al,Ge)$. The experimental XRD data were processed using the crystallographic information files from the elements, their main secondary phases and all A15 phases. Owing to the severe multiphase nature and the large broadening of our nanocrystalline peaks, the author underlines that the XRD data refinement of these nanocrystalline materials cannot be considered unique (subsection 4.5). For details on the phase diagrams the reader is referred to section 3.3. The XRD data presentation is followed by a summary of our conclusions.

Group 1: ET(3Nb + 0.7Al + 0.3Ge) M6 + HIPYYY, ET(3Nb + 0.7Al + 0.3Ge) M20 + HIPYYY, CT(0.7Nb_3Al + 0.3Nb_3Ge) M20 + HIPYYY, Nb_3Al M20 + HIPYYY. Representative XRD patterns for HIP'ed samples are shown in Figure 8.16 and Figure 8.17 for ET M6 + HIPYYY and ET 20 + HIPYYY. The increase of HIP'ing temperatures produces increased grain size in our nanocrystalline samples. The crystallite size against the HIP'ing temperature is summarised by Figure 8.18. Results are reported by Table 8.6 and Table 8.7 for ET M6 + HIPYYY, ET M20 + HIPYYY, CT M20 + HIPYYY and Nb_3Al M20 + HIPYYY, respectively.

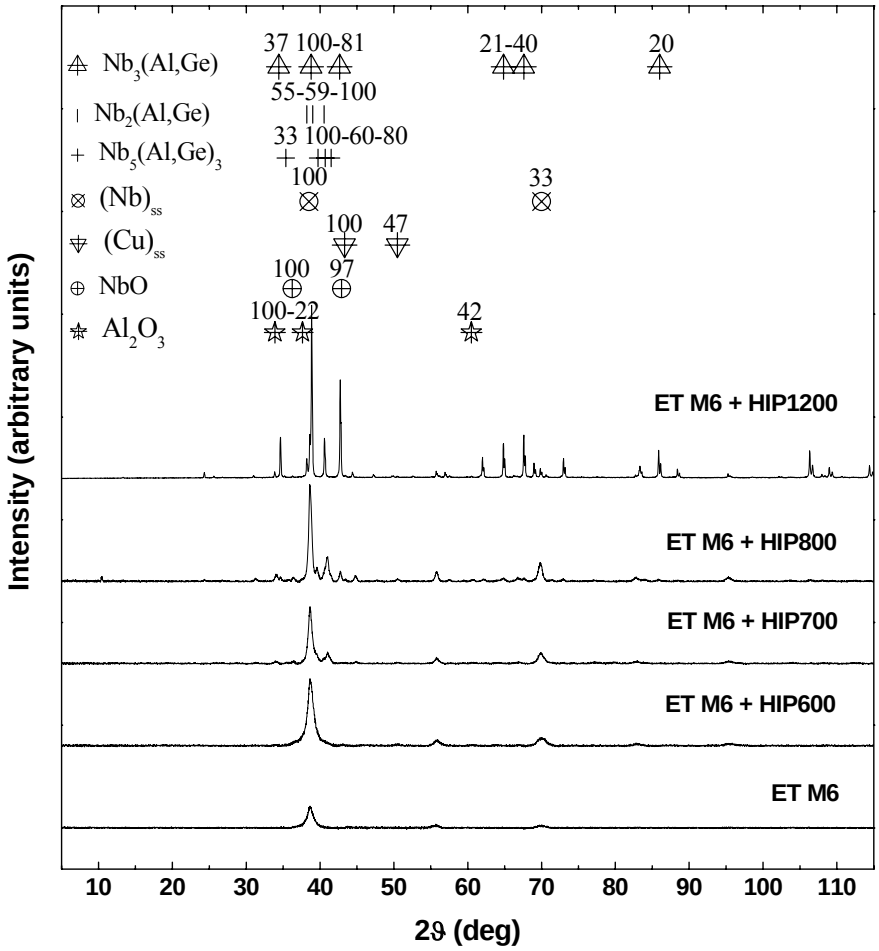

Figure 8.16 XRD scans for ET(3Nb + 0.7Al + 0.3Ge) M6 + HIPYYY and precursor powder prior to HIP'ing. The peaks specified above, for the important phases, are only those which are greater than 20 % of the largest peak for the structure.

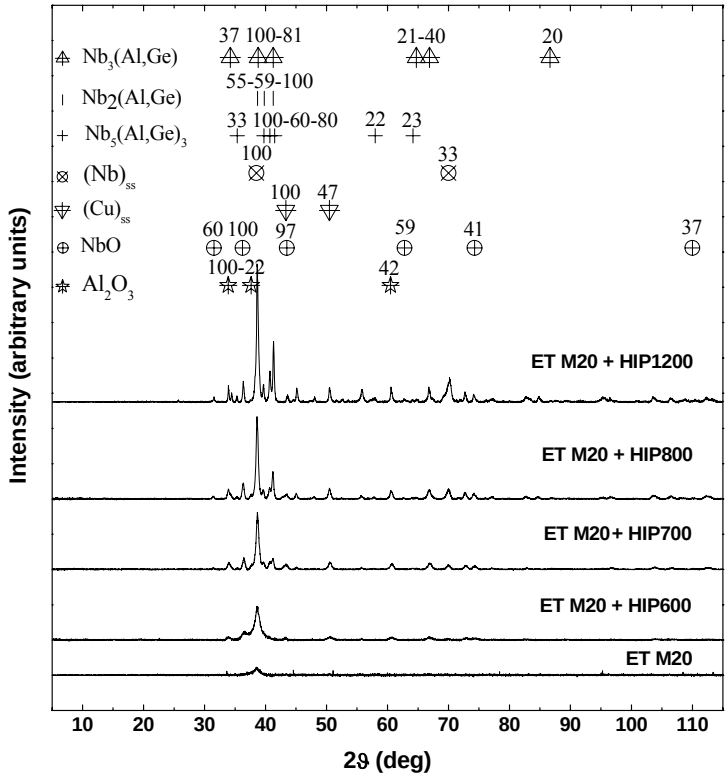

Figure 8.17 XRD scans for ET(3Nb + 0.7Al + 0.3Ge) M20 + HIPYYY and precursor powder prior to HIP'ing. The peaks specified above, for the important phases, are only those which are greater than 20 % of the largest peak for the structure .

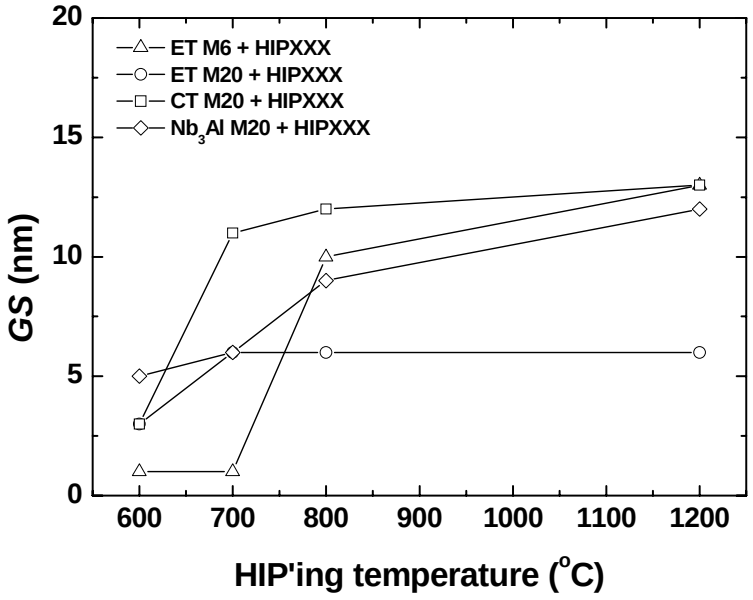

Figure 8.18 Grain size (*GS*) versus processing temperature for ET(3Nb + 0.7Al + 0.3Ge) M6 (triangle), ET(3Nb + 0.7Al + 0.3Ge) M20 (circle), CT($0.7Nb_3Al$ + $0.3Nb_3Ge$) M20 (square) and Nb_3Al M20 (rhombus) processed using HIPYYY.

HIPYYY	ET M6 + HIPYYY					ET M20 + HIPYYY				
	GS **(nm)**	a_{Nb3Al} **(Å)**	a_{Nb3Ge} **(Å)**	$a_{Nb3(Al,Ge)}$ **(Å)**	$T_{C,onset}$ **(K)**	***GS*** **(nm)**	a_{Nb3Al} **(Å)**	a_{Nb3Ge} **(Å)**	$a_{Nb3(Al,Ge)}$ **(Å)**	$T_{C,onset}$ **(K)**
HIP600	1(3)	5.187(3)	5.157(2)	5.175(2)	9.23 {4.85}	3(4)	5.187(3)	5.157(3)	5.177(4)	9.10
HIP700	1(2)	5.187(3)	5.158(1)	5.177(3)	9.26 {5.30}	6(4)	5.187(3)	5.157(1)	5.174(3)	9.01 {4.92}
HIP800	10(5)	5.187(3)	5.158(2)	5.174(2)	10.88 {7.11}	6(5)	5.188(1)	5.158(2)	5.173(3)	9.86 {5.81}
HIP1200	13(5)	5.188(1)	5.157(2)	5.173(4)	6.80 {17.59}	6(9)	5.187(3)	5.158(2)	5.175(3)	8.16

Table 8.6 Grain size (*GS*), lattice parameter (a) and $T_{C,onset}$ for ET(3Nb + 0.7Al + 0.3Ge) M6 and ET(3Nb + 0.7Al + 0.3Ge) M20 processed using HIPYYY. In curly brackets, the second transition temperature is recorded.

HIPYYY	CT M20 + HIPYYY					Nb_3Al M20 + HIPYYY		
	GS **(nm)**	a_{Nb3Al} **(Å)**	a_{Nb3Ge} **(Å)**	$a_{Nb3(Al,Ge)}$ **(Å)**	$T_{C,onset}$ **(K)**	***GS*** **(nm)**	a_{Nb3Al} **(Å)**	$T_{C,onset}$ **(K)**
HIP600	5(3)	5.187(3)	5.167(1)	5.173(2)	9.30	3(5)	5.188(2)	9.21
HIP700	6(1)	5.187(3)	5.167(1)	5.174(1)	9.29	11(8)	5.189(3)	8.67 {13.84}
HIP800	9(4)	5.187(4)	5.167(1)	5.174(2)	9.19 {16.33}	12(7)	5.188(2)	9.04 {13.81}
HIP1200	12(6)	5.187(4)	5.168(1)	5.173(3)	7.81	13(7)	5.190(2)	9.16 {4.26}

Table 8.7 Grain size (*GS*), lattice parameter and $T_{C,onset}$ for CT($0.7Nb_3Al + 0.3Nb_3Ge$) M20 and Nb_3Al M20 processed using HIPYYY. In curly brackets, the second transition temperature is recorded.

Group 2: ET(3Nb + 0.7Al + 0.3Ge) M6 + HIP600 + AZZZ, ET(3Nb + 0.7Al + 0.3Ge) M20 + HIP600 + AZZZ, CT($0.7Nb_3Al + 0.3Nb_3Ge$) M20 + HIP600 + AZZZ, Nb_3Al M20 + HIP600 + AZZZ. XRD of samples HIP600 + AZZZ are shown from Figure 8.19 to Figure 8.21 for ET M6, ET M20 and Nb_3Al M20, respectively. The crystallite size against the HIP'ing temperature is summarised by Figure 8.22. Results are reported by Table 8.8 and Table 8.9. Similarly to identically processed Nb_3Ge, the precursor phase (HIP) has small grains which gradually increase with high temperature heat treatment characterised by an increase of the number of the XRD peaks, intensity and a progressive reduction of the peak width due to the GS growth. The samples HIP'ed at 600 ^oC fabricated from elemental powders milled for up to 6 h show predominantly bcc peaks whereas those milled for up to 20 h show much broader peaks.

Sample ET M6 + HIP600 + A900 shows an improved critical temperature of 1.3 K compared to that of the precursor state (Nb-bcc structure). Sample ET M20 + HIP600 + A800 shows an improved critical temperature of ~ 3 K compared to that of the precursor state (disordered structure). A similar T_C improvement was encountered in the previous literature (section 3.2) and was also achieved in our nanocrystalline Nb_3Ge samples (section 7.4). We suggest a similar explanation for the optimal superconducting properties of our best sample ET M20 + HIP600 + A800 (Figure 8.20). Namely the optimal temperature is sufficiently high to crystallise A15 material but not so high that oxides and competing secondary phases crystallise. As before, one can broadly track the growth of the A15 and the various secondary phases by considering the non-overlapping peaks in: (321) at ~ 66.8 ^{o} for $Nb_3(Al,Ge)$; (100) at ~ 21 ^{o} and (110) at ~ 30^o for NbO; (110) at ~ 60 ^{o} for Al_2O_3; (412) at ~ 50^o for $Nb_2(Al,Ge)$; (210) at ~ 35.4^o for $Nb_5(Al,Ge)_3$. $T_{C,onset}$ variation (see tables Table 8.8 and Table 8.9) depends on heat treatment.

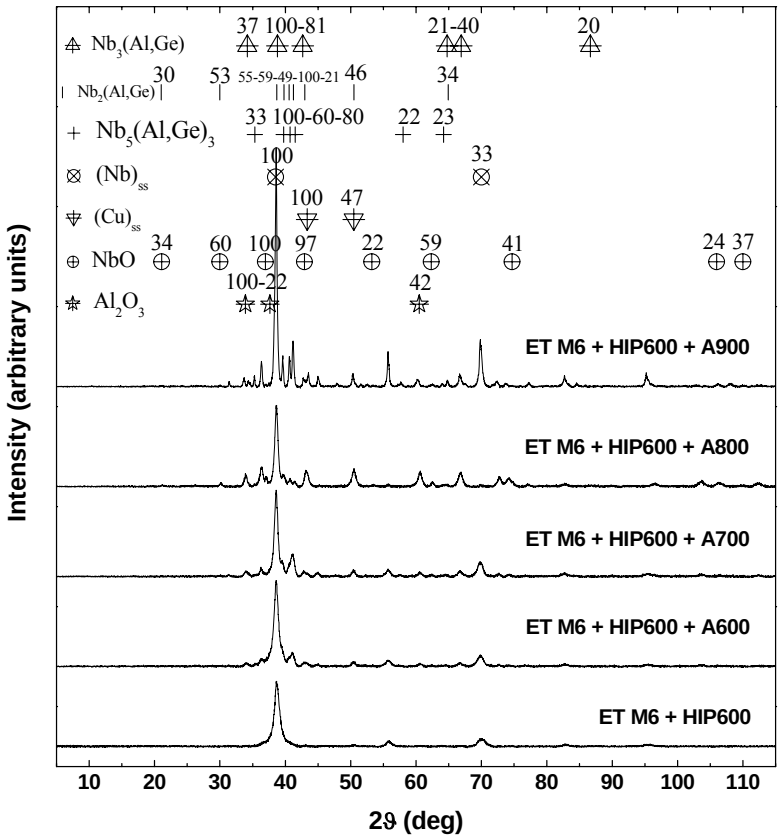

Figure 8.19 XRD scans for ET(3Nb + 0.7Al + 0.3Ge) M6 + HIP600 + AZZZ and precursor material prior to HIP'ing. The peaks specified above, for the important phases, are only those which are greater than 20 % of the largest peak for the structure.

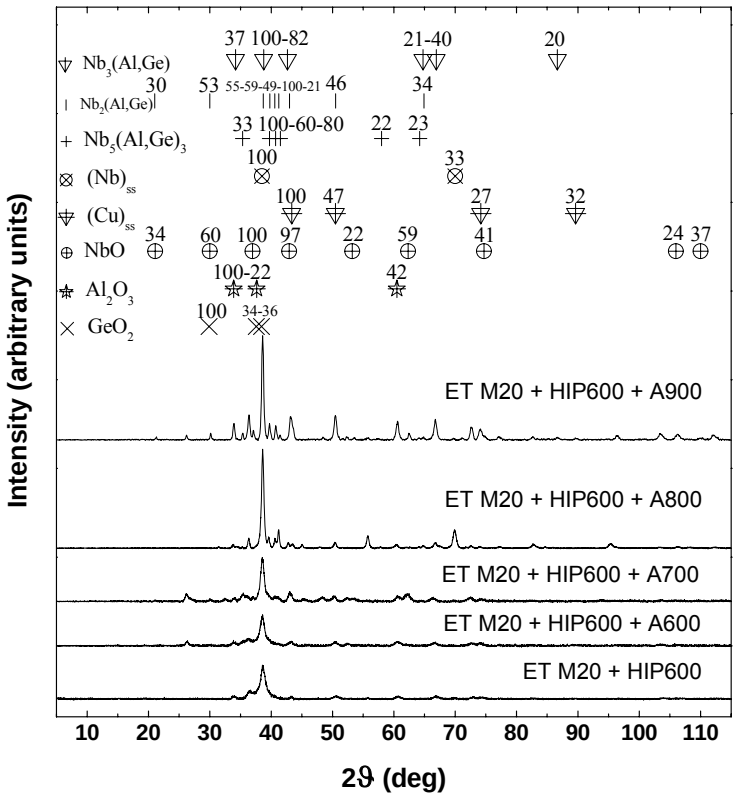

Figure 8.20 XRD scans for ET(3Nb + 0.7Al + 0.3Ge) M20 + HIP600 + AZZZ and precursor material prior to annealing. The peaks specified above, for the important phases, are only those which are greater than 20 % of the largest peak for the structure.

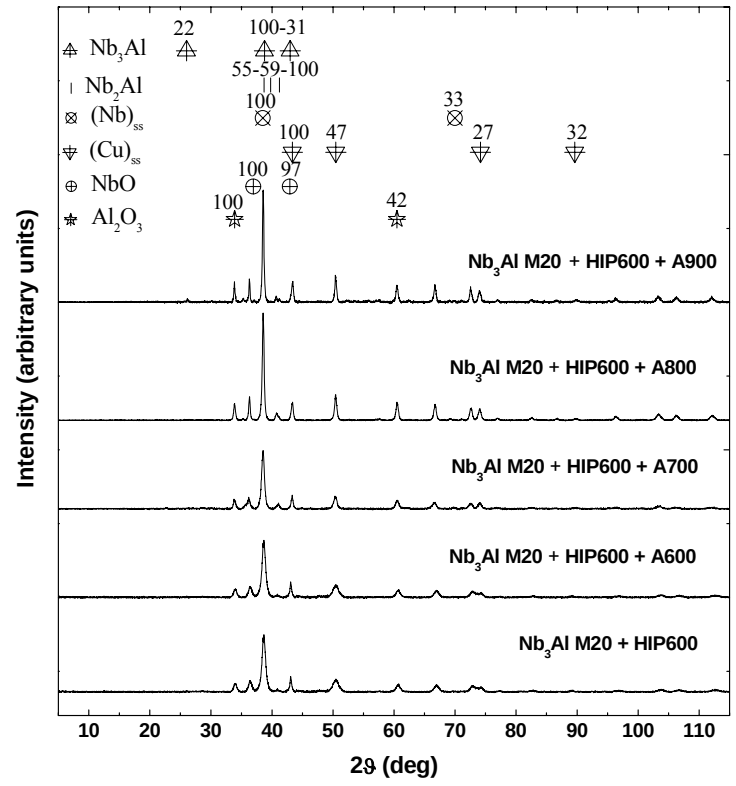

Figure 8.21 XRD scans for Nb_3Al M20 + HIP600 + AZZZ and precursor material prior to annealing. The peaks specified above, for the important phases, are only those which are greater than 20 % of the largest peak for the structure.

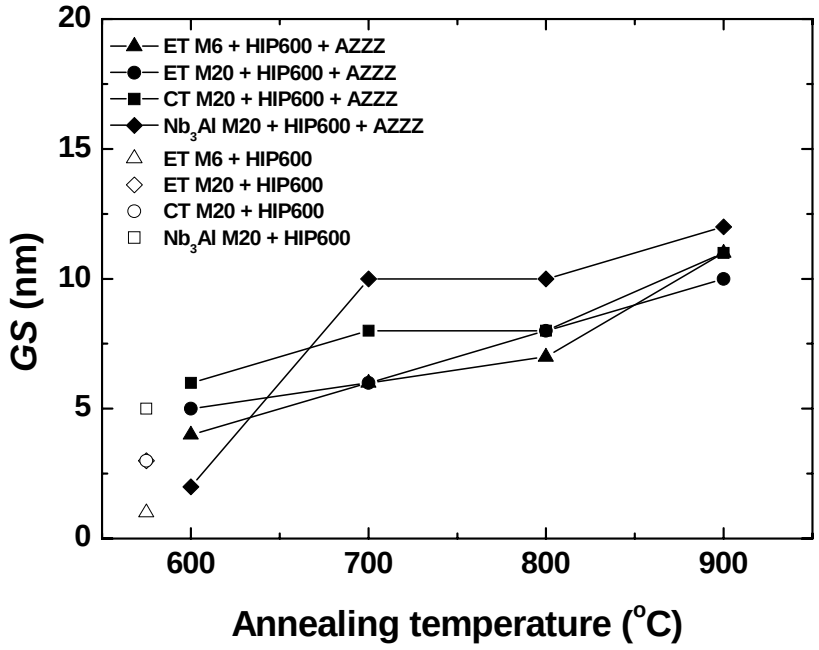

Figure 8.22 Grain size (*GS*) versus processing temperature for ET(3Nb + 0.7Al + 0.3Ge) M6 (triangle), ET(3Nb + 0.7Al + 0.3Ge) M20 (circle), CT($0.7Nb_3Al$ + $0.3Nb_3Ge$) M20 (square) and Nb_3Al M20 (rhombus) processed using HIP600 + AZZZ. The empty symbol represents the precursor material prior to annealing.

HIP600+AZZZ	**ET M6 + HIP600 + AZZZ**					**ET M20 + HIP600 + AZZZ**				
	GS **(nm)**	a_{Nb3Al} **(Å)**	a_{Nb3Ge} **(Å)**	$a_{Nb3(Al,Ge)}$ **(Å)**	$T_{C,onset}$ **(K)**	***GS*** **(nm)**	a_{Nb3Al} **(Å)**	a_{Nb3Ge} **(Å)**	$a_{Nb3(Al,Ge)}$ **(Å)**	$T_{C,onset}$ **(K)**
HIP600	1(3)	5.187(3)	5.157(2)	5.175(2)	9.23 {4.85}	3(4)	5.187(3)	5.157(3)	5.177(4)	9.10
HIP600 + A600	4(5)	5.187(3)	5.157(2)	5.175(2)	9.43 {16.94}	5(1)	5.187(3)	5.157(3)	5.177(4)	9.22 {15.73}
HIP600 + A700	6(4)	5.187(3)	5.158(2)	5.176(3)	9.19	6(3)	5.187(3)	5.158(1)	5.174(3)	9.32
HIP600 + A800	7(7)	5.187(4)	5.159(3)	5.174(3)	9.30	8(4)	5.187(3)	5.158(2)	5.175(2)	11.98
HIP600 + A900	11(13)	5.187(3)	5.157(1)	5.174(3)	10.57 {16.70}	10(6)	5.187(3)	5.158(1)	5.174(2)	8.85 {7.76}

Table 8.8 Grain size (*GS*), lattice parameter (*a*) and $T_{C,onset}$ for ET(3Nb + 0.7Al + 0.3Ge) M6 and ET(3Nb + 0.7Al + 0.3Ge) M20 processed using HIP600 + AZZZ and precursor material prior to annealing. In curly brackets, the second transition temperature is recorded.

HIP600+AZZZ	CT M20 + HIP600 + AZZZ					Nb_3Al M20 + HIP600 + AZZZ		
	GS **(nm)**	a_{Nb3Al} **(Å)**	a_{Nb3Ge} **(Å)**	$a_{Nb3(Al,Ge)}$ **(Å)**	$T_{C,onset}$ **(K)**	***GS*** **(nm)**	a_{Nb3Al} **(Å)**	$T_{C,onset}$ **(K)**
HIP600	5(3)	5.187(3)	5.167(1)	5.173(2)	9.30	3(5)	5.188(2)	9.21
HIP600 + A600	6(2)	5.187(3)	5.167(1)	5.174(3)	9.15	2(4)	5.188(2)	9.22 {16.64}
HIP600 + A700	8(4)	5.187(3)	5.167(1)	5.174(1)	9.38	10(8)	5.188(1)	9.30
HIP600 + A800	8(3)	5.187(3)	5.168(1)	5.174(1)	8.56	10(9)	5.188(2)	9.17
HIP600 + A900	11(4)	5.187(3)	5.167(1)	5.173(1)	6.90	12(8)	5.188(2)	8.96

Table 8.9 Grain size (*GS*), lattice parameter (*a*) and $T_{C,onset}$ for CT($0.7Nb_3Al + 0.3Nb_3Ge$) M20 and Nb_3Al M20 processed using HIP600 + AZZZ and precursor material prior to annealing. In curly brackets, the second transition temperature is recorded.

Group 3: ET(3Nb + 0.7Al + 0.3Ge) M6 + HIP1200 + AZZZ, ET(3Nb + 0.7Al + 0.3Ge) M20 + HIP1200 + AZZZ, CT($0.7Nb_3Al + 0.3Nb_3Ge$) M20 + HIP1200 + AZZZ, Nb_3Al M20 + HIP1200 + AZZZ. XRD of samples HIP1200 + AZZZ are represented in Figure 8.23. The crystallite size against the HIP'ing temperature is summarised in Figure 8.24. The XRD analysis is reported in Table 8.10 and Table 8.11. All precursor samples (HIP1200) fabricated both from elemental powders and compounds show several peaks, whose intensity and number remain approximately the same after post-HIP annealing. This indicates that the crystalline structure of all samples HIP1200 is in a stable state.

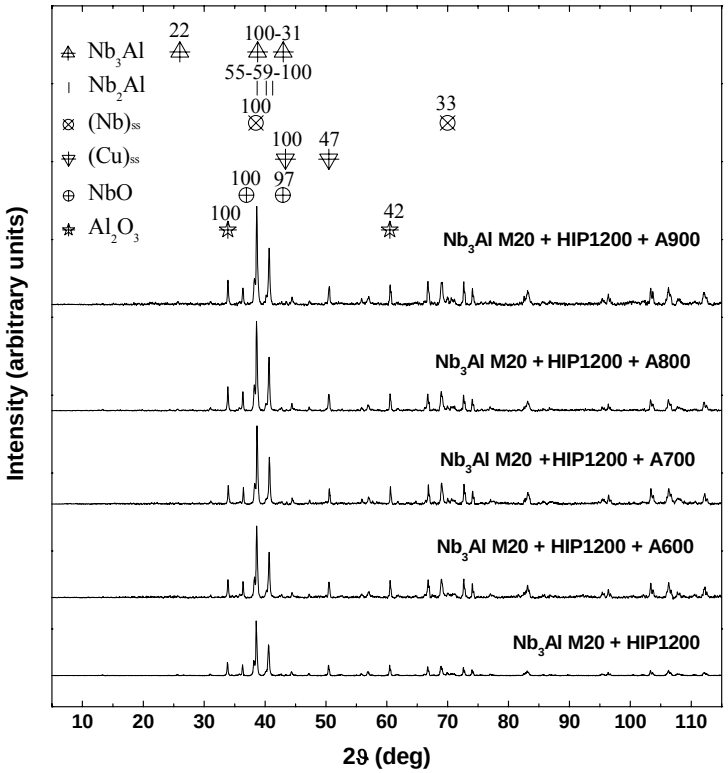

Figure 8.23 XRD scans for Nb_3Al M20 + HIP1200 + AZZZ and precursor state prior to annealing. The peaks specified above, for the important phases, are only those which are greater than 20 % of the largest peak for the structure.

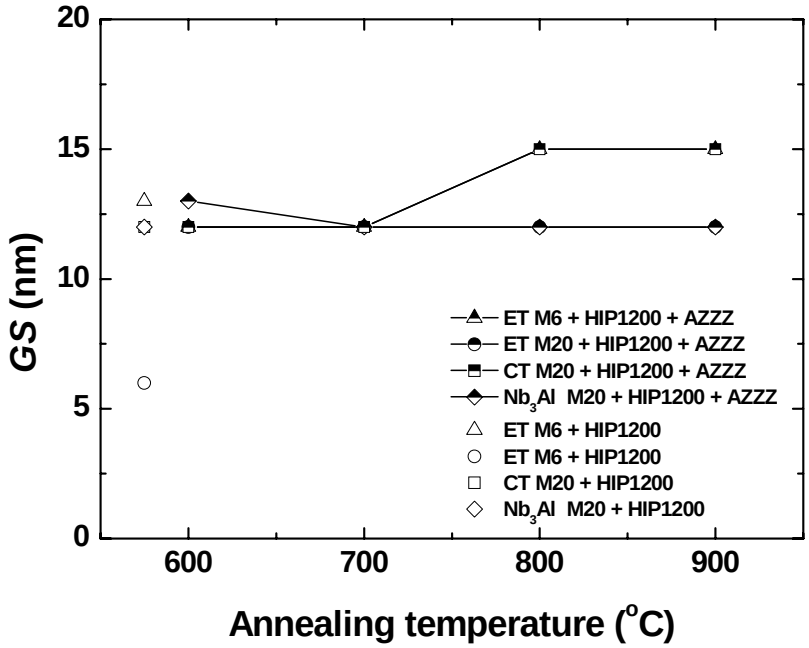

Figure 8.24 Grain size (*GS*) versus processing temperature for ET(3Nb + 0.7Al + 0.3Ge) M6 (triangle), ET(3Nb + 0.7Al + 0.3Ge) M20 (circle), CT($0.7Nb_3Al$ + $0.3Nb_3Ge$) M20 (square), Nb_3Al M20 (rhombus) processed using HIP1200 + AZZZ. The empty symbol represents the precursor material prior to annealing.

HIP1200+AZZZ	ET M6 + HIP 1200 + AZZZ					ET M20 + HIP 1200 + AZZZ				
	GS **(nm)**	a_{Nb3Al} **(Å)**	a_{Nb3Ge} **(Å)**	$a_{Nb3(Al,Ge)}$ **(Å)**	$T_{C,onset}$ **(K)**	***GS*** **(nm)**	a_{Nb3Al} **(Å)**	a_{Nb3Ge} **(Å)**	$a_{Nb3(Al,Ge)}$ **(Å)**	$T_{C,onset}$ **(K)**
HIP1200	13(5)	5.188(1)	5.157(2)	5.173(4)	9.30 {17.59}	6(9)	5.187(3)	5.158(2)	5.175(3)	8.16
HIP1200 + A600	12(6)	5.188(1)	5.157(2)	5.173(4)	7.09	12(9)	5.187(3)	5.158(2)	5.175(3)	8.93
HIP1200 + A700	12(5)	5.185(2)	5.157(2)	5.179(4)	8.15 {16.23}	12(7)	5.187(4)	5.157(2)	5.175(4)	8.37 {15.52}
HIP1200 + A800	15(6)	5.188(2)	5.157(2)	5.177(4)	8.46	12(7)	5.187(4)	5.158(3)	5.175(3)	8.36
HIP1200 + A900	15(5)	5.186(2)	5.159(1)	5.174(1)	8.82	12(9)	5.187(4)	5.157(3)	5.178(3)	9.04

Table 8.10 Grain size (*GS*), lattice parameter (*a*) and $T_{C,onset}$ for ET(3Nb + 0.7Al + 0.3Ge) M6 and ET(3Nb + 0.7Al + 0.3Ge) M20 processed using HIPYYY and precursor state prior to annealing. In curly brackets, the second transition temperature is recorded.

HIP1200+AZZZ	CT M20 + HIP 1200 + AZZZ					Nb_3Al M20 + HIP 1200 + AZZZ		
	GS **(nm)**	a_{Nb3Al} **(Å)**	a_{Nb3Ge} **(Å)**	$a_{Nb3(Al,Ge)}$ **(Å)**	$T_{C,onset}$ **(K)**	***GS*** **(nm)**	a_{Nb3Al} **(Å)**	$T_{C,onset}$ **(K)**
HIP1200	12(6)	5.187(4)	5.168(1)	5.173(3)	7.81	13(7)	5.190(2)	9.16 {4.26}
HIP1200 + A600	12(6)	5.187(4)	5.168(1)	5.175(1)	8.80	12(9)	5.188(2)	9.58 {4.58}
HIP1200 + A700	12(5)	5.187(4)	5.168(1)	5.175(1)	7.10	12(7)	5.188(1)	9.11 {4.06}
HIP1200 + A800	15(6)	5.187(4)	5.167(1)	5.175(1)	7.98	12(7)	5.188(2)	9.58 {4.45}
HIP1200 + A900	15(5)	5.187(4)	5.166(2)	5.174(2)	8.10	12(9)	5.188(2)	9.97 {4.65}

Table 8.11 Grain size (*GS*), lattice parameter (*a*) and $T_{C,onset}$ for CT($0.7Nb_3Al$ + $0.3Nb_3Ge$) M20 and Nb_3Al M20 processed using HIPYYY and precursor state prior to annealing. In curly brackets, the second transition temperature is recorded.

Group 4: ET(3Nb + 0.7Al + 0.3Ge) M6 + AZZZ, ET(3Nb + 0.7Al + 0.3Ge) M20 + AZZZ, CT($0.7Nb_3Al$ + $0.3Nb_3Ge$) M20 + AZZZ, Nb_3Al M20 + AZZZ. XRD patterns representative of samples ET M6 + AZZZ and CT M20 + AZZZ are Figure 8.25 and Figure 8.26. The crystallite size against the HIP'ing temperature is summarised in Figure 8.27. Results are reported in Table 8.12 and Table 8.13. Similarly to group 1

(MX + HIPYYY) and group 2 (MX + HIP600 + AZZZ), we find that the heat treatment after milling produces an increase of the number and the intensity of peaks.

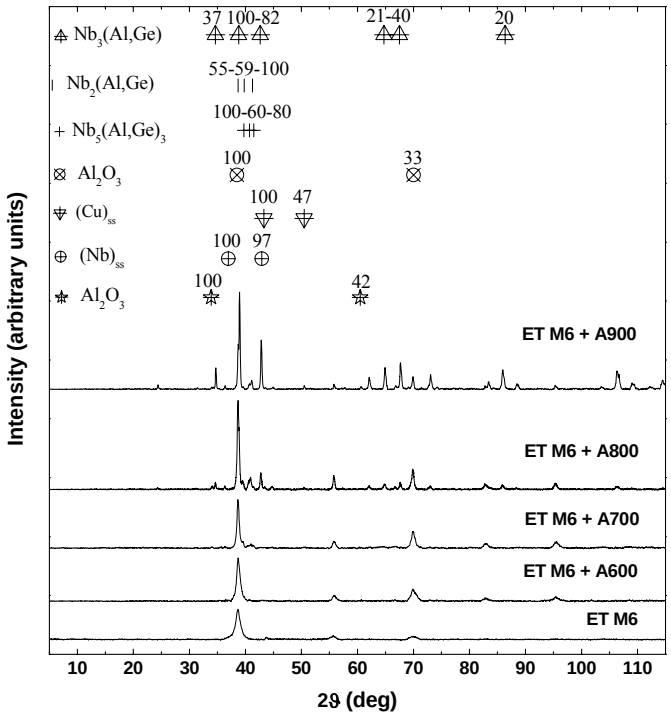

Figure 8.25 XRD scans for ET(3Nb + 0.7Al + 0.3Ge) M6 + AZZZ and precursor powder prior to annealing. The peaks specified above, for the important phases, are only those which are greater than 20 % of the largest peak for the structure.

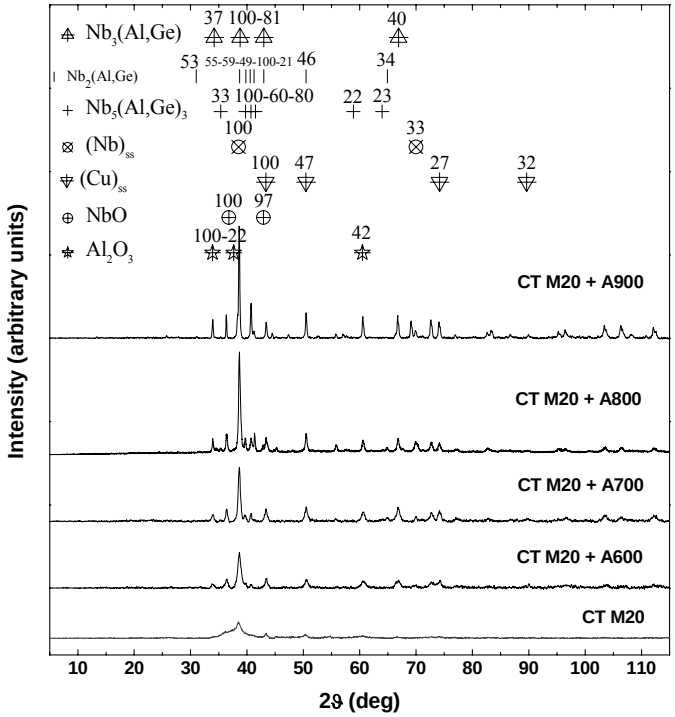

Figure 8.26 XRD scans for CT($0.7Nb_3Al$ + $0.3Nb_3Ge$) M20 + AZZZ and precursor powder prior to annealing. The peaks specified above, for the important phases, are only those which are greater than 20 % of the largest peak for the structure.

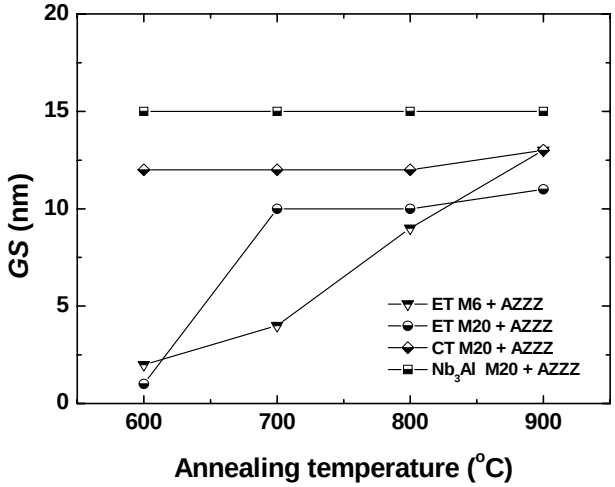

Figure 8.27 Grain size (*GS*) versus processing temperature ET(3Nb + 0.7Al + 0.3Ge) M6 (triangle), ET(3Nb + 0.7Al + 0.3Ge) M20 (circle), CT($0.7Nb_3Al$ + $0.3Nb_3Ge$) M20 (square), Nb_3Al M20 (rhombus) processed using AZZZ.

AZZZ	ET M6 + AZZZ					ET M20 + AZZZ				
	GS **(nm)**	a_{Nb3Al} **(Å)**	a_{Nb3Ge} **(Å)**	$a_{Nb3(Al,Ge)}$ **(Å)**	$T_{C,onset}$ **(K)**	***GS*** **(nm)**	a_{Nb3Al} **(Å)**	a_{Nb3Ge} **(Å)**	$a_{Nb3(Al,Ge)}$ **(Å)**	$T_{C,onset}$ **(K)**
A600	2(3)	5.187(4)	5.157(2)	5.174(3)	9.23	1(5)	5.187(4)	5.156(2)	5.173(3)	9.31
A700	4(4)	5.187(3)	5.160(3)	5.177(3)	10.8	10(6)	5.185(4)	5.157(5)	5.172(5)	9.60 {4.42}
A800	9(6)	5.186(2)	5.161(4)	5.176(3)	11.93	10(7)	5.187(4)	5.158(5)	5.171(5)	9.21 {6.68}
A900	13(3)	5.187(4)	5.156(3)	5.178(2)	11.31	11(5)	5.187(5)	5.160(3)	5.177(5)	9.14 {7.08}

Table 8.12 Grain size (*GS*), lattice parameter (*a*) and $T_{C,onset}$ for ET(3Nb + 0.7Al + 0.3Ge) M6 and ET(3Nb + 0.7Al + 0.3Ge) M20 processed using AZZZ. In curly brackets, the second transition temperature is recorded.

AZZZ	CT M20 + AZZZ					Nb_3Al M20 + AZZZ		
	GS **(nm)**	a_{Nb3Al} **(Å)**	a_{Nb3Ge} **(Å)**	$a_{Nb3(Al,Ge)}$ **(Å)**	$T_{C,onset}$ **(K)**	***GS*** **(nm)**	a_{Nb3Al} **(Å)**	$T_{C,onset}$ **(K)**
A600	15(6)	5.187(4)	5.168(1)	5.175(2)	9.22	12(8)	5.187(2)	9.25
A700	15(7)	5.187(3)	5.167(1)	5.175(2)	9.20	12(7)	5.187(2)	9.20
A800	15(6)	5.187(3)	5.168(1)	5.175(2)	12.19	12(5)	5.187(2)	9.18
A900	15(7)	5.187(4)	5.168(1)	5.173(1)	9.11	13(6)	5.187(2)	9.08

Table 8.13 Grain size (*GS*), lattice parameter (*a*) and $T_{C,onset}$ for CT($0.7Nb_3Al$ + $0.3Nb_3Ge$) M20 and Nb_3Al M20 processed using AZZZ.

Summary for XRD. In agreement with the literature (section 3.2), the crystallite size was found to increase with increasely elevated heat treatments - HIP and/or annealing from 2-3 nm up to 15 nm. The heat treatments were found to change the number, the intensity, and the width of the crystalline peaks for samples MX + HIPYYY (group 1), MX + HIP600 + AZZZ (group 2) and MX + AZZZ (group 4) whereas those for samples HIP1200 + AZZZ (group 3) remained approximately the same. Several phases, like $Nb_3(Al_{1-x}Ge_x)$ (A15), $Nb_2(Al_{1-x}Ge_x)$, $Nb_5(Al_{1-x}Ge_x)_3$ and various oxides, progressively crystallise as the isochronal heat treatment increases. We have found that the role of the optimal post-HIP anneal of highly disordered material is to enhance the A15 crystal nucleation while minimising the crystallisation of unavoidable oxides and secondary phases, which occurs noticeably at higher temperatures and competes with superconductivity.

8.4.2 Scanning electron microscopy

The compositions and spatial distribution of the nanocrystalline multiphase samples were investigated by means of the SEM coupled with energy dispersive X-ray and X-ray quantification maps (XQM). Four samples were analysed: ET M20 + HIP600, ET M20 + HIP1200, Nb_3Al M20 + HIP 600 and Nb_3Al M20 + HIP 1200. Firstly, the compositional results from the energy dispersive X-ray spectroscopy are presented. Secondly, the SEM images and X-ray quantification maps (XQM) are reported for these four samples. For this second part, well-known phase diagrams were used to produce educated guesses of the various phases and their volume percent. Indeed, strictly we cannot exclude that each pixel volume (~ 0.15 μm^3) contains also unreacted elements rather than compounds and/or their terminal solid solution. Diffraction studies using TEM is required for more definite results. For the XRQM analysis, the reader is referred to subsection 7.4.2.

Compositional results from Energy Dispersive X-ray Spectroscopy (Macroscopic spatial averages). The stoichiometry of HIP'ed samples was evaluated using SEM coupled with the EDX. The calibration was performed using a cobalt standard at 20 KeV (cf section 5.8). The measurements were made on the standard and our material with identical operating conditions. However the collected X-ray intensity for each characteristic line depends on several properties of the sample (matrix effects) such as the efficiency of X-ray generation and the absorption of X-ray radiation. These effect

may cause the low X-ray counts for Ge and Al that occur in the ternary compounds (but not in the binary materials). Table 8.14 and Table 8.15 report the normalised atomic percentages, the resulting Nb:(Al+Ge) atomic ratio and the stoichiometry. The copper contamination from milling media is ~ 12 % in both HIP'ed ET M20 and Nb_3Al M20 samples and is close to that estimated from the yield measurements (subsection 8.3.2). Figure 8.28 and Figure 8.29 are typical EDX spectrum for ET M20 + HIP600/HIP1200 and CT M20 + HIP600/HIP1200. It shows the X-ray emission lines for Nb, Al and Ge and also contamination lines from oxygen and copper.

Sample	Nb (at. %)	Al (at. %)	Ge (at. %)	Cu (at. %)	Nb:(Al+Ge)	Ge/Al	Stoichiometry
ET M20 + HIP1200	66.4(2)	15.9(2)	5.8 (1)	11.9(4)	3.1(1)	0.4(1)	$Nb_3Al_{0.6}Ge_{0.4}$

Table 8.14 Normalised atomic percentages for ET(3Nb+ 0.7Al + 0.3Ge) M20 + HIP1200. Errors are reported in brackets.

Sample	Nb (at. %)	Al (at. %)	Cu (at. %)	Nb:Al	Stoichiometry
Nb_3Al M20 + HIP1200	67.1(6)	20.8(3)	12.2(6)	3.4(1)	$Nb_3Al_{0.9}$

Table 8.15 Normalised atomic percentages for Nb_3Al M20 + HIP1200. Errors are reported in brackets.

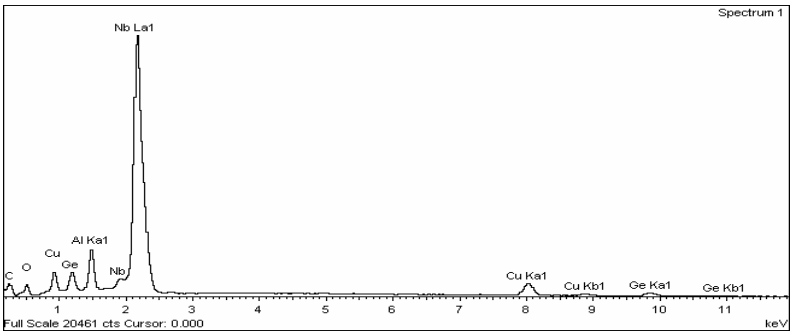

Figure 8.28 Typical EDX spectrum for ET(3Nb+ 0.7Al + 0.3Ge) M20 + HIP1200. Undesired elements are also present: Cu is from the milling procedure; C is introduced during polishing; O is from the various oxides.

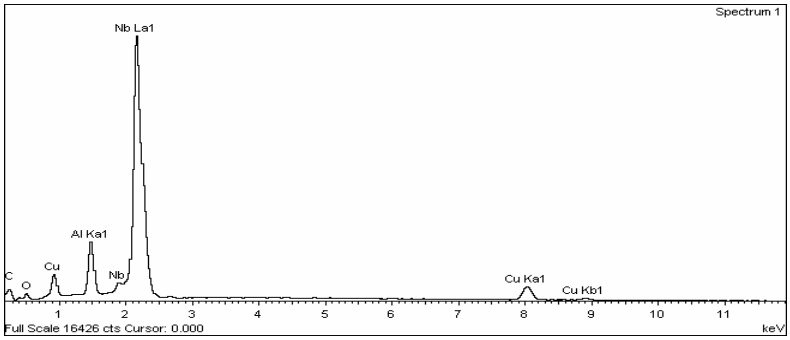

Figure 8.29 Typical EDX spectrum for Nb_3Al M20 + HIP1200. Undesired elements are also present: Cu is from the milling procedure; C is introduced during polishing; O is from the various oxides.

X-ray Quantification Maps for ET + M20 + HIP600 and Nb_3Al M20 + HIP600 (Local compositions and structures). Typical SE, BSE images and quantification maps for sample ET M20 + HIP600 and Nb_3Al M20 + HIP600 are given in turn. Both images show a granular and porous microstructure. The dark regions shown by SE are due both to porosity and the BSE images confirm that these regions have Cu-Al-Ge segregation. We associate the segregation of Al-Cu and Cu-Ge with the eutectic Ge-Cu alloy that forms at 644 ^oC and with the peritectic Al-Cu alloy formed at 591 ^oC. The distribution of copper is not uniform as also found for sample Nb_3Ge M6 + HIP600 (subsection 7.4.2).

The data for sample ET M20 + HIP600 are now given. Figure 8.30 shows the SE, BSE images and the X-ray quantification maps of the various elements. The author underlines that the Al and Ge quantification maps show very low counts/intensity. This might be caused by a failed detection of their characteristic X-ray lines. This can be corrected using a calibration procedure performed with a different standard (e.g. Al) that can produce a more accurate estimation of the X-ray count/concentration of Al and Ge atoms. However we think it is more probable that the Ge + Al counts are low. Relatively high Ge concentration were found in the low copper (high Nb) and high copper regions (compare tables 8.18, 8.19 and 8.20).

A local analysis on phase type and volume was carried out in three different regions: a low copper content (Table 8.16), a typical copper content (Table 8.17) and a high copper content region (Table 8.18). The results for the typical copper content region indicate a dominant composition of Nb and Al whereas Ge was consistently found in the remaining regions. The fact that standard deviations for any collection of pixels cover a few atomic percent ($\leq$ 5 at.%), indicates that at the micron level the material consists of a limited number of phases with specific compositions. Nb_3Al was found to be the major A15 phase and to form mostly at compositions (17 ± 2) at.% Al and (23 ± 1) at.%Al, compositions located in the regions $(Nb)_{ss}$ + Nb_3Al, and Nb_3Al + Nb_2Al, respectively (figure 3.8). The phase $Nb_3(Al_{1-x}Ge_x)$ formed mainly in the three-phase regions $Nb_3(Al_{1-x}Ge_x)$ + $Nb_2(Al_{1-x}Ge_x)$ + $Nb_5(Al_{1-x}Ge_x)_3$ (figure 3.13). Very small traces of Nb_3Ge were formed in the single-phase region of the Nb-Ge phase diagram (figure 3.5).

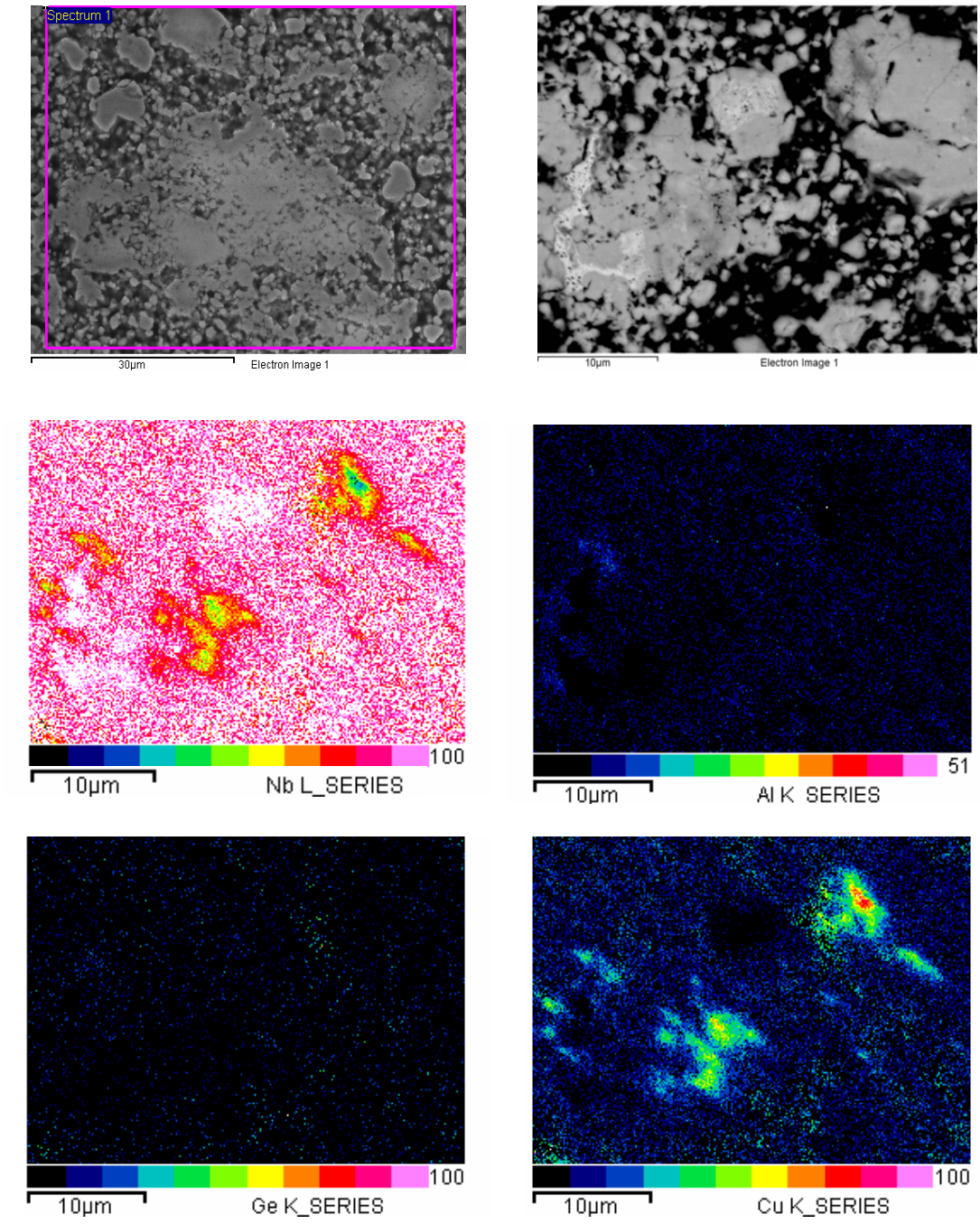

Figure 8.30 SE image (top left), BSE image (top right) with corresponding X-ray quantification maps for ET (3Nb + 0.7Al + 0.3Ge) M20 + HIP600. The distribution of copper is not uniform throughout the material.

Low copper region				
Elements	**at. (%)**	**n**	**Volume (%)**	**Phase diagram data**
Al K Cu K Ge K Nb L	0 0 0 100	17	11	Nb
Al K Cu K Ge K Nb L	24 (± 1) 0 0 76 (± 1)	9	6	$Nb_3Al + Nb_2Al$ 21.8 < Al < 30 at. %
Al K Cu K Ge K Nb L	16 (± 2) 0 0 84 (± 2)	9	6	$(Nb)_{ss} + Nb_3Al$ 9 < Al < 18.8 at. %
Al K Cu K Ge K Nb L	16 (± 3) 0 17(± 1) 66 (± 4)	7	5	$Nb_3(Al_{1-x}Ge_x) + Nb_2(Al_{1-x}Ge_x) + Nb_5(Al_{1-x}Ge_x)_3$ $Nb_3(Al_{1-x}Ge_x)$ with Ge = 7 at.%
Al K Cu K Ge K Nb L	20.6 (± 0.4) 0 0 79.4 (± 0.4)	5	3	Nb_3Al 18.8 ≤ Al ≤ 21.8 at. %
Al K Cu K Ge K Nb L	0 0 19 (± 2) 81 (± 2)	2	1	Nb_3Ge 19 ≤ Ge ≤ 20 at. %
Al K Cu K Ge K Nb L	14 (±2) 0 10 (±2) 76 (±2)	1	1	$Nb_3(Al_{1-x}Ge_x) + Nb_5(Al_{1-x}Ge_x)_3$ $Nb_3(Al_{1-x}Ge_x)$ with 7 ≤Ge ≤ 27.5

Table 8.16 The average compositional points (at. %) in the low copper content region for ET(3Nb + 0.7Al + 0.3Ge) M20 + HIP600. 50 pixels were used to estimate the crystalline phases and the corresponding volume percent (n/50). Previous phase diagrams from the literature [50,55,67] were used to identify the resulting phase. Also provided is the associated range of composition within the relevant region of the phase diagram.

Typical copper region				
Elements	**at. (%)**	**n**	**Volume (%)**	**Phase diagram data**
Al K Cu K Ge K Nb L	0 21 (± 5) 0 79 (± 5)	11	22	$(Nb)_{ss}$ + $(Cu)_{ss}$ 0 < Nb < 100 at. %
Al K Cu K Ge K Nb L	17 (± 1) 0 0 83 (± 1)	8	16	$(Nb)_{ss}$ + Nb_3Al 9 < Al < 18.8 at. %
Al K Cu K Ge K Nb L	0 0 0 100	7	14	Nb
Al K Cu K Ge K Nb L	15 (± 3) 21 (± 3) 0 64 (± 3)	5	10	$(Nb)_{ss}$ + $Nb_2(Al,Cu)$ + $(Cu)_{ss}$ $Nb_2(Al,Cu)$ with Cu = 29 at. %
Al K Cu K Ge K Nb L	20.4 (± 0.4) 0 0 79.6 (± 0.4)	5	10	Nb_3Al 18.8 ≤ Al ≤ 21.8 at. %
Al K Cu K Ge K Nb L	15 (± 2) 14 (± 1) 0 71 (± 4)	5	10	$Nb_2(Al,Cu)$ + $(Nb)_{ss}$ $Nb_2(Al,Cu)$ with 26 ≤ Cu ≤ 29 at. %
Al K Cu K Ge K Nb L	23 (± 1) 0 0 77 (± 1)	4	8	Nb_3Al + Nb_2Al 21.8 < Al < 30 at. %
Al K Cu K Ge K Nb L	20 (± 2) 16 (± 2) 0 64 (± 3)	4	8	$Nb_2(Al,Cu)$ + $(Nb)_{ss}$ $Nb_2(Al,Cu)$ with Cu = 10 and 26 at. %

Table 8.17 The average compositional points (at. %) in the typical copper content region for ET(3Nb + 0.7Al + 0.3Ge) M20 + HIP600. 50 pixels were used to estimate the crystalline phases and the corresponding volume percent (n/50). Previous phase diagrams from the literature [50,55,67] were used to identify the resulting phase. Also provided is the associated range of composition within the relevant region of the phase diagram.

High copper region				
Element	**at. (%)**	**n**	**Volume (%)**	**Phase diagram data**
Al K Cu K Ge K Nb L	0 56 (± 9) 0 44 (± 9)	33	66	$(Nb)_{ss} + (Cu)_{ss}$
Al K Cu K Ge K Nb L	15 (± 3) 45 (± 5) 0 40 (± 4)	11	20	$(Nb)_{ss} + Nb_2AlCu + (Cu)_{ss}$ $Nb_2(Al,Cu)$ with Cu = 29 at. %
Al K Cu K Ge K Nb L	26 (± 1) 34 (± 1) 0 40.2 (± 0.2)	2	4	$NbAlCu + Nb_2(Al,Cu) + (Cu)_{ss}$ $Nb_2(Al,Cu)$ with Cu = 28.9 at. % NbAlCu with Cu = 34 at. %
Al K Cu K Ge K Nb L	23 (±2) 0 0 77 (±2)	1	2	Nb_3Al $19 \leq Al \leq 21.8$ at. %
Al K Cu K Ge K Nb L	31 (±2) 22 (±2) 0 47 (±2)	1	2	$NbAlCu + Nb_2(Al,Cu)$ NbAlCu with Cu = 24 at. % $Nb_2(Al,Cu)$ with Cu = 10 and 26 at.%
Al K Cu K Ge K Nb L	0 47 (±2) 9 (±2) 44 (±2)	1	2	$(Nb)_{ss} + Nb_5(Ge,Cu)_3 + (Cu)_{ss}$ $Nb_5(Ge,Cu)_3$ with Nb = 50 at. %
Al K Cu K Ge K Nb L	0 100 (±2) 0 0	1	2	Cu

Table 8.18 The average compositional points (at. %) in the high copper content region for ET(3Nb + 0.7Al + 0.3Ge) M20 + HIP600. 50 pixels were used to estimate the crystalline phases and the corresponding volume percent (n/50). Previous phase diagrams from the literature [50,55,67] were used to identify the resulting phase. Also provided is the associated range of composition within the relevant region of the phase diagram.

The data for sample Nb_3Al M20 + HIP600 are now given. Figure 8.31 and Figure 8.32 show the SE and BSE image with X-ray quantification maps for the various elements, respectively. Similarly to previous samples, the distribution of copper is not uniform throughout the material. A local analysis on the composition and phase volume was carried out in three different regions: a low copper content region (Table 8.19), a typical copper content region (Table 8.20) and a high copper content region (Table 8.21) were

investigated. Tables 8.20-8.22 indicate that the Nb_3Al phase formed mostly in the compositional ranges: (25 ± 2) at.% Al located in region $Nb_3Al + Nb_2Al$, respectively (figure 3.8). Several Nb-Al-Cu phases were formed in the high copper region.

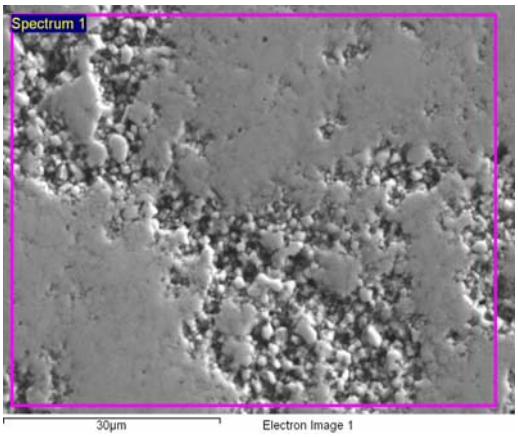

Figure 8.31 Typical SE image for Nb_3Al M20 + HIP600.

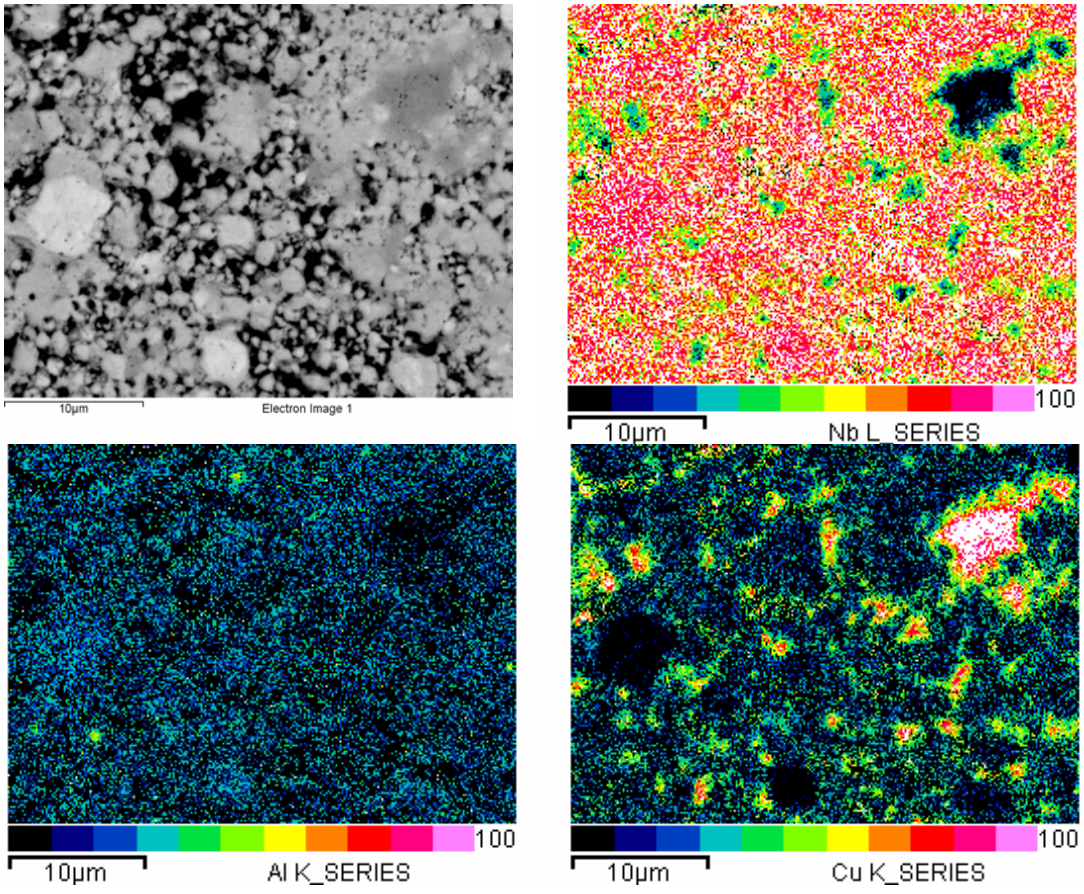

Figure 8.32 BSE image and corresponding X-ray quantification maps for Nb_3Al M20 + HIP600. The distribution of copper is not uniform throughout the material.

Low copper region				
Elements	**at. (%)**	**n**	**Volume (%)**	**Phase diagram data**
Al K Cu K Nb L	0 0 100	11	22	Nb
Al K Cu K Nb L	25 (± 1) 0 75 (± 1)	24	48	$Nb_3Al + Nb_2Al$ 21.8 < Al < 30 at. %
Al K Cu K Nb L	20.6 (± 0.5) 0 79.4 (± 0.5)	4	8	Nb_3Al 19 ≤ Al ≤ 21.5 at. %
Al K Cu K Nb L	17 (± 1) 0 83 (± 1)	4	8	$(Nb)_{ss} + Nb_3Al$ 9 < Al < 18.8 at. %
Al K Cu K Nb L	0 11 (± 2) 89 (± 2)	3	6	$(Nb)_{ss} + (Cu)_{ss}$ 0 < Nb < 100 at. %
Al K Cu K Nb L	20 (± 1) 12 (± 1) 68 (± 1)	2	4	$Nb_2(Al,Cu) + (Nb)_{ss}$ $Nb_2(Al,Cu)$ with Cu = 10 and 26 at. %
Al K Cu K Nb L	32 (± 1) 0 68 (± 1)	2	4	Nb_2Al 30 ≤ Al ≤ 34.5 at. %

Table 8.19 The average compositional points (at. %) in the low copper content region for Nb_3Al M20 + HIP600. 50 pixels were used to estimate the crystalline phases and the corresponding volume percent (n/50). Previous phase diagrams from the literature [50,55,67] were used to identify the resulting phase. Also provided is the associated range of composition within the relevant region of the phase diagram.

Typical copper region				
Elements	**at. (%)**	**n**	**Volume (%)**	**Phase diagram data**
Al K Cu K Nb L	25 (± 2) 0 75 (± 2)	17	34	$Nb_3Al + Nb_2Al$ 21.8 < Al < 30 at. %
Al K Cu K Nb L	0 31 (± 12) 69 (± 12)	10	20	$(Nb)_{ss} + (Cu)_{ss}$ 0 < Nb < 100 at. %
Al K Cu K Nb L	20 (± 1) 0 80 (± 1)	6	12	Nb_3Al 19 ≤ Al ≤ 21.5 at. %
Al K Cu K Nb L	17.6 (± 0.1) 0 82.4 (± 0.1)	2	4	$(Nb)_{ss} + Nb_3Al$ 9 < Al < 18.8 at. %
Al K Cu K Nb L	18.6 (± 0.5) 18.7 (± 0.5) 62.7 (± 0.6)	2	4	$Nb_2(Al,Cu) + (Nb)_{ss}$ $Nb_2(Al,Cu)$ with 26 ≤ Cu ≤ 29 at. %

Table 8.20 The average compositional points (at. %) in the typical copper content region for Nb_3Al M20 + HIP600. 50 pixels were used to estimate the crystalline phases and the corresponding volume percent (n/50). Previous phase diagrams from the literature were used to identify the resulting phase [50,55,67]. Also provided is the associated range of composition within the relevant region of the phase diagram.

High copper region				
Elements	**at. (%)**	**n**	**Volume (%)**	**Phase diagram data**
Al K Cu K Nb L	0 65 (± 10) 35 (± 10)	24	46	$(Nb)_{ss} + (Cu)_{ss}$ 0 < Nb < 100 at. %
Al K Cu K Nb L	0 100 0	13	26	Cu
Al K Cu K Nb L	23 (± 5) 77 (± 5) 0	6	10	$(Al)_{ss} + Al_2Cu$ 0 < Al < 32.5 at. %
Al K Cu K Nb L	20 (± 1) 57 (± 2) 23 (± 2)	3	4	$NbAlCu + Nb_2(Al,Cu) + (Cu)_{ss}$ NbAlCu with Cu = 34 at. % $Nb_2(Al,Cu)$ with Cu = 28.9 at. %
Al K Cu K Nb L	28 (±2) 46 (±2) 26 (±2)	1	2	$NbAlCu + (Cu)_{ss}$ NbAlCu with 31 ≤ Nb ≤ 34 at. %
Al K Cu K Nb L	28 (±2) 11 (±2) 61 (±2)	1	2	$Nb_2(Al,Cu)$ Cu = 10 and 26 at. %
Al K Cu K Nb L	33 (±2) 67 (±2) 0	1	2	Al_2Cu 32.5 < Al < 33 at. %
Al K Cu K Nb L	17 (±2) 39 (±2) 44 (±2)	1	2	$(Nb)_{ss} + Nb_2(Al,Cu) + (Cu)_{ss}$ $Nb_2(Al,Cu)$ with Cu = 29 at. %

Table 8.21 The average compositional points (at. %) in the high copper content region for Nb_3Al M20 + HIP600. 50 pixels were used to estimate the crystalline phases and the corresponding volume percent (n/50). Previous phase diagrams from the literature were used to identify the resulting phase [50,55,67]. Also provided is the associated range of composition within the relevant region of the phase diagram.

X-ray Quantification Maps for ET(3Nb + 0.7Al + 0.3Ge) + M20 + HIP1200 and Nb_3Al M20 + HIP1200 (Local compositions and structures). Typical SE, BSE images and quantification maps are in turn given for samples ET M20 + HIP1200 and Nb_3Al M20 + HIP1200. Both SE and BSE images show a severe porosity, which has been observed also in other Nb_3Al-based materials [99,174]. The brightest region of the BSE image (Figure 8.33 and Figure 8.35) can be attributed to high Nb concentration. In contrast to the samples HIP'ed at 600 ^oC, these samples show a uniform Cu distribution, because this HIP'ing temperature was above the Cu melting point (1084,62 ^oC). The data for sample ET M20 + HIP1200 are now given. Nb_3Al was found to be the major

A15 phase. Tables 8.23-8.24 indicate that the Nb_3Al and Nb_3Ge phase formation occurred mostly in the regions Nb_3Al + Nb_2Al and Nb_3Ge + Nb_5Ge_3 at composition (25 ± 2) at.% Al and (26 ± 4) at.% Ge, respectively. The phase $Nb_3(Al_{1-x}Ge_x)$ formed mainly in the three-phase regions shown by figure 3.13.

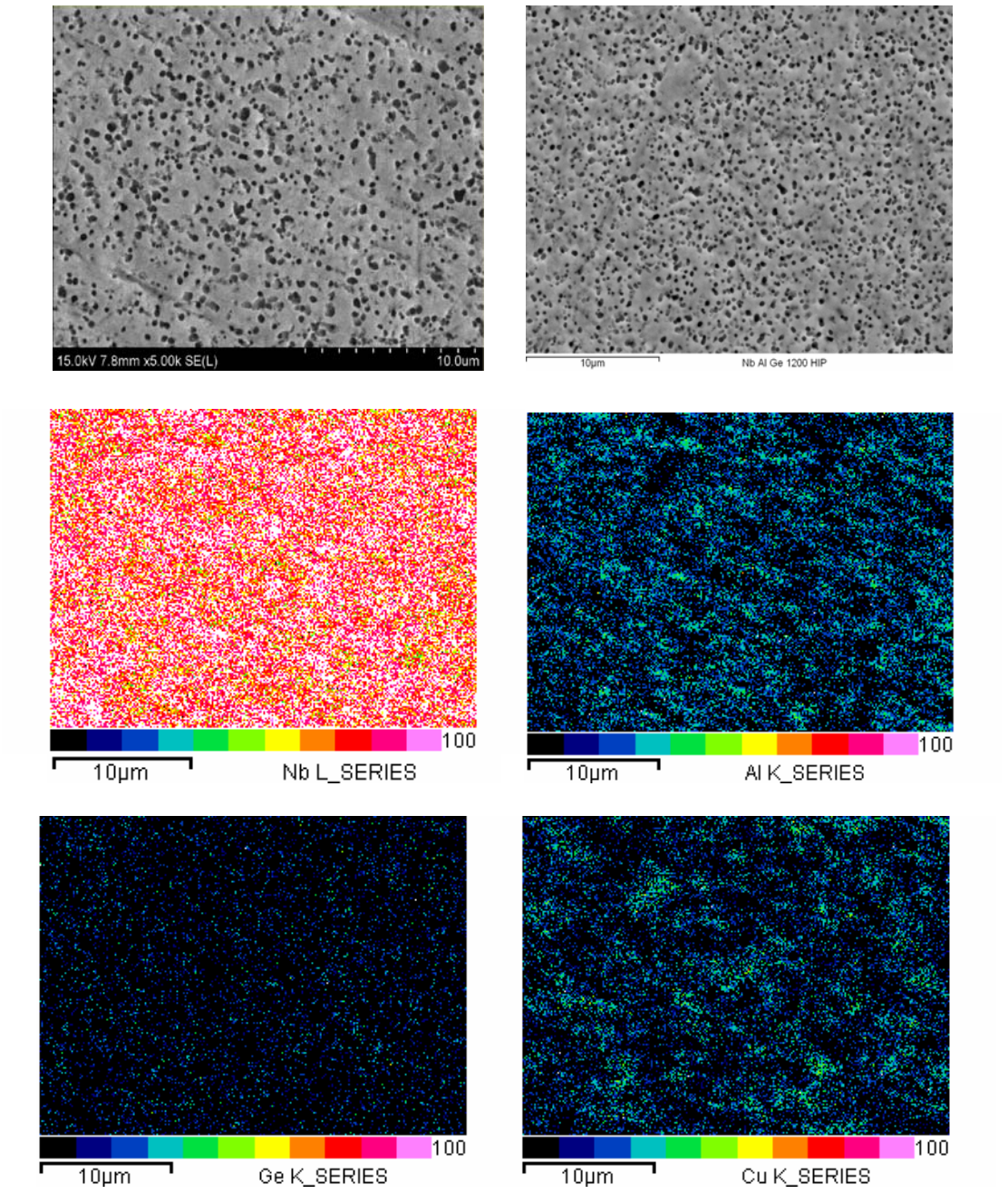

Figure 8.33 Typical SE image (top left), and BSE (top right) with the corresponding X-ray quantification maps for ET(3Nb + 0.7Al + 0.3Ge) M20 + HIP1200. The distribution of niobium, germanium and copper is uniform throughout the material.

Elements	at. (%)	n	Volume (%)	Phase diagram data (table 1/2)
Al K Cu K Ge K Nb L	0 0 0 100	41	27	Nb
Al K Cu K Ge K Nb L	25 (± 2) 0 0 75 (± 2)	34	23	$Nb_3Al + Nb_2Al$ 21.8 < Al < 30 at. %
Al K Cu K Ge K Nb L	0 24 (± 5) 0 76 (± 5)	18	12	$(Nb)_{ss} + (Cu)_{ss}$ 0 < Nb < 100 at. %
Al K Cu K Ge K Nb L	0 0 26 (± 4) 74 (± 4)	12	8	$Nb_3Ge + Nb_5Ge_3$ 20 < Ge < 38 at. %
Al K Cu K Ge K Nb L	0 0 12 (± 4) 88 (± 4)	7	5	$(Nb)_{ss} + Nb_3Ge$ 4 < Ge < 19 at. %
Al K Cu K Ge K Nb L	0.00 20 (± 5) 12 (± 6) 68 (± 9)	6	4	$(Nb)_{ss} + Nb_5(Ge,Cu)_3 + (Cu)_{ss}$ $Nb_5(Ge,Cu)_3$ with Nb = 50 at. %
Al K Cu K Ge K Nb L	32 (± 1) 0 0 68 (± 1)	5	3	Nb_2Al 30 ≤ Al ≤ 34.5 at. %
Al K Cu K Ge K Nb L	21 (± 4) 0 16 (± 4) 63 (± 5)	5	3	$Nb_3(Al_{1-x}Ge_x) + Nb_2(Al_{1-x}Ge_x) + Nb_5(Al_{1-x}Ge_x)_3$ $Nb_3(Al_{1-x}Ge_x)$ with Ge = 7 at.%
Al K Cu K Ge K Nb L	21.2 (± 0.3) 0 0 78.8 (± 0.3)	4	3	Nb_3Al 18.8 ≤ Al ≤ 21.8 at. %
Al K Cu K Ge K Nb L	19 (± 2) 21 (± 2) 0 60 (± 4)	3	2	$Nb_2(Al,Cu) + (Nb)_{ss}$ $Nb_2(Al,Cu)$ with 26 ≤ Cu ≤ 29 at. %

Table 8.22 (Table I of II for ET(3Nb + 0.7Al + 0.3Ge) M20 + HIP1200). The average compositional points (at. %) for ET(3Nb + 0.7Al + 0.3Ge) M20 + HIP1200. 150 pixels were used to estimate the crystalline phases and the corresponding volume percent (n/150). Previous phase diagrams from the literature were used to identify the resulting phase [50,55,67]. Also provided is the associated range of composition within the relevant region of the phase diagram.

Elements	at. (%)	n	Volume (%)	Phase diagram data (table 2/2)
Al K Cu K Ge K Nb L	20 (± 2) 16 (± 1) 0 64 (± 2)	3	2	$Nb_2(Al,Cu) + (Nb)_{ss}$ $Nb_2(Al,Cu)$ with Cu = 10 and 26 at. %
Al K Cu K Ge K Nb L	17.3 (± 0.4) 0.00 0.00 82.7 (± 0.4)	2	1	$(Nb)_{ss} + Nb_3Al$ 9 < Al < 18.8 at. %
Al K Cu K Ge K Nb L	19 (± 1) 0 5 (± 1) 75 (± 1)	2	1	$Nb_3(Al_{1-x}Ge_x) + Nb_2(Al_{1-x}Ge_x)$ $Nb_3(Al_{1-x}Ge_x)$ with 0 < Ge ≤ 7
Al K Cu K Ge K Nb L	0 0 19 (± 1) 80 (± 1)	2	1	Nb_3Ge 19 ≤ Ge ≤ 20 at. %
Al K Cu K Ge K Nb L	22 (± 1) 28 (± 1) 0 50 (± 1)	2	1	$(Nb)_{ss} + Nb_2(Al,Cu) + (Cu)_{ss}$ $Nb_2(Al,Cu)$ with Cu = 29 at. %
Al K Cu K Ge K Nb L	49 (±2) 0 0 51 (±2)	1	1	$Nb_2Al + NbAl_3$ 34 ≤ Al ≤ 74.5 at. %
Al K Cu K Ge K Nb L	0 0 39 (±2) 61 (±2)	1	1	Nb_5Ge_3 38 ≤ Ge ≤ 41.2 at. %
Al K Cu K Ge K Nb L	24 (±2) 6 (±2) 0 70 (±2)	1	1	$Nb_2(Al,Cu) + Nb_3(Al,Cu)$ $Nb_2(Al,Cu)$ with 0 < Cu ≤ 10 at. % $Nb_3(Al,Cu)$ with 0 < Cu ≤ 5 at. %
Al K Cu K Ge K Nb L	29 (±2) 22 (±2) 0 49(±2)	1	1	$NbAlCu + Nb_2(Al,Cu)$ NbAlCu with Cu = 24 at. % $Nb_2(Al,Cu)$ with Cu = 10 and 26 at. %

Table 8.23 (Table II of II for ET(3Nb + 0.7Al + 0.3Ge) M20 + HIP1200). The average compositional points (at. %) for ET(3Nb + 0.7Al + 0.3Ge) M20 + HIP1200. 150 pixels were used to estimate the crystalline phases and the corresponding volume percent (n/150). Previous phase diagrams from the literature were used to identify the resulting phase [50,55,67]. Also provided is the associated range of composition within the relevant region of the phase diagram.

The data for sample Nb_3Al M20 + HIP1200 are now given. The SEM image collection for each sample is followed by the compositional analysis. Table 8.24 shows that the Nb_3Al formed mostly at (25 ± 2) at.% Al in the region Nb_3Al +Nb_2Al.

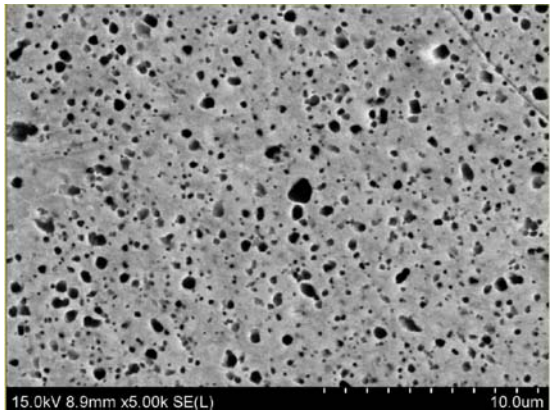

Figure 8.34 Typical SE image for Nb_3Al M20 + HIP1200.

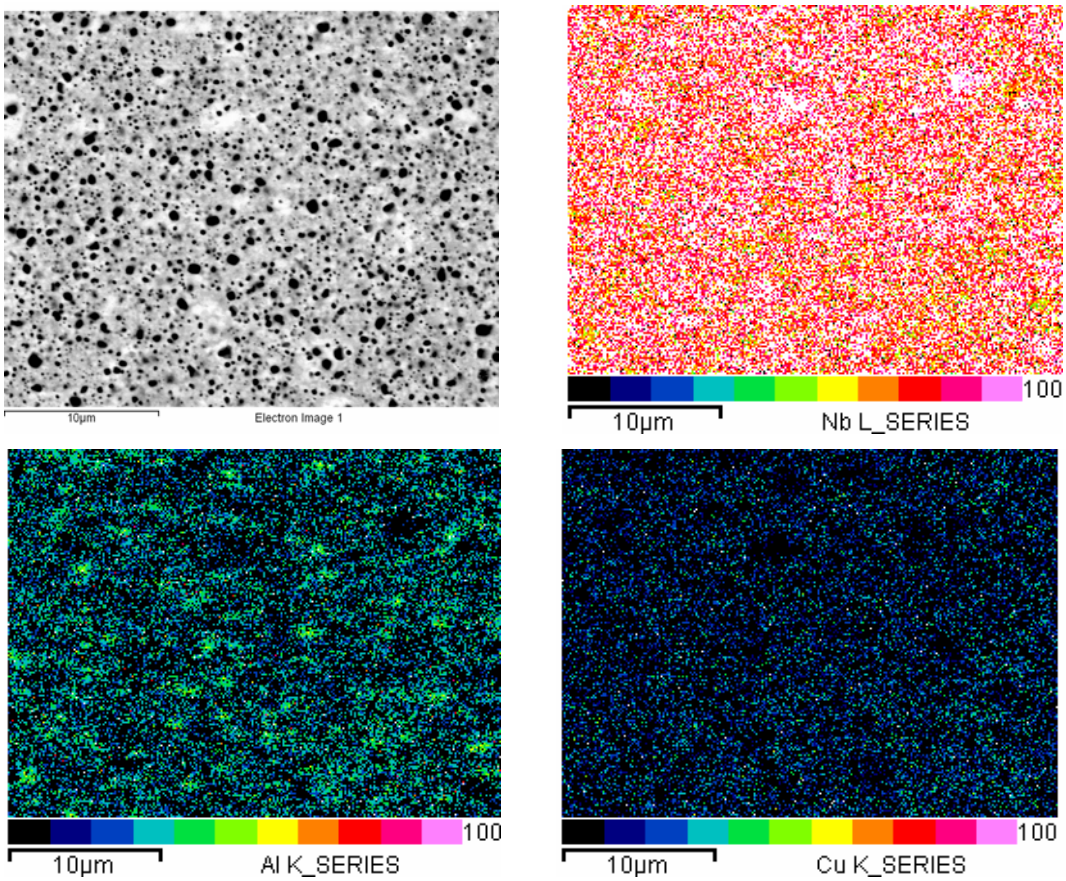

Figure 8.35 BSE image and corresponding X-ray quantification maps Nb_3Al M20 + HIP1200. The distribution of niobium, aluminum and copper is uniform throughout the material.

Elements	at. (%)	n	Volume (%)	Phase diagram data
Al K Cu K Nb L	0 0 100	38	25	Nb
Al K Cu K Nb L	25 (± 2) 0 75 (± 2)	34	22	Nb_3Al +Nb_2Al 21.8 < Al < 30 at. %
Al K Cu K Nb L	0 21 (± 8) 79 (± 8)	26	17	$(Nb)_{ss}$ + $(Cu)_{ss}$ 0 < Nb < 100 at. %
Al K Cu K Nb L	32 (± 2) 0 68 (± 2)	25	17	Nb_2Al 30 ≤ Nb ≤ 34 at. %
Al K Cu K Nb L	36 (± 3) 14 (± 3) 50 (± 7)	6	4	NbAlCu + Nb_2(Al,Cu) NbAlCu with 14 ≤ Cu ≤ 24 at. % Nb_2(Al,Cu) with 2 < Cu ≤ 10 at. %
Al K Cu K Nb L	39 (±1) 0 61 (±1)	5	3	Nb_2Al + $NbAl_3$ 34 ≤ Al ≤ 74.5 at. %
Al K Cu K Nb L	30 (± 2) 17 (± 3) 53 (± 3)	5	3	NbAlCu + Nb_2(Al,Cu) NbAlCu with Cu = 24 at. % Nb_2AlCu with Cu =10 and 26 at. %
Al K Cu K Nb L	21 (± 3) 14 (± 3) 65 (± 3)	4	3	Nb_2(Al,Cu) + $(Nb)_{ss}$ Nb_2AlCu with Cu =10 and 26 at. %
Al K Cu K Nb L	20 (± 1) 0 80 (±1)	3	2	Nb_3Al 18.8 ≤ Al ≤ 21.8 at. %
Al K Cu K Nb L	29.2 (± 0.3) 6 (±1) 65 (±1)	2	1	Nb_2(Al,Cu) 0 ≤ Cu ≤ 10 at. %
Al K Cu K Nb L	40 (±2) 6 (±2) 54 (±2)	1	1	Nb_2(Al,Cu) + NbAlCu + Al_3(Cu,Nb) Nb_2AlCu with Nb = 65 at. % NbAlCu with Nb = 34 at. % Al_3(Cu,Nb) with Nb =25 at. %
Al K Cu K Nb L	27 (±2) 20 (±2) 53 (±2)	1	1	Nb_2(Al,Cu) Cu = 10 and 26 at. %

Table 8.24 The average compositional points (at. %) for Nb_3Al M20 + HIP1200. 150 pixels were used to estimate the crystalline phases and the corresponding volume percent (n/150). Previous phase diagrams from the literature were used to identify the resulting phase [50,55,67]. Also provided is the associated range of composition within the relevant region of the phase diagram.

Discussion. SEM data are discussed in two parts: the average (EDX) and the local compositional information (XQM) for the four samples measured: ET M20 + HIP600/HIP1200 and Nb_3Al M20 + HIP600/HIP1200. The average Nb:(Al+Ge) and Ge:Al ratios are nominally 3 and 0.43 respectively for sample ET M20 + HIP 1200 are (3.2 ± 0.2) and (0.4 ± 0.1). The average Nb:Al ratio for Nb_3Al M20 + HIP1200 is nominally (3.4 ± 0.1) although we suspect that the overall composition is close to that intended but that the error in the Nb:(Al+Ge) is larger than quoted because these values are not produced using standards in the EDX measurements. Table 8.25 shows the compositions extracted from Table 8.16 to Table 8.24 associated with those regions that include the A15 phases and corresponding phase diagram compositional data in turn for samples ET M20 + HIP600/HIP1200, Nb_3Al M20 + HIP600/HIP1200. There was always more Nb_3Al formed than Nb_3Ge formed in the ternary compounds – for example ET M20 + HIP600 and ET M20 + HIP1200. The average composition of the components in any two/three phase region is approximately the same for the different materials: Nb_3Al + Nb_2Al (Figure 3.8), Nb_3Ge + Nb_5Ge_3 (Figure 3.5) and $Nb_3(Al_{1-x}Ge_x)$ + $Nb_2(Al_{1-x}Ge_x)$ + $Nb_5(Al_{1-x}Ge_x)_3$ (Figure 3.13). Table 8.26 and
Table 8.27 use the Lever rule to calculate the volume phase percentage of the phases present for ET M20 + HIP600/HIP1200 and Nb_3Al M20 + HIP600/HIP1200, respectively. For both samples Nb_3Al M20 + HIP600 and Nb_3Al M20 + HIP1200, in the double phase region Nb_3Al + Nb_2Al, the amount of Al was similar. Table 8.26 compares the volume phase percentage for samples ET M20 + HIP600 and ET M20 + HIP1200. For the first sample, the A15 phase content is 45 % and 30 % in the low copper content and typical copper content region, respectively. This suggests that the copper limits the A15 phase formation. The average Nb + $(Nb)_{ss}$ volume percentages are ~ 35 % in all regions. In the Cu high region, the total volume of Cu + $(Cu)_{ss}$ was found to be 40 %. For sample ET M20 + HIP1200 the volume percentages of the A15 phase and the bcc Nb + $(Nb)_{ss}$ phase are 24 % and 40 %, respectively.

Sample	Region	Composition
ET M20 + HIP600	$(Nb)_{ss} + Nb_3Al$ 9 < Al < 18.8 at. %	(17 ± 2) at.% Al
	Nb_3Al 18.8 ≤ Al ≤ 21.8 at. %	(20.5 ± 0.4) at.% Al
	$Nb_3Al + Nb_2Al$ 21.8 < Al < 30 at. %	(23 ± 1) at.% Al
	Nb_3Ge 19 ≤ Ge ≤ 20 at. %	(20 ± 2) at.% Ge
	$Nb_3(Al_{1-x}Ge_x) + Nb_2(Al_{1-x}Ge_x) + Nb_5(Al_{1-}Ge_x)_3$ $Nb_3(Al_{1-x}Ge_x)$ with Ge = 7 at.%	(16 ± 3) at.% Al (17 ± 1) at.% Ge (66 ± 4) at.% Nb
ET M20 + HIP1200	$(Nb)_{ss} + Nb_3Al$ 9 < Al < 18.8 at. %	(17.3 ± 0.4) at.%Al
	Nb_3Al 18.8 ≤ Al ≤ 21.8 at. %	(21.2 ± 0.3) at.%Al
	$Nb_3Al + Nb_2Al$ 21.8 < Al < 30 at. %	(25 ± 2) at.%Al
	$(Nb)_{ss} + Nb_3Ge$ 4 < Ge < 19 at. %	(12 ± 4) at.%Ge
	Nb_3Ge 19 ≤ Ge ≤ 20 at. %	(19 ± 1) at.%Ge
	$Nb_3Ge + Nb_5Ge_3$ 20 < Ge < 38 at. %	(26 ± 4) at.%Ge
	$Nb_3(Al_{1-x}Ge_x) + Nb_2(Al_{1-x}Ge_x) + Nb_5(Al_{1-}Ge_x)_3$ $Nb_3(Al_{1-x}Ge_x)$ with Ge = 7 at.%	(21 ± 4) at.% Al (16 ± 4) at.% Ge (63 ± 5) at.% Nb
Nb_3Al M20 + HIP600	$(Nb)_{ss} + Nb_3Al$ 9 < Al < 18.8 at. %	(17.3 ± 0.4) at.%Al
	Nb_3Al 18.8 ≤ Al ≤ 21.8 at. %	(20 ± 1) at.%Al
	$Nb_3Al + Nb_2Al$ 21.8 < Al < 30 at. %	(25 ± 2) at.%Al
Nb_3Al M20 + HIP1200	Nb_3Al 18.8 ≤ Al ≤ 21.8 at. %	(20 ± 1) at.%Al
	$Nb_3Al + Nb_2Al$ 21.8 < Al < 30 at. %	(25 ± 2) at.%Al

Table 8.25 TA compilation of data from tables 8.17, 8.18, and 8.19 then 8.23 and 8.24 then 8.20, 8.21 and 8.25 for samples ET(3Nb + 0.7Al + 0.3Ge) M20 and Nb_3Al M20 processed with HIP600 and HIP1200 respectively. The average compositional points (at. %) for the Al or Ge in all regions on the phase diagrams of the A15 phases [50,55,67].

Phase	ET M20 + HIP 600			ET M20 + HIP 1200
	Low Cu	Typical Cu	High Cu	
Nb	34 %	14 %	-	27 %
$(Nb)_{ss}$	3 %	24 %	34 %	13 %
Nb_3Al	35 %	30 %	1 %	14 %
Nb_3Ge	4 %	-	-	8 %
$Nb_3(Al,Ge)$	6 %	-	-	2 %
Nb_2Al	7 %	2 %	-	16 %
$Nb_2(Al,Ge)$	5 %	-	-	2 %
Nb_5Ge_3	-	-	-	5 %
$Nb_5(Al,Ge)_3$	6 %	-	-	1 %
$Nb_5(Ge,Cu)_3$	-	-	1 %	2 %
$Nb_2(Al,Cu)$	-	26 %	22 %	6 %
NbAlCu	-	-	2 %	< 1 %
$(Cu)_{ss}$	-	4 %	38 %	3 %
Cu	-	-	2 %	-
$Nb_3(Al,Cu)$	-	-	-	< 1 %
$NbAl_3$	-	-	-	< 1 %

Table 8.26 Estimated volume phase percentage for ET(3Nb + 0.7Al + 0.3Ge) M20 + HIP600 and ET(3Nb + 0.7Al + 0.3Ge) M20 + HIP1200.

Phase	Nb_3Al M20 + HIP 600			Nb_3Al M20 + HIP 1200
	Low Cu	Typical Cu	High Cu	
Nb	22 %	26 %	-	25 %
$(Nb)_{ss}$	7 %	15 %	19 %	15 %
Nb_3Al	37 %	16 %	-	12 %
Nb_2Al	30 %	34 %	-	32 %
$Nb_2(Al,Cu)$	3 %	4 %	6 %	11 %
NbAlCu			3 %	1 %
Cu	-	-	26 %	-
$(Cu)_{ss}$	1 %	5 %	31 %	3 %
$(Al)_{ss}$	-	-	2 %	-
Al_2Cu	-	-	12 %	-
Al_3Nb				< 1 %
$Al_3(Cu, Nb)$	-	-	-	< 1 %

Table 8.27 Estimated volume phase percentage for Nb_3Al M20 + HIP600 and Nb_3Al M20 + HIP1200.

Table **8.27** compares the volume phase percentage for samples Nb_3Al M20 + HIP600 and Nb_3Al M20 + HIP1200. For the first sample, the A15 phase content is ~ 40 % and ~ 20 % in the low copper content and typical copper content region, respectively. The Nb + $(Nb)_{ss}$ volume percentages are ~ 30 %, ~ 40 % and ~ 20 % in turn for the three regions in that particular order. In the high Cu region, the total volume of Cu + $(Cu)_{ss}$ was found to be ~ 60 %. For Nb_3Al M20 + HIP1200 the Nb_3Al phase and Nb + $(Nb)_{ss}$ volume percentages are 12 % and 40 %, respectively.

Summary. The EDX results indicate large contamination levels from milling media of (11.9 ± 0.4) at.% Cu and (12.2 ± 0.6) at.% Cu for ET M20 and Nb_3Al bulk materials, respectively. They are in agreement with the yield increase (subsection 8.3.3). The Nb:(Al+Ge) and Nb/Al ratios indicate a relatively large Nb-excess compared to the ideal nominal ratio 3:1. These ratios indicate that Al and Ge loss can occur without going to very high temperatures where volatility becomes an issue. The XQMs for $Nb_3(Al_{1-x}Ge_x)$ bulk materials indicates that the dominant A15 phase is Nb_3Al rather than a solid solution of Nb_3Al and Nb_3Ge (section 3.4.1). Nb_3Al formed mostly in the double-phase regions Nb_3Al + Nb_2Al at approximately the same composition for samples $Nb_3(Al,Ge)$ + HIP1200 and Nb_3Al + HIP600/1200. The formation of the A15 materials on the Al/Ge-rich side of the phase diagram is consistent with the lattice parameters for Nb_3Al and Nb_3Ge. These results are similar to those found for Nb_3Ge (sub-section 7.4.2), which formed predominantly on the Ge-rich side of the phase diagram. Further investigation on the structural distribution of the compositions requires a detailed analysis at nanometre level using eventually the TEM.

8.4.3 ACMS results

The superconducting properties were investigated using ac magnetometry. The superconducting parameters derived from these measurements are $T_{C,onset}$ and $B_{C2}(0)$. Zero-field and in-field data are composed of four groups: HIPYYY, HIP600 + AZZZ, HIP1200 + AZZZ and AZZZ. For each processing technique, the materials data will be presented in the order: ET M6, ET M20, CT M20 and Nb_3Al M20. We report ac magnetisation data for all samples in zero field and typical data for one or more samples in field. Summary plots of $T_{C,onset}$ vs. processing temperature and corresponding tables are provided. $T_{C,onset}$, $B_{C2}(0)$ and background signal will be discussed in turn.

Group 1: ET(3Nb + 0.7Al + 0.3Ge) M6 + HIPYYY, ET(3Nb + 0.7Al + 0.3Ge) M20 + HIPYYY, CT(0.7Nb_3Al + 0.3Nb_3Ge) M20 + HIPYYY, Nb_3Al M20 + HIPYYY.
The zero field data for ET M6, CT M20, CT M20 and Nb_3Al M20 processed via HIP'ing are shown by Figure 8.36, Figure 8.39, Figure 8.41 and Figure 8.43 respectively. Figure 8.45 and Figure 8.46 compare the $T_{c,onset}$ versus processing temperature for ET M6/M20 and CT M20/Nb_3Al M20, respectively. Table 8.28 summarises the superconducting properties for the HIPYYY group.

Samples ET M6 + HIPYYY and ET M20 + HIPYYY show similar T_C changes (Figure 8.45). For HIP'ing temperatures up to 800 ^oC, the ac magnetization shows a double transition at low temperatures from ~ 5 K to 7 K and at high temperature transition from ~ 9 K to 11 K. A maximum of T_C is reached for ET M6 and ET M20 after HIP800. Sample ET M6 + HIP1200 (Figure 8.48) shows a double transition with high T_C of 17.59 K and lower T_Cs of 6.80 K, respectively. The high T_C indicates that there is a small remnant amount of highly ordered A15 phase. Unfortunately, this phase does not produce a superconducting transition at 0.5 T indicating that $B_{C2}(0)$ is produced by the low T_C phase. Indeed the high quality A15 grain distribution does not screen the samples in any applied magnetic fields. The transition at 6.80 K indicates an A15 phase whose associated $B_{C2}(0)$ is ~ 4 T.

The T_Cs for samples CT M20 + HIPYYY and Nb_3Al M20 + HIPYYY were found to slightly decrease ~ 9 to ~ 8 K (Figure 8.46) in correspondence to an increase of annealing temperature. A high T_C phase of 16.33 K was found for sample CT M20 + HIP800 (Figure 8.42). Samples Nb_3Al M20 + HIP700/800/1200 have double T_Cs with estimated $B_{C2}(0)$ in agreement with the in-field data. Figure 8.44 show the data for Nb_3Al M20 + HIP700.

The majority of HIP'ed samples have a small $B_{C2}(0)$ below 3 T. The highest $T_{C,onset}$ and $B_{C2}(0)$ were achieved by sample ET M6 + HIP800 with values 10.88 K and 9.86 T, respectively. Better superconducting properties were achieved for group HIPYYY by the 6 h milled sample. This might be attributed to a smaller contamination but also to a reduced disordering. Bulk materials show a small paramagnetic background (i.e. 1 - 5 $A \cdot m^{-1}$) in zero fields whereas for higher fields is slightly diamagnetic and very close to zero.

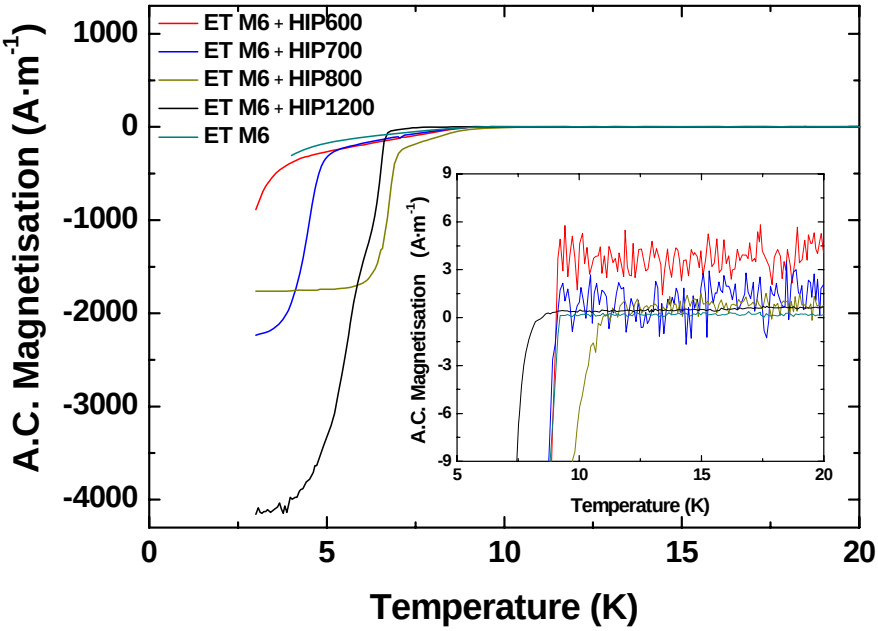

Figure 8.36 Zero field a.c.magnetisation versus temperature for ET(3Nb+0.7Al+0.3Ge) M6 + HIPYYY and precursor powder prior to HIP'ing.

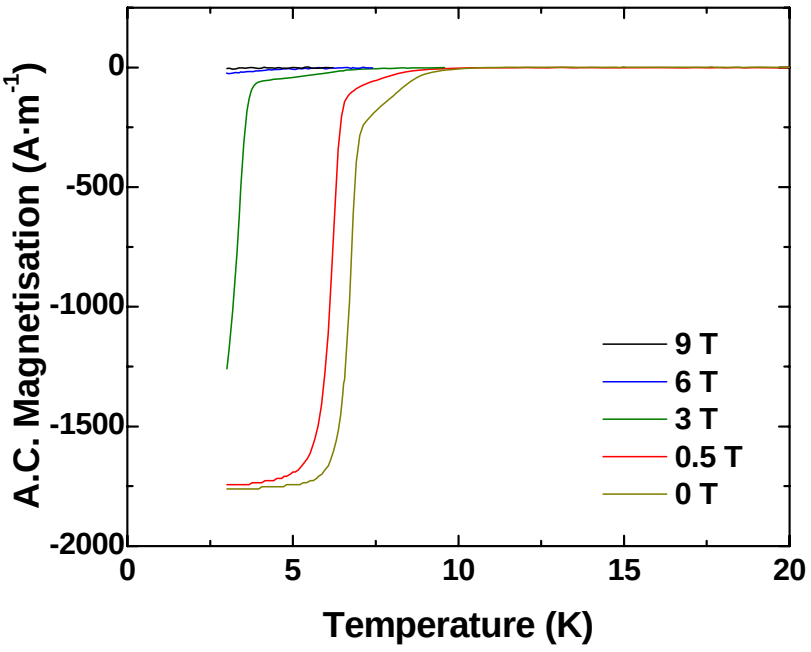

Figure 8.37 A.C. magnetisation versus temperature for sample ET(3Nb+0.7Al+0.3Ge) M6 + HIP800.

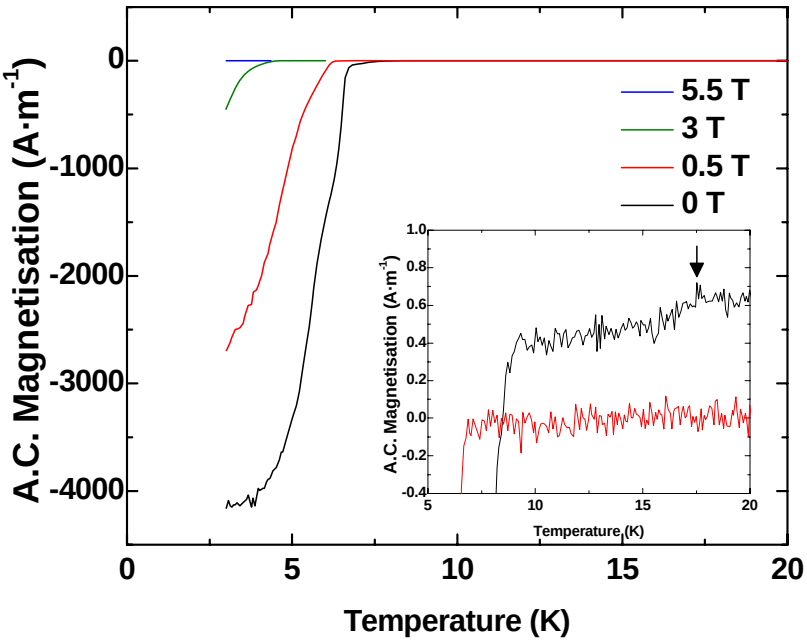

Figure 8.38 A.C. magnetisation versus temperature for sample ET(3Nb+0.7Al+0.3Ge) M6 + HIP1200. The arrow shows remnant high T_C at 17.59 K.

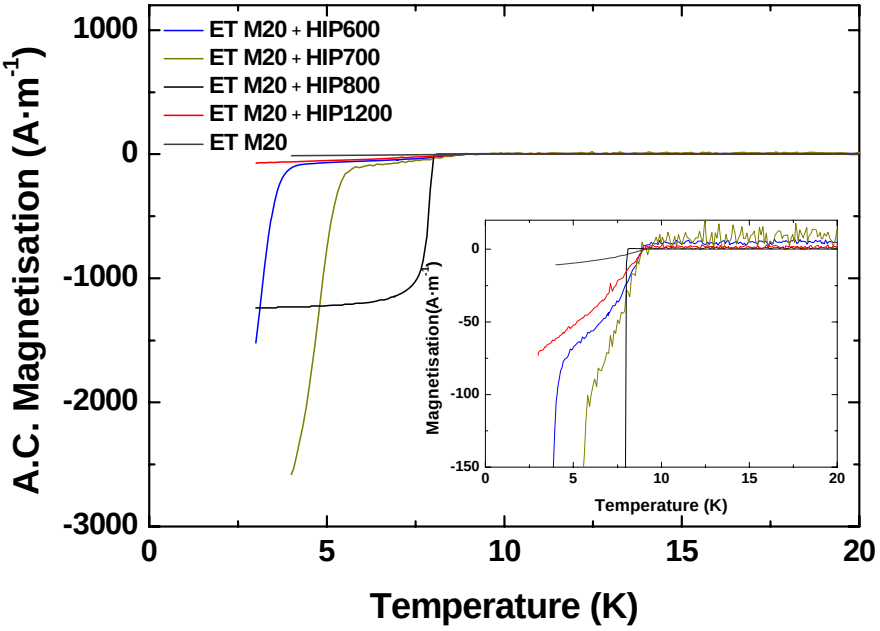

Figure 8.39 Zero field a.c. magnetisation versus temperature for samples ET(3Nb+0.7Al+0.3Ge) M20 + HIPYYY and precursor powder prior to HIP'ing.

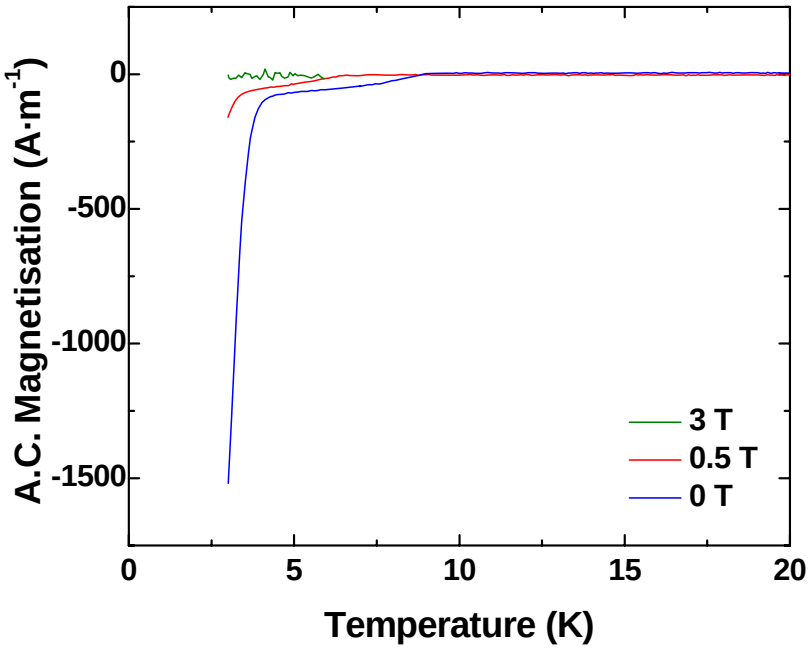

Figure 8.40 A.C. magnetisation versus temperature for ET(3Nb+0.7Al+0.3Ge) M20 + HIP700.

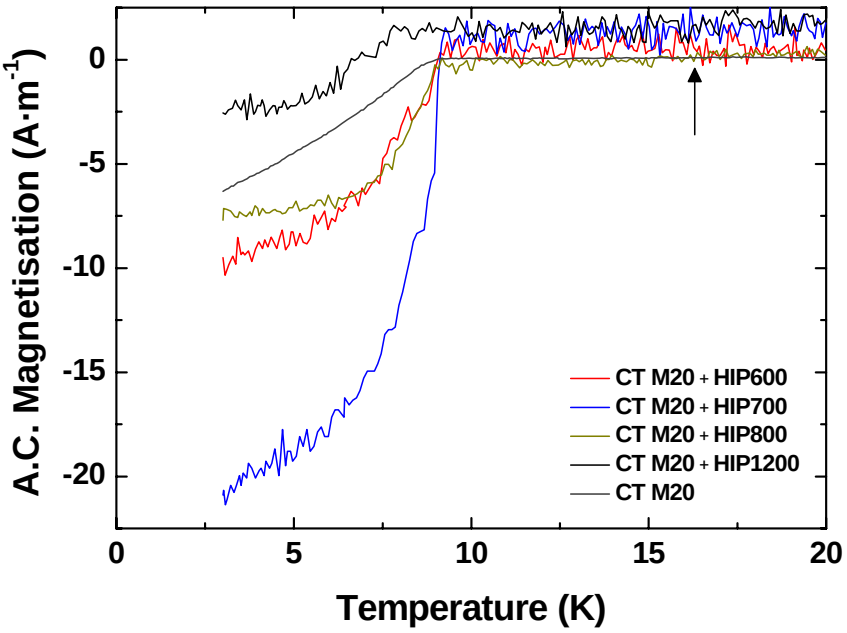

Figure 8.41 Zero field a.c. magnetisation versus temperature for CT(0.7Nb_3Al + 0.3Nb_3Ge) M20 + HIPYYY and precursor powder prior to HIP'ing. The remnant high T_C at 16.33 K is shown more clearly in Figure 8.42.

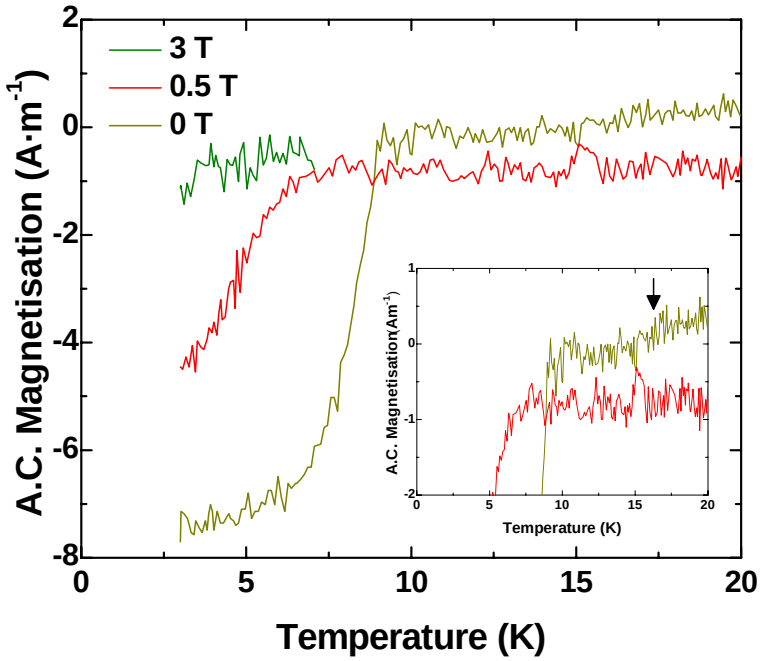

Figure 8.42 A.C. magnetisation versus temperature for CT(0.7Nb_3Al + 0.3Nb_3Ge) M20 + HIP800. The arrow shows remnant high T_C at 16.33 K

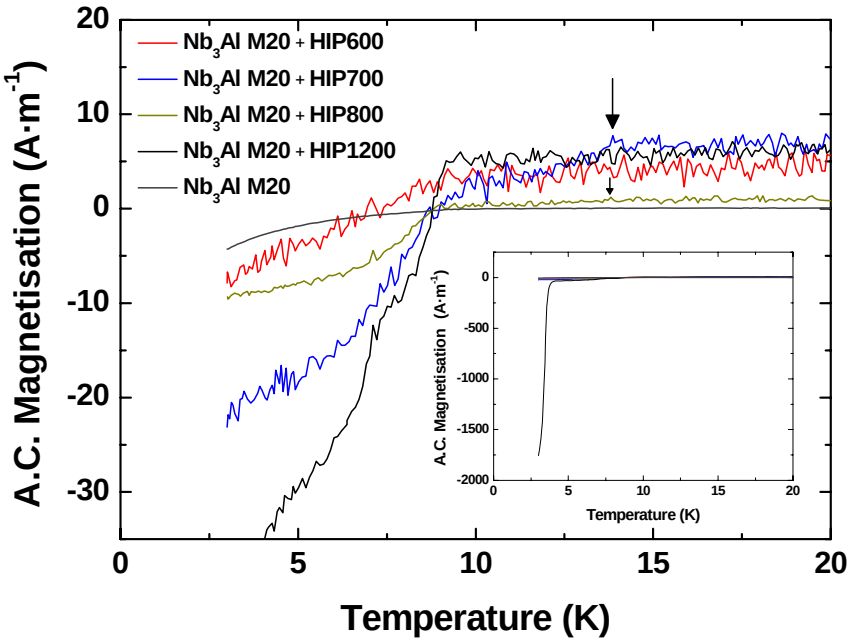

Figure 8.43 Zero field a.c. magnetisation versus temperature for Nb_3Al M20 + HIPYYY and precursor powder prior to HIP'ing. The arrows show remnant T_C at ~ 13.80 for Nb_3Al M20 + HIP700/HIP800.

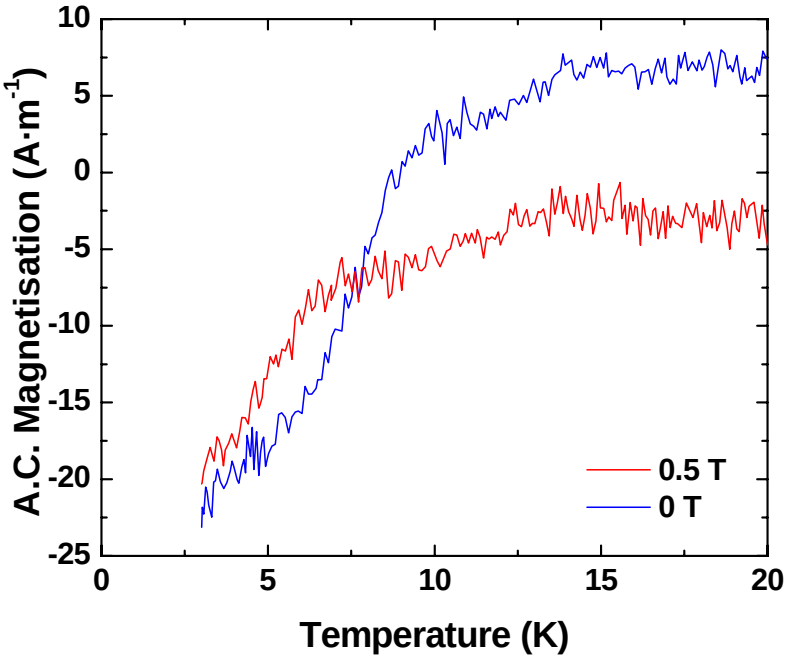

Figure 8.44 A.C. magnetisation versus temperature for sample Nb_3Al M20 + HIP700. The arrow shows remnant T_C at 13.85 K for Nb_3Al M20 + HIP700/HIP800.

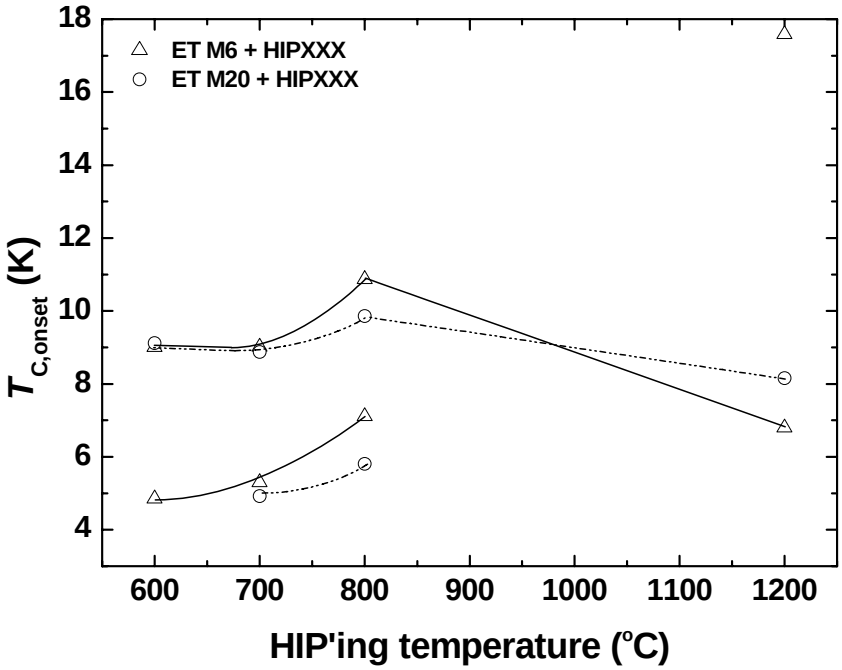

Figure 8.45 $T_{C,onset}$ for ET(3Nb + 0.7Al + 0.3Ge) M6 (triangle) and ET(3Nb + 0.7Al + 0.3Ge) M20 (circle) processed using HIPYYY.

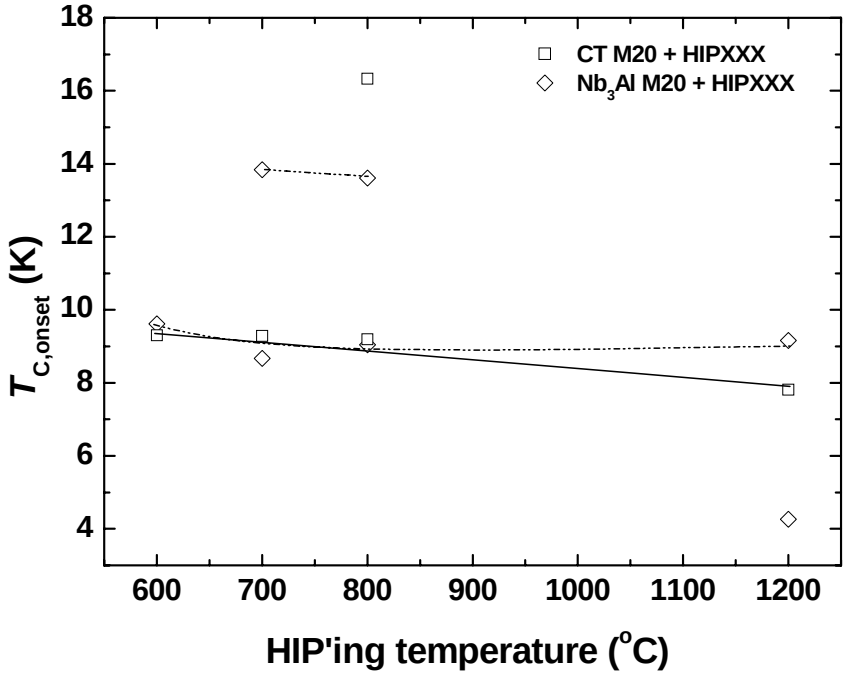

Figure 8.46 $T_{C,onset}$ for CT($0.7Nb_3Al + 0.3Nb_3Ge$) M20 (square) and Nb_3Al M20 (rhombus) processed using HIPYYY.

HIPYYY	ET M6		ET M20		CT M20		Nb_3Al M20	
	$T_{C,onset}$ (K)	$B_{C2}(0)$ (T)	$T_{C,onset}$ (K)	$B_{C2}(0)$ (T)	$T_{C,onset}$ (K)	$B_{C2}(0)$ (T)	$T_{C,onset}$ (K)	$B_{C2}(0)$ (T)
HIP600	9.23 {4.85}	1.22 {1.05}	9.12	1.30	9.30	1.24	9.21	1.38
HIP700	9.26 {5.30}	1.41 {2.91}	9.01 {4.92}	1.27 {1.48}	9.29	1.16	8.67 {13.84}	2.05 {2.98}
HIP800	10.88 {7.11}	9.73 {5.04}	9.86 {5.81}	1.76 {2.89}	9.19 {16.33}	2.42	9.04 {13.81}	1.31 {2.56}
HIP1200	6.80 {17.59}	4.06 -	8.16	1.89	7.81	1.33	9.16 {4.26}	2.63 {2.62}

Table 8.28 $T_{C,onset}$ and B_{C2} for ET($3Nb + 0.7Al + 0.3Ge$) M6, ET($3Nb + 0.7Al + 0.3Ge$) M20, CT($0.7Nb_3Al + 0.3Nb_3Ge$) M20 and Nb_3Al M20 processed using HIPYYY. In curly brackets, the second transition temperature is recorded.

Group 2: ET(3Nb + 0.7Al + 0.3Ge) M6 + HIP600 + AZZZ, ET(3Nb + 0.7Al + 0.3Ge) M20 + HIP600 + AZZZ, CT(0.7Nb_3Al + 0.3Nb_3Ge) M20 + HIP600 + AZZZ, Nb_3Al M20 + HIP600 + AZZZ. The zero field data for ET M6, ET M20, CT M20 and Nb_3Al M20 processed after HIP'ing at 600 ^oC and subsequently annealed are shown in Figure 8.47, Figure 8.49, Figure 8.51 and Figure 8.52, respectively. They are followed by representative in-field data. Figure 8.53 and Figure 8.54 compare the $T_{c,onset}$ versus processing temperature for ET M6, ET M20 and CT M20 and Nb_3Al, respectively. Table 8.29 summarises the superconducting properties for all samples of group 2.

The T_Cs for samples ET M6 + HIP600 + AZZZ and ET M20 + HIP600 + AZZZ show two different behaviours versus processing temperature. In series ET M6 + HIP600 + AZZZ, the transition temperature monotonically increases from ~ 9 to ~ 10.5 K with an increase of annealing temperature. Samples ET M6 + HIP600 + A600/A900 show a double transition with high T_C of 16.94 K/16.70K and lower T_C of 9.43 K/10.57 K, respectively. We note that the optimum annealing (A900) of the precursor bcc sample ET M6 + HIP600 produced $T_{C,onset}$ and B_{C2} with values 10.57 K and 5 T, respectively. In series ET M20 + HIP600 + AZZZ, post annealing (A800) of a structurally disordered sample ET M20 + HIP600 produced the highest $T_{C,onset}$ and B_{C2} of all the group 2 samples with values 11.98 K and 7.53 T, respectively (Figure 8.49). Despite major copper and oxygen contamination, the superconducting properties of ET M20 + HIP600 + A800 are superior compared to that of the identically heat treated ET M6 + HIP600 + A800 sample. We suggest that the phase transition from highly disordered to A15 phase produced better results than the well-known bcc to A15 transition. The T_Cs of CT M20 + HIP600 + AZZZ was found to decrease from ~ 9 to ~ 7 K (Figure 8.54). The T_Cs of Nb_3Al M20 + HIP600 + AZZZ was found to be approximately ~ 9 K. Sample Nb_3Al M20 + HIP600 + A600 shows a double transition with high T_C of 16.64 K and lower T_C of 9.22 K. As with all the remnant material, the high *T*c phases do not produce a superconducting transition at 0.5 T.

In these group 2 samples, only those two samples with the highest T_C have a B_{C2} above 2 Tesla. The background signal of precursor samples (~ 5 $A{\cdot}m^{-1}$) from ET M6 + HIP600 and Nb_3Al M20 + HIP600 disappears after annealing. This suggests that the background of the ac measurements depends on the microstructure.

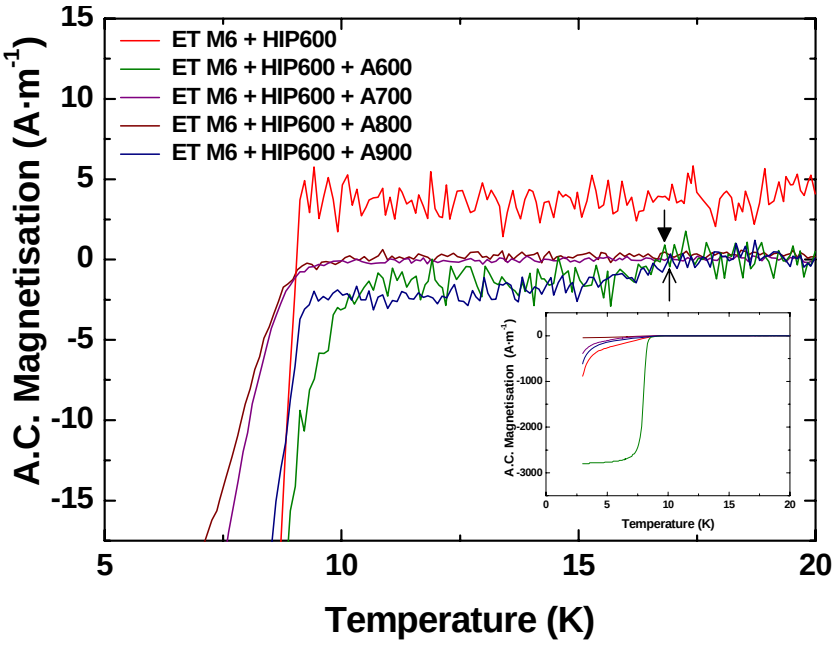

Figure 8.47 Zero field a.c. magnetization versus temperature for ET(3Nb + 0.7Al + 0.3Ge) M6 + HIP600 + AZZZ and precursor material prior to annealing. The arrows show remnant high T_C at 16.94 K and 16.70 K for ET(3Nb + 0.7Al + 0.3Ge) M6 + HIP600 + A600/A900.

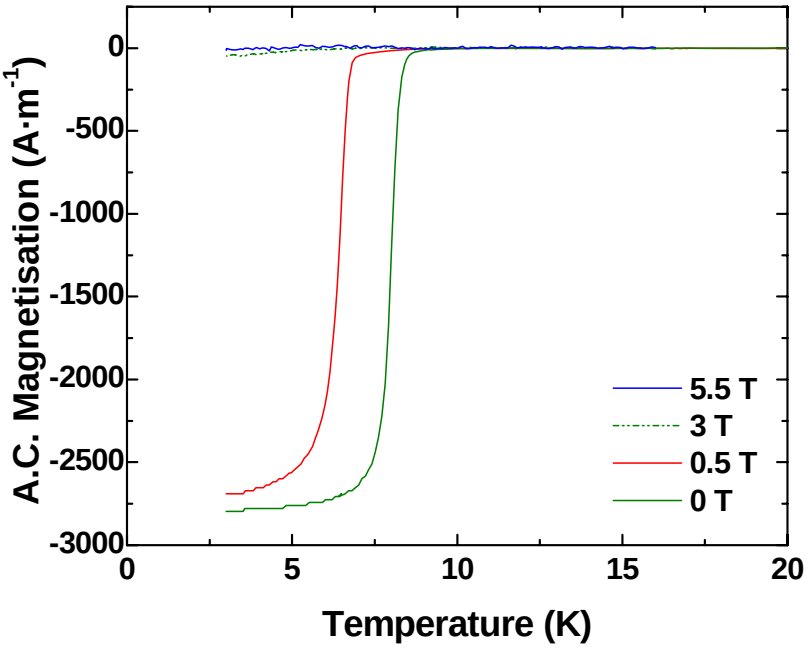

Figure 8.48 A.C. magnetisation versus temperature for ET(3Nb + 0.7Al + 0.3Ge) M6 + HIP600 + A900.

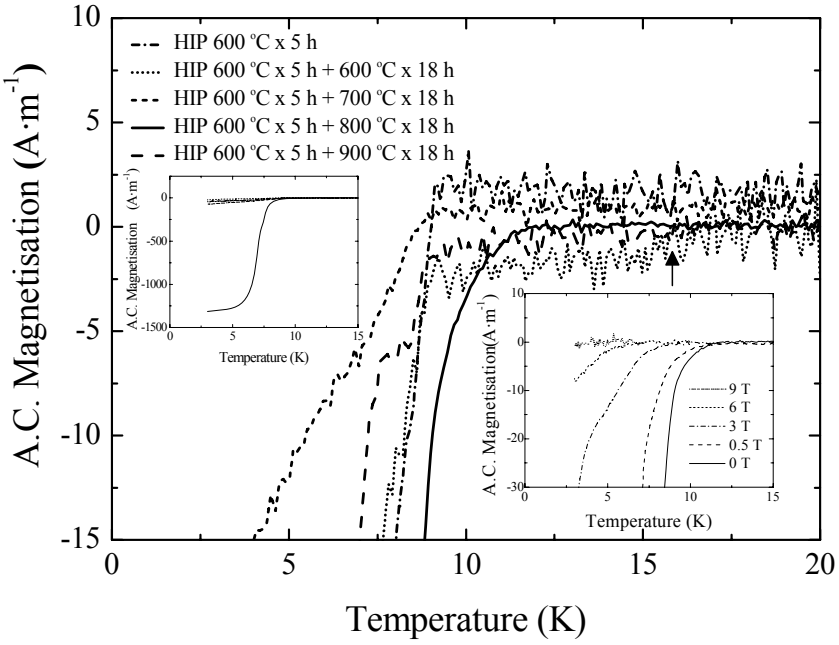

Figure 8.49 Zero field A.C. magnetisation versus temperature for ET(3Nb + 0.7Al + 0.3Ge) M20 + HIP600 + AZZZ and precursor material prior to annealing. The arrow shows remnant high T_C at 15.73 K ET(3Nb + 0.7Al + 0.3Ge) M20 + HIP600 + A600. Inset a: full-scale y-axis for zero field A.C magnetisation. Inset b: In-field A.C. magnetisation versus temperature for ET M20 + HIP600 + A800.

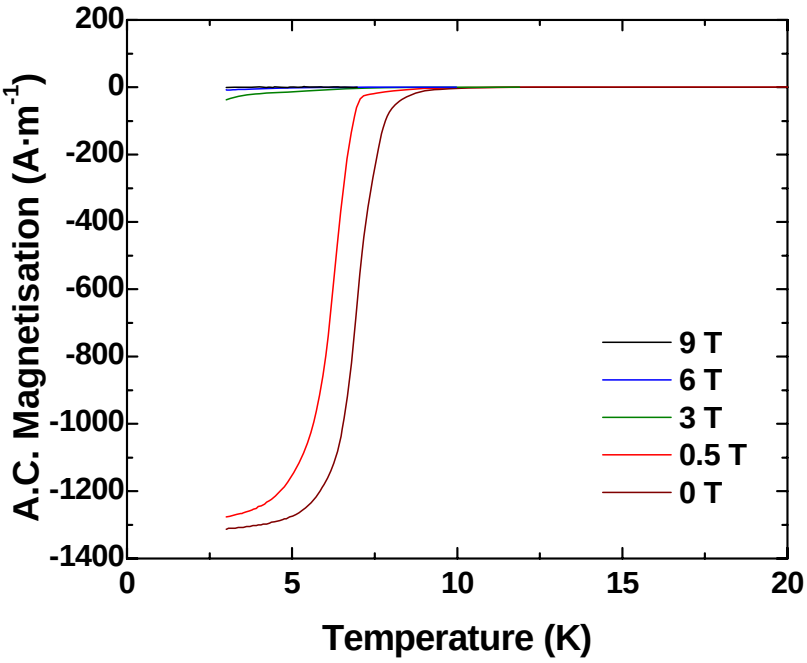

Figure 8.50 A.C. magnetization versus temperature for ET (3Nb + 0.7Al + 0.3Ge) M20 + HIP600 + A800.

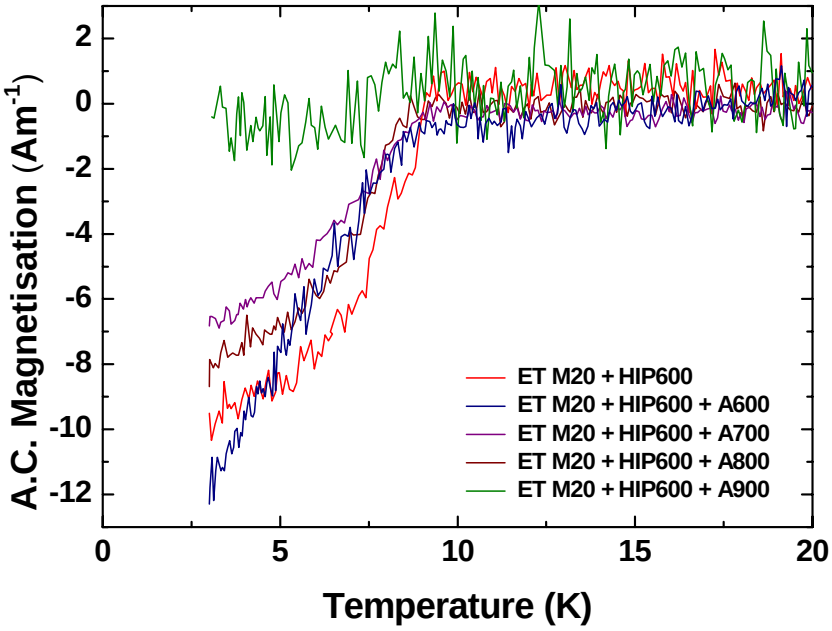

Figure 8.51 Zero field a.c. magnetisation versus temperature for CT($0.7Nb_3Al + 0.3Nb_3Ge$) M20 + HIP600 + AZZZ and precursor material prior to annealing.

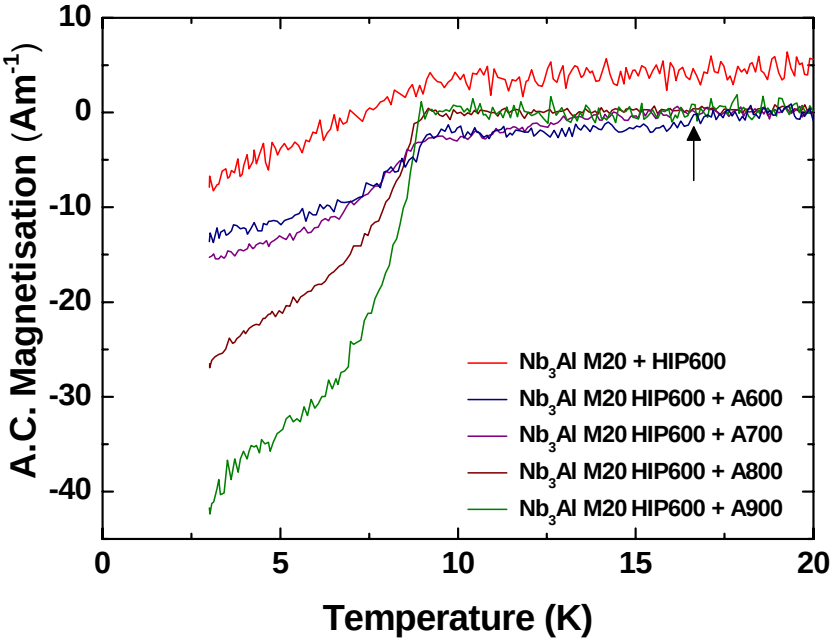

Figure 8.52 Zero field a.c. magnetisation versus temperature for Nb_3Al M20 + HIP600 + AZZZ and precursor material prior to annealing. The arrow shows remnant high T_C at 16.64 K for Nb_3Al M20 + HIP600 + A600.

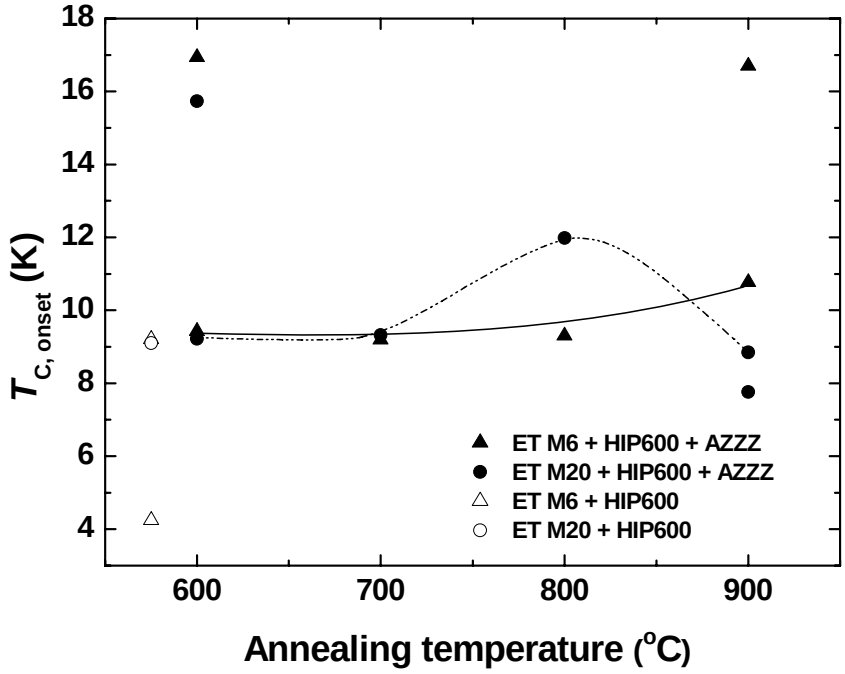

Figure 8.53 $T_{C,onset}$ for ET(3Nb + 0.7Al + 0.3Ge) M6 (triangle) and ET(3Nb + 0.7Al + 0.3Ge) M20 (circle) processed using HIP600 + AZZZ. The empty symbol represents the precursor material prior to annealing.

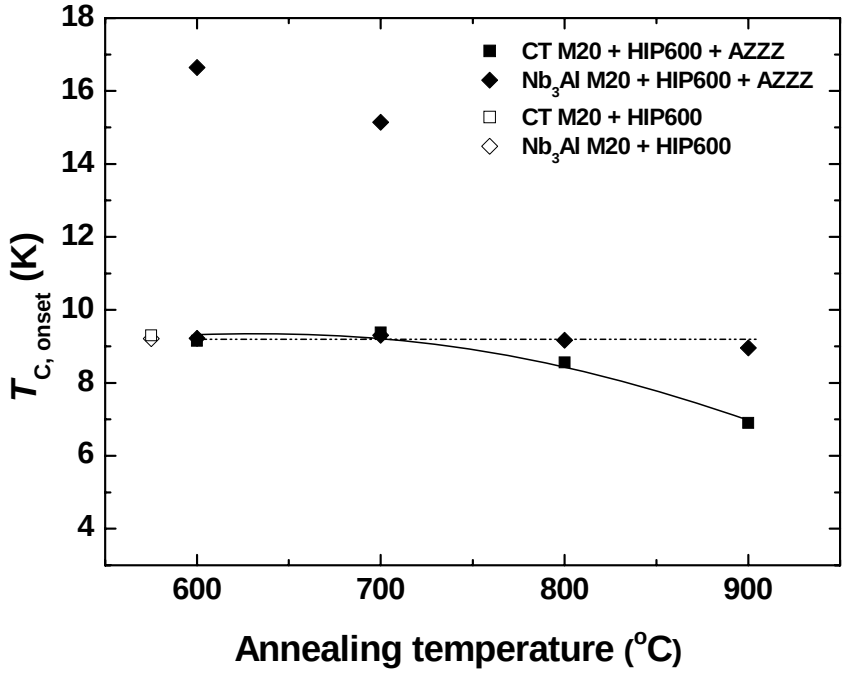

Figure 8.54 $T_{C,onset}$ for CT(Nb_3Al + Nb_3Ge) M20 (square) and Nb_3Al M20 (rhombus) processed using HIP600 + AZZZ. The empty symbol represents the precursor material prior to annealing.

HIP600+AZZZ	ET M6		ET M20		CT M20		Nb_3Al M20	
	$T_{C,onset}$ (K)	$B_{C2}(0)$ (T)	$T_{C,onset}$ (K)	$B_{C2}(0)$ (T)	$T_{C,onset}$ (K)	$B_{C2}(0)$ (T)	$T_{C,onset}$ (K)	$B_{C2}(0)$ (T)
HIP 600	9.23 {4.85}	1.22 {1.05}	9.10	1.30	9.21	1.38	9.30	1.24
HIP600+A600	9.43 {16.94}	1.13	9.22 {15.73}	1.28	9.15	1.33	9.22 {16.64}	1.21
HIP600+A700	9.19	1.70	9.32	1.37	9.38	1.01	9.30 {15.14}	1.41
HIP600+A800	9.30	1.61	11.98	7.53	8.56	1.38	9.17	1.67
HIP600+A900	10.57 {16.70}	5.13	8.85 {7.76}	1.63	6.90	< 0.5	8.96	0.95

Table 8.29 $T_{C,onset}$ and B_{C2} for ET(3Nb + 0.7Al + 0.3Ge) M6, ET(3Nb + 0.7Al + 0.3Ge) M20, CT($0.7Nb_3Al$ + $0.3Nb_3Ge$) M20, Nb_3Al M20 processed using HIP600 + AZZZ and precursor material prior to annealing. In curly brackets, the second transition temperature is recorded.

Group 3: ET(3Nb + 0.7Al + 0.3Ge) M6 + HIP1200 + AZZZ, ET(3Nb + 0.7Al + 0.3Ge) M20 + HIP1200 + AZZZ, CT($0.7Nb_3Al$ + $0.3Nb_3Ge$) M20 + HIP1200 + AZZZ, Nb_3Al M20 + HIP1200 + AZZZ. The zero field data for ET M6, CT M20, CT M20 and Nb_3Al M20 processed via HIP'ing at 1200 ^oC and subsequent annealing are shown by Figure 8.55, Figure 8.57, Figure 8.59 and Figure 8.60, respectively. Figure 8.61 and Figure 8.62 compare the $T_{C,onset}$ versus processing temperature for ET M6/M20 and CT/Nb_3Al M20 processed via HIP1200 + AZZZ, respectively.

Table 8.30 summarises the superconducting properties for the HIP1200 + AZZZ group. The T_Cs for samples ET M6 + HIP1200 + AZZZ and ET M20 + HIP1200 + AZZZ show two different behaviours versus processing temperature (Figure 8.61). In series ET M6 + HIP1200 + AZZZ, the transition temperature increases from ~ 7 to 9 K with increasing annealing temperature. In series ET M20 + HIP1200 + AZZZ, T_C is approximately constant to ~ 9 K. Both samples ET M6 + HIP1200 + A700 for ET M20 + HIP1200 + A700 show a high T_C of ~ 16 K. Similarly to HIP'ed samples with remnant high T_C, high T_C phases do not produce a superconducting transition at 0.5 T indicating that the B_{C2} associated with the large-scale screening is produced by the low Tc phase.

The T_C's for samples CT M20 + HIP1200 + AZZZ and Nb_3Al M20 + HIP1200 + AZZZ are reported in Figure 8.54. The T_Cs of CT M20 + HIP600 + AZZZ were approximately

constant at ~ 8 K. Similarly to the precursor material (HIP1200), samples Nb_3Al M20 + HIP1200 + AZZZ have constantly double transitions at ~ 4.5 K and ~ 9.5 K. The majority of HIP1200 + AZZZ samples have a small $B_{C2}(0)$ below 3 T. Only the series ET M6 + HIP1200 + AZZZ have B_{C2} values of ~ 3.7 T. The background signal is generally small.

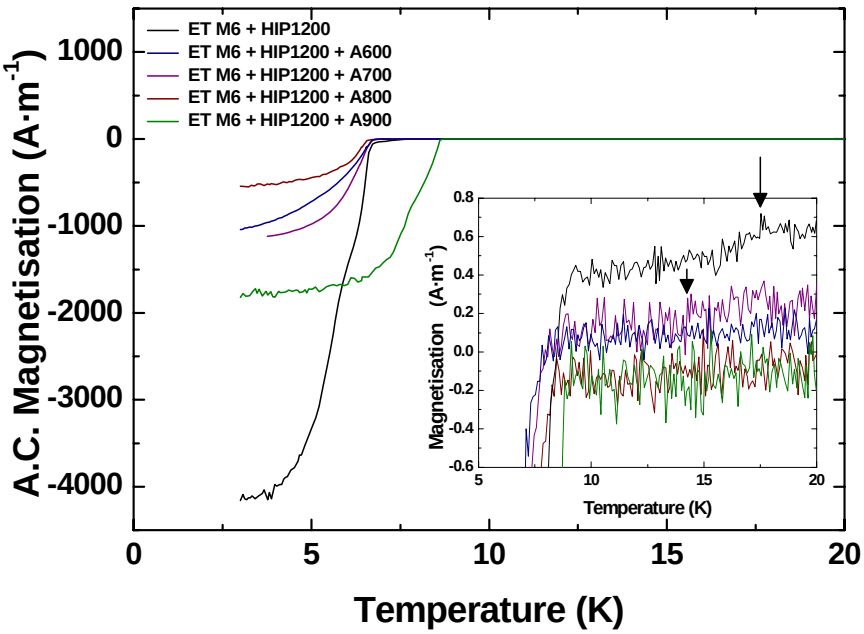

Figure 8.55 Zero field a.c. magnetisation versus temperature for ET(3Nb + 0.7Al + 0.3Ge) M6 + HIP1200 + AZZZ and precursor material prior to annealing.

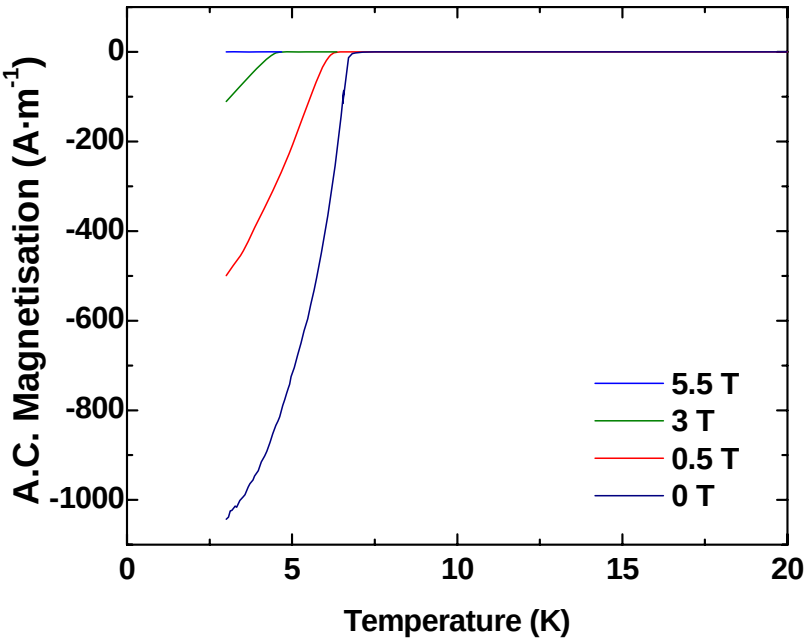

Figure 8.56 A.C. magnetisation versus temperature for ET(3Nb + 0.7Al + 0.3Ge) M6 + HIP 1200 + A600.

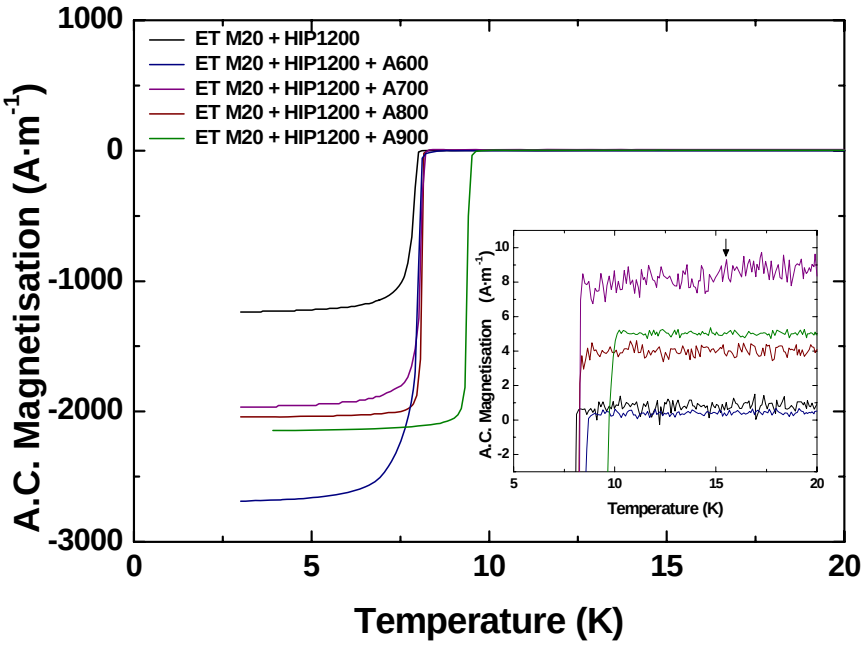

Figure 8.57 Zero field a.c. magnetisation versus temperature for ET(3Nb + 0.7Al + 0.3Ge) M20 + HIP1200 + AZZZ and precursor material prior to annealing. The remnant high T_C at 15.52 K is shown more clearly in Figure 8.58

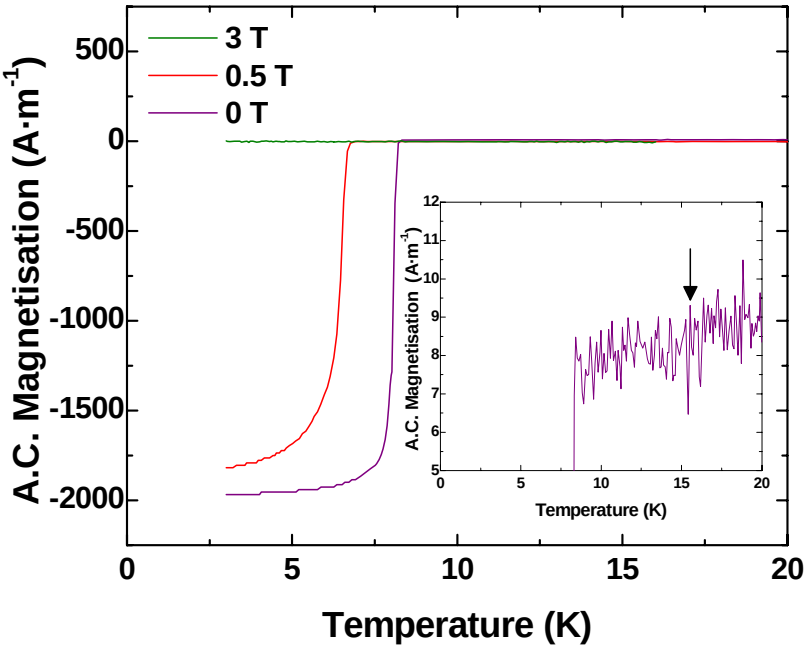

Figure 8.58 A.C. magnetisation versus temperature for ET(3Nb + 0.7Al + 0.3Ge) M20 + HIP 1200 + A700. The arrow shows remnant high T_C at 15.52 for Nb_3Al M20 + HIP600 + A600.

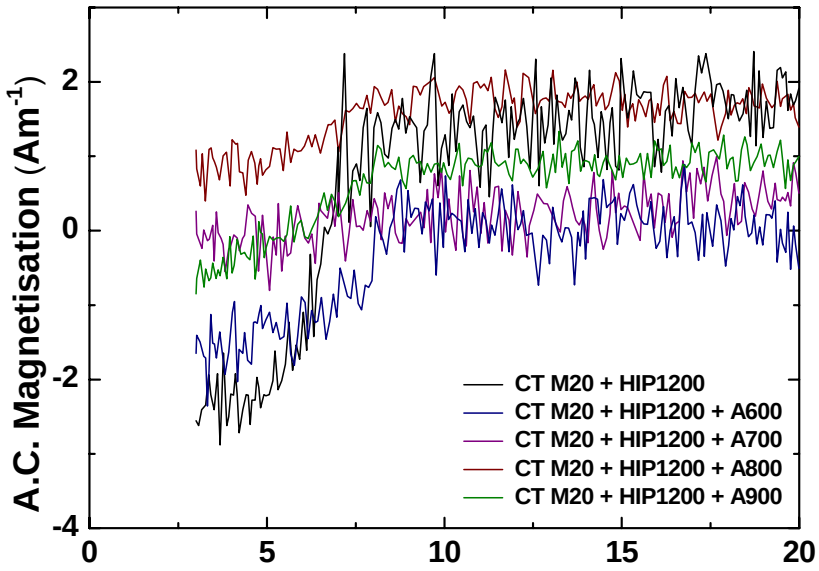

Figure 8.59 Zero field a.c. magnetisation versus temperature for CT($0.7Nb_3Al$ + $0.3Nb_3Ge$) M20 + HIP1200 + AZZZ and precursor material prior to annealing.

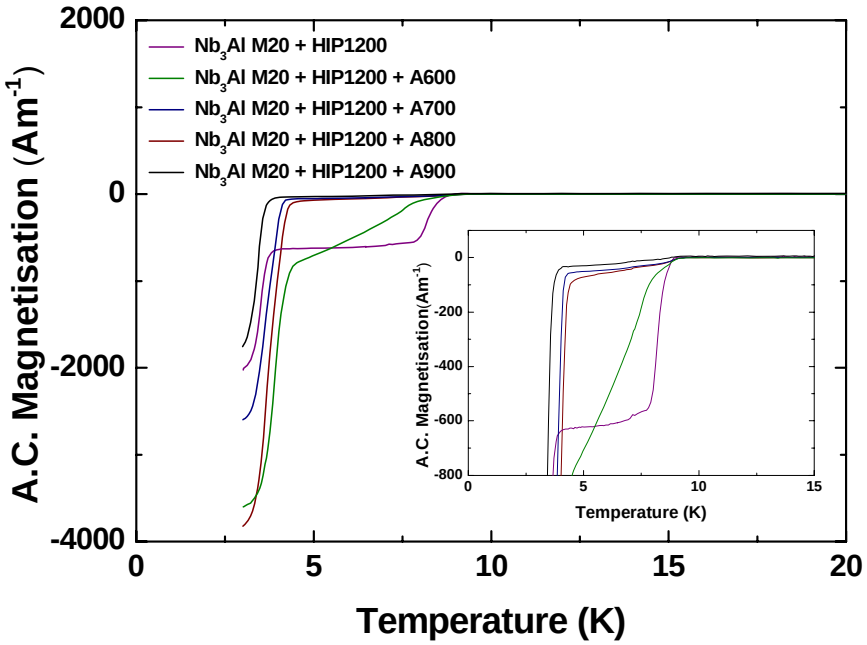

Figure 8.60: Zero field a.c. magnetisation versus temperature for Nb_3Al M20 + HIP1200 + AZZZ and precursor material prior to annealing.

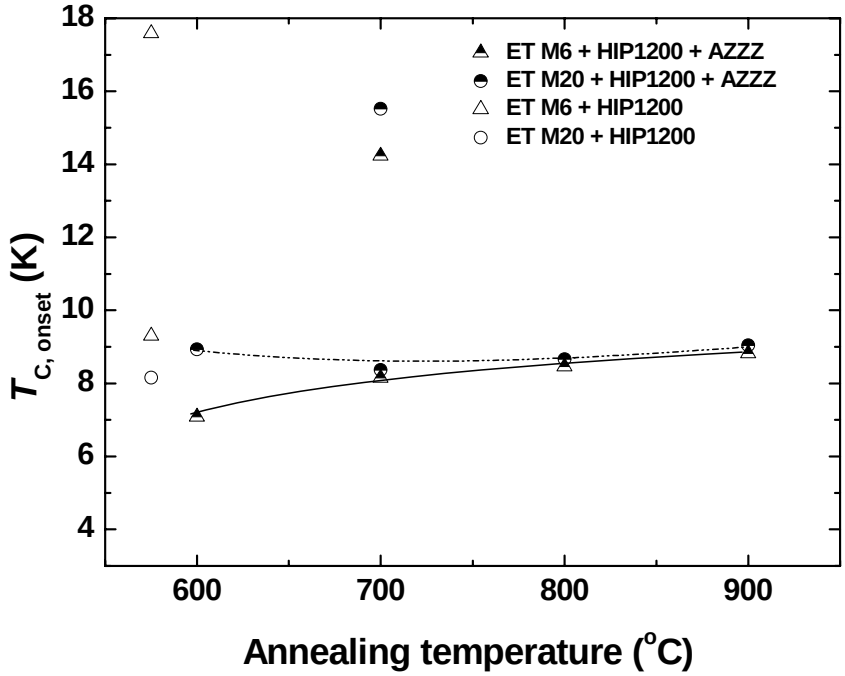

Figure 8.61 $T_{C,onset}$ for ET(3Nb + 0.7Al + 0.3Ge) M6 (triangle) and ET(3Nb + 0.7Al + 0.3Ge) M20 (circle) processed using HIP1200 + AZZZ. The empty symbol represents the precursor material prior to annealing.

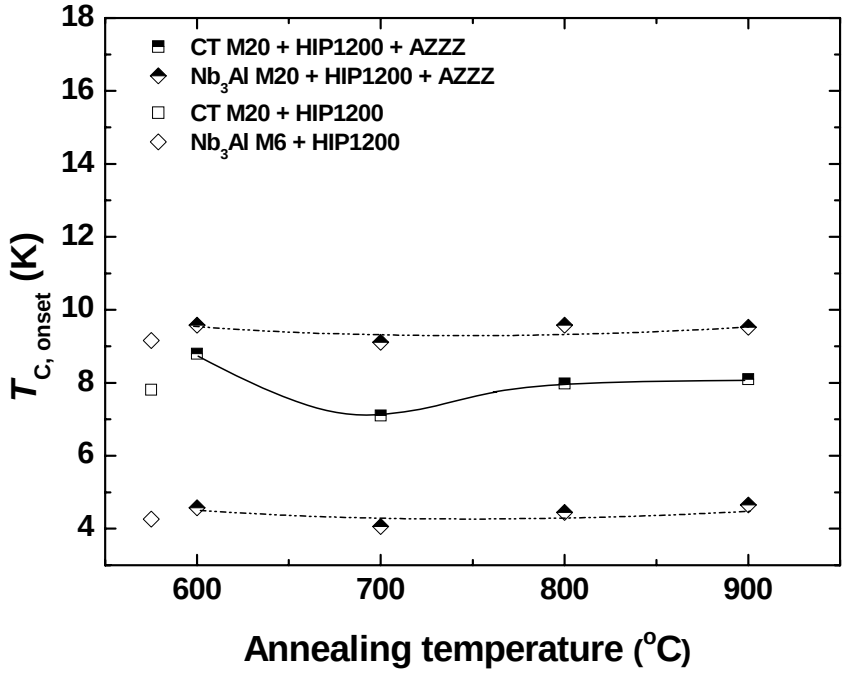

Figure 8.62 $T_{C,onset}$ for CT($0.7Nb_3Al + 0.3Nb_3Ge$) M20 (square) and Nb_3Al M20 (rhombus) processed using HIP1200 + AZZZ. The empty symbol represents the precursor material prior to annealing.

HIP1200 + AZZZ	ET M6		ET M20		CT M20		Nb_3Al M20	
	$T_{C,onset}$ (K)	$B_{C2}(0)$ (T)	$T_{C,onset}$ (K)	$B_{C2}(0)$ (T)	$T_{C,onset}$ (K)	$B_{C2}(0)$ (T)	$T_{C,onset}$ (K)	$B_{C2}(0)$ (T)
HIP1200	6.80 {17.59}	4.06 -	8.16	1.89	7.81	1.33	9.16 {4.26}	2.63 {2.62}
HIP1200 + A600	7.09	3.89	8.93	1.53	8.80	2.02	9.58 {4.58}	2.79 {2.47}
HIP1200 + A700	8.15 {14.23}	3.85	8.37 {15.52}	2.31	7.10	< 0.5	9.11 {4.06}	2.72 {2.34}
HIP1200 + A800	8.46	3.78	8.36	2.02	7.98	1.20	9.58 {4.45}	2.96 {2.61}
HIP1200 + A900	8.82	3.26	9.04	1.65	8.10	1.25	9.47 {4.65}	2.65 {2.55}

Table 8.30 $T_{C,onset}$ and B_{C2} for ET(3Nb + 0.7Al + 0.3Ge) M6, ET(3Nb + 0.7Al + 0.3Ge) M20, CT(0.7Nb_3Al + 0.3Nb_3Ge) M20, Nb_3Al M20 processed using HIP1200 + AZZZ and precursor material prior to annealing. In curly brackets, the second transition temperature is recorded.

Group 4: ET(3Nb + 0.7Al + 0.3Ge) M6 + AZZZ, ET(3Nb + 0.7Al + 0.3Ge) M20 + AZZZ, CT(0.7Nb_3Al + 0.3Nb_3Ge) M20 + AZZZ, Nb_3Al M20 + AZZZ. The zero field data for isochronally annealed samples ET M6, CT M20, CT M20 and Nb_3Al M20 are shown by Figure 8.63, Figure 8.65, Figure 8.67 and Figure 8.69, respectively. Figure 8.71 and Figure 8.72 compare the $T_{c,onset}$ versus processing temperature for ET M6 + AZZZ, ET M20 + AZZZ and CT M20 + AZZZ and Nb_3Al + AZZZ, respectively. Table 8.31 summarises the superconducting properties for the HIP1200 + AZZZ group. The T_Cs for samples ET M6 + AZZZ and ET M20 + AZZZ show two different behaviours versus the processing temperature (Figure 8.71). In series ET M6 + AZZZ, the transition temperature reached a maximum of 11.93 K at A800. In series ET M20 + AZZZ, T_C is approximately constant to ~ 9 K. The annealing temperatures A700, A800, A900 produced simultaneously a secondary phase whose T_C increases progressively from ~ 4 to ~ 7 K. The T_C's for samples CT M20 + AZZZ and Nb_3Al M20 + AZZZ show two different behaviours versus processing temperature (Figure 8.72). Series CT M20 + AZZZ have a maximum Tc of 12.19 K. Samples Nb_3Al M20 + HIP1200 + AZZZ have a constant Tc of ~ 9 K. Samples ET M20 + A700 and Nb_3Al M20 + A900 have a double T_C of ~ 9 K and ~ 4 K. The majority of AZZZ samples have a small $B_{C2}(0)$ below 3 T. The highest $T_{C,onset}$ and B_{C2} were achieved by sample CT M20 + HIP800 with values 12.19 K and 9.21 T, respectively (Figure 8.68). The annealed samples do not show any double transitions with high T_C phases.

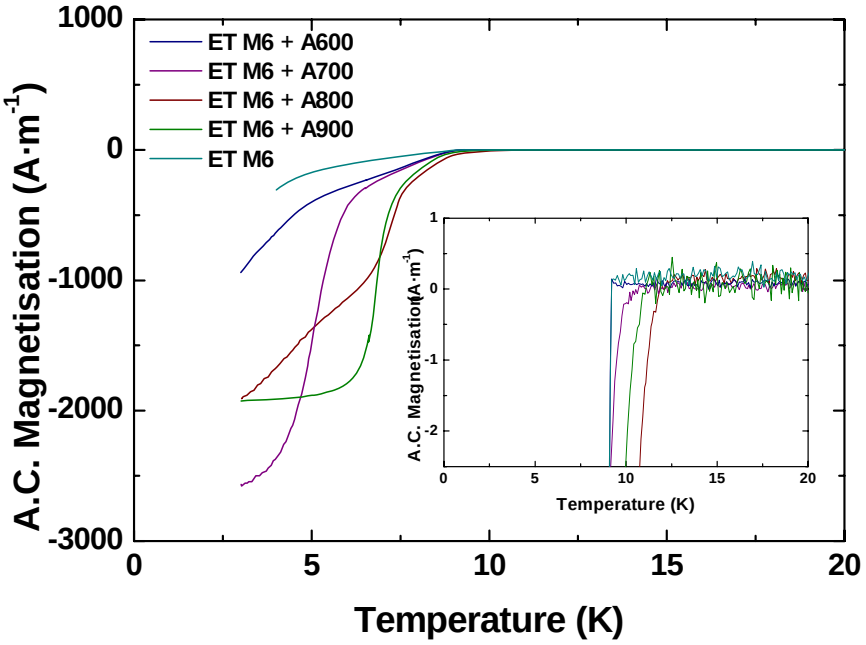

Figure 8.63 Zero field a.c. magnetisation versus temperature for ET(3Nb + 0.7Al + 0.3Ge) M6 + AZZZ and precursor powder prior to annealing.

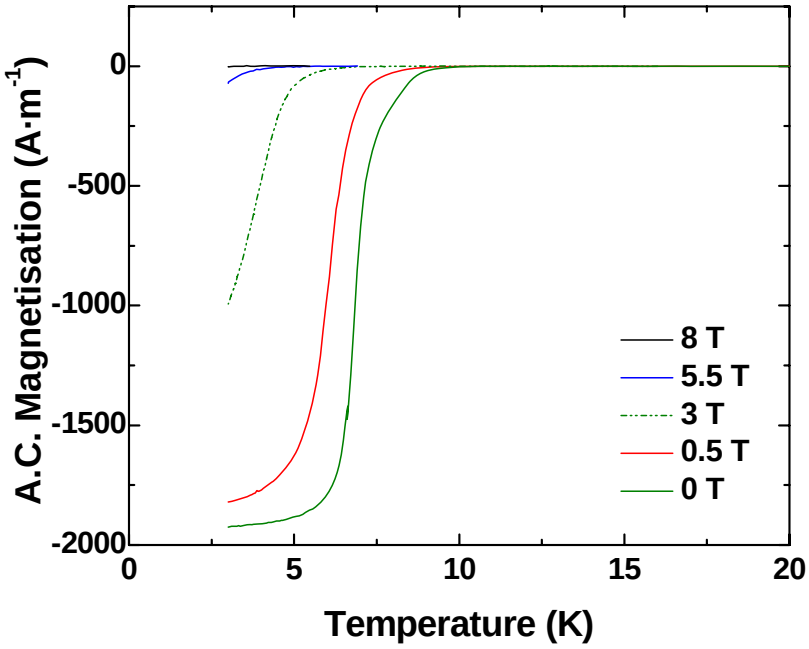

Figure 8.64 A.C. magnetisation versus temperature for ET(3Nb + 0.7Al + 0.3Ge) M6 + A900.

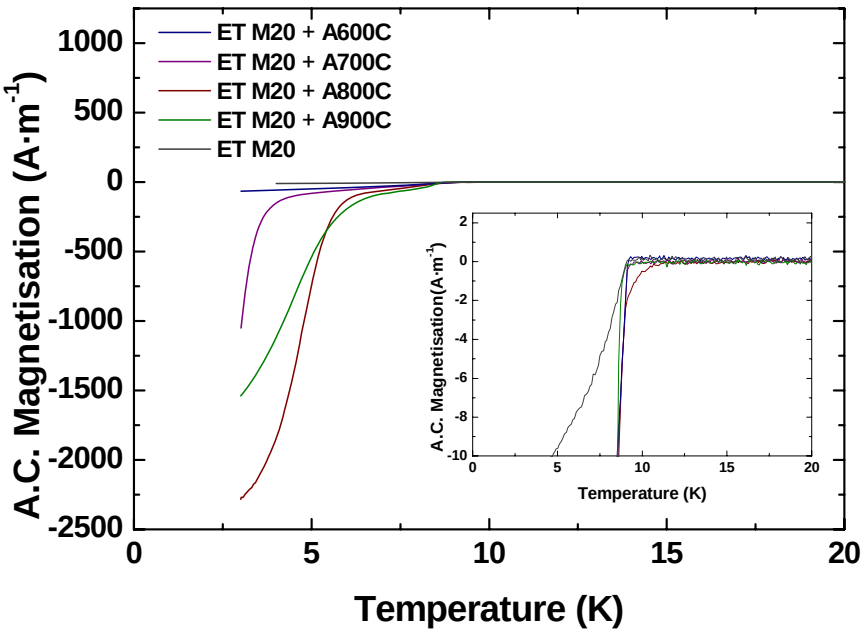

Figure 8.65 Zero field a.c. magnetisation versus temperature for ET(3Nb + 0.7Al + 0.3Ge) M20 + AZZZ and precursor powder prior to annealing.

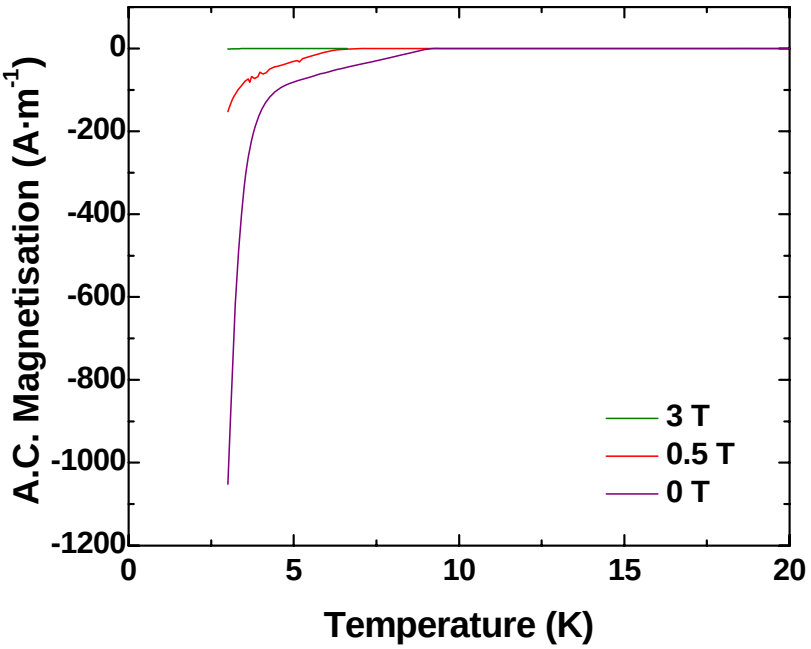

Figure 8.66 A.C. magnetisation versus temperature for ET(3Nb + 0.7Al + 0.3Ge) M20 + A700.

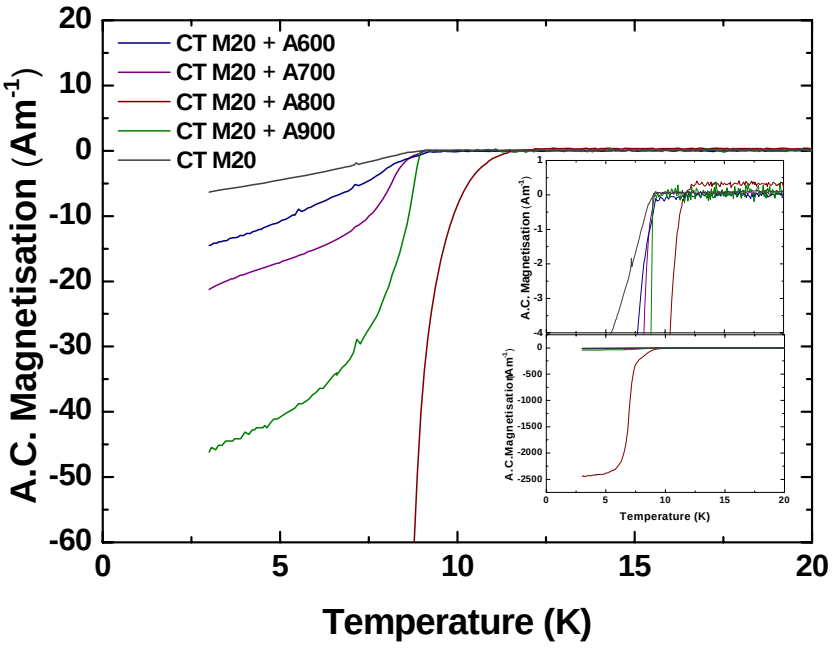

Figure 8.67 Zero field a.c. magnetisation versus temperature for CT($0.7Nb_3Al$ + $0.3Nb_3Ge$) M20 + AZZZ and precursor powder prior to annealing.

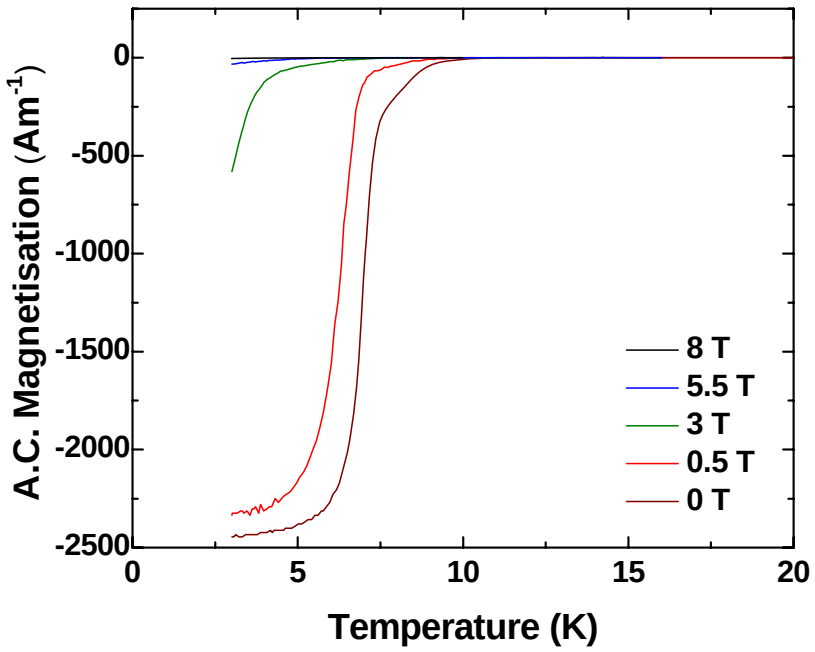

Figure 8.68 A.C. magnetisation versus temperature for CT($0.7Nb_3Al$ + $0.3Nb_3Ge$) M20 + A800.

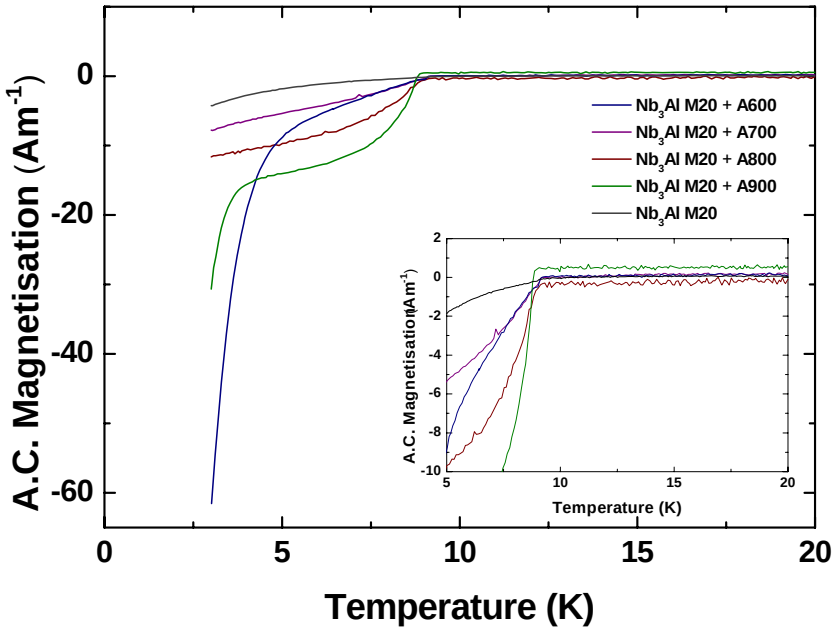

Figure 8.69 Zero field a.c. magnetisation versus temperature for Nb_3Al M20 + AZZZ and precursor powder prior to annealing.

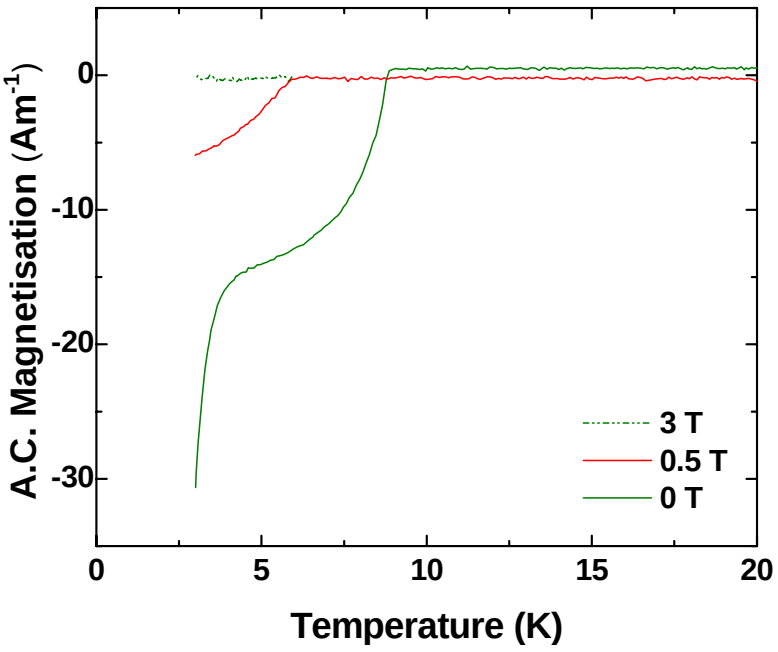

Figure 8.70 A.C. magnetisation versus temperature for Nb_3Al M20 + A900.

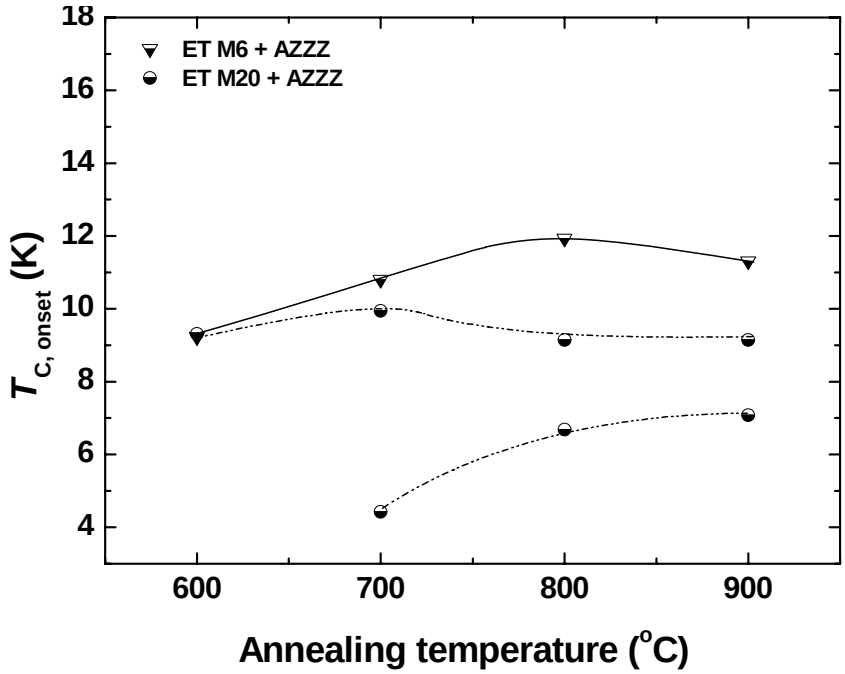

Figure 8.71 $T_{C,onset}$ for ET(3Nb + 0.7Al + 0.3Ge) M6 (triangle) and ET(3Nb + 0.7Al + 0.3Ge) M20 (circle) processed using AZZZ.

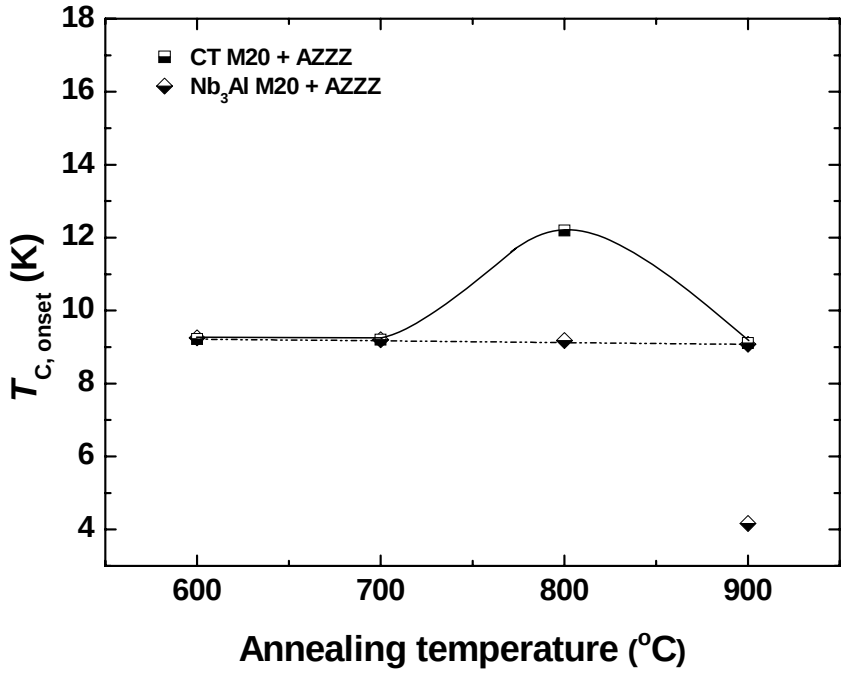

Figure 8.72 $T_{C,onset}$ for CT($0.7Nb_3Al + 0.3Nb_3Ge$) M20 (square) and Nb_3Al M20 (rhombus) processed using AZZZ.

AZZZ	ET M6		ET M20		CT M20		Nb_3Al M20	
	$T_{C,onset}$ (K)	$B_{C2}(0)$ (T)	$T_{C,onset}$ (K)	$B_{C2}(0)$ (T)	$T_{C,onset}$ (K)	$B_{C2}(0)$ (T)	$T_{C,onset}$ (K)	$B_{C2}(0)$ (T)
A600	9.23	1.48	9.31	1.48	9.22	1.18	9.25	1.52
A700	10.8	3.40	9.60 {4.42}	2.27 {1.40}	9.20	1.43	9.20	1.15
A800	11.93	7.24	9.21 {6.68}	1.58 {1.45}	12.19	9.21	9.18	1.18
A900	11.31	8.84	9.14 {7.08}	1.70	9.11	1.60	9.08 {4.16}	1.13

Table 8.31 $T_{C,onset}$ and B_{C2} for ET(3Nb + 0.7Al + 0.3Ge) M6, ET(3Nb + 0.7Al + 0.3Ge) M20, CT($0.7Nb_3Al + 0.3Nb_3Ge$) M20 and Nb_3Al M20 processed using AZZZ. In curly brackets, the second transition temperature is recorded.

Summary of discussion for ACSM. The phase transition from a HIP'ed and structurally disordered phase to the A15 phase produced an improvement of T_C and $B_{C2}(0)$ of ~ 3 K and ~ 6 T, respectively. In contrast, the bcc to A15 transition produced a lower improvement of T_C and $B_{C2}(0)$ of ~ 1 K and ~ 4 T. The superconducting properties of the highly milled material $Nb_3(Al,Ge)$ M20 + HIP600 + AZZZ, despite its major contamination was higher than $Nb_3(Al,Ge)$ milled for just 6 h and identically processed. Almost all the a.c. magnetisation curves show broad superconducting transitions, which indicate that our samples are multiphase in agreement with XRD (subsection 8.4.1) and EDX (subsection 8.4.2).

8.4.4 Discussion and conclusion

Finally we review the superconducting properties, composition and the microstructure shown in nanocrystalline $Nb_3(Al,Ge)$ and Nb_3Al (A15) bulk superconductors. Data presentation and discussion are structured around the four groups of materials processed using MX + HIPYYY, MX + HIP600 + AZZZ, MX + HIP1200 + AZZZ and MX + AZZZ. Summary plots show the $T_{C,onset}$ versus the main A15 Nb-Al lattice parameter, $a_{Nb\text{-}Al}$, for different thermal processing. Table 8.32 and Table 8.33 give the grain size, the lattice parameter for the A15 phases and the $T_{C,onset}$ for bulk materials processed from powders ET M6, ET M20, CT M20 and Nb_3Al respectively. In agreement with the literature, the GS changes are limited (≤ 15 nm) and the lattice parameter is

approximately constant. However, the native high reactivity of Al and Nb makes them difficult to work with. Table 8.34 reports the lattice constant of the $Nb_3(Al_{1-x}Ge_x)$ bulk materials with $0 \leq x \leq 0.3$, corresponding solid solubility and expected T_C from microcrystalline materials [50,51,63,83].

Group 1: MX + HIPYYY and MX + HIP600 + AZZZ. Figure 8.73 and Figure 8.74 report the $T_{C,onset}$ versus the lattice parameter of Nb_3Al, which is the main A15 phase in (both binary and) ternary compounds. The maximum $T_{C,onset}$ changes are ~ 4 K, ~ 2 K, ~ 1.5 K and ~ 0.5 K for ET M6 + HIPYYY, ET M20 + HIPYYY, CT M20 + HIPYYY and Nb_3Al M20 + HIPYYY, respectively (Figure 8.73).

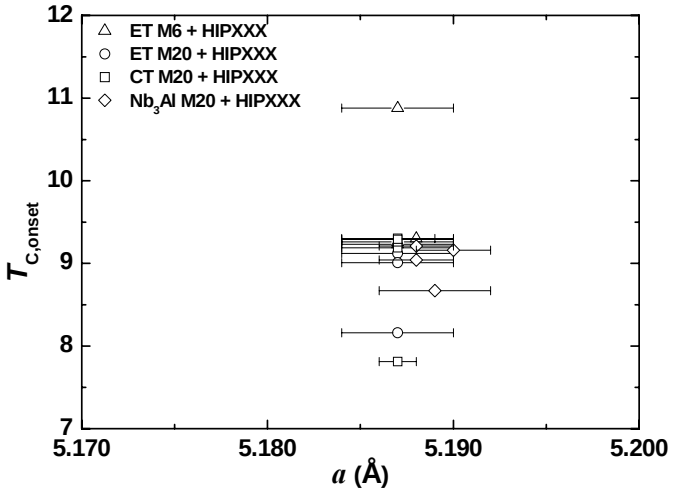

Figure 8.73 $T_{C,onset}$ versus Nb_3Al lattice parameter (a) for ET(3Nb + 0.7Al + 0.3Ge) M6 (triangle), ET(3Nb + 0.7Al + 0.3Ge) M20 (circle), CT($0.7Nb_3Al$+ $0.3Nb_3Ge$) M20 (square) and Nb_3Al M20 (rhombus) processed using HIPYYY.

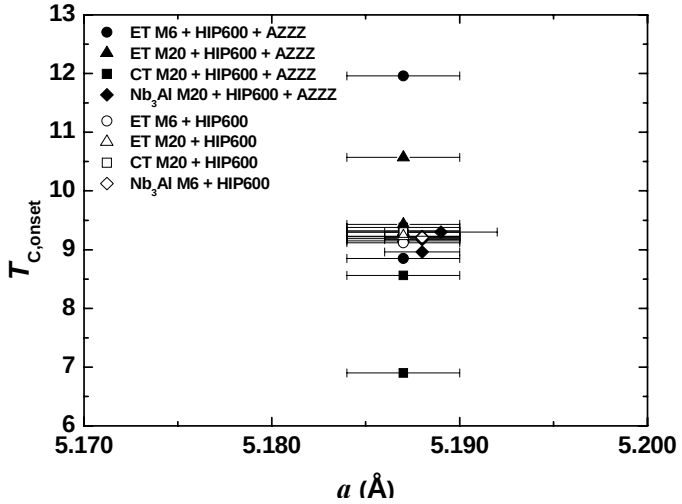

Figure 8.74 $T_{C,onset}$ versus Nb_3Al lattice parameter (a) for ET(3Nb + 0.7Al + 0.3Ge) M6 (triangle), ET(3Nb + 0.7Al + 0.3Ge) M20 (circle), CT($0.7Nb_3Al$+ $0.3Nb_3Ge$) M20 (square) and Nb_3Al M20 (rhombus) processed using HIP600 + AZZZ. The empty symbol represents the precursor material prior to annealing.

Group 2: The maximum changes for $T_{C,onset}$ are ~ 1.5 K, ~ 3 K, 2.5 K and ~ 0.3 K for ET M6 + HIP600 + AZZZ, ET M20 + HIP600 + AZZZ, CT M20 + HIP600 + AZZZ and Nb_3Al M20 + HIP600 + AZZZ, respectively. As shown in Figure 8.74, T_Cs were found below 9.4 K for CT M20+ HIP600 + AZZZ and Nb_3Al M20 + HIP600 + AZZZ. The maximum improvement starting from the precursor state MX + HIP600 was achieved in ET M20 + HIP600 + A800 with a T_C of 11.98 K and will be now discussed in detail together with ET M6 + HIP600 + AZZZ data using Figure 8.75 and Figure 8.76.

Figure 8.75 reports the critical temperatures and the lattice constants for nanocrystalline $Nb_3(Al,Ge)$ from series ET M6 + HIP600 + AZZZ, M20 + HIP600 + AZZZ as a function of annealing temperature. Despite major contamination, the highest T_C and B_{C2} belong to sample M20 + HIP600 + A800 rather than its equivalent milled only for up to 6 h. In order to acquire a better understanding of these results, we note that the corresponding precursor microstructures after HIP'ing have two different phases both highly dense: a crystalline disordered phase for M20 + HIP600 and a bcc structured phase for M6 + HIP600. The critical temperatures show a maximum improvement of ~ 3 K for M20 + HIP600 + A800 and ~ 1.5 K for M6 + HIP600 + A900. It is not to exclude that an increase of T_C occurs at higher temperatures for samples M6 + HIP600 + AZZZ. We have found that, better superconducting properties are found if the sample to be annealed is in the highly disordered phase (milled for 20 h) rather than the bcc phase (milled for 6 h) [90].

Figure 8.76 reports the lattice constant for Nb_3Ge, $Nb_3(Al,Ge)$ and Nb_3Al with the corresponding critical temperatures of precursor (ET M6/M20 + HIP600) and post-HIP annealed samples. The A15 phases with T_C ~ 16 - 17 K may be produced by a small volume fraction of highly ordered/superior short-range order superconducting grains, with a lattice parameter of the A15 phase that is approximately constant up to ~ 1600 ^oC [50]. There is an important similarity between the lattice parameter associated with our high T_C data and previous data for thin films of Nb_3Ge [50] and Nb_3Al conventional bulk samples [175] – Figure 8.76. Figure 8.76 and Figure 8.20 together can provide an explaination for the optimum increase of ~ 3 K for T_C and ~ 6 T for $B_{C2}(0)$ achieved in M20 + HIP600 + A800 - which similarly to chapter 7 [165] suggests a competition between the A15 crystallisation and the crystallisation of the oxides and secondary phases, which occur noticeably at higher temperatures (and compete with superconductivity).

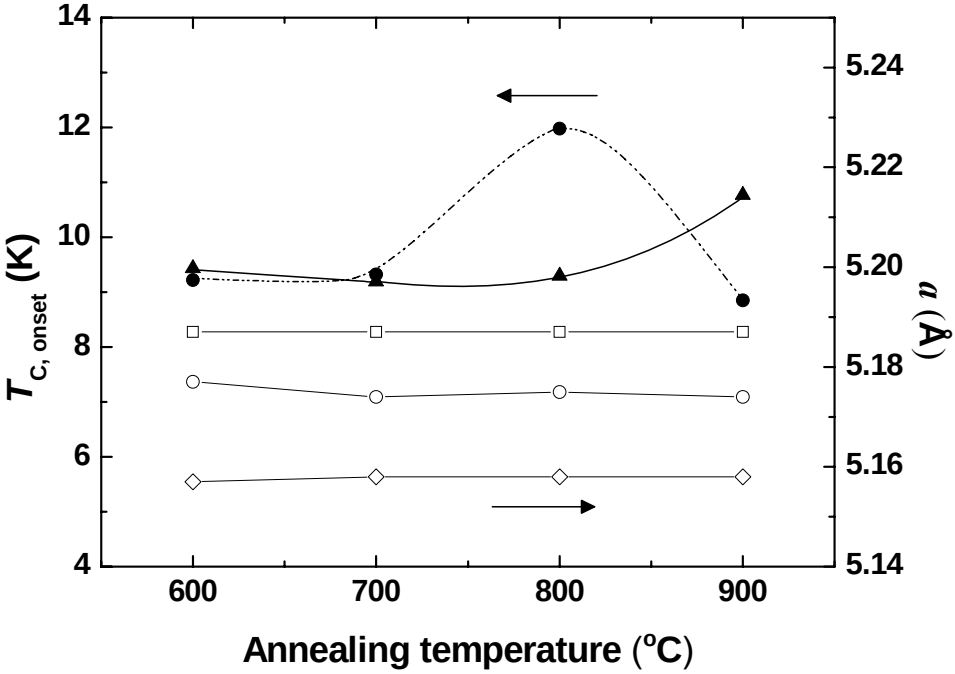

Figure 8.75 Critical temperature and lattice constant for ET(3Nb + 0.7Al + 0.3Ge) M6 (triangle) and M20 (circle) processed using HIP600 + A. Lattice constant for the A15 phases: Nb_3Al (square), $Nb_3(Al,Ge)$ (empty circle), Nb_3Ge (rhombus).

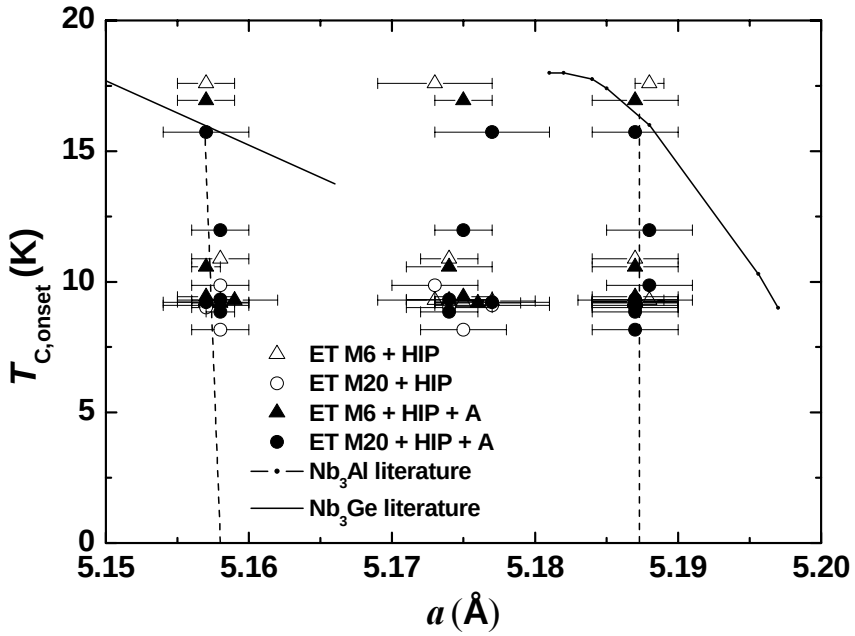

Figure 8.76 Critical temperature versus lattice constant for multiphase A15 ET(3Nb + 0.7Al + 0.3Ge), starting from M6 (circle) and M20 (triangle) powders and subsequently processed using HIP (empty symbol) and HIP600 + A (full symbol). Data are from Nb_3Ge films [83] and Nb_3Al bulk materials [175] also reported. See text for details.

Groups 3 and 4: MX + HIP1200 + AZZZ and MX + AZZZ. Figure 8.77 and Figure 8.78 report the $T_{C,onset}$ versus the lattice constant of the Nb_3Al for samples MX + HIP1200 + AZZZ and MX + AZZZ, respectively. The maximum change for $T_{C,onset}$ are ~ 1.7 K for ET M6/CT M20 + HIP1200 + AZZZ and ~ 0.8 K for ET M20/Nb_3Al M20 + HIP1200 + AZZZ, respectively. The maximum change for $T_{C,onset}$ are ~ 3 K for both ET M6 + AZZZ and CT M20 + AZZZ, ~ 0.5 for CT M20 + AZZZ and ~ 0.2 K for Nb_3Al M20 + AZZZ, respectively.

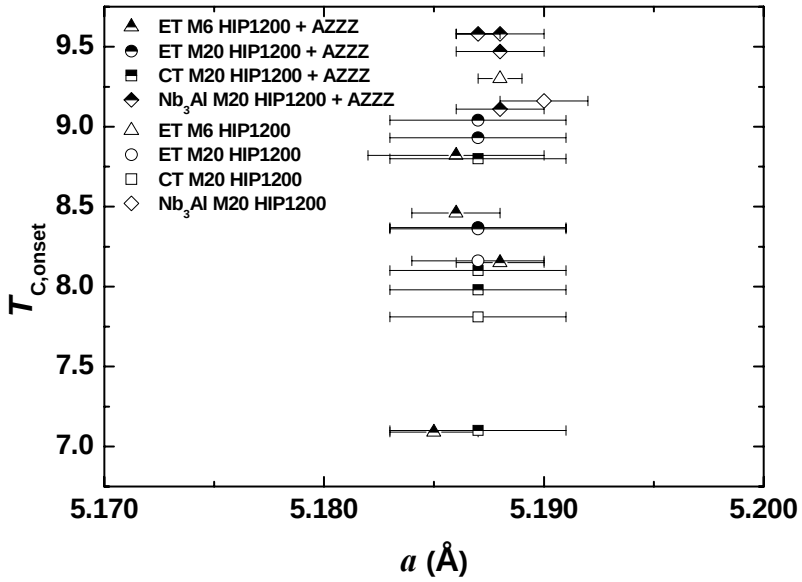

Figure 8.77 $T_{C,onset}$ versus Nb_3Al lattice parameter for ET(3Nb + 0.7Al + 0.3Ge) M6 (triangle), ET(3Nb + 0.7Al + 0.3Ge) M20 (circle), CT($0.7Nb_3Al$+ $0.3Nb_3Ge$) M20 (square), Nb_3Al M20 (rhombus) processed using HIP1200 + AZZZ. The empty symbol represents the precursor material prior to annealing.

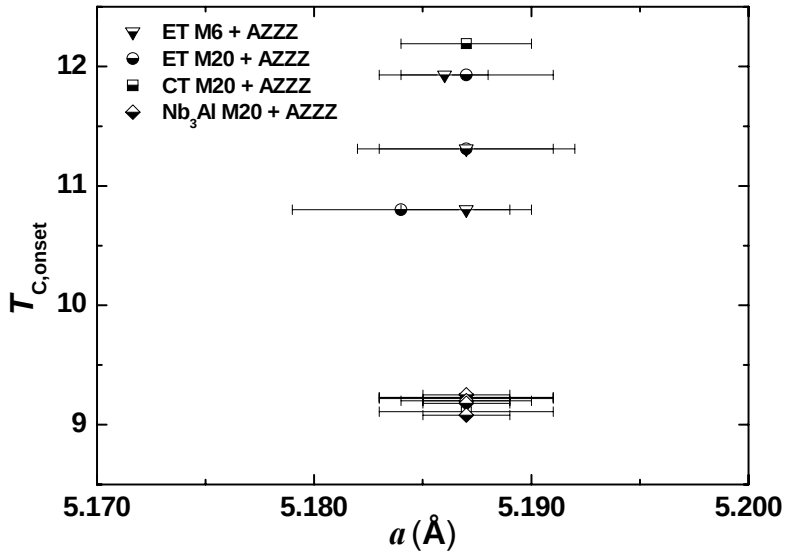

Figure 8.78 $T_{C,onset}$ versus Nb_3Al lattice parameter (a) for series ET(3Nb + 0.7Al + 0.3Ge) M6 (triangle), ET(3Nb + 0.7Al + 0.3Ge) M20 (circle), CT($0.7Nb_3Al$+ $0.3Nb_3Ge$) M20 (square), Nb_3Al M20 (rhombus) processed using AZZZ.

Group	ET M6					ET M20				
	GS **(nm)**	a_{Nb3Al} **(Å)**	a_{Nb3Ge} **(Å)**	$a_{Nb3(Al,Ge)}$ **(Å)**	$T_{C,onset}$ **(K)**	***GS*** **(nm)**	a_{Nb3Al} **(Å)**	a_{Nb3Ge} **(Å)**	$a_{Nb3(Al,Ge)}$ **(Å)**	$T_{C,onset}$ **(K)**
HIP600	1(3)	5.187(3)	5.157(2)	5.175(2)	9.23 {4.85}	3(4)	5.187(3)	5.157(3)	5.177(4)	9.10
HIP700	1(2)	5.187(3)	5.158(1)	5.177(3)	9.26 {5.30}	6(4)	5.187(3)	5.157(1)	5.174(3)	9.01 {4.92}
HIP800	10(5)	5.187(3)	5.158(2)	5.174(2)	10.88 {7.11}	6(5)	5.188(1)	5.158(2)	5.173(3)	9.86 {5.81}
HIP1200	13(5)	5.188(1)	5.157(2)	5.173(4)	6.80 {17.59}	6(9)	5.187(3)	5.158(2)	5.175(3)	8.16
HIP600 + A600	4(5)	5.187(3)	5.157(2)	5.175(2)	9.43 {16.94}	5(1)	5.187(3)	5.157(3)	5.177(4)	9.22 {15.73}
HIP600 + A700	6(4)	5.187(3)	5.158(2)	5.176(3)	9.19	6(3)	5.187(3)	5.158(1)	5.174(3)	9.32
HIP600 + A800	7(7)	5.187(4)	5.159(3)	5.174(3)	9.30	8(4)	5.187(3)	5.158(2)	5.175(2)	11.98
HIP600 + A900	11(13)	5.187(3)	5.157(1)	5.174(3)	10.57 {16.70}	10(6)	5.187(3)	5.158(1)	5.174(2)	8.85 {7.76}
HIP1200+A600	12(6)	5.188(1)	5.157(2)	5.173(4)	7.09	12(9)	5.187(3)	5.158(2)	5.175(3)	8.93
HIP1200+A700	12(5)	5.185(2)	5.157(2)	5.179(4)	8.15 {16.23}	12(7)	5.187(4)	5.157(2)	5.175(4)	8.37 {15.52}
HIP1200 +A800	15(6)	5.188(2)	5.157(2)	5.177(4)	8.46	12(7)	5.187(4)	5.158(3)	5.175(3)	8.36
HIP1200+A900	15(5)	5.186(2)	5.159(1)	5.174(1)	8.82	12(9)	5.187(4)	5.157(3)	5.178(3)	9.04
A600	2(3)	5.187(4)	5.157(2)	5.174(3)	9.23	1(5)	5.187(4)	5.156(2)	5.173(3)	9.31
A700	4(4)	5.187(3)	5.160(3)	5.177(3)	10.8	10(6)	5.185(4)	5.157(5)	5.172(5)	9.60 {4.42}
A800	9(6)	5.186(2)	5.161(4)	5.176(3)	11.93	10(7)	5.187(4)	5.158(5)	5.171(5)	9.21 {6.68}
A900	13(3)	5.187(4)	5.156(3)	5.178(2)	11.31	11(5)	5.187(5)	5.160(3)	5.177(5)	9.14 {7.08}

Table 8.32 Grain size (*GS*), lattice constant of the A15 phases (a) and $T_{C,onset}$ for (3Nb + 0.7Al + 0.3Ge) M6 and ET(3Nb + 0.7Al + 0.3Ge) M20 processed using different methods. In curly brackets, the second transition temperature is recorded.

Group	CT M20					Nb_3Al M20		
	GS **(nm)**	a_{Nb3Al} **(Å)**	a_{Nb3Ge} **(Å)**	$a_{Nb3(Al,Ge)}$ **(Å)**	$T_{C,onset}$ **(K)**	***GS*** **(nm)**	a_{Nb3Al} **(Å)**	$T_{C,onset}$ **(K)**
HIP600	5(3)	5.187(3)	5.167(1)	5.173(2)	9.30	3(5)	5.188(2)	9.21
HIP700	6(1)	5.187(3)	5.167(1)	5.174(1)	9.29	11(8)	5.189(3)	8.67 {13.84}
HIP800	9(4)	5.187(4)	5.167(1)	5.174(2)	9.19 {16.33}	12(7)	5.188(2)	9.04 {13.81}
HIP1200	12(6)	5.187(4)	5.168(1)	5.173(3)	7.81	13(7)	5.190(2)	9.16 {4.26}
HIP600 + A600	6(2)	5.187(3)	5.167(1)	5.174(3)	9.15	2(4)	5.188(2)	9.22 {16.64}
HIP600 + A700	8(4)	5.187(3)	5.167(1)	5.174(1)	9.38	10(8)	5.188(1)	9.30 {15.14}
HIP600 + A800	8(3)	5.187(3)	5.168(1)	5.174(1)	8.56	10(9)	5.188(2)	9.17
HIP600 + A900	11(4)	5.187(3)	5.167(1)	5.173(1)	6.90	12(8)	5.188(2)	8.96
HIP1200+A600	12(6)	5.187(4)	5.168(1)	5.175(1)	8.80	12(9)	5.188(2)	9.58 {4.58}
HIP1200+A700	12(5)	5.187(4)	5.168(1)	5.175(1)	7.10	12(7)	5.188(1)	9.11 {4.06}
HIP1200 +A800	15(6)	5.187(4)	5.167(1)	5.175(1)	7.98	12(7)	5.188(2)	9.58 {4.45}
HIP1200+A900	15(5)	5.187(4)	5.166(2)	5.174(2)	8.10	12(9)	5.188(2)	9.97 {4.65}
A600	15(6)	5.187(4)	5.168(1)	5.175(2)	9.22	12(8)	5.187(2)	9.25
A700	15(7)	5.187(3)	5.167(1)	5.175(2)	9.20	12(7)	5.187(2)	9.20
A800	15(6)	5.187(3)	5.168(1)	5.175(2)	12.19	12(5)	5.187(2)	9.18
A900	15(7)	5.187(4)	5.168(1)	5.173(1)	9.11	13(6)	5.187(2)	9.08

Table 8.33 Grain size (*GS*), lattice constant of the A15 phases (*a*) and $T_{C,onset}$ for CT($0.7Nb_3Al$ + $0.3Nb_3Ge$) M20 and Nb_3Al M20 processed using different methods. In curly brackets, the second transition temperature is recorded.

Series	Phase	*a* (Å)	Solid. Sol. (at.%)	Expected T_C (K)
ET(3Nb+0.7Al+0.3Ge) M6 and ET(3Nb+0.7Al+0.3Ge)M20	Nb_3Al	5.187 ± 0.003	(22 ± 1) at.% Al	range 14.5 – 17
	Nb_3Ge	5.158 ± 0.002	(20.5 ± 0.5) at.% Ge	15.5 ± 0.1
	$Nb_3(Al,Ge)$	5.175 ± 0.003	75 at.% Nb 25 ≤ Ge ≤ 30 at.%	20.2 ± 0.5
CT(Nb_3Al+Nb_3Ge) M20	Nb_3Al	5.187 ± 0.004	(22 ± 2) at.% Al	range 10 - 17.9
	Nb_3Ge	5.167 ± 0.001	(19.0 ± 0.2) at.% Ge	6.90
	$Nb_3(Al,Ge)$	5.175 ± 0.002	75 at.% Nb 25 ≤ Ge ≤ 30 at.%	20.2 ± 0.5
Nb_3Al M20	Nb_3Al	5.188 ± 0.002	(22.2 ± 0.8) at.% Al	range 14.5 – 17

Table 8.34 Typical A15 phase lattice constants (*a*) for the $Nb_3(Al_{1-x}Ge_x)$ bulk materials in this chapter with x = 0 and 0.3 and corresponding solid solubility estimated from the phase diagrams in the literature. The expected T_C is derived from lattice constant data of microcrystalline samples in the literature [50,51,63,83].

In summary, we find that milling and subsequent annealing ET M20 + HIP600 + A800 for $Nb_3(Al,Ge)$ produced a critical temperatures and the estimated upper critical field with a maximum improvement of ~ 3 K and ~ 6 T reaching values of 11.98 K for T_C and of 7.53 T for $B_{C2}(0)$. Although similar values were also achieved in ET M6 + A800, the sample ET M20 + HIP600 + A800 achieved these high values despite its higher contamination from milling media and impurities from the atmosphere due a prolonged milling. We suggest that the crystallisation of the A15 phase without oxides and secondary phases crystallising at higher temperatures may produce yet higher T_Cs. The corresponding $Nb_3(Al,Ge)$ (ET M20) annealed or HIP'ed show T_Cs of ~ 9 K.

Under identical post-HIP thermal processing, a structurally disordered and a highly dense precursor microstructure produced at lower heat treatment had better superconducting properties than the well-known Nb-bcc phase [90] transformation to A15. Although arc-melting is the best fabrication technology for $Nb_3Al_{0.7}Ge_{0.3}$ and Nb_3Al superconductors with record values for Nb_3Al are 18.72 K for T_C and 32.4 T for $B_{C2}(0)$ [61] and record values for $Nb_3Al_{0.7}Ge_{0.3}$ of 20.7 K for T_C and 41 T for $B_{C2}(0)$ [62], we conclude that milling under conditions with lower contamination may yet produce a means to produce large amounts of materials with very high critical superconducting parameters.

Chapter 9

Future Work

In this final chapter, we will consider future developments of the investigations described in this thesis. The innovative combination of HIP'ing and subsequent annealing was shown to improve dramatically superconducting nanocrystalline materials. We find that the role of the optimal post-HIP anneal of highly disordered material is to enhance the A15 crystal nucleation while minimising the crystallisation of oxides and secondary phases, which occurs noticeably at higher temperatures and competes with superconductivity. We propose the use of harder milling media (i.e. hardened steel) and short milling times (< 6 h) might limit the contamination from milling media and atmosphere. This should not compromise the grain size refinement and the various transformations: from a bcc structure to a disordered HIP'ed phase toward the A15 phase driven by thermal processing. We also expect further enhancement of superconducting properties can be achieved by different milling media, HIP'ing and annealing temperature/time and a variation of composition. We also propose that investigating HIP'ing temperatures lower than 600 ^{o}C may also promote dense nano-structured phase from compound starting materials. A change of composition might also usefully be investigated to reduce the nucleation of detrimental secondary phases. The TEM investigation might provide detailed information on the different concentration of Al/Ge in the nanosized grains and structural information on the grains themselves. Some progress in the understanding the physics of nanocrystalline superconductors requires the comparison between grain size and the fundamental length scales like coherence length and penetration depth. An interesting direction for future work will include the investigation of phenomena such as the electron-phonon and electron-electron correlations [32] performing heat capacity measurements. Critical current density measurements as a function of magnetic field will contribute to work out the specific mechanism of current flow and flux pinning in nanocrystalline superconductors where the penetration depth is much larger than the typical grain size [32].We have chosen to study $Nb_3Al_{1-x}Ge_x$ superconductors because they are the prime candidate for next generation of high-field superconducting magnets. We believe that this research will be relevant for novel fabrication of superconducting nanowires and to understand the nature of superconductivity at nanometre scale length.

Appendix 1: Phase Diagrams

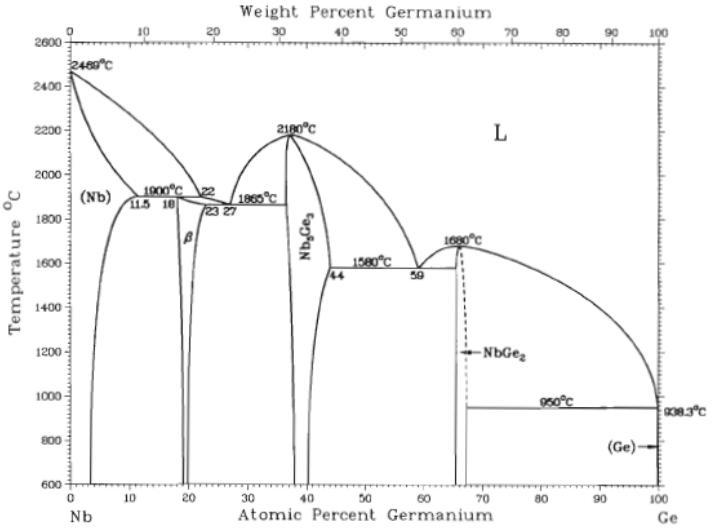

Appendix 1 Ge-Nb phase diagram [55].

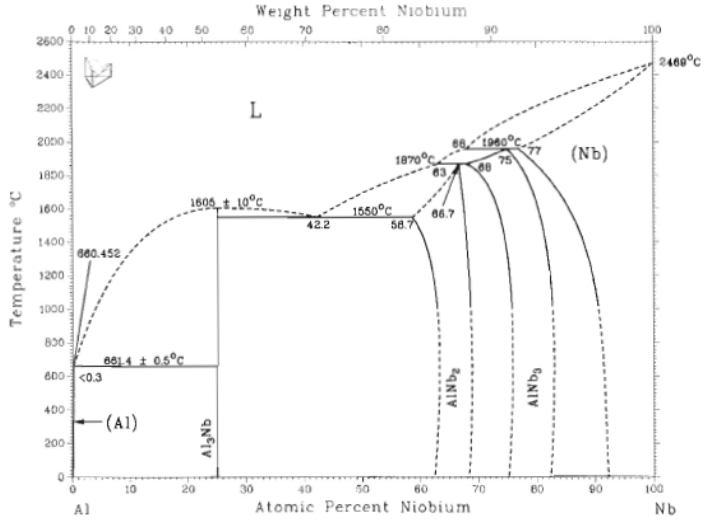

Appendix 2 Al-Nb phase diagram [55].

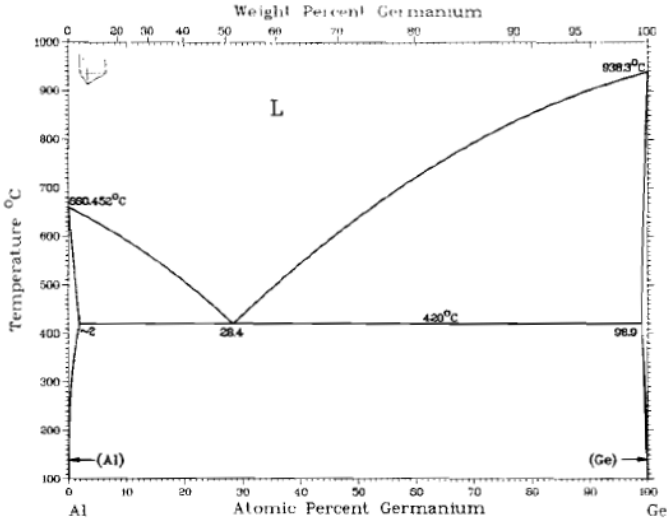

Appendix 3 Al-Ge phase diagram [55].

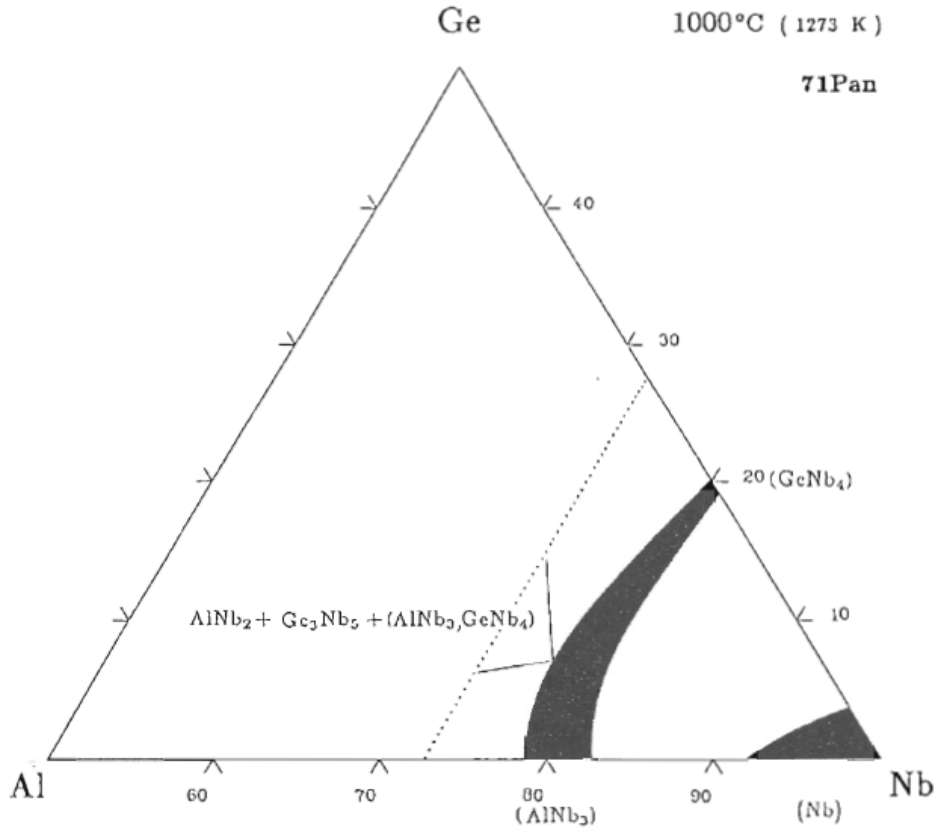

Appendix 4 Nb-Al-Ge phase diagram at 1000 ^{o}C [67].

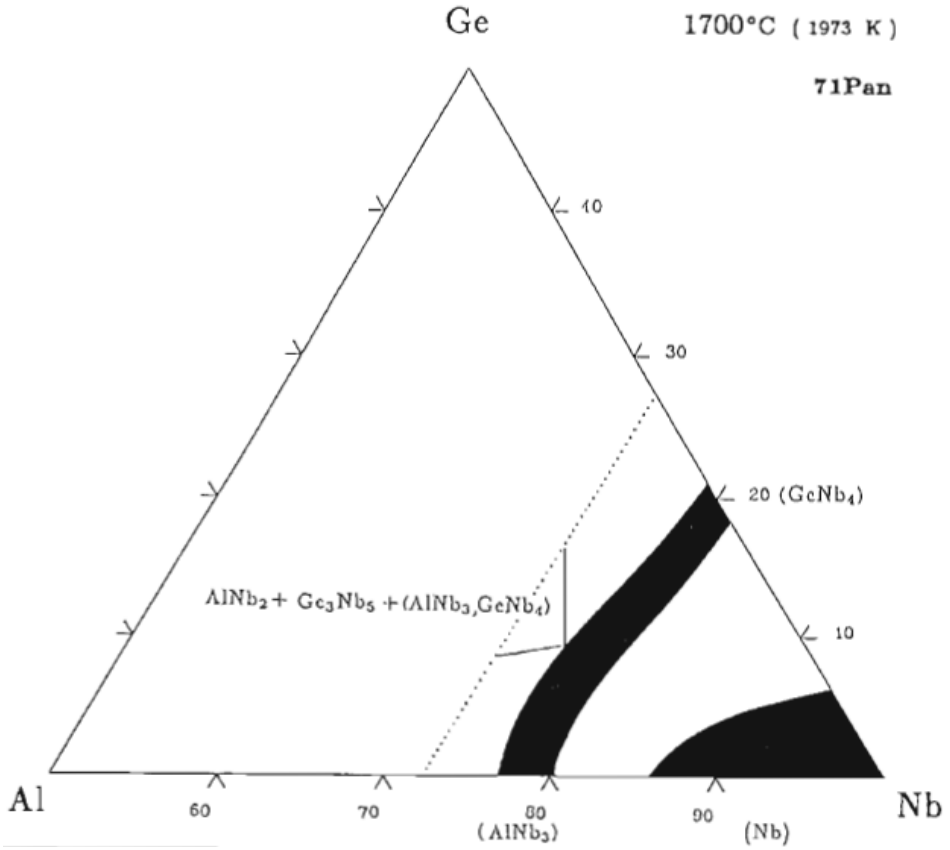

Appendix 5 Nb-Al-Ge phase diagram at 1700 ^{o}C [67].

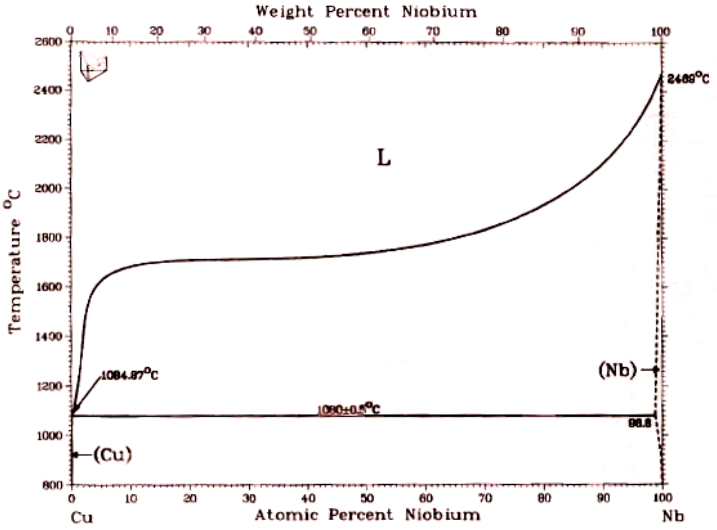

Appendix 6 Nb-Cu phase diagram [55]

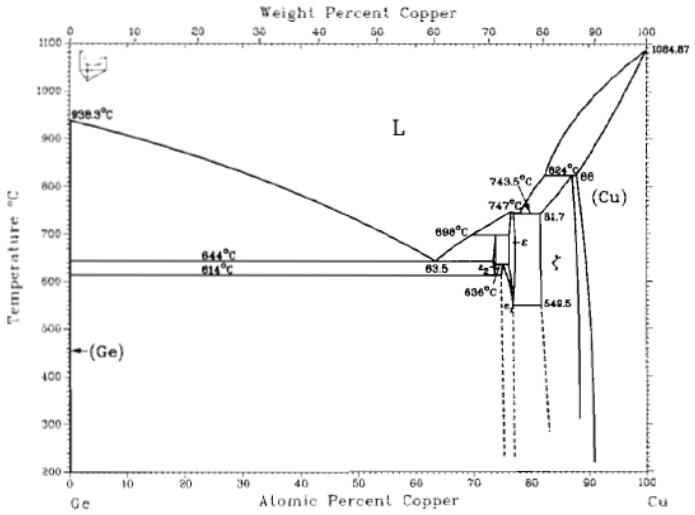

Appendix 7 Ge-Cu phase diagram [55]

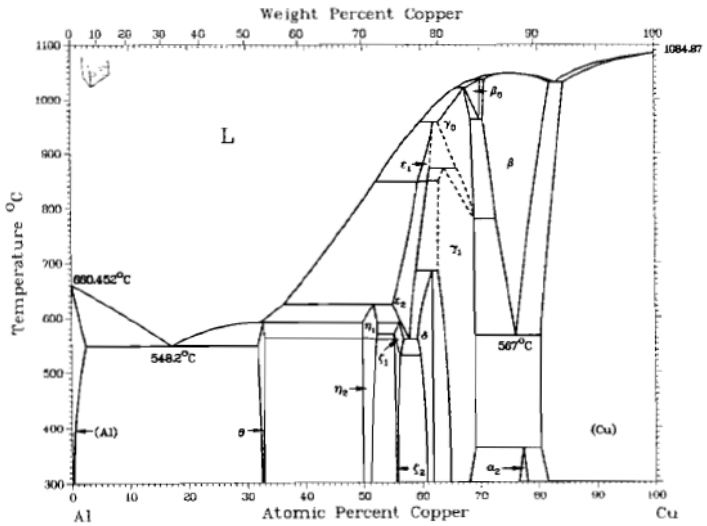

Appendix 8 Al-Cu phase diagram [55]

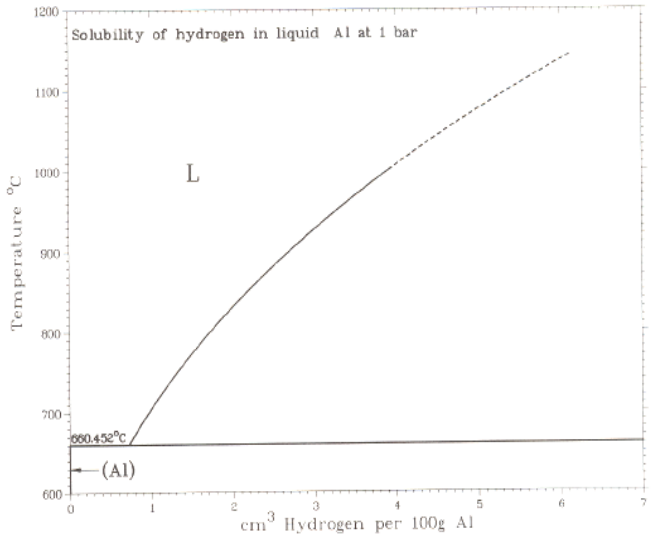

Appendix 9 Al-H phase diagram [55].

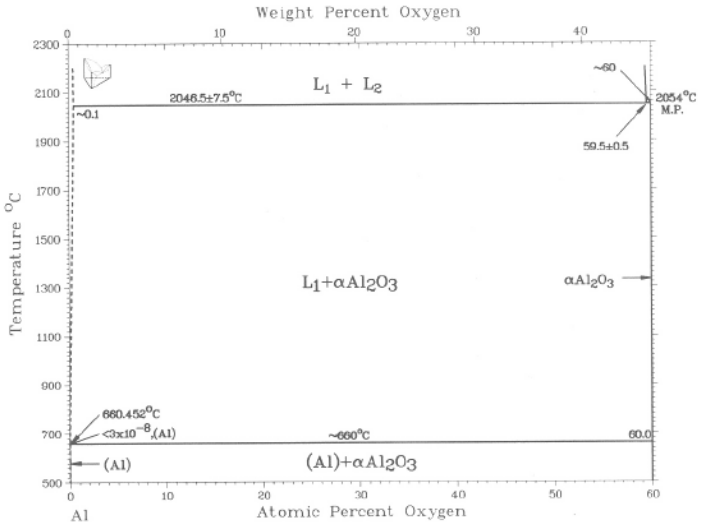

Appendix 10 Al-O phase diagram [55].

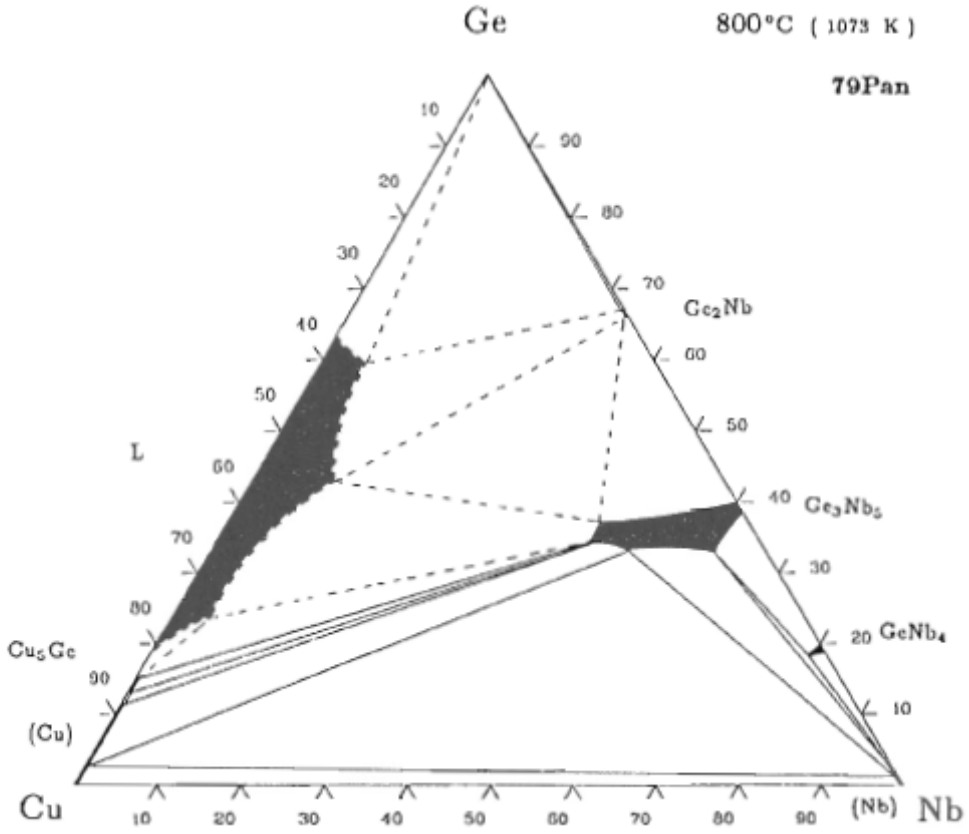

Appendix 11 Cu-Ge-Nb phase diagram at 800 °C [67].

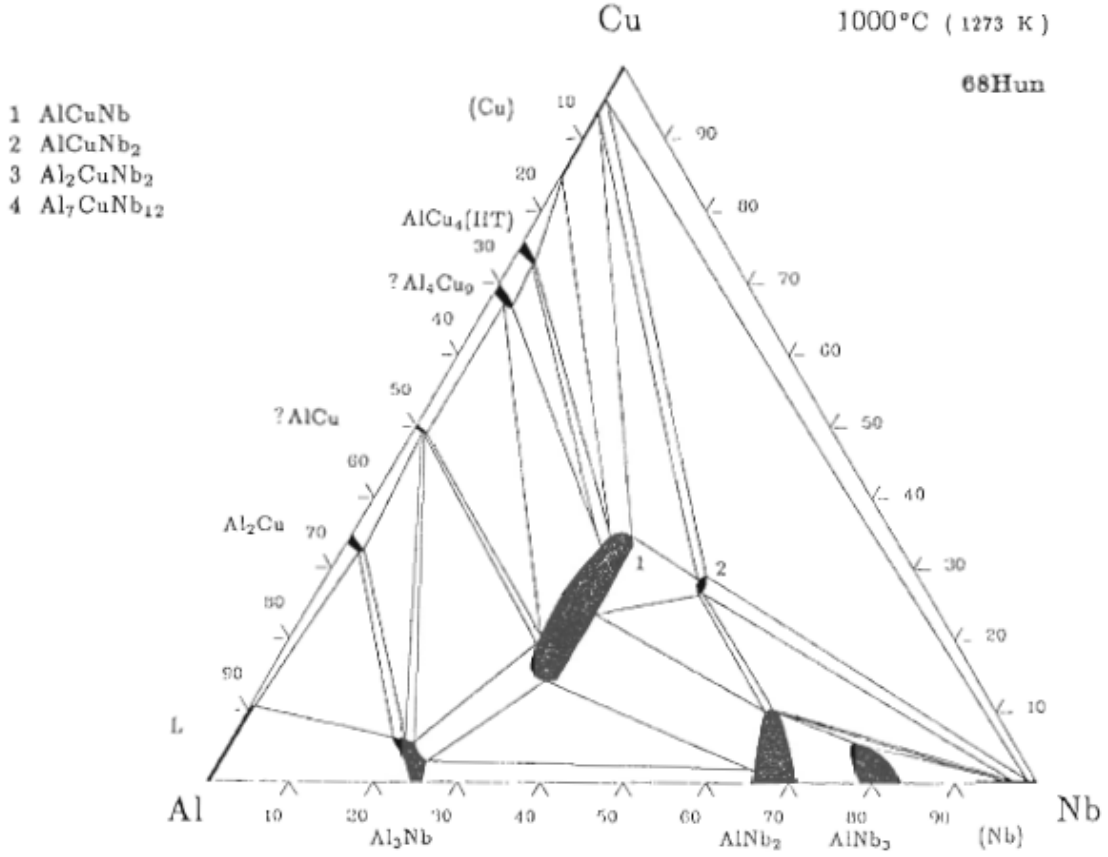

Appendix 12 Al-Cu-Nb phase diagram at 1000 °C [67].

Appendix 2: Computer Programs

The measurements performed in this thesis are listed below together with the computer programs used.

1. X-ray Powder Diffraction

DIFFRAC plus XRD commander (Bruker AXS), EVA (Bruker AXS), PowderCell (BAM Berlin), Jedit and Topas Academic (Bruker AXS);

2. Differential Scanning Calorimetry and Thermo-gravimetric Analysis

STA 449C on 18-414/4 (NETZSCH), Proteus Thermal analysis (NETZSCH);

3. ICP-AES and ICP-MS

ELAN Instrument control (Siemens)

4. Resistivity

Labview

5. DC Magnetic Measurements

MPMS MultiVu Application (Quantum Design);

6. AC Magnetic Measurements

PPMS MultiVu (Quantum Design);

7. Electron Scanning Microscopy coupled with X-ray energy dispersive

INCA Software (Oxford Instruments).

References

[1] ASC, in Short Course on Superconducting Materials Development - Current Status and Future Directions (Chicago, Illinois USA 2008).

[2] B. Seeber, Handbook of Applied Superconductivity. (Institute of Physics, Bristol, 1998).

[3] L. Rossi, Superconductor Science and Technology **23**, 034001 (2010).

[4] B. A. Glowacki, X.-Y. Yan, D. Fray, G. Chen, M. Majoros, and Y. Shi, Physica C: Superconductivity **372-376** (Part 3), 1315 (2002).

[5] Website, http://public.web.cern.ch/public/en/lhc/LHCExperiments-en.html (2010).

[6] A. Vostner and E. Salpietro, Superconductor Science & Technology **19**, S90 (2006).

[7] X. F. Lu and D. P. Hampshire, Superconductor Science & Technology **23**, 025002 (2010).

[8] H. K. Onnes, Communications from the Physical Laboratory of the University of Leiden **124C**, 21 (1911).

[9] M. Cyrot and D. Pavuna, Introduction to superconductivity and high-Tc materials. (World Scientific, Singapore, 1992).

[10] W. Meissner and R. Ochsenfeld, Naturwissenschaften **21**, 787 (1933).

[11] D. P. Hampshire, Lecture on Ginzburg-Landau Theory in Cambridge Winter School (Jan 2007) - Private communication.

[12] B. A. Glowacki, Intermetallics **7** (2), 117 (1999).

[13] W. A. Fietz and W. W. Webb, Physical Review **161** (2), 423 (1967).

[14] R. G. Hampshire, Journal of Physics D - Applied Physics **7**, 1847 (1974).

[15] U. Essmann and H. Trauble, Physics Letters **24A** (10), 526 (1967).

[16] E. J. Kramer, Journal of Applied Physics **44** (3), 1360 (1973).

[17] C. Buzea and K. Robbie, Supercond. Sci. Technol. **18**, R1–R8 (2005).

[18] Flukiger, Oral presentation at IoP Superconductivity General Annual Meeting (Jan 2009) - Private communication.

[19] D. M. J. Taylor, Ph.D. Thesis. (Durham University, 2004).

[20] D. P. Hampshire and H. J. Niu, Patent No. International patent number WO03/094251 A2 (2002).

[21] Y. Kamihara, T. Watanabe, M. Hirano, and H. Hosono, Journal of the American Chemical Society **130** (11), 3296 (2008).

[22] Z. Ren, W. Lu, J. Yang, W. Yi, and X. Shen, Chinese Phys. Lett. **25**, 2215 (2008).

[23] R. M. Norman, Physics **1**, 21 (2008).

[24] S. Bose, P. Raychaudhuri, R. Banerjee, and P. Ayyub, Physical Review B **74** (22), 224502 (2006).

[25] P. Mondal, M. Manekar, R. Kumar, T. Ganguli, and S. B. Roy, Applied Physics Letters **92** (5), 052507 (2008).

[26] S. Bose, P. Raychaudhuri, R. Banerjee, P. Vasa, and P. Ayyub, Physical Review Letters **95** (14), 147003 (2005).

[27] S. Neeleshwar, Y. Y. Chen, C. R. Wang, M. N. Ou, and P. H. Huang, Physica C: Superconductivity **408-410**, 209 (2004).

[28] R. L. Filler, P. Lindenfeld, T. Worthington, and G. Deutscher, Physical Review B **21** (11), 5031 LP (1980).

[29] H. J. Niu and D. P. Hampshire, Physical Review Letters **91** (2), 027002 (2003).

[30] D. M. J. Taylor, M. Al-Jawad, and D. P. Hampshire, Superconductor Science & Technology **21**, 125006 (2008).

[31] D. Belitz, Physical Review B **36**, 47 (1987).

[32] P. Mondal, M. Manekar, A. K. Srivastava, and S. B. Roy, Physical Review B **80**, 024502 (2009).

[33] D. Dew-Hughes, Philosophical Magazine **30**, 293 (1974).

[34] W. Wunderlich, K. Pixius, and J. Schilz, Nanostructured Materials **6** (1-4), 441 (1995).

[35] H. Gleiter, Acta Materialia **48**, 1 (2000).

[36] D. Dew-Hughes, Cryogenics **15** (8), 435 (1975).

[37] B. T. Matthias, T. H. Geballe, R. H. Willens, E. Corenzwit, and G. W. Hull, Physical Review **139** (5A), A1501 LP (1965).

[38] A. I. Goldman, E. Canova, and Y. H. Kao, Solid State Communications **58** (4), 277 (1986).

[39] B. T. Matthias, Science **156**, 645 (1968).

[40] L. R. Newkirk, F. A. Valencia, A. L. Giorgi, E. G. Szklarz, and T. C. Wallace, IEEE Transactions on Magnetics **11** (2), 221 (1975).

[41] N. L. Saini, M. Filippi, H. Oyanagi, H. Ihara, A. Iyo, and A. Bianconi, Physical Review B **68** (10), 104507 (2003).

[42] M. Ashkin and J. R. Gavaler, Journal of Low Temperature Physics **31**, 285 (1978).

[43] V. F. Zackay and M. F. Merriam, in Phase diagrams : materials science and technology, edited by A. M. Alper. (Academic Press, New York, 1970), Vol. 6-III, pp. 87.

[44] M. Fähnle and H. Kronmüller, Journal of Nuclear Materials **72** (1-2), 249 (1978).

[45] H. Bakker, L. M. Di, H. Yang, and G. F. Zhou, Proceedings of the 2nd International Conference on Structural Applications of Mechanical Alloying ASM International, edited by F. H. Froes and J. J. deBarbadillo, (Metals Park, Ohio 1993), p. 213.

[46] A. R. Sweedler and D. E. Cox, Physical Review B **12** (1), 147 (1975).

[47] R. Flükiger, P. Spitzkli, F. Heiniger, and J. Muller, Physics Letters **29A** (7), 407 (1969).

[48] R. Bormann, H. U. Krebs, and A. D. Kent, in Advances in Cryogenic Engineering, edited by K. D. Timmerhaus, R. W. Fast, A. F. Clark, and R. P. Reed (Plenum, New York, 1986), Vol. 32, pp. 1041.

[49] R. H. Willens, T. H. Geballe, A. C. Gossard, J. P. Maita, A. Menth, G. W. Hull, and R. R. Soden, Solid State Communications **7** (11), 837 (1969).

[50] J. L. Jorda, R. Flükiger, and J. Muller, Journal of the Less Common Metals **62**, 25 (1978).

[51] J. L. Jorda, R. Flükiger, and J. Muller, Journal of the Less Common Metals **75**, 227 (1980).

[52] R. Flukiger and J. L. Jorda, in Applications of Phase Diagrams in Metallurgy and Ceramics (NBS Spec. Pubbl., Gaithersburg,Md.,USA, 1977), Vol. 1, pp. 375.

[53] V. M. Pan, V. I. Latysheva, and A. I. Sudovtsov, Metallofizika **36**, 92 (1971).

[54] J. Muller, Naturforsch. Teil A **25**, 1659 (1970).

[55] B. T. Massalski, Binary Alloy Phase Diagrams. (American Society for Metals, Ohio, 1986).

[56] J. L. Jorda, R. Flukiger, A. Junod, and J. Muller, IEEE Transactions on Magnetics **17** (1), 557 (1981).

[57] J. H. Carpenter and A. W. Searcey, J. Am. Chem. Soc. **79**, 2079 (1956).

[58] L. R. Testardi, R. L. Meek, J. M. Poate, W. A. Royer, A. R. Storm, and J. H. Wernick, Physical Review B **11** (11), 4304 LP (1975).

[59] M. S. Kim, North Carolina State University, 1987.

[60] E. A. Wood, V. B. Compton, B. T. Matthias, and E. Corenzwit, Acta Cryst Sect B **11**, 604 (1958).

[61] S. M. J. Foner, E. J. Geballe, T. H. Willens, R. H. Buerhler, E., Physica **55**, 534 (1971).

[62] S. Foner, E. J. McNiff, B. T. Matthias, T. H. Geballe, R. H. Willens, and E. Corenzwit, Physics Letters A **31** (7), 349 (1970).

[63] S. Foner, E. J. McNiff Jr., B. T. Matthias, and E. Corenzwit, Proceedings of the Eleventh International Conference on Low Temperature Physics, edited by J. F. Allen, D. M. Finlayson, and D. M. Mc Call, (AIP 1969), p. 1025.

[64] K. Tachikawa, K. Sakinada, and M. Kobayashi, Cryogenics **33** (11), 1091 (1993).

[65] E. Kannatey-Asibu, Jr., Journal of Applied Physics **56** (6), 1769 (1984).

[66] C. C. Koch, O. B. Cavin, C. G. McKamey, and J. O. Scarbrough, Applied Physics Letters **43** (11), 1017 (1983).

[67] P. Villars, A. Prince, and H. Okamoto, Handbook of ternary alloy phase diagrams. (Materials Park, OH, ASM International, 1995).

[68] C. L. H. Thieme, S. Pourrahimi, and S. Foner, Magnetics, IEEE Transactions on **25** (2), 1992 (1989).

[69] Y. K. Iijima, M. Takeuki, T., Advances in Cryogenics Engineering **40**, 899 (1994).

[70] N. Koizumi, T. Takeuchi, and K. Okuno, Nuclear Fusion **45**, 431 (2005).

[71] Y. K. Iijima, A. Inoue, K. Takeuki, T., IEEE Transactions on Applied Superconductivity **9**, 2696 (1999).

[72] A. Kikuchi, Y. Iijima, and K. Inoue, Physica C-Superconductivity and Its Applications **372**, 1307 (2002).

[73] A. Kikuchi, Y. Iijima, and K. Inoue, IEEE Transactions on Applied Superconductivity **11** (1), 3968 (2001).

[74] K. I. Inoue, Y.; Kikuchi, A., IEEE Transactions on Applied Superconductivity **12** (1), 1041 (2002).

[75] S. A. Keys, N. Koizumi, and D. P. Hampshire, Superconductor Science and Technology **15**, 991 (2002).

[76] N. Banno, T. Takeuchi, M. Kosuge, M. Yuyama, and H. Wada, IEEE Transactions on Applied Superconductivity **13** (3), 3450 (2003).

[77] A. I. Kikuchi, Y.; Inoue, K.; Kosuge, M.; Itoh, K., IEEE Transactions on Applied Superconductivity **11** (1), 3984 (2001).

[78] I. C. S. Database, in https://cds.dl.ac.uk/ (2009).

[79] J. R. Gavaler, Applied Physics Letters **23** (8), 480 (1973).

[80] S. Foner, E. J. McNiff Jr., J. R. Gavaler, and M. A. Janoko, Physics Letters **47A** (6), 485 (1974).

[81] L. R. Testardi, J. H. Wernick, and W. A. Royer, Solid State Communications **14**, 1 (1974).

[82] B. C. Giessen and R. H. Willens, in Phase diagrams : materials science and technology, edited by A. M. Alper (Academic Press, New York, 1970), Vol. 6-III.

[83] D. A. Rogowski and R. Roy, Journal of Applied Physics **47** (10), 4635 (1976).

[84] R. Bormann, G. Yu, R. H. Hammond, A. F. Marshall, and T. H. Geballe, Proceedings of Rapidly Quenched Metals V, edited by S. Steeb and H. Warlimont, (Elsevier Science Publishers B.V. 1984), p. 879.

[85] S. D. K. Dahlgren, D.M., IEEE Transactions on Magnetics **MAG-11** (2), 217 (1975).

[86] K. Togano, T. Takeuchi, and K. Tachikawa, Applied Physics Letters **41** (2), 199 (1982).

[87] C. Politis, Physica B+C **135** (1-3), 286 (1985).

[88] E. A. Kenik, R. J. Bayuzick, M. S. Kim, and C. C. Koch, Scripta Metallurgica **21** (8), 1137 (1987).

[89] J. Larson, T. Luhman, and H. Merrick, Manufacture of superconducting materials, edited by R. W. Meyerhoff, (American Society for Metals 1976), p. 155.

[90] E. Hellstern, L. Schultz, R. Bormann, and D. Lee, Applied Physics Letters **53** (15), 1399 (1988).

[91] M. Oehring and R. Bormann, Colloque de Physique **51** (C4/14), C4169 (1990).

[92] M. Oehring and R. Bormann, Materials Science and Engineering A **134**, 1330 (1991).

[93] Z. Peng, C. Suryanarayana, and F. H. Froes, Metall. Mater. Trans. A **27**, 41 (1996).

[94] C. Rock and K. Okazaki, Nanostructured Materials **5** (6), 657 (1995).

[95] J. Saida, Y. Tanaka, and K. Okazaki, Trans. JIM **37**, 265 (1996).

[96] F. H. (Sam)Froes, C. Suryanarayana, K. Russell, and C.-G. Li, Materials Science and Engineering A **192-193** (2), 612 (1995).

[97] C. Rock, J. Qiu, and K. Okazaki, Journal Mat Sci **33**, 241 (1998).

[98] S. Dymek, M. Dollar, and K. Leonard, Materials Science and Engineering A **239-240**, 507 (1997).

[99] A. Dollar and S. Dymek, Intermetallics **11** (4), 341 (2003).

[100] C. Suryanarayana, Progress in Materials Science **46**, 1 (2001).

[101] C. Suryanarayana, Bulletin of Materials Science **17** (4), 307 (1994).

[102] M. Wagner, Physical Review B **45** (2), 635 (1992).

[103] R. W. Siegel and G. J. Thomas, Ultramicroscopy **40** (3), 376 (1992).

[104] K. Lu, Materials Science and Engineering: R: Reports **16** (4), 161 (1996).

[105] C. Suryanarayana and F. H. (Sam)Froes, Metallurgical and Materials Transactions **23A**, 1071 (1992).

[106] M. J. Schulz, A. D. Kelkar, and M. J. Sundaresan, Nanoengineering of Structural, Functional and Smart Materials. (CRC Press, 2005).

[107] C. C. Koch, Nanostructured Materials **2**, 109 (1993).

[108] P. S. Gilman and J. S. Benjamin, Annual Review of Materials Science **13**, 279 (1983).

[109] D. R. Maurice and T. H. Courtney, Metall Trans A **21** (2), 289 (1990).

[110] S. Palaniandy, K. Azizli, H. Hussin, and S. Hashim, Journal of materials processing technology **205**, 119–127 (2008).

[111] Website, http://www.sturtevantinc.com/ (2009).

[112] D. Eskin, S. Voropayev, and O. Vasilkov, Powder Technology **105**, 257–265 (1999).

[113] Website, http://www.fluidenergype.com/microjet_brochure.pdf (2009).

[114] Y. H. Park, H. Hashimoto, and R. Watanabe, Material Science Forum **88-90**, 56 (1992).

[115] W. Guo, A. Iasonna, M. Magini, S. Martelli, and F. Padella, Journal of Material Science **29**, 2436 (1994).

[116] L. Takacs, Processing and properties of nanocrystalline materials. (Warrendale, PA: TMS, 1996).

[117] C. Kuhrt, H. Schropf, L. Schultz, and E. Arzt, Mechanical alloying for structural applications. (Materials Park, OH: ASM International, 1993).

[118] Z. Fu and W. Johnson, Nanostructured Materials. **3**, 175 (1993).

[119] M. Miki, T. Yamasaki, and O. Y., Materials Transactions **33**, 839 (1992).

[120] Y. Chen and J. Williams, Mater Sci Forum ; **225-227**, 881 (1996).

[121] C. Suryanarayana, Intermetallics **3**, 153 (1995).

[122] J. H. Weber, in Solid state powder processing, edited by A. H. Clauer and J. J. deBarbadillo (Warrendale, PA: TMS, 1990), pp. 227.

[123] S. Ochiai, edited by S. Ochiai, J. D. Whittenberger, T. K. Glasgow, M. Taya, and H. Lilholt (Marcel Dekker, Inc., New York, Basel, Hong Kong, 1993).

[124] J. J. Sunol, A. Gonzalez, J. Saurina, L. Escoda, and P. Bruna, Materials Science and Engineering A **375-377**, 874 (2004).

[125] D. C. Gillies and D. Lewis, Journal of the Less Common Metals **13** (2), 179 (1967).

[126] V. Gauthier, F. Bernard, E. Gaffet, Z. A. Munir, and J. P. Larpin, Intermetallics **9** (7), 571 (2001).

[127] M. N. R. V. Perdigão, J. A. R. Jordão, C. S. Kiminami, and W. J. Botta F., Materials Science Forum **235 - 238**, 151 (1997).

[128] C. C. Koch, Materials Science and Technology **15**, 193 (1991).

[129] H. S. Kim, D. S. Suhr, G. H. Kim, and D. W. Kum, Metals and Materials **2** (15-21) (1996).

[130] C. N. J. Wagner, Journal of Non-Crystalline Solids **150** (1-3), 1 (1992).

[131] Y. S. Cho and C. C. Koch, Journal of Alloys and Compounds **194** (2), 287 (1993).

[132] H. Bakker, L. M. Di, and P. H. Shingu, Materials Science Forum **88-90**, 27 (1992).

[133] P. P. Chatterjee, S. K. Pabi, and I. Manna, Journal of Applied Physics **86** (10), 5912 (1999).

[134] L. M. Di, P. I. Loeff, and H. Bakker, Journal of the Less-Common Metals **168** (2), 183 (1991).

[135] R. B. Schwarz and R. R. Petrich, Journal of the Less Common Metals **140**, 171 (1988).

[136] Website, http://www.kobelco.co.jp/ (2009).

[137] S. Charlton, The upper critical field of nanocrystalline Nb_3Al fabricated by wet mechanical milling, MSc. Thesis, Durham (2007).

[138] A. L. Patterson, Physical Review **56** (10), 978 LP (1939).

[139] G. K. Williamson and W. H. Hall, Acta Metallurgica **1** (1), 22 (1953).

[140] Website, http://www.mrfn.org/ucsb/chem/icp.pdf (2009).

[141] Website, http://en.wikipedia.org/wiki/Spectrometer (2009).

[142] Website, http://en.wikipedia.org/wiki/Mass_spectrometry (2009).

[143] B. L. Brandt, D. W. Liu, and L. G. Rubin, Review of Scientific Instruments **70**, 104 (1999).

[144] Website, http://www.qdusa.com/resources/pdf/FundPrimer.pdf (2009).

[145] Website, http://openlearn.open.ac.uk/mod/resource/view.php?id=192978 (2009).

[146] Website, http://www.qdusa.com/products/ppms.html (2009).

[147] C. Jones, SU-70 introduction to FE SEM - High resolution imaging and analysis, SU 70 Training tutorial, Hitachi High Techologies (2009).

[148] P. J. Goodhew, J. Humphreys, and R. Beanland, Electron microscopy and analysis. (Taylor and Francis Inc, 2001).

[149] M. Sato and T. Ogashiwa, Physics Procedia, Proceedings of the Seventh International Conference on Charged Particle Optics (CPO-7) **1** (1), 127 (2008).

[150] K. Durose, Electron microsopy and analysis - Postgraduate lecture course. (Durham University, 2007).

[151] E. Pusceddu, S. Charlton, and D. P. Hampshire, Journal of Physics: Conference Series **97**, 012241 (2007).

[152] E. Gaffet, M. Harmelin, and F. Faudot, Journal of Alloys and Compounds **194**, 23 (1993).

[153] M. Hussain, Y. Oku, A. Nakahira, and K. Niihara, Materials Letters **26** (3), 177 (1996).

[154] F. W. Dynys and J. W. Halloran, Comunication of the American Ceramic Society **C**, 62 (1981).

[155] A. Vajpei and G. Upadhyaya, (Trans Tech Publication Ltd, Switzerland, 1992).

[156] C. Fleck, Fabrication and characterization of the superconductor $YBa_2Cu_3O_{7-d}$, MSc. Thesis, Durham (2007).

[157] M. W. J. Chase, NIST-JANAF Thermochemical Tables, 4th ed. (1998).

[158] M. S. El-Eskandarany, K. Aoki, and K. Suzuki, Scripta Metallurgica et Materialia **25** (7), 1695 (1991).

[159] A. R. Miedema, Philippine technology journal **36**, 217 (1976).

[160] R. P. Elliot, Transactions of the American Society of Mechanical Engineers **52**, 990 (1960).

[161] J. S. Benjamin, Metallurgical Transactions **1** (10), 2943 (1970).

[162] L. Liu, F. Padella, W. Guo, and M. Magini, Acta Metallurgica et Materialia **43** (10), 3755 (1995).

[163] D. R. Lide, Handbook of chemistry and physics. (Boca Raton ; London : CRC Press, c2001., 2002).

[164] M. Eisterer and H. W. Weber, Supercond. Sci. Technol. **23**, 034006 (2007).

[165] E. Pusceddu and D. P. Hampshire, Applied Physics Letters, Submitted (2010).

[166] E. Botcharova, M. Heilmaier, J. Freudenberger, G. Drew, D. Kudashow, U. Martin, and L. Schultz, Journal of Alloys and Compounds **351** (1-2), 119 (2003).

[167] G. Lefranc and A. Müller, Journal of the Less Common Metals **45** (2), 339 (1976).

[168] J. R. Taylor, An introduction to error analysis. The Study of Uncertainties in Physical Measuements. (University Science Books, 1982).

[169] G.-f. Zhou and H. Bakker, Materials Science and Engineering A **179-180** (Part 1), 453 (1994).

[170] E. Pusceddu and D. P. Hampshire, Journal of Applied Physics, Submitted (2010).

[171] S. Foner, E. J. McNiff Jr., B. T. Matthias, and E. Corenzwit, Proceedings of the Eleventh International Conference on Low Temperature Physics, edited by J. F. Allen, D. M. Finlayson, and D. M. Mc Call, (St. Andrews University, St. Andrews, Scotland 1968), p. 1025.

[172] L. M. Di and H. Bakker, Journal of Applied Physics **71** (11), 5650 (1992).

[173] S. Geller, Acta Crystallographica **9**, 885 (1956).

[174] F. Buta, PhD thesis, The Ohio State University, 2003.

[175] R. Flukiger, J. L. Jorda, A. Junod, and P. Fischer, Applied Physics Communications **1**, 9 (1981).